# Insulating Van Vleck paramagnets at high magnetic fields (Review)

M. S. Tagirov and D. A. Tayurskiĭ[a)]

*Kazan State University, ul. Kremlevskaya 18, 420008 Kazan, Russia*
(Submitted November 8, 2001)
Fiz. Nizk. Temp. **28**, 211–234 (March 2002)

Theoretical and experimental results are presented on the magnetic properties of insulating Van Vleck paramagnets at high magnetic fields, where the Zeeman energy of an ion becomes comparable to the characteristic energies of the Stark splittings.  [DOI: 10.1063/1.1468518]

## INTRODUCTION

Van Vleck or polarization paramagnets comprise a rather wide class of solid-state magnets that has been studied for a long time. Van Vleck paramagnetism is as universal a magnetic property of solids as diamagnetism. It is caused by the elastic deformation of the electron shell of an atom or ion by an external magnetic field, giving rise to an induced magnetic moment. Thus, unlike orientational paramagnetism, where already-formed magnetic moments of atoms or ions are ordered in a magnetic field, Van Vleck paramagnetism is of a polarizational nature. The static magnetic susceptibility of these magnets obeys a Curie law at high temperatures and becomes constant at low temperatures. The quantum-mechanical theory developed by Van Vleck[1,2] explains this behavior of the magnetic susceptibility by the absence of a magnetic moment in the ground state of the ion (the electronic ground state is either a singlet or a nonmagnetic doublet) and the appearance of a contribution to the susceptibility due to virtual transitions induced by the Zeeman interaction with the external magnetic field between the ground and excited states of the ion. Van Vleck paramagnetism most often occurs in crystals containing non-Kramers rare-earth (RE) ions, i.e., RE ions with an even number of electrons in the unfilled $4f$ shells (e.g., $Pr^{3+}$, $Eu^{3+}$, $Tb^{3+}$, $Ho^{3+}$, $Tm^{3+}$), where the crystalline electric field lifts the degeneracy of the ground multiplet $^{2S+1}L_J$, leading to typical splittings of the Stark structure of the order of 10–100 $cm^{-1}$. These splittings greatly exceed the energy of the RE ion in the usual magnetic fields, so that the Zeeman effect can be calculated using perturbation theory. A clear example of a Van Vleck ion is $Eu^{3+}$, with a ground state $^7F_0$, which is separated from the first excited state $^7F_1$ by an interval of 300 $cm^{-1}$. Because of this, at low temperatures (below 100 K) the magnetic susceptibility of $Eu^{3+}$ compounds is independent of temperature and has an appreciable value ($\sim 10^{-2}$ $mole^{-1}$).

The isotopes $^{141}$Pr, $^{159}$Tb, $^{165}$Ho, and $^{169}$Tm have a 100% abundance (the abundances of the europium isotopes $^{151}$Eu and $^{153}$Eu are 47.8% and 52.2%, respectively) and a nonzero nuclear spin, and therefore compounds of these elements posses nuclear as well as electronic magnetism. The rather strong hyperfine interaction makes these substances extremely interesting from the standpoint of studying electronic–nuclear magnetism. The magnetic field induced at the nucleus of the Van Vleck RE ion is many times greater than the applied external magnetic field and leads to enormous values (up to several hundred) of the paramagnetic shifts of the NMR lines. This causes many interesting features in the NMR of rare-earth ions, which accordingly can be classified as a phenomenon intermediate between ordinary nuclear magnetic resonance (NMR) and electron paramagnetic resonance (EPR). This so-called ''enhanced'' NMR is one of the most important methods for studying the magnetic properties of Van Vleck paramagnets (VVPs). The results of these studies have been reviewed in Refs. 3–6.

The majority of crystals of intermetallic compounds with non-Kramers RE ions have cubic symmetry, while the symmetry of crystals of insulating compounds is ordinarily lower; this leads to extremely high anisotropy of the effective gyromagnetic ratio of the nuclear spins of Van Vleck ions. Such anisotropy, which is not observed in ordinary NMR, emphasizes further the intermediate character of ''enhanced'' NMR.

Because of these features, VVPs can be used for cooling nuclear spin systems[7] and for studying the effects of nuclear magnetic ordering at higher temperatures than in the case of ordinary nuclear paramagnets.[3]

Many insulating VVPs also exhibit the cooperative Jahn–Teller (JT) effect, i.e., a change in the symmetry of the crystal lattice and the related lowering of the energy due to splitting of the degenerate ground state of the RE ion.[8,9] An external magnetic field has a substantial influence on the temperature of structural phase transitions in such systems and can sometimes suppress such a transition completely. Concentrated VVPs can also exhibit the so-called Davydov splitting—splitting of the states of a RE ion without a change of symmetry of the crystal lattice, due to magnetic dipole–dipole interactions between ions and to the interaction via the phonon field.[10]

The magnetic properties of insulating VVPs have been quite well studied in the region of low temperatures and moderate magnetic fields, where the energy of the Zeeman interaction is many times smaller than the characteristic energies of the Stark splitting. As we have said, the main method of experimental study of these substances under such conditions is ''enhanced'' NMR.[3–5] Optical spectroscopy is not very informative because of the rather large inhomogeneous broadening, and ordinary EPR has been observed only on impurity paramagnetic ions, which can sometimes introduce substantial local distortions to the crystal lattice of the

 

VVP. Further increase of the magnetic field leads to violation of the conditions of applicability of perturbation theory, which has been used in obtaining all of the theoretical results concerning VVPs. It is impossible to say, *a priori*, what physical effects will be observed in systems of this sort at high magnetic fields.

Furthermore, it is of definite interest to determine whether an rf paramagnetic resonance due to transitions between the lower sublevels of the ground Stark multiplet can be observed in VVPs. It is clear from general arguments that at high magnetic fields (such that the Zeeman energy is comparable to the characteristic energies of the Stark splitting) the energy intervals between states of a Stark multiplet should depend on the value of the applied magnetic field. From this standpoint the theoretical studies of the influence of high magnetic fields on the energy spectrum of a Van Vleck ion and the experimental observations of the rf resonance transitions are extremely topical.[11,12] In the case of thulium compounds the frequencies of these transitions lie in the terahertz range. We also note that at moderate magnetic fields the use of rf (submillimeter) EPR technique makes it possible to investigate transitions between Zeeman sublevels of the Stark structure of non-Kramers ions having a ground state in the form of either a doublet[13–18] or a quasi-doublet with a small initial splitting.[15,19] As to VVPs, the submillimeter EPR spectra of $Ho^{3+}$ ions in $KY_3F_{10}$:Ho due to transitions between the ground state and an excited singlet state at moderate magnetic fields (up to 1 T) were studied in Refs. 20 and 21.

This review is organized as follows. In Sec. 1 the data on the structure and magnetic properties of insulating VVPs in moderate magnetic fields (at which the Zeeman energy of the RE ion is substantially less than the value of the Stark splittings in the crystalline field) are summarized for the particular examples of thulium ethyl sulfate $Tm(C_2H_5SO_4)_3\cdot 9H_2O$ and thulium double fluoride $LiTmF_4$. Section 2 is devoted to a detailed description of the theoretical and experimental results which we obtained in studies of insulating VVPs at high magnetic fields. The main results are stated in the Conclusion.

## 1. INSULATING VAN VLECK PARAMAGNETS AT MODERATE MAGNETIC FIELDS

### 1.1. Crystal structure of some insulating VVPs

As typical examples of insulating VVPs, let us consider thulium ethyl sulfate $Tm(C_2H_5SO_4)_3\cdot 9H_2O$ (TmES) and the double fluoride of thulium $LiTmF_4$. The TmES crystal has a rather complex but well-studied structure. The projection of the unit cell on a plane perpendicular to the symmetry axis $c$ is shown in Fig. 1a. The unit cell contains two molecules (128 atoms), and the two magnetically equivalent positions of the thulium ions have $C_{3h}$ symmetry. The nearest-neighbor environment of the Van Vleck ion [Fig. 1b] is formed by nine $O^{2-}$ ions of water molecules, three of which lie in the plane of the $Tm^{3+}$ ion while the other six form a regular triangular prism. The distance between two nearest-neighbor thulium ions is $\sim 7$ Å.

The double fluoride of thulium $LiTmF_4$ has a structure of the scheelite type (Fig. 2) with space group $C_{4h}^6$ and point group $S_4$ at the thulium ion positions. The unit cell contains two molecules, and the nearest-neighbor environment of the RE ion is formed by two deformed tetrahedra of fluorine ions. The distance between two nearest-neighbor thulium ions is $\sim 3.75$ Å.

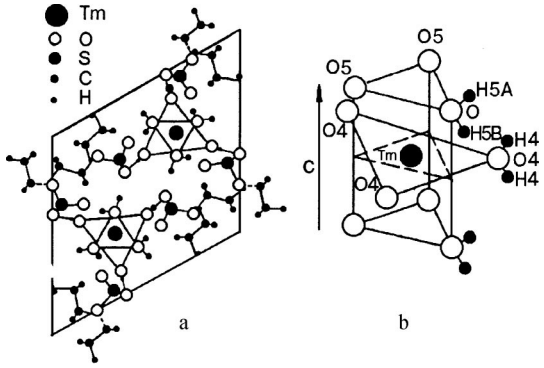


FIG. 1. Projection of the unit cell of TmES on a plane perpendicular to the $c$ axis (a); the nearest-neighbor environment of the $Tm^{3+}$ ion in TmES (b).

### 1.2. Electronic–nuclear magnetism of insulating VVPs (as illustrated by the case of TmES)

The theoretical description of the magnetic properties of insulating VVPs at moderate magnetic fields is based on the use of perturbation theory and has been set forth in detail in several review articles.[4–6] For illustration of the differences in the behavior of the electronic–nuclear spin system of VVPs at moderate and high magnetic fields, let us briefly consider for the case of TmES the usual scheme for calculating the magnetization of rare-earth Van Vleck ions in a situation where perturbation theory is applicable. The Hamiltonian of an isolated Van Vleck ion can be written as

$$H = H_{\rm cr} + H_{eZ} + H_{nZ} + H_{hf}, \tag{1.1}$$

where the Hamiltonian $H_{\rm cr}$ of the crystalline electric field determines the structure (the so-called Stark structure) of the electronic levels of the ion in the absence of magnetic field.

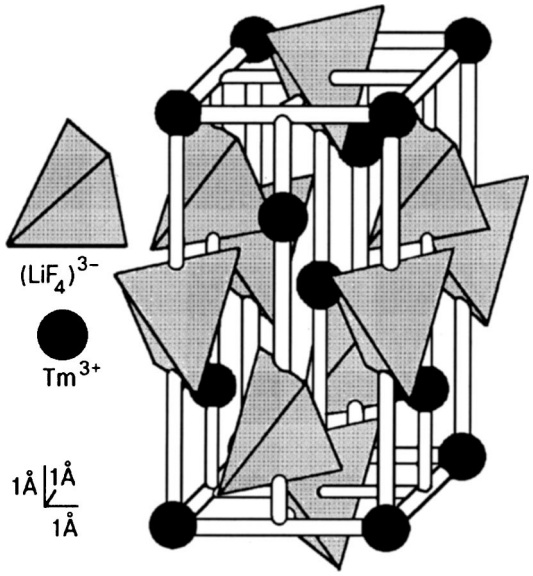


FIG. 2. Crystal lattice of $LiTmF_4$.

TABLE I. Crystal-field parameter (in $cm^{-1}$) in thulium ethyl sulfate TmES according to the data of Ref. 24.

| $B_{20}$ | $B_{40}$ | $B_{60}$ | $B_{66}$ |
|---|---|---|---|
| 130.5 | −65.0 | −28.6 | 427.3 |

The magnetic properties of RE ions are determined by the relative position and wave functions of the Stark sublevels arising on account of the crystal-field splitting of the ground multiplet $^{2S+1}L_J$ of the free ion. The other multiplets ordinarily lie at an interval of the order of $10^4$–$10^5$ $cm^{-1}$ from the ground multiplet, and the total splitting of the individual multiplets is of the order of $10^3$ $cm^{-1}$. The projection of the Hamiltonian $H_{cr}$ on the states of the ground multiplet in the case of TmES can be written in the form

$$H_{cr}=\alpha B_{20}O_2^0+\beta B_{40}O_4^0+\gamma(B_{60}O_6^0+B_{66}B_6^6), \tag{1.2}$$

where $\alpha$, $\beta$, $\gamma$ are the Stevens coefficients and in the case of the $Tm^{3+}$ ion ($J=6$) are equal to $1/3^2\cdot 11$, $2^3/3^4\cdot 5\cdot 11^2$, and $-5/3^4\cdot 7\cdot 11^2\cdot 13$, respectively; the operators $O_k^q$ are operator equivalents whose matrix elements have been tabulated in Refs. 22 and 23 for different values of the angular momentum $J$; the crystal-field parameters $B_{kq}$ are given in Table I.

In formula (1.1) the Hamiltonian $H_{eZ}$ describes the Zeeman interaction of the electron shell of the ion with the external magnetic field **H** and can be written as

$$H_{eZ}=g_J\mu_B\mathbf{H}\cdot\mathbf{J}, \tag{1.3}$$

where $\mu_B$ is the Bohr magneton, $J$ is the electron angular momentum operator, and $g_J$ is the Landé factor. The interaction of the nuclear magnetic moment ($\gamma_I$ is the gyromagnetic ratio of the free nuclei) with the external magnetic field is described in (1.1) by the Hamiltonian

$$H_{nZ}=-\gamma_1\hbar\mathbf{H}\cdot\mathbf{I}. \tag{1.4}$$

In accordance with what we have said, here and below we consider the $^{169}$Tm nucleus, with spin $I=1/2$, so that it is unnecessary to take quadrupole interaction effects into account. This same circumstance allows us to treat the interaction Hamiltonian of the nuclei with the electron cloud as only a contact hyperfine interaction with an interaction constant $A_J$:

$$H_{hf}=A_J\mathbf{J}\cdot\mathbf{I}. \tag{1.5}$$

In the TmES crystal the lower level of the RE ion $Tm^{3+}$ ($^3H_6$) in the crystalline electric field is a singlet. The energy levels and wave functions of the $Tm^{3+}$ ion in the absence of external magnetic field are listed in Table II.

At helium temperatures only the lower levels of the ground multiplet—the ground singlet and the first excited doublet $|d_{1,2}\rangle$—are occupied, and therefore we can limit consideration below to only these energy sublevels. In an external magnetic field that can be treated as a small perturbation, the doublet $|d_{1,2}\rangle$, with excitation energy $\Delta\approx 32$ $cm^{-1}$, is split (see Fig. 3; the value of the splitting is denoted as $\hbar\Omega$). With allowance for the nuclear spin $I=1/2$, each of the energy states obtained is twofold degenerate, and the influence of the nuclear Zeeman and hyperfine interactions $H_{nZ}$ and

TABLE II. Energy levels and wave functions of the $Tm^{3+}$ ion in the crystalline field in TmES.

| Energy, $cm^{-1}$ | | |
|---|---|---|
| Calculation (Ref. 6 and present study) | Experiment (Ref. 24 ) | Wave functions (present study ) |
| 304.1 | 302.5 | $0.707\|+3\rangle - 0.707\|-3\rangle$ |
| 277.0 | 274.0 | $0.895\|\pm 4\rangle - 0.446\|\mp 2\rangle$ |
| 220.6 | – | $0.697\|+6\rangle - 0.17\|0\rangle + 0.697\|-6\rangle$ |
| 214.2 | – | $\|s\rangle = 0.707\|+6\rangle - 0.707\|-6\rangle$ |
| 199.7 | 198.9 | $\|p_{1,2}\rangle = 0.95\|\pm 5\rangle - 0.307\|\mp 1\rangle$ |
| 159.2 | 157.3 | $0.707\|+3\rangle + 0.707\|-3\rangle$ |
| 111.5 | 110.9 | $0.446\|\pm 4\rangle + 0.895\|\mp 2\rangle$ |
| 31.7 | 32.1 | $\|d_{1,2}\rangle = 0.307\|\pm 5\rangle + 0.952\|\mp 1\rangle$ |
| 0 | 0 | $\|0\rangle = 0.12\|+6\rangle + 0.985\|0\rangle + 0.12\|-6\rangle$ |

$H_{hf}$ reduces to a further splitting of the electronic–nuclear states. Interestingly, the energy spectrum presented in Fig. 3 is reminiscent of the model spectrum considered in the theory of nuclear magnetism for studying the coupling of the nuclear and electronic spins.[25,26] This coupling is modeled by artificially singling out a pair of spins $S=1$ and $I=1/2$. In Van Vleck systems such a pair is singled out in a natural way, and the spectrum in Fig. 3 can be regarded as the spectrum of an electron–nucleus pair with $S=1$ and $I=1/2$ in the presence of an initial splitting of the electronic states described by the Hamiltonian $\Delta S_z^2$ with $\Delta>0$.

The equilibrium magnetization per ion is calculated by the standard methods of perturbation theory. The ion magnetic moment operator,

$$\mathbf{M}=-g_J\mu_B\mathbf{J}+\gamma_I\hbar\mathbf{I}=\mathbf{M}_J+\mathbf{m}_I, \tag{1.6}$$

is averaged with the density matrix

$$\rho=\frac{\exp(-\beta_0 H)}{\mathrm{Tr}\exp(-\beta_0 H)}, \tag{1.7}$$

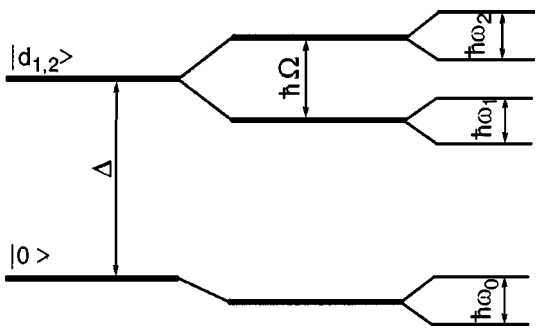


FIG. 3. Diagram of the lower electronic–nuclear levels of a Van Vleck ion with nuclear spin 1/2.

where $\beta_0 = 1/k_B T$ is the inverse temperature. At temperatures that are not too low and at moderate magnetic fields the thermal energy $k_B T$ is many times greater than the energies due to the terms $H_{eZ}$ and $H_{hf}$, and one can use the initial terms of the expansion of the density matrix by the Kubo formula:

$$\exp(-\beta_0 H) = \exp(-\beta_0 H_{\rm cr})\left[1 - \int_0^{\beta_0} d\lambda H_{\rm per}(\lambda) + \int_0^{\beta_0} d\lambda_1 \int_0^{\lambda_1} d\lambda_2 H_{\rm per}(\lambda_1) H_{\rm per}(\lambda_2) - \ldots\right], \tag{1.8}$$

where

$$H_{\rm per}(\lambda) = \exp(\lambda H_{\rm cr})(H_{eZ} + H_{nZ} + H_{hf})\exp(\lambda H_{\rm cr}) = -g_J \mu_B \mathbf{H}\cdot\mathbf{J}(\lambda) - \gamma_I \hbar \mathbf{H}\cdot\mathbf{I} + A_J \mathbf{I}\cdot\mathbf{J}(\lambda).$$

To the first order the electronic magnetization is given by

$$\mathbf{M}_H = \tilde{\chi}\mathbf{H}, \quad \chi_{\alpha\beta} = g_J^2 \mu_B^2 \int_0^{\beta_0} d\lambda \,\mathrm{Tr}\{\rho_0 J_\beta(\lambda) J_\alpha\}, \tag{1.9}$$

where $\rho_0$ is the density matrix with the unperturbed Hamiltonian $H_{\rm cr}$. Calculations of the trace of the product of matrices in the representation in which $H_{\rm cr}$ is diagonal, i.e., using the energy levels and wave functions from Table II, give the Van Vleck formula for the susceptibility:

$$\chi_{\alpha\beta} = g_J^2 \mu_B^2 \frac{\Sigma_l[\exp(-\beta_0 E_l^0)\{\beta_0 \Sigma_{l'} \langle l|J_a|l'\rangle\langle l'|J_\beta|l\rangle + \langle l|J_\alpha C_l J_\beta + J_\beta C_l J_\alpha|l\rangle\}]}{\Sigma_l \exp(-\beta_0 E_0^1)}, \tag{1.10}$$

where

$$C_l = \sum_m \frac{|m\rangle\langle m|}{E_m^0 - E_l^0}, \tag{1.11}$$

$|l\rangle, |l'\rangle$ are states with the same (unperturbed) energy $E_l^0$. For systems with a nonmagnetic ground state, as is the case in VVPs, formula (1.10) is also good at low temperatures ($\Delta \sim k_B T$), where only the ground level is occupied. For the ground singlet state in this case we obtain a temperature-independent susceptibility:

$$\chi_{\alpha\beta}^0 = g_J^2 \mu_B^2 T_{\alpha\beta}, \quad T_{\alpha\beta} = \langle 0|J_\alpha C_0 J_\beta + J_\beta C_0 J_\alpha|0\rangle. \tag{1.12}$$

The nuclear magnetization to the first order of perturbation theory is the same as usual:

$$\mathbf{m}_I^{(1)} = \frac{1}{3} I(I+1)\gamma_I^2 \hbar^2 \beta_0 \mathbf{H},$$

but it can happen that the dominant contribution comes from the terms of second order:

$$m_I^{(2)} = \frac{1}{3}\gamma_I \hbar A_J g_J \mu_B I(I+1) \times \int_0^{\beta_0} d\lambda_1 \int_0^{\lambda_1} d\lambda_2 \mathrm{Tr}\{\rho_0[J_\beta(\lambda_1)J_\alpha(\lambda_2) + J_\alpha(\lambda_1)J_\beta(\lambda_2)]\}H_\beta.$$

Simple calculations lead to the following expression for the nuclear magnetization:

$$\mathbf{m}_I = \mathbf{m}_I^{(1)} + \mathbf{m}_I^{(2)} = \frac{\gamma_I^2 \hbar^2 I(I+1)}{3}\left(1 + \frac{A_J}{g_J \mu_B \gamma_I \hbar}\tilde{\chi}\right)\mathbf{H}, \tag{1.13}$$

which corresponds to an ''enhanced'' external magnetic field.

The contributions to $\mathbf{M}_J = \mathrm{Tr}(\rho \mathbf{M}_J)$ in the second and third orders of perturbation theory are the magnetization induced in the electron shells by the nuclear moments. This twice-enhanced magnetism is especially noticeable at very low temperatures ($\Delta \sim k_B T$). Under this condition the calculation of the magnetization simplifies because of the fact that only the nuclear sublevels of the ground electronic singlet are occupied. The energy and wave functions of the nuclear multiplet for $I = 1/2$ can be calculated using the spin Hamiltonian

$$H_I = -\gamma_I \hbar\left(\delta_{\alpha\beta} + \frac{A_J g_J \mu_B}{\gamma_I \hbar} T_{\alpha\beta}\right)H_\alpha I_\beta = -\gamma_I \hbar \mathbf{H}(1+\tilde{\alpha})\mathbf{I} = -\hbar \mathbf{H}\tilde{\gamma}\mathbf{I}. \tag{1.14}$$

Here we have introduced the NMR paramagnetic shift tensor $\tilde{\alpha}$ and the effective gyromagnetic ratio tensor $\tilde{\gamma}$. The Hamiltonian (1.14) can be rewritten in the form

$$H_I = -\hbar \mathbf{H}\tilde{\gamma}\mathbf{I} = -\gamma_I \hbar \mathbf{H}'\cdot\mathbf{I}, \tag{1.15}$$

by introducing a so-called ''enhanced'' magnetic field $\mathbf{H}'$, which in general has a different direction from that of the external magnetic field $\mathbf{H}$. In fact, as is seen from expression (1.15), the nuclear spin quantization axis Z coincides with the direction of the ''enhanced'' magnetic field. The splitting of the nuclear doublet for an arbitrary orientation of the external magnetic field is equal to

$$\hbar\omega_n = \gamma_I \hbar H', \quad H' = \sqrt{\mathbf{H}'^2}, \tag{1.16}$$

and the electronic–nuclear stationary states can be written as

$$|01\rangle = N_1|0\rangle\left(\left|+\frac{1}{2}\right\rangle + \frac{H_x' - iH_y'}{H_z' + H'}\left|-\frac{1}{2}\right\rangle\right),$$
$$|02\rangle = N_2|0\rangle\left(\left|-\frac{1}{2}\right\rangle + \frac{H_z' - H'}{H_x' + iH_y'}\left|+\frac{1}{2}\right\rangle\right), \tag{1.17}$$

where $N_1$ and $N_2$ are normalizing factors. If the occupation of the other electronic–nuclear states is neglected completely, then instead of (1.17) one obtains the following expressions for the magnetization:

$$\mathbf{M} = \mathbf{m}_I + \mathbf{M}_J, \quad \mathbf{M}_J = \mathbf{M}_H + \mathbf{M}_I, \tag{1.18}$$

$$\mathbf{m}_I=\frac{\gamma_I\hbar}{2}\left(1+\frac{A_J g_J\mu_B}{\gamma_I\hbar}\tilde{T}\right)\frac{\mathbf{H}}{H'}\tanh\frac{\hbar H'}{2kT}, \tag{1.19}$$

$$\mathbf{M}_H=g_J^2\mu_B^2\tilde{T}\mathbf{H}=\tilde{\chi}^0\mathbf{H}, \tag{1.20}$$

$$\mathbf{M}_I=\frac{A_J g_J\mu_B}{\gamma_I\hbar}\tilde{T}\mathbf{m}_I=\frac{1}{2}A_J g_J\mu_B\tilde{T}\times\left(1+\frac{A_J g_J\mu_B}{\gamma_I\hbar}\tilde{T}\right)\frac{\mathbf{H}}{H'}\tanh\frac{\gamma_I\hbar H'}{2kT}. \tag{1.21}$$

At high temperatures ($k_B\gg\hbar\omega_0$) the nuclear magnetization is described by (1.13), as expected. The direction of $\mathbf{m}_I$ is in general different from the direction of the Van Vleck magnetization $\mathbf{M}_H$. Usually $\mathbf{M}_H$ is much greater than all the other contributions to the magnetization of an ion, but, as was mentioned back in Ref. 27, at ultralow temperatures, when the nuclear spin system is noticeably polarized even by a weak magnetic field, the contribution $\mathbf{M}_I$ can be dominant. A high polarization of the nuclear spin system means a substantial difference in the populations of the two nuclear sublevels of the singlet state of the Van Vleck ion. Later on, we shall see that in high magnetic fields the electronic and nuclear states are so strongly mixed together that it makes sense to speak of electronic–nuclear states of the ion, and even at low temperatures of the order of 1 K the occupation of the two lowest electronic–nuclear states differ quite strongly, and in this sense one can speak of a large polarization of the electronic–nuclear spin system (see Sec. 2.4).

In the second-order perturbation theory used above, the spin Hamiltonian of the $^{169}$Tm nuclei in the TmES crystal can be written in the form

$$H_I=-\gamma_\perp\hbar H(I_x\sin\theta\cos\varphi+I_y\sin\theta\sin\varphi)-\gamma_\parallel\hbar H I_z\cos\theta, \tag{1.22}$$

where $\theta$ and $\varphi$ are the polar angles of the magnetic field vector $\mathbf{H}$ in the system of principal axes of the tensor $\tilde{\gamma}$. NMR measurements on thulium in TmES at temperatures of 1.6–4.2 K[28,29] have shown that the parameters of the spin Hamiltonian (1.22) differ by more than a factor of 50:

$$\left|\frac{\gamma_\parallel}{2\pi}\right|=0.4802(5)\,\text{kHz/Oe},\qquad\left|\frac{\gamma_\perp}{2\pi}\right|=26.12(10)\,\text{kHz/Oe} \tag{1.23}$$

(in the $LiTmF_4$ crystal the analogous parameters have the values 0.965 and 24.11 kHz/Oe, respectively).[29,30] Because of the extremely high anisotropy of the effective gyromagnetic ratio the angular dependence of the resonance field at a fixed spectrometer frequency has a very narrow and sharp peak (Fig. 4). Using the values of the effective gyromagnetic ratio tensor (1.23), one can easily obtain from formula (1.14) the principal values of the NMR paramagnetic shift tensor at helium temperatures:

$$\alpha_\parallel=0.364(2),\quad\alpha_\perp=73.2(3). \tag{1.24}$$

The cause of this strong anisotropy of the susceptibility is easily established from the form of the wave functions of the thulium ion (see Table II): a longitudinal field (the operator $J_z$) mixes into the ground singlet $|0\rangle$ only the high-lying state $|s\rangle$, whereas the transverse field (the operator $J_x$) couples $|0\rangle$ with the nearest excited state—the doublet $|d_{1,2}\rangle$.

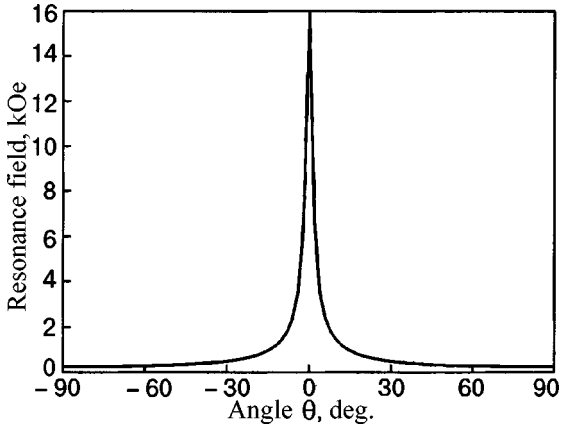


FIG. 4. Angular dependence of the value of the resonance field in the TmES crystal at a fixed spectrometer frequency of 7.5 MHz.

### 1.3. Some features of the behavior of the electronic–nuclear spin system of the $LiTmF_4$ crystal

In the crystalline electric field of tetragonal symmetry in $LiTmF_4$, the lower multiplet level $^3H_6$ ($J=6$) of the $Tm^{3+}$ ion is split into seven singlets and three doublets. The corresponding crystal-field Hamiltonian has the form

$$H_{\text{cr}}=\alpha B_{20}O_2^0+\beta B_{40}O_4^0+\beta(B_{44}O_4^4+iB_{4-4}O_4^{-4})+\gamma(B_{60}O_6^0+B_{64}O_6^4+iB_{6-4}O_6^{-4}. \tag{1.25}$$

The values of the crystal-field parameters are given in Table III. The calculated energy levels and wave functions of the $Tm^{3+}$ ion for this Hamiltonian are presented in Table IV together with the experimentally measured values of the energy levels. As we see from this table, in $LiTmF_4$ at low temperatures the ground singlet and the first excited doublet are occupied, and so the situation in regard to the electronic–nuclear states is identical to that discussed in detail above for TmES.

A characteristic feature of $LiTmF_4$ is the rather strong interaction of the $4f$ electron shell of the $Tm^{3+}$ ion with deformations of the crystal lattice, which gives rise to a giant magnetostriction.[32] Therefore, for correct analysis of the energy levels of the thulium ion in $LiTmF_4$ in an external magnetic field it is necessary to take the electron–deformation interaction into account (see the review[6] and Sec. 2.2 of this article).

TABLE III. Crystal-field parameters in ($cm^{-1}$) in the double fluoride $LiTmF_4$ according to the data of Ref. 31.

| $B_{20}$ | $B_{40}$ | $B_{60}$ | $B_{44}$ | $B_{4-4}$ | $B_{64}$ | $B_{6-4}$ |
|---|---|---|---|---|---|---|
| 184 | −89.6 | −4.06 | −727 | −628.5 | −328 | −284 |

TABLE IV. Energy levels and wave functions of the $Tm^{3+}$ ion in the crystalline field in the thulium double fluoride $LiTmF_4$.

| Energy, $cm^{-1}$ | | Wave functions |
|---|---|---|
| Calculation (Ref. 32 and present study) | Experiment (Ref. 31 and 33) | |
| 437.6 | – | $(0.18-0.18i)\|-6\rangle+(0.66-0.05i)\|-2\rangle+(-0.52-0.39i)\|2\rangle+(-0.06-0.25i)\|6\rangle$ |
| 426.8 | – | $(-0.06+0.65i)\|-4\rangle+(0.22-0.32i)\|0\rangle+(-0.63+0.16i)\|4\rangle$ |
| 412.9 | – | $(-0.64+0.55i)\|-3\rangle+0.54\|1\rangle+(-0.03-0.02i)\|5\rangle;$ $(-0.006+0.03i)\|-5\rangle+(0.41-0.35i)\|-1\rangle-0.84\|3\rangle$ |
| 384.6 | – | $(0.006-0.03i)\|-3\rangle+(-0.01+0.01i)\|1\rangle-0.99\|5\rangle;$ $(-0.77+0.62i)\|-5\rangle-0.01\|-1\rangle+(0.02+0.02i)\|3\rangle$ |
| 371.8 | 363 | $(0.63-0.32i)\|-4\rangle+(-0.45-0.58i)\|4\rangle$ |
| 321.5 | 319 | $(-0.38-0.59i)\|-6\rangle+(0.02-0.11i)\|-2\rangle+(0.08-0.07i)\|2\rangle+0.7\|6\rangle$ |
| 294.4 | 282 | $(0.14-0.64i)\|-6\rangle+(-0.21+0.16i)\|-2\rangle+(0.26-0.02i)\|2\rangle+(-0.46-0.46i)\|6\rangle$ |
| 60.61 | 56 | $-0.27\|-4\rangle+(-0.7-0.6i)\|0\rangle+(-0.04-0.27i)\|4\rangle;$ |
| 31.12 | 31 | $\|d_1\rangle=-0.004\|-5\rangle+(-0.66-0.52i)\|-1\rangle+(-0.1-0.53i)\|3\rangle;$ $\|d_2\rangle=-0.54\|-3\rangle+(-0.64-0.55i)\|1\rangle+0.004i\|5\rangle$ |
| 0 | 0 | $\|0\rangle=(-0.06-0.09i)\|+6\rangle+(-0.1-0.69i)\|2\rangle+(-0.53-0.46i)\|-2\rangle+0.11\|2\rangle$ |

*Note*: The wave functions given in Ref. 32 have been refined in the present study.

## 2. INSULATING VAN VLECK PARAMAGNETS AT HIGH MAGNETIC FIELDS

### 2.1. Energy spectrum of the Van Vleck ion

In magnetic fields above 5 T, where the Zeeman energy of the Van Vleck ion [the Hamiltonian $H_{eZ}$ in (1.1)] becomes comparable to the distances between energy levels of the Stark structure, which is determined by the term $H_{\rm cr}$ in (1.1), the perturbation theory usually used to calculate the magnetic characteristics of the Van Vleck ion becomes inapplicable, and one is faced with the problem of how to investigate the influence of the external magnetic field on the states of the Van Vleck paramagnetic ion. High magnetic fields should alter both the energy intervals between levels of the Stark structure and also the form of the corresponding wave functions. The latter circumstance can lead to qualitatively new effects, since the strong mixing of the wave functions within the ground multiplet changes the selection rules for resonance transitions. We note here that, as before, we are considering the ground multiplet, since the distance between adjacent terms is usually tens of thousands of reciprocal centimeters, much greater than the Zeeman energy of the ion. From a fundamental standpoint our calculations (the techniques and results of which are described below) can be generalized without particular difficulty to include the mixing of states of different terms by the magnetic field. However, calculations of that kind are rather awkward, and for a clearer illustration of the effect of high magnetic fields on the properties of VVPs we shall restrict discussion to the states of the ground multiplet only.

For the $Tm^{3+}$ ion in the TmES crystal, the spin Hamiltonian within the ground multiplet can be written as

$$H=H_{\rm cr}+H_{eZ}=\alpha B_{20}O_2^0+\beta B_{40}O_4^0+\gamma(B_{60}O_6^0+B_{66}O_6^6)+g_J\mu_B\mathbf{H}_0\cdot\mathbf{J}, \tag{2.1}$$

where $J=6$, and the values of the Stevens coefficients $\alpha$, $\beta$, and $\gamma$, the operators $O_k^q$, and the values of the crystal-field parameters $B_{kq}$ are given in the discussion of formula (1.2). For simplicity we shall for now neglect the hyperfine and nuclear Zeeman interactions, the influence of which will be studied in Sec. 2.5. The eigenstates and the corresponding eigenvalues of the Hamiltonian (2.1) are found by numerical diagonalization of a $13\times13$ matrix ($J=6$) for arbitrarily specified values and directions of the magnetic field $\mathbf{H}_0$. Figure 5 shows the curves obtained for the field dependence of the energy levels of the Stark structure for a magnetic field orientation perpendicular to the crystallographic axis $c$. We see that high magnetic fields lead not only to splitting of the states and changes in the intervals between energy levels but also to changes in the order of succession of the levels. At helium temperatures the magnetic properties of the ion are determined by the lower levels: the singlet $|g\rangle$ and the first excited doublet $|d_{1,2}\rangle$, which is split by the magnetic field. The wave functions obtained by numerical diagonalization of

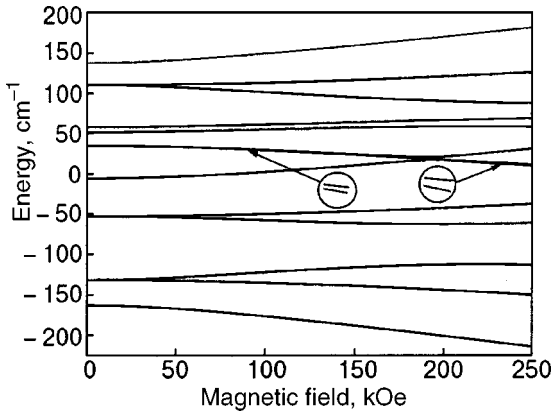


FIG. 5. Positions of the energy levels of the Stark structure of the $Tm^{3+}$ ion (ground term $^3H_6$, $J=6$) in the TmES crystal as functions of the magnitude of a magnetic field directed perpendicular to the crystallographic axis $c$.[11]

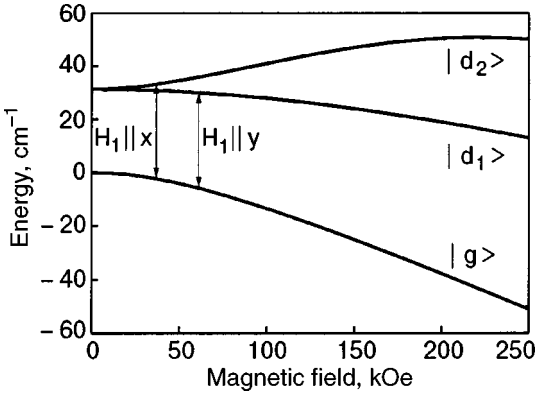


FIG. 6. Positions of the three lower energy levels of the ground multiplet $^3H_6$ of the $Tm^{3+}$ ion in TmES in a magnetic field $\mathbf{H}_0 \perp c$. Also shown are resonance transitions for a molecular gas laser line at frequency 1043.45 GHz and for different polarizations of the alternating field $\mathbf{H}_1$ under the condition that $\mathbf{H}_0 \| x$ (Refs. 11 and 12).

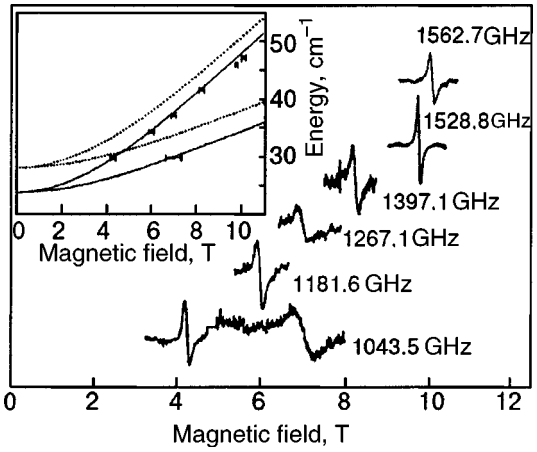


FIG. 7. EPR spectra for the system LaES:$Tm^{3+}$ (from Ref. 12). The inset shows the experimental positions of the resonance lines and the theoretical curves obtained with the use of the crystal-field parameters of Ref. 24 (dotted curves) and the parameters "reduced" with allowance for the difference of the ionic radii (solid curves).

the Hamiltonian (2.1) can be used to calculate the matrix elements of arbitrary operators, including the angular momentum operators of the ion. Such calculations show that magnetic dipole transitions between the singlet state and the states of the doublet can be induced by an alternating magnetic field $\mathbf{H}_1$ with a suitable orientation. For example, if the static magnetic field is assumed to be directed along the $x$ axis, then an alternating magnetic field directed along the $y$ axis will induce transitions $|g\rangle \rightarrow |d_1\rangle$, while an alternating magnetic field directed along the $x$ axis (i.e., $\mathbf{H}_0 \| \mathbf{H}_1$) will induce transitions to the other sublevel of the excited doublet: $|g\rangle \rightarrow |d_2\rangle$. The corresponding transition frequencies lie in the far-infrared, and one can devise an experiment for observation of these resonance transitions with the use of far-IR laser sources. Figure 6 shows the positions of the three lowest energy levels of the $Tm^{3+}$ ion as a function of the magnetic field strength and the transitions for a 1043.45 GHz line of a molecular gas laser (the working medium of which was trideuteromethanol $CD_3OH$).

### 2.2. Radio-frequency EPR of thulium ions in thulium and lanthanum ethyl sulfate crystals

For observation of the predicted rf EPR, crystals of lanthanum ethyl sulfate containing thulium impurity ions (LaES:$Tm^{3+}$) and thulium ethyl sulfate TmES were placed inside a waveguide in the central part of a superconducting solenoid in such a way that $\mathbf{H}_0 \perp c$ and the waveguide axis lay in the direction of $\mathbf{H}_0$ (Ref. 12). For plane waves propagating along the axis of the waveguide the latter condition means that $\mathbf{H}_1 \perp \mathbf{H}_0$, but the propagation direction of far-IR radiation in a waveguide does not necessarily coincide with the waveguide axis, and so the direction of the alternating magnetic field $\mathbf{H}_1$ is not known precisely.

To generate in the far-IR radiation we used a molecular gas laser pumped by a $CO_2$ laser: for lasing at frequencies of 1043.45 and 1181.587 GHz we chose trideuteromethanol $CD_3OH$ as the working medium, while difluoromethane $CH_2F_2$ was used for lasing at 1267.08, 1397.12, 1528.77, and 1562.66 GHz.

Figure 7 shows the rf EPR signals in a dilute LaES:$Tm^{3+}$ system at a temperature of 1.2 K. At a frequency of 1043.45 GHz we observed two EPR signals, corresponding to transitions from the singlet state to one of the states of the excited doublet, while for the other frequencies, because of limitations on the magnetic field strength of the superconducting solenoid, we observed only the transition to the upper state of the doublet. The EPR lines had an approximately Lorentzian shape with a width of the order of 20 GHz for transitions to the upper state of the doublet, and 30 GHz for transitions to the lower state. Although the nuclear spin of $^{169}Tm$ is equal to 1/2, the hyperfine structure of the EPR lines was not observed because of the weakness of the hyperfine interaction. The difference in the intensities of the two EPR lines at 1043.45 GHz (the integrated intensity of the "low-field" transition $|g\rangle \rightarrow |d_2\rangle$ is smaller by a factor of 10 than that of the "high-field" transition $|g\rangle \rightarrow |d_1\rangle$) can be explained by the fact that the $y$ component of the field $\mathbf{H}_1$ (which induces transitions $|g\rangle \rightarrow |d_1\rangle$) is many times greater than the $x$ component (which induces transitions $|g\rangle \rightarrow |d_2\rangle$), since the latter is directed along the waveguide axis, i.e., along the direction of propagation of the radiation.

The inset in Fig. 7 shows the experimentally determined positions of the resonance lines and the theoretical curves of the transition energies calculated using the crystal-field parameters from Ref. 24 (dotted curves). We see that the calculated curves differ quite strongly from the observed dependence of the transition energies. Much better agreement of the theoretical curves with the experimental points is obtained using the crystal-field parameters for the concentrated TmES system after they are reduced in an identical way to reflect the difference in the ionic radii of $Tm^{3+}$ and $La^{3+}$. The best agreement is obtained for a 9% reduction (the solid curves in the inset of Fig. 7), which gives the following values for the crystal-field parameters: $B_{20}=118.8$ cm$^{-1}$, $B_{40}=-60$ cm$^{-1}$, $B_{60}=-26$ cm$^{-1}$, and $B_{66}=388.8$ cm$^{-1}$. In zero magnetic field the splitting $\Delta E$ between the singlet state and the first excited doublet for these values of the crystal-field parameters comes out to be 28.9 cm$^{-1}$.

Figure 8 (curves *1*) shows the rf EPR signals of the $Tm^{3+}$ ions in the TmES crystal at a temperature of 1.2 K. The complex structure of the signal should apparently be

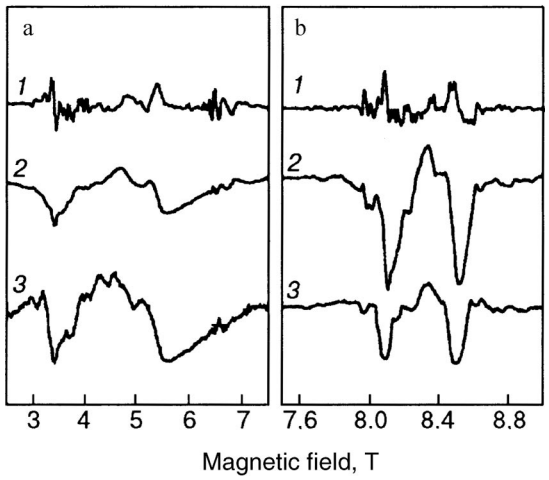


FIG. 8. EPR spectrum (*1*), integrated spectrum (*2*), and ''direct'' absorption spectrum (*3*) in the TmES crystal at frequencies of 1043.45 (a) and 1397.12 GHz (b) for $\mathbf{H}_0 \perp c$ and a temperature of 1.2 K (from Ref. 12).

attributed to the influence of spin–spin and spin–phonon interaction effects. As the temperature is raised, this complex structure of the EPR signal becomes less and less noticeable, so that at 20 K the signals for both transitions $|g\rangle \rightarrow |d_1\rangle$ and $|g\rangle \rightarrow |d_2\rangle$ were completely structureless. The integrated spectrum (see curve *2* of Fig. 8) is simpler for analysis. We note that in this system the absorption of the alternating field is strong enough that it becomes possible to measure directly the absorption as a function of field without field modulation. The integrated EPR spectrum correlates well with the ''direct absorption'' signal measured in this way (curve *3* in Fig. 8). From the rather asymmetric absorption lines obtained, we can obtain a good estimate of the resonance fields.

For the transition $|g\rangle \rightarrow |d_2\rangle$ an unexpected line splitting was observed at frequencies of 1043.45 and (especially) 1397.12 GHz. This prompted additional studies of the absorption spectra on a far-IR Fourier spectrometer (Bruker IFS113v) at liquid-helium temperatures in magnetic fields up to 10.53 T. The results of these studies are presented in Fig. 9. In zero magnetic field one sees only a single absorption line, corresponding to a transition between the singlet ground

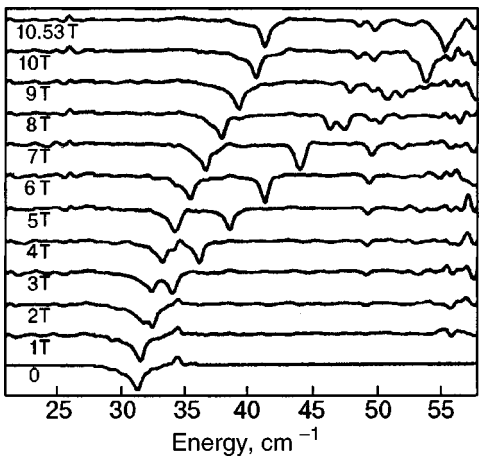


FIG. 9. Absorption spectra in the TmES crystal, obtained with the use of an IR Fourier spectrometer for $\mathbf{H}_0 \perp c$ at a temperature of 4.2 K (from Ref. 12).

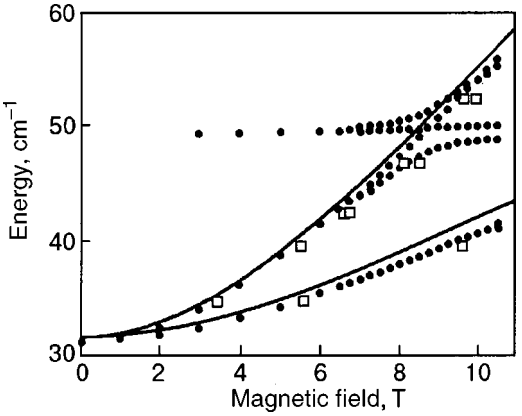


FIG. 10. Energies of transitions between the singlet state and the states of the first excited doublet in the TmES crystal: (●)—data of IR Fourier spectroscopy, (□)—rf EPR data, solid curves—calculation of Ref. 12.

state and the unsplit doublet state, with a transition energy $\Delta E = 31.3$ cm$^{-1}$, in good agreement with calculations of the Stark structure, optical studies, and the results of ''enhanced'' NMR.[4] In magnetic fields above 2 T applied perpendicular to the crystallographic axis *c*, the absorption line is split, in complete agreement with our calculations presented in Sec. 2.1. In higher fields an additional absorption line rises in the spectrum, at an energy of 49 cm$^{-1}$, the position of which is initially independent of the magnetic field. For this reason it is natural to attribute this line to some vibrational or phonon level. Vibrational energy levels close to 49 cm$^{-1}$ were observed in the TmES crystal in Ref. 34. However, in magnetic fields above 6 T both the line of the $|g\rangle \rightarrow |d_2\rangle$ transition and this line of the vibrational level begin to split, exhibiting a surprising ''crossing–anticrossing'' behavior, the causes of which are discussed in detail in the next Section. We note only that this behavior is most likely due to the interaction between the $4f$ electron shell and phonons in the TmES crystal.

On the whole, we can say that the results of IR Fourier spectroscopy and rf EPR studies of the influence of high magnetic fields on the energy levels of the Van Vleck ion $Tm^{3+}$ in a crystal are in good agreement with each other and with the results of our theoretical calculations (Fig. 10). In magnetic fields up to 6 T the states of the ion are well described by the single-particle Hamiltonian (2.1), apparently because of the rather large distance between nearest thulium ions (7 Å). In higher magnetic fields, however, the single-particle approximation is invalid, and the splitting of the $|g\rangle \rightarrow |d_2\rangle$ transition line, like the surprising ''crossing–anticrossing'' behavior, cannot be explained without taking the spin–spin and spin–phonon interactions into account.

### 2.3. Radio-frequency EPR of thulium ions in $LiTmF_4$ crystals

As we have said, magnetostriction measurements on $LiTmF_4$ single crystals in magnetic fields with inductions of 2–4 T have shown that the field-induced deformations reach giant values of the order of $10^{-3}$ (Ref. 32). Therefore, the theoretical study of the behavior of the energy levels of the thulium ion at high magnetic fields requires self-consistent allowance for the electron–deformation interaction, the con-

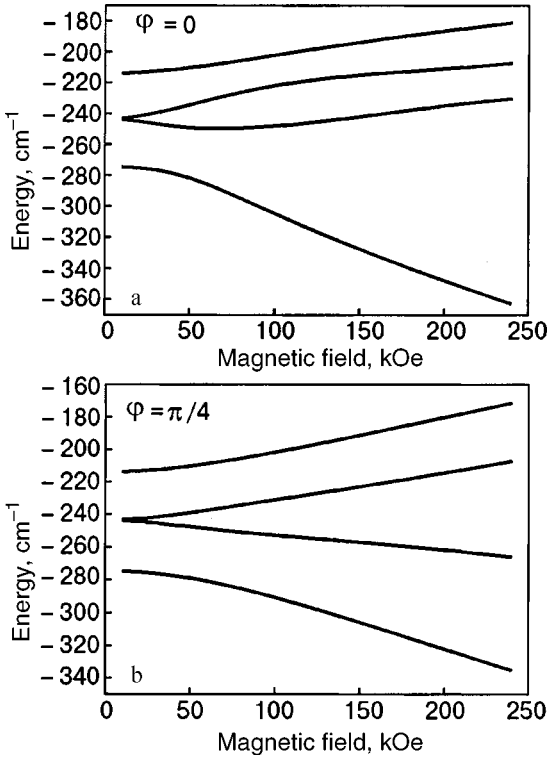


FIG. 11. Field dependence of the lower levels of the ground multiplet $^3H_6$ of the $Tm^{3+}$ ion in a $LiTmF_4$ single crystal for different orientations of the magnetic field in the plane perpendicular to the $c$ axis: along the $x$ axis (a), at an angle $\varphi=\pi/4$ to the $x$ axis (b).

stants of which depend on the value of the applied magnetic field. Since the thulium ion in the $LiTmF_4$ crystal occupies positions with local symmetry $S_4$, the position of the energy levels of the thulium ion depend on the direction of the magnetic field in the plane perpendicular to the local symmetry axis. If, in order to simplify the calculations, the variation of the elastic constants with magnetic field is neglected, then the behavior of the lower energy levels of the ground multiplet $^4H_6$ of the thulium ion—the ground singlet $\Gamma_2^1$ and the first excited doublet $\Gamma_{34}^1$ (30 $cm^{-1}$) and singlet $\Gamma_1^1$ (60 $cm^{-1}$)—depend on the value and direction of the magnetic field $\mathbf{H}_0$, as is shown in Fig. 11. Splitting of the non-Kramers doublet due to the direct (Zeeman) interaction of the electron magnetic moment with a magnetic field perpendicular to the symmetry axis of the crystalline field is possible only when the doublet is mixed with singlet states, and this splitting is a nonlinear even function of the field strength. The calculated values of the corresponding splittings are shown by the dotted curves in Figs. 12 and 13. It turned out to be possible to measure in the luminescence spectra the splitting of the lines corresponding to the transition $\Gamma_1^1(^3H_4)\rightarrow\Gamma_{34}^1(^3H_6)$ from the ground sublevel of the multiplet $^3H_4$ in a magnetic field applied perpendicular to the symmetry axis of the crystal, as a function of the magnitude and direction of the field in the basal plane at a temperature of 4.2 K.[35] The results of the measurements are shown in Figs. 12 and 13. The measured values of the splittings differ from the corresponding characteristics of the spectrum of an isolated RE ion in a magnetic field because of the linear interaction of the non-Kramers doublet with the deformations $e_{xx}-e_{yy}$ and $e_{xy}$ induced by the field in a concentrated paramagnet.[36] The calculated values of the splittings (the solid curves in Figs. 12 and 13; the variations of the elastic constants in the magnetic field were not taken into account) with the use of the electron–deformation interaction constants obtained in the framework of a semi-phenomenological model of the crystalline field agree satisfactorily with the data from measurements in fields $B_0<6$ T.

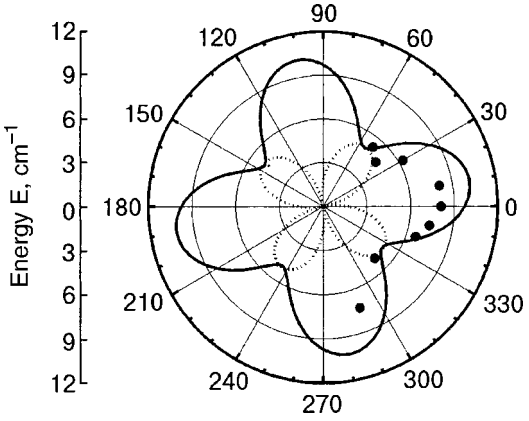


FIG. 12. Angular dependence of the splitting of the doublet $\Gamma_{34}^1(^3H_6)$ in a field perpendicular to the symmetry axis of the $LiTmF_4$ crystal ($H_0=4.05$ T).

The presence of the electron–phonon interaction and the rather strong spin–spin interaction (the distance between thulium ions in $LiTmF_4$ is nearly a factor of two smaller than in TmES) causes both the rf EPR line and the ''direct'' far-IR absorption line to acquire complex shapes (Fig. 14). Nevertheless, the energies of the transitions from the ground singlet state to the states of the first excited doublet could be determined; these data are shown by the unfilled symbols in Fig. 13. As we see from Fig. 14a, the line shape of the rf EPR line of the $Tm^{3+}$ ions in the $LiTmF_4$ crystal is complex; this, we believe, is due to transient processes in the spin–spin and spin–phonon interaction systems. Specially recorded EPR spectra of $Tm^{3+}$ ions at low modulation and slow sweep of the magnetic field confirmed our conjectures [see Fig. 14b]. Unfortunately, at this stage we are still far from having a complete understanding of all the processes that determine the line shape, and this is a subject for individual studies of the rf EPR in concentrated insulating VVPs.

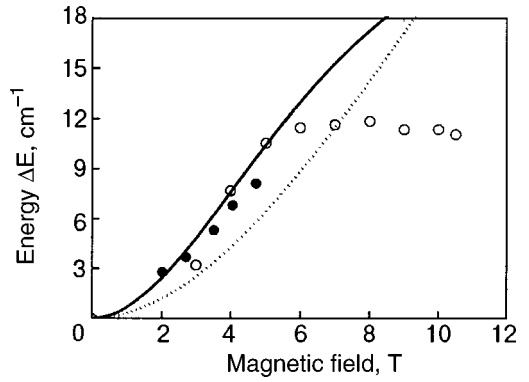


FIG. 13. Splitting of the doublet $\Gamma_{34}^1(^3H_6)$ as a function of the magnitude of the magnetic field $\mathbf{H}_0$ for an orientation of the field in the basal plane at an angle of 342° to the [100] axis, according to the EPR (○) and luminescence (●) data.

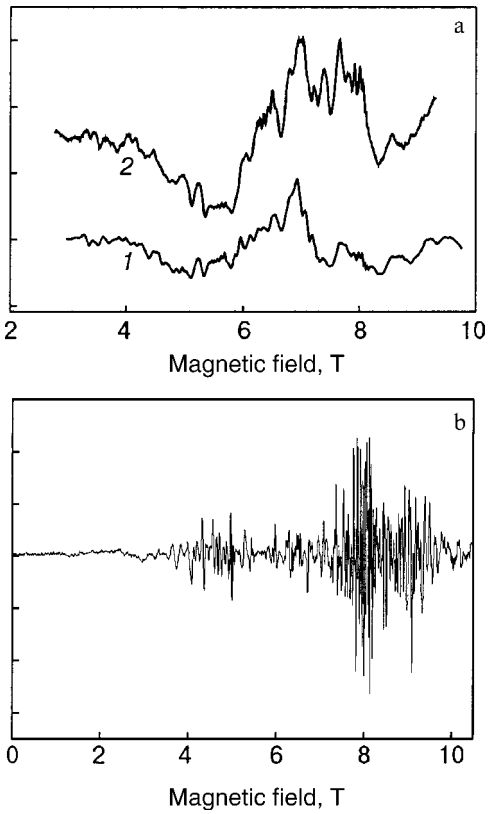


FIG. 14. Radio-frequency EPR spectrum (*1*) and direct IR absorption spectrum (*2*) in the $LiTmF_4$ crystal at a frequency of 1397.1186 GHz in a magnetic field $\mathbf{H}_0$ perpendicular to the *c* axis, at a temperature of 1.3 K (a); EPR spectrum of $Tm^{3+}$ ions in a $LiTmF_4$ crystal at a low modulation and slow sweep of the magnetic field (b).

Another extremely interesting manifestation of the strong electron–deformation interaction in thulium fluoride crystals is the presence of magnetic-field-induced (in fields around 5 T) structural phase transitions, which were observed in Refs. 37 and 38 (similar magnetic-field-induced structural phase transitions were observed in $TmPO_4$ in Ref. 39). However, since the physical features of these phase transitions are still the subject of intensive investigation, these questions will not be considered in this review article.

### 2.4. Coupled 4*f*-electron–phonon excitations in TmES

*2.4.1 Electron–phonon interaction in insulating Van Vleck paramagnets.* Electron–phonon interaction effects in RE compounds have been studied for a long time now. Among the various manifestations of the interaction between optical or acoustic phonons and localized $4f$ electrons it is necessary to recall, first of all, the cooperative Jahn–Teller effect—a phase transition observed in certain RE zircons, pnyctides, and spinels.[9] This phase transition consists in the ''freezing in'' of a static deformation of the crystal lattice and a simultaneous orientation of the electric and magnetic multipole moments of the RE ions and can be considered to be the result of an indirect interaction of the RE ion via the phonons.

Another effect of the interaction between multipole moments of the RE ions in the ground state and optical phonons is observed in a number of RE trifluorides and trichlorides in an external magnetic field at low temperatures [e.g., in the paramagnets $CeF_3$ (Ref. 40) and $CeCl_3$ (Ref. 41) and in the Ising ferromagnet $LiTbF_4$ (Ref. 42)]. If the magnetic field and temperature are such that ordering of the magnetic moments of the RE ions in the external field can occur, then because of the strong spin–orbit interaction this will also lead to ordering of the multipole moments, which, in turn, causes changes in the phonon spectrum even in the absence of the cooperative Jahn–Teller effect. In particular, splitting of the twofold degenerate phonon states in a magnetic field has been observed by the methods of Raman and IR spectroscopy;[41,42] this splitting is described by the expression

$$\Delta\omega = \Delta\omega_s \tanh\left(\frac{g\mu_B B}{kT}\right), \tag{2.2}$$

where $g$ is the $g$ factor of the electronic ground state, and $\Delta\omega_s$ is the maximum value of the splitting. Furthermore, in the compounds mentioned an ''anticrossing'' effect between the optical phonons and excitations in the system of $4f$ electrons was observed. The $4f$-electron–phonon interaction is also manifested in RE compounds, where the ground electronic state is a nonmagnetic one. For example, splitting of the twofold degenerate phonon states in a magnetic field and collective $4f$-electron excitations of the Frenkel type have been observed in the VVP $PrF_3$ (Refs. 43–45).

Let us consider the effect of a resonance interaction between $4f$ electrons and optical phonons in TmES. The electron–phonon interaction in ethyl sulfate crystals has also been the subject of earlier studies and is manifested, e.g., in an effective exchange interaction between the Kramers RE ions $Ce^{3+}$ via the phonon field under pressure.[46] In Sec. 2.2 we presented our results on the first observation of electron paramagnetic resonance and IR absorption in TmES due to transitions between the singlet ground state and the first excited doublet of the Van Vleck ion $Tm^{3+}$ in magnetic fields up to 10.5 T. In the IR absorption experiments in magnetic fields above 2 T an additional absorption line appears around 49 $cm^{-1}$ (see Fig. 9), the position of which is independent of the magnetic field in fields up to 6 T; this line was attributed to a phonon level. In fields above 6 T the additional phonon line and a line corresponding to a transition in the Stark structure of the $Tm^{3+}$ ion from the singlet ground state to one of the states of the nearest doublet (the degeneracy of which is lifted by the magnetic field) began to split, leading to surprising ''crossing–anticrossing'' behavior in fields of around 8.5 T (Fig. 10). This was also manifested in a rather complex structure of the EPR spectrum (see Fig. 8). This sort of behavior cannot be described without taking the spin–phonon and spin–spin interactions into account. In Ref. 47 we proposed a simple model describing the ''crossing–anticrossing'' behavior in terms of a resonance interaction between the $4f$ electrons and optical phonons; good agreement with the experimental data was obtained.

*2.4.2. Model Hamiltonian of the problem.* The effect of high magnetic fields ($>5$ T) on the Stark structure of the $Tm^{3+}$ ion in the TmES crystal (ground term $^3H_6$ ($J=6$)) was investigated in Sec. 2.1. At helium temperatures the magnetic properties of the ions are determined by the three lowest levels: a nonmagnetic singlet $|g\rangle$ and the first excited doublet $|d_{1,2}\rangle$, split by the magnetic field. Since the distance between $|g\rangle$ and $|d_1\rangle, |d_2\rangle$ in such magnetic fields is more

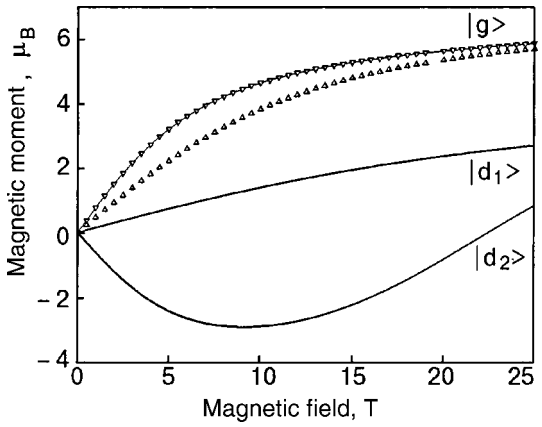


FIG. 15. Field dependence of the magnetic moments of the $|g\rangle$, $|d_1\rangle$, and $|d_2\rangle$ states of the $Tm^{3+}$ ion (solid curves) and the average magnetic moment of the $Tm^{3+}$ ion at $T=4.2$ K ($\nabla$) and 30 K ($\triangle$) (from Ref. 47).

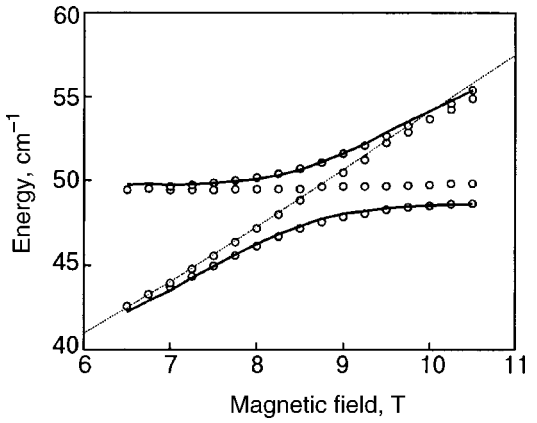


FIG. 16. Energies of elementary excitations in the TmES crystal as a function of magnetic field: ($\bigcirc$)—experimental data from far-IR Fourier spectroscopy,[12] dotted line—energy of the transition $|g\rangle \rightarrow |d_2\rangle$ in the system of Stark levels of the $Tm^{3+}$ ion (the function $\varepsilon(B)$ in Eq. (2.3b), solid curves—calculated spectrum of coupled $4f$-electron–phonon excitations (2.7) (from Ref. 47).

than 30 $cm^{-1}$ ($\approx$45 K), only the ground singlet is significantly occupied at $T=4.2$ K. We see in Fig. 15 that the magnetic moment of the $Tm^{3+}$ ion at 4.2 K is determined completely by the magnetic moment of the singlet state, while at 30 K, for example, the contribution of the excited doublet states is substantial. Transitions to the sublevels of the exchange doublet can be induced by an oscillatory magnetic field having a suitable direction with respect to the external magnetic field.[11,12] The dependence of the polarizational magnetic moment (due to the mixing of the wave functions of the states of the Stark structure as a result of the Zeeman interaction with the external magnetic field) on the magnitude of the magnetic field $\mathbf{B}_0$ for each of the states $|g\rangle$, $|d_1\rangle$, and $|d_2\rangle$ of the $Tm^{3+}$ ion is shown in Fig. 15. It is clearly seen that the values of the magnetic moments in the ground singlet state and in the excited doublet states are different. This means that the transition of the $Tm^{3+}$ ion from $|g\rangle$ to $|d_1\rangle$ or $|d_2\rangle$ is accompanied by a change of the magnetic moment, and each such transition can be treated as a transition in a two-level system. Thus, if it is additionally taken into account that, according to Ref. 48, the lifetime of thulium ions in excited states is rather short, it can be assumed that under the experimental conditions of Ref. 12 the number of ions in the excited states $|d_1\rangle$ and $|d_2\rangle$ is small, so that one may use the ''elementary excitations'' representation and introduce two types of mutually noninteracting excitations, corresponding to each of the excited states of the doublet. Since ''crossing–anticrossing'' behavior was observed in the experiment for the phonon line and the transition $|g\rangle \rightarrow |d_2\rangle$, we shall henceforth limit consideration to only one type of elementary excitations corresponding to this transition and described by the Hamiltonian:

$$H_{d2}=\sum_q \varepsilon_{\mathbf{q}}(B)a_{\mathbf{q}}^{+}a_{\mathbf{q}}. \tag{2.3a}$$

Here $a_{\mathbf{q}}^{+}$ and $a_{\mathbf{q}}$ are the Bose creation and annihilation operators for excitations with wave vector $\mathbf{q}$ (Bose statistics are chosen on considerations that the states $|g\rangle$ and $|d_2\rangle$ of the ''two-level'' system can be described with the use of an effective spin $S=1/2$, and in view of the smallness of the number of excitations the Holstein–Primakoff transformation can be used); $\varepsilon_{\mathbf{q}}(B)$ is the spectrum of elementary excitations as a function of the magnetic field $\mathbf{B}$. In the IR absorption experiments at helium temperatures the single-particle excitations appear only at the Brillouin zone center ($\mathbf{q}=0$), so that we drop the summation over wave vectors in (2.3a) and use the Hamiltonian

$$H_{d2}=\varepsilon(B)a^{+}a, \tag{2.3b}$$

where the function $\varepsilon(B)$ is found from experiment (see the dashed line in Fig. 16).

The rise of the phonon line (49 $cm^{-1}$) in magnetic fields above 2 T is due, we believe, to growth of the polarizational moment of the $Tm^{3+}$ ion and is one of the manifestations of the $4f$-electron–phonon interaction. Specifically, either a rather large polarization moment in the singlet ground state can lead to ''freezing in'' of the static deformation and the appearance of localized phonons or these phonons appear as a result of a reorientation of the magnetic moment of the ion when the alternating magnetic field induces a transition of the ion from the singlet state to a state of the excited doublet (see Fig. 15; the magnetic moments in the states $|g\rangle$ and $|d_2\rangle$ are of opposite sign). The answer to the question of which of these two mechanisms is operating can be given by experiments investigating the dependence of the energy of the phonon line on the amplitude of the alternating magnetic field (on the intensity of the irradiation of the crystal by a laser in the far-IR range). Here, of course, the number of these phonons depends on both the number of thulium ions in the excited state and on the value of their polarization moment. Therefore, the phonons can be described using the following Hamiltonian ($\mathbf{q}=0$):

$$H_{\mathrm{ph}}=(\omega-\mu(B))b^{+}b, \tag{2.4}$$

where $b^{+}$,$b$ are the creation and annihilation operators for phonons with energy $\omega=49$ $cm^{-1}$, and the function $\mu(B)$ plays the role of the chemical potential and can be approximated by the first term of the series in $B$: $\mu(B)\approx\mu_0+\eta B$. The parameters $\mu_0$ and $\eta$ are found from the condition of best agreement of the theoretical calculations with the experimental data.

The interaction between $Tm^{3+}$ ions and localized phonons is represented in our formalism by the Hamiltonian

$$H_{\rm int}=u(B)a^+b+u^*(B)ab^+ +\nu(B)a^+b^+ +\nu^*(B)ab, \tag{2.5}$$

where a linear approximation is used for the functions $u(B)$ and $\nu(B)$:

$$u(B)=u_0+u_1B, \quad \nu(B)=\nu_0+\nu_1B. \tag{2.6}$$

The interaction parameters $u_0$, $u_1$, $\nu_0$, and $\nu_1$ are also treated as adjustable parameters and are found from the condition of best fit of the calculations with the experimental data.

Thus the model Hamiltonian describing the system can be represented in the form

$$H=H_{d2}+H_{\rm ph}+H_{\rm int}=\varepsilon(B)a^+a+[\omega-\mu(B)]b^+b +u(B)a^+b+u^*(B)ab^+ +\nu(B)a^+b^+ +\nu(B)ab. \tag{2.7}$$

*2.4.3. Coupled $4f$-electron–phonon excitations.* The problem of finding the spectrum of excitations in a system consisting of two types of mutually interacting bosons and described by Hamiltonian (2.7) can be solved by the standard methods of the theory of Green's functions.[49,50] We construct the equations of motion for the commutator Green's functions

$$G_1=\langle\langle a|a^+\rangle\rangle, \quad G_2=\langle\langle b|a^+\rangle\rangle,$$

$$G_3=\langle\langle b^+|a^+\rangle\rangle, \quad G_4=\langle\langle a^+|a^+\rangle\rangle$$

and obtain a closed system of linear equations, for which one can find an explicit form of the Green's function $G_i$. The spectrum of elementary excitations is determined by the poles of the Green's functions. Ultimately, in the region where the frequencies of the phonons and excited states of the thulium ions coincide, the resonance interaction gives rise to two branches of coupled electron–phonon excitations:

$$E^2_{1,2}(B)=\frac{1}{2}[(\omega-\mu(B))^2+\varepsilon^2(B)] +|u(B)|^2+|\nu(B)|^2\pm\sqrt{D}, \tag{2.8}$$

$$D=\frac{1}{4}[(\omega-\mu(B))^2-\varepsilon^2(B)]^2+[(\omega-\mu(B))^2+\varepsilon^2(B)] \times[|u(B)|^2+|\nu(B)|^2]+4|u(B)|^2|\nu(B)|^2 +2(|u(B)|^2+|\nu(B)|^2)(\omega-\mu(B))\varepsilon(B).$$

In Fig. 16 the experimental points from Ref. 12 are shown along with the calculated curves obtained for the following values of the fitting parameters:

$\mu_0=-1.08$; $\rm cm^{-1}$; $\eta=0.17$ $\rm cm^{-1}/T$; $u_0=1.3$ $\rm cm^{-1}$;

$\nu_0=0.5$ $\rm cm^{-1}$; $u_1=0.04$ $\rm cm^{-1}/T$;

$\nu 1=0.008$ cm$-1$/T.

It is seen from the experimental curves that, in addition to the two branches of coupled excitations, there also appear a purely phononic absorption line and an absorption line due to the transition $|g\rangle\rightarrow|d_2\rangle$ in the system of thulium ions. This "crossing–anticrossing" behavior is unsurprising for the TmES system. The symmetry group of the crystal contains the inversion operation, so that the phonon branch is twofold degenerate. The unit cell of the crystal contains two $Tm^{3+}$ ions, and the equivalence of these two ions can be partially broken by a sufficiently high magnetic field, since the interaction of the ions with the magnetic field depends on the orientation of $\mathbf{B}_0$ relative to the local symmetry axes of the ion, which have different directions for the two $Tm^{3+}$ ions in the unit cell.

We note in conclusion that the simple model proposed for the description of coupled $4f$-electron–phonon excitations is, of course, a first approximation to the real situation. The complex structure observed in the EPR spectra[12] cannot be explained in the framework of a model of noninteracting excitations in the system of $Tm^{3+}$ ions. This structure quite likely corresponds to Davydov splitting and the onset of collective magnetic moments as a result of the $4f$-electron–phonon interaction (as to the possibility of observing Davydov splitting in VVPs, see, e.g., Ref. 10). Answering these and other questions will require additional experiments, e.g., by the method of IR Fourier spectroscopy (as a function of the irradiating power on the crystal) and by the method of neutron spectroscopy, to obtain more information about the magnetic properties of the coupled excitations. However, there can be no doubt about the fact that coupled $4f$-electron–phonon excitations have indeed been observed in the VVP TmES. Moreover, we see in Fig. 10 that in fields above 11 T the absorption line corresponding to the transition $|g\rangle\rightarrow|d_1\rangle$ "crosses" both the phonon line (49 $\rm cm^{-1}$) and one of the branches of coupled $4f$-electron–phonon excitations, so that at such magnetic fields one should expect new branches of electron–phonon excitations to appear. Preliminary measurements made by the present authors[51] at

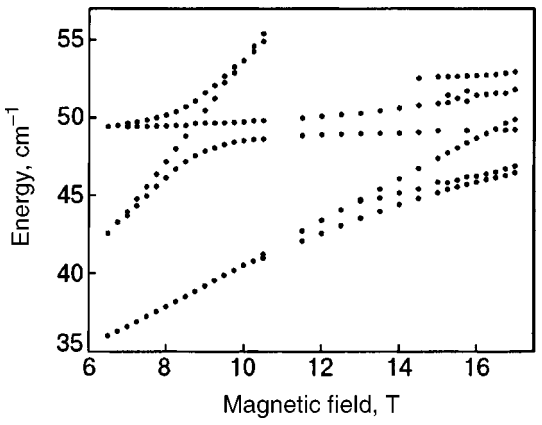


FIG. 17. Energies of elementary excitations in the TmES crystal as functions of magnetic field. The data of IR Fourier spectroscopy in magnetic fields up to 10.53 T are from Ref. 12 and the data at higher magnetic fields are from Ref. 51.

higher magnetic fields (up to 17 T) with an IR Fourier spectrometer confirm this hypothesis (see Fig. 17).

### 2.5. Coupled electron–nuclear states in insulating VVPs

As we have said, at a high magnetic field ($B_0 > 5$ T) the electron Zeeman interaction (1.3) cannot be treated as a perturbation. Moreover, a sufficiently high magnetic field will cause distortion of the electron shell and a redistribution of the electron density, inevitably altering the hyperfine field at the nucleus and the hyperfine interaction constants $A_J$. However, taking the resulting change in the interaction constants into account would unduly complicate the calculations, and for clarity in setting forth the essential changes arising in the properties of the electronic–nuclear spin system of an insulating VVP under the influence of a high magnetic field, we shall restrict discussion to Hamiltonian (1.1) with the same parameter values as were used in Sec. 1.1. Let us also mention here the recent attempts[53,54] to go beyond the framework of perturbation theory in analyzing the behavior of the coupled electronic–nuclear spin system in the intermetallic VVP $PrNi_5$.

For studying the influence of high magnetic fields it is necessary to do an exact diagonalization of Hamiltonian (1.1) by numerical means and to find the corresponding wave functions. This will make it possible to calculate the matrix elements of the operators of the electronic and nuclear spin systems and to evaluate both the magnetic moment of the Van Vleck ion in any state and the total magnetization.

As an initial basis for the wave functions we can choose the 26 wave functions in the form of a direct product of the electronic and nuclear wave functions:

$$|J=6,M_J\rangle|I=\frac{1}{2},m_1\rangle, \tag{2.9}$$

where $M_J = 6,5,\ldots,-6$ and $m_I = 1/2,-1/2$ are the electronic and nuclear magnetic quantum numbers, respectively. The field dependence of the electronic levels of the $Tm^{3+}$ ion in TmES in high magnetic fields was investigated in Sec. 2.1 (plots of this dependence for the ground singlet and the first excited doublet are given in Fig. 6). Let us first take up the influence of a high magnetic field on the nuclear magnetic sublevels. We note that the use of the term ''nuclear magnetic sublevels'' in analyzing the influence of high magnetic fields seems unfortunate to us, since, whereas at low magnetic fields the energy spectrum of a paramagnetic ion and the wave functions have the forms listed in Table II, and when the hyperfine and nuclear Zeeman interactions are taken into account the electronic–nuclear wave functions can be represented in the form

$$|0\rangle\left|+\frac{1}{2}\right\rangle,\ |0\rangle\left|-\frac{1}{2}\right\rangle\text{—for the ground singlet,}$$
$$|d_{1,2}\rangle\left|+\frac{1}{2}\right\rangle,\ |d_{1,2}\rangle\left|-\frac{1}{2}\right\rangle\text{—for the first excited doublet, etc.,} \tag{2.10}$$

so that one can indeed speak of nuclear sublevels, in high magnetic fields, as we have said, such a representation is not applicable and it is better to speak of electronic–nuclear sublevels. Figure 18 gives the field dependence of the frequencies of the transition between the electron–nuclear sublevels of the ground singlet for different values of the angle $\theta$ characterizing the direction of the magnetic field relative to the crystallographic axis $c$. We note two things. First, at high magnetic fields with orientations close to perpendicular (i.e., for maximum mixing of the wave functions by the external magnetic field), the transition frequencies approach the X band typical of electron paramagnetic resonance. Second, nonlinearity effects, manifested in nonmonotonic dependence of the transition frequencies in a given field as functions of the angle $\theta$, begin to appear. Figure 19 shows a plot of this dependence in a magnetic field of 150 kOe.

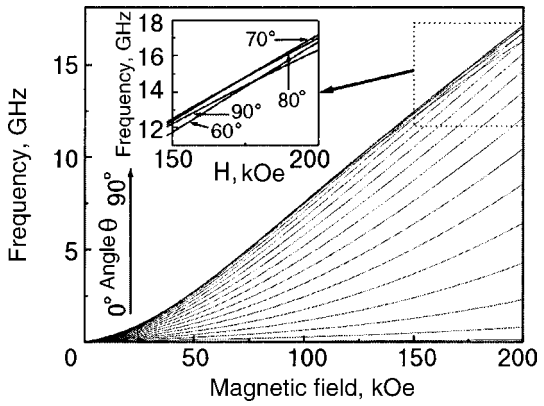


FIG. 18. Field dependence of the frequencies of transition between electronic–nuclear sublevels of the ground singlet for different orientations of the magnetic field with respect to the crystallographic axis $c$. The inset shows the nonmonotonic behavior of the transition frequency as a function of the angle $\theta$ in high magnetic fields.

As to the wave functions of the Van Vleck ion at high magnetic fields, they are a complicated combination of electronic–nuclear functions of the form (2.9). For example, in a magnetic field of the same strength (150 kOe) but directed perpendicular to the $c$ axis, the wave functions of the electronic–nuclear sublevels of the ground singlet are a linear combination of the functions (2.9) with the coefficients given in Table V.

As we see from Table V, the wave functions of the electronic–nuclear sublevels of the ground singlet at high magnetic fields are not described by (2.10) and, as a conse-

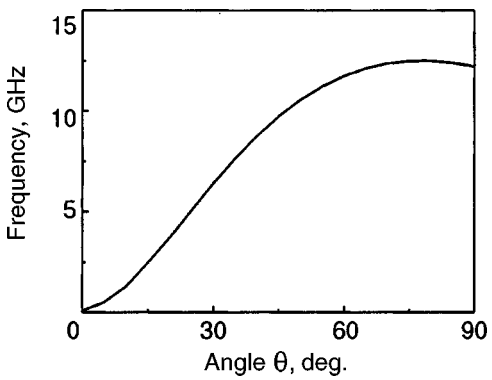


FIG. 19. Angular dependence of the frequencies of transition between the electronic–nuclear sublevels of the ground singlet in a magnetic field of 150 kOe.

TABLE V. Expansion coefficients of the wave functions of the electronic–nuclear sublevels $|0_1\rangle$ and $|0_2\rangle$ of the ground singlet in a basis of direct products of the electronic and nuclear wave functions in a magnetic field of 150 kOe.

| $\|J=6,M_J\rangle\|I=\frac{1}{2},m_I\rangle$ | $\|0_1\rangle$ | $\|0_2\rangle$ |
|---|---|---|
| $\|6\rangle\|\frac{1}{2}\rangle$ | −0.0414 | −0.0852 |
| $\|6\rangle\|-\frac{1}{2}\rangle$ | 0.0847 | −0.0419 |
| $\|5\rangle\|\frac{1}{2}\rangle$ | 0.0436 | −0.0229 |
| $\|5\rangle\|-\frac{1}{2}\rangle$ | −0.0889 | 0.0900 |
| $\|4\rangle\|\frac{1}{2}\rangle$ | −0.0111 | 0.0443 |
| $\|4\rangle\|-\frac{1}{2}\rangle$ | 0.0226 | −0.0113 |
| $\|3\rangle\|\frac{1}{2}\rangle$ | 0.0055 | 0.0110 |
| $\|3\rangle\|-\frac{1}{2}\rangle$ | −0.0111 | 0.0053 |
| $\|2\rangle\|\frac{1}{2}\rangle$ | −0.0314 | −0.0621 |
| $\|2\rangle\|-\frac{1}{2}\rangle$ | 0.0634 | −0.0300 |
| $\|1\rangle\|\frac{1}{2}\rangle$ | 0.1722 | 0.3422 |
| $\|1\rangle\|-\frac{1}{2}\rangle$ | −0.3486 | 0.1663 |
| $\|0\rangle\|\frac{1}{2}\rangle$ | −0.3545 | −0.7277 |
| $\|0\rangle\|-\frac{1}{2}\rangle$ | 0.7247 | −0.3577 |
| $\|-1\rangle\|\frac{1}{2}\rangle$ | 0.1696 | 0.3493 |
| $\|-1\rangle\|-\frac{1}{2}\rangle$ | −0.3455 | 0.1718 |
| $\|-2\rangle\|\frac{1}{2}\rangle$ | −0.0309 | −0.0635 |
| $\|-2\rangle\|-\frac{1}{2}\rangle$ | 0.0627 | −0.0313 |
| $\|-3\rangle\|\frac{1}{2}\rangle$ | 0.0055 | 0.0110 |
| $\|-3\rangle\|-\frac{1}{2}\rangle$ | −0.0111 | 0.0054 |
| $\|-4\rangle\|\frac{1}{2}\rangle$ | −0.0115 | −0.0219 |
| $\|-4\rangle\|-\frac{1}{2}\rangle$ | 0.0231 | −0.0105 |
| $\|-5\rangle\|\frac{1}{2}\rangle$ | 0.0477 | 0.0800 |
| $\|-5\rangle\|-\frac{1}{2}\rangle$ | −0.0929 | 0.0375 |
| $\|-6\rangle\|\frac{1}{2}\rangle$ | −0.0389 | −0.0799 |
| $\|-6\rangle\|-\frac{1}{2}\rangle$ | 0.0849 | −0.0415 |

quence, the matrix elements of the electron angular momentum operator **J** and nuclear spin operator **I** in a perpendicularly oriented magnetic field $B=150$ kOe, for example, have the following values:

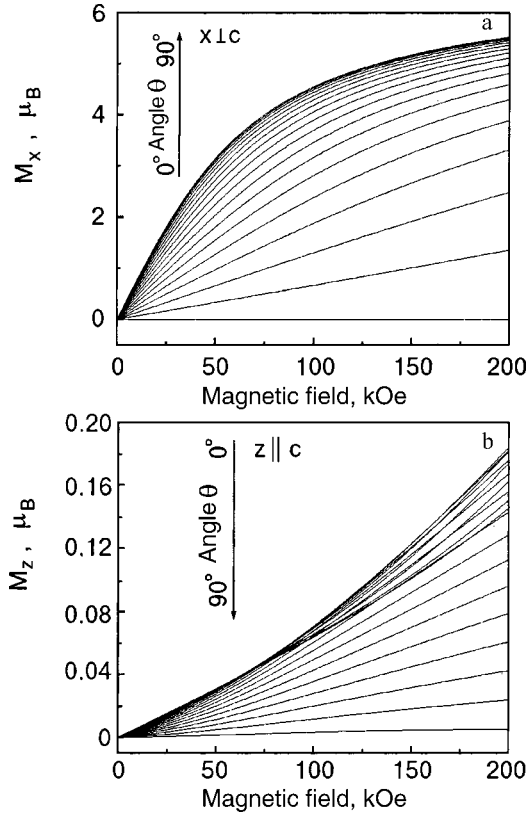


FIG. 20. Field dependence of the components of the magnetic moment of the $Tm^{3+}$ ion in the TmES crystal for different orientations of the magnetic field relative to the crystallographic axis $c$ at $T=4.2$ K: the component $M_x$ (a), the component $M_z$ (b).

$$
\begin{aligned}
&\langle 0_1|J_z|0_1\rangle=-0.0014, \quad \langle 0_2|J_z|0_2\rangle=0.0098;\\
&\langle 0_1|J_x|0_1\rangle=-4.5025, \quad \langle 0_2|J_x|0_2\rangle=-4.4498;\\
&\langle 0_1|J_z|0_2\rangle=0.0018, \quad \langle 0_1|J_x|0_2\rangle=0;\\
&\langle 0_1|I_z|0_1\rangle=-0.3063, \quad \langle 0_2|I_z|0_2\rangle=0.3059;\\
&\langle 0_1|I_x|0_1\rangle=-0.3952, \quad \langle 0_2|I_x|0_2\rangle=0.3955;\\
&\langle 0_1|I_z|0_2\rangle=0.3953, \quad \langle 0_1|I_x|0_2\rangle=-0.3060.
\end{aligned}
\tag{2.11}
$$

It is clearly seen from formula (2.11) that transitions between electronic–nuclear sublevels of the ground singlet can be induced by an alternating magnetic field oriented either along the static magnetic field or perpendicular to it (i.e., parallel to the crystallographic axis $c$). The frequencies of those transitions lie almost in the X band of ultrahigh EPR frequencies (see Fig. 18), and their probabilities are determined by the matrix elements of the nuclear spin operator.

Our results on the spectrum of energy levels of the Hamiltonian (1.1) and the corresponding wave functions at high magnetic fields allow us to calculate many characteristics of the $Tm^{3+}$ ion. As a specific example we present the results of a calculation of the field dependence of the magnetic moment of an ion in high magnetic fields for different orientations of the external magnetic field relative to the crystallographic axis $c$. Figure 20 shows these field curves for the components of the magnetic moment $M$ along the $x$ and $z$ axes (the latter coincides with the $c$ axis) at liquid helium temperature. At this low temperature only the electronic–nuclear sublevels of the ground singlet are occu-

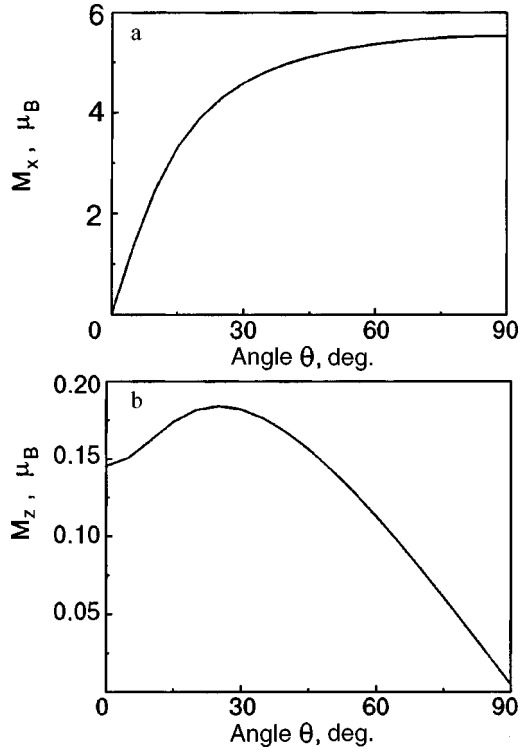


FIG. 21. Angular dependence of the components of the magnetic moment of the $Tm^{3+}$ ion in the TmES crystal in a magnetic field of 200 kOe at $T=4.2$ K: the component $M_x$ (a), the component $M_z$ (b).

pied significantly, so that the presence of an extremely high magnetic moment of the $Tm^{3+}$ ion is evidence of appreciable polarization of the electronic–nuclear system. From the curves shown it is clearly seen that the magnetic moment exhibits nonlinear behavior both as a function of the applied magnetic field and as a function of its direction. The angular dependence of the components of the magnetic moment $M$ in a magnetic field of 200 kOe is presented in Fig. 21.

### 2.6. Dynamic polarization of nuclei with the use of insulating VVPs

Systems with a high polarization of the nuclear spins are objects of intensive research in both elementary-particle and solid-state physics.[55] In comparison with the ''brute force'' method (high magnetic fields and ultralow temperatures) the methods of dynamic polarization of nuclei (DPN)[55,56] are more accessible. One of the DPN methods is the so-called ''solid effect,'' based on the transfer of polarization from impurity paramagnetic centers to the nuclear spin system. Let us consider a modification of this method for insulating VVPs, in which the Van Vleck ions are located at sites of a regular crystal lattice and act as paramagnetic centers for the transfer of polarization to the nuclei.

The nuclear spins of the Van Vleck ions and diamagnetic atoms of the crystal lattice are effectively coupled with the $4f$ electron shell of the Van Vleck ion by the hyperfine interaction. An external magnetic field induces a magnetic moment in the electron shell in the nonmagnetic ground state. However, the transfer of polarization from the electron shell to the nuclear spins of the ligands at low temperatures (thermal energy $k_BT$ less than the energy interval $\Delta$ between the ground and first excited states of the Van Vleck ion) is impossible because of the static character of the hyperfine field. Therefore, the application of the solid effect to this situation means that it is necessary to transfer the electron shell into the excited state (in this sense to ''depolarize'' it; see, e.g., the dependence of the magnetic moments of the $Tm^{3+}$ ion on the external magnetic field in the TmES crystal in different states, presented in Fig. 15), upon the relaxation of which a portion of the electronic polarization will be transferred to the nuclear spin system on account of the hyperfine interaction. As we showed in Sec. 2.2, such an excitation of the electron shell is brought about at high magnetic fields by using laser radiation in the far-infrared. Here we note that the use of high magnetic fields ($B>5$ T) leads to a change of the intervals between levels of the Stark structure (see Sec. 2.1), which is extremely important from an experimental standpoint, since it lets one use an applied magnetic field to achieve coincidence of the separation between the ground and excited levels with the energy of a given line of laser radiation.

The use of high magnetic fields is also necessary to reduce the leakage of nuclear polarization due to nuclear spin–lattice relaxation processes. Let us discuss this in more detail. Crystals of VVPs contain paramagnetic impurities ($Er^{3+}$, $Yb^{3+}$, etc.). Fluctuations of the magnetic fields of these impurity ions bring about a well-known nuclear spin–lattice relaxation mechanism[57] whose rate is proportional to the factor $1-p_0^2$, where $p_0$ is the polarization of the paramagnetic impurity. At high magnetic fields the polarization of the impurity approaches unity, so that efficiency of this channel for leakage of the nuclear polarization is substantially reduced.

As to the possibilities for polarizing the nuclear spins of the Van Vleck ions themselves, the appearance of highly mixed electronic–nuclear states in high magnetic fields (see Sec. 2.5) makes it meaningless to speak of polarization of the nuclear subsystem individually in such fields. In this situation it is apparently more correct to speak of the overall magnetic polarization of the Van Vleck ion.

In the framework of the ''classical'' approach to enhancement of the nuclear magnetism in VVPs[4] one obtains the following picture: because of the polarization of the electron shell by the magnetic field and the hyperfine interaction, a so-called ''enhanced'' magnetic field is induced at the position of the nuclear spin; this enhanced field differs from the

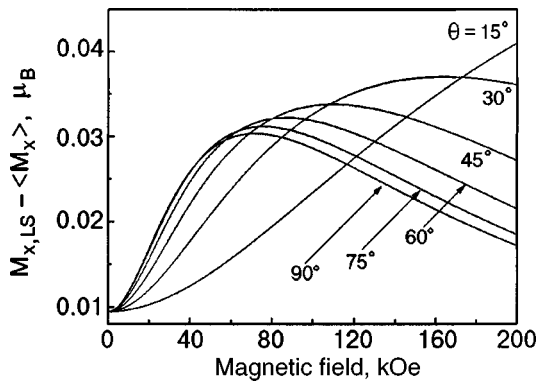


FIG. 22. Field dependence of the difference of the average value of the magnetic moment component $M_x$ of the thulium ion in the TmES crystal at $T=1$ K from the value of this component in the LS state (see text).

external applied magnetic field in both magnitude and direction. This enhanced magnetic field can be treated as a quantizing field, and one can write the corresponding nuclear spin Hamiltonian with spin 1/2 (nuclear, because it is assumed that the electronic state, a singlet, is not affected by the turning on of the magnetic field). Here it should be noted that the eigenstates of this Hamiltonian are not pure states of the real nuclear spin, i.e., states of the type $|m_I=1/2\rangle$ and $|m_I=-1/2\rangle$, but some linear combination of these states, with coefficients that depend on the magnitude and direction of the external magnetic field relative to the crystallographic axis.

Upon an exact diagonalization of the total Hamiltonian in an arbitrary external magnetic field we also obtain two low-lying states (and only they are occupied significantly at helium temperatures) separated by an energy interval. The dependence on the magnitude and orientation of the external magnetic field is shown in Fig. 18 in frequency units. As to the wave functions of these two states, it is seen from Table V that for the thulium ion in the TmES crystal they are extremely complicated combinations of products of all the electronic wave functions of the type $|J=6,\ M_J\rangle$ and nuclear wave functions of the type $|I=1/2,\ m_I\rangle$. The actually measurable quantity—the (total) magnetic moment **M** of the ion—is not codirectional with the external magnetic field, and the plots of the field dependence of its $M_y$ and $M_z$ components (the $z$ axis is codirectional with the crystallographic axis $c$, while the $x$ axis is perpendicular to it; the angle $\theta$ between the external magnetic field and the $c$ axis is measured in the $zx$ plane) are shown in Fig. 20.

At a temperature of absolute zero only the lower of the two levels—the lowest state (LS)—should be occupied. We shall call the higher-lying level the upper state (US). Then the value of the $x$ or $z$ component of the magnetic moment, $M_{x(z),LS}$, is the limiting value for the given magnetic field. At helium temperature a second high-lying level is also occupied, and as a result the components of the magnetic moment of the ion have values $\langle M_{x(z)}\rangle$ different from $M_{x(z)LS}$. The differences of these values for $M_x$ at $T=1$ K are plotted in Figs. 22 and 23 as functions of the magnitude and direction of the magnetic field. The nonmonotonic dependence seen is characteristic for the component $M_z$ as well, but the value of the latter component is substantially smaller on account of the selection rules for the matrix elements of the magnetic moment. It follows from these plots that the direction of the total magnetic moment vector of an ion at zero temperature, $\mathbf{M}_{LS}$, does not coincide with that of the magnetic moment vector $\langle\mathbf{M}\rangle$ at finite temperature in the same

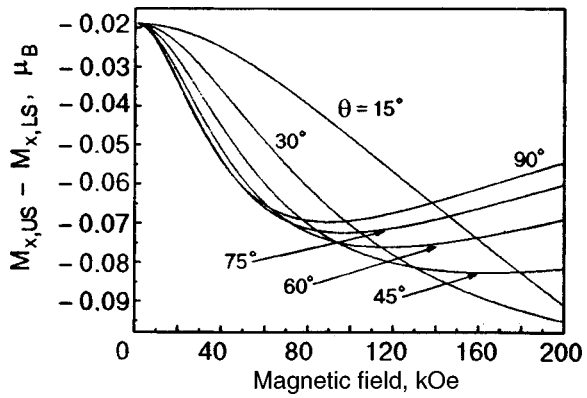


FIG. 23. Field dependence of the difference of the average value of the magnetic moment component $M_x$ of the thulium ion in the TmES crystal at $T=1$ K from the value of this component in the US and LS states (see text).

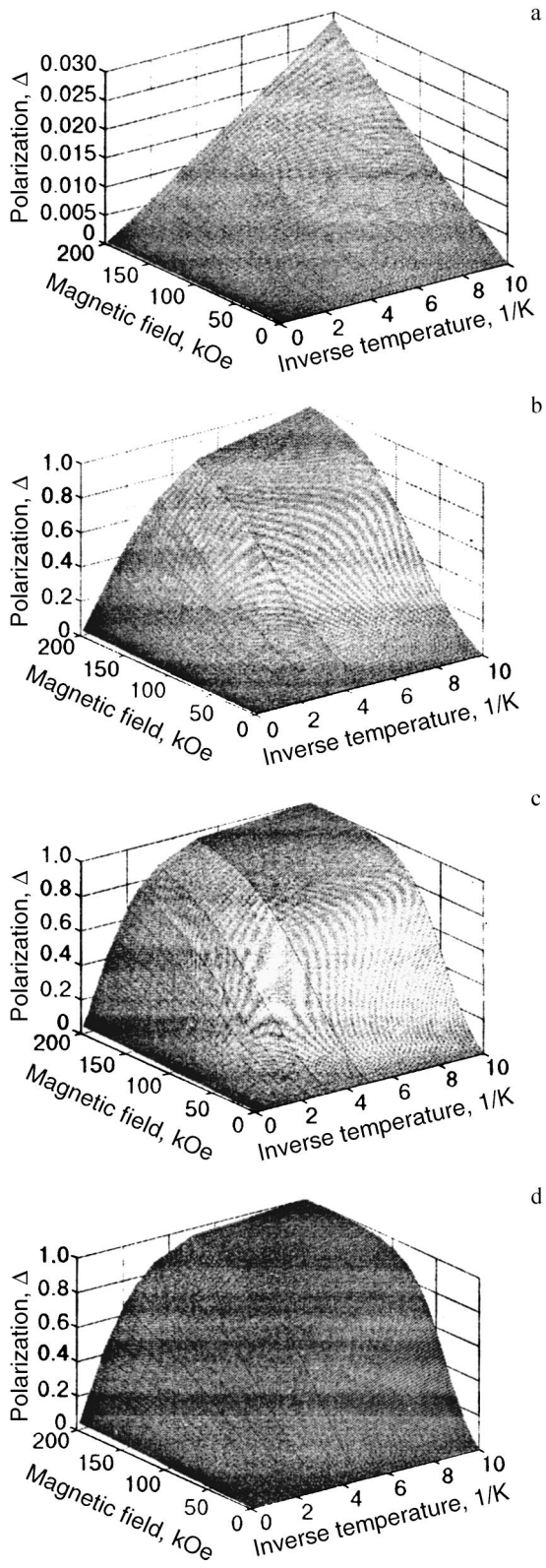


FIG. 24. Temperature and magnetic-field dependence of the polarization of the thulium ion in the TmES crystal, as defined by formula (2.12), for different angles between the magnetic field direction and the crystallographic axis $c$: $\theta=0$ (a), 30° (b), 60° (c), 90° (d).

external magnetic field. The reason is that other energy levels (primarily US) are occupied. Thus a change in temperature will lead to a change in not only the magnitude of the magnetic moment but also its direction.

In such a situation it seems more logical to characterize the Van Vleck ion in high magnetic fields by the total magnetic moment and a ''polarization'' defined exactly as in the solid effect, viz.,

$$\Delta = \frac{N_{LS} - N_{US}}{N_{LS} + N_{US}}, \tag{2.12}$$

where $N$ denotes the occupation of the corresponding state. Then for a model system consisting of a thulium ion in ethyl sulfate at temperatures from 0.1 to 10 K and in magnetic fields up to 200 kOe we obtain the plots shown in Fig. 24 for the polarization as a function of temperature and magnetic field at different orientations of the external magnetic field relative to the crystallographic axis $c$.

## CONCLUSION

Let us conclude by summarizing the main results of research on the effect of high magnetic fields on the magnetic properties of insulating Van Vleck paramagnets. We note first of all that when the Zeeman energy of the Van Vleck ion becomes comparable to the characteristic energies of the Stark splittings, the magnetic field begins to have a substantial effect on the distance between levels, and it becomes possible to observe the rf electron paramagnetic resonance due to transitions between the ground and excited levels. The predicted rf resonance was first observed experimentally in TmES and LaES:$Tm^{3+}$ crystals; these compounds also exhibit resonance absorption of radiation in the far-IR region due to transitions between the ground and excited levels. Our preliminary studies suggest that this resonance is also observed in another system—in $LiTmF_4$ crystals. We note that the experimental data on rf EPR can be used to correct the values obtained from optical measurements for the crystal-field parameters of rare-earth ions. In addition, the luminescence spectra in $LiTmF_4$ crystals, observed by the authors for the first time, correlate well with the rf EPR data and with the data on direct absorption of far-IR radiation.

High magnetic fields lead to rather unexpected effects. For example, coupled $4f$-electron–phonon excitations in TmES crystals have been observed experimentally and described theoretically, while in moderate fields no manifestations of an electron–deformation interaction have been observed in such systems.

As to the electronic–nuclear spin system of Van Vleck ions at high magnetic fields, the main result of these studies can be considered to be the prediction that coupled electronic–nuclear states appear, the frequencies of transitions between them lying in the usual EPR frequency range, while the transitions themselves are induced by the interaction of both the nuclear and electronic spins with the magnetic field; this allows one to speak of ''ultrahigh-frequency'' NMR at high magnetic fields, in contrast to the ''enhanced'' NMR at moderate magnetic fields. The observation and experimental study of such resonance effects is undoubtedly an interesting problem for the near future.

The prediction of a substantial increase in the efficicency of the method of dynamic polarization of nuclear spin moments of ligands with the use of insulating VVPs in high magnetic fields is yet another reflection of the fact that high magnetic fields lead to extremely substantial changes in the magnetic properties of insulating VVPs.

This study was done with the support of the Russian Foundation for Basic Research (Grant 99-02-17536) and the Science Education Center CRDF (REC-007). One of the authors (D.A.T.) gratefully acknowledges support from the German Science Foundation (DFG, Grant Es 43/11-1).

[a)]E-mail: dtayursk@mi.ru

[1] J. H. Van Vleck and A. Frank, Phys. Rev. **34**, 1494 (1929).
[2] J. H. Van Vleck, *Theory of Electric and Magnetic Susceptibilities*, Oxford University Press, Oxford (1932).
[3] A. Abragam and B. Bleaney, Proc. R. Soc. London, Ser. A **387**, 221 (1983).
[4] L. K. Aminov and M. A. Teplov, Usp. Fiz. Nauk **147**, 49 (1985) [Sov. Phys. Usp. **28**, 762 (1985)].
[5] L. K. Aminov and M. A. Teplov, Sov. Sci. Rev., Sect. A **14**, 1 (1990).
[6] L. K. Aminov, B. Z. Malkin, and M. A. Teplov, in *Handbook on the Physics and Chemistry of Rare Earths*, edited by K. A. Gshneidner and L. Eyring, Vol. 22, North-Holland (1996), Chap. 150, p. 296.
[7] S. A. Al'tshuler, JETP Lett. **3**, 112 (1966).
[8] R. J. Elliot, R. T. Harley, W. Hayes, and S. R. P. Smith, Proc. R. Soc. London, Ser. A **328**, 217 (1972).
[9] G. A. Gehring and K. A. Gehring, Rep. Prog. Phys. **38**, 1 (1975).
[10] L. K. Aminov, Fiz. Tverd. Tela (Leningrad) **23**, 2167 (1981) [Sov. Phys. Solid State **23**, 1266 (1981)].
[11] M. S. Tagirov and D. A. Tayurskiĭ, JETP Lett. **61**, 672 (1995).
[12] H. P. Moll, J. van Toll, P. Wyder, M. S. Tagirov, and D. A. Tayurskii, Phys. Rev. Lett. **77**, 3459 (1996).
[13] J. Boettcher, K. Dransfeld, and K. F. Renk, Phys. Lett. A **26A**, 146 (1968).
[14] E. A. Vinogradov, G. A. Zvereva, N. A. Irisova, T. S. Mandel'shtam, A. M. Prokhorov, and T. A. Shmaonov, Fiz. Tverd. Tela (Leningrad) **11**, 335 (1969) [Sov. Phys. Solid State **11**, 268 (1969)].
[15] J. Magarino, J. Tuchendler, P. Beauvillain, and I. Laursen, Phys. Rev. B **21**, 18 (1980).
[16] I. de Wolf, P. Janssen, and B. Bleaney, Phys. Lett. A **108A**, 221 (1985).
[17] J. Magarino, J. Tuchendler, J. P. Haenens, and A. Linz, Phys. Rev. B **13**, 2805 (1976).
[18] P. Janssen, I. de Wolf, and I. Laursen, J. Phys. Chem. Solids **46**, 1387 (1985).
[19] P. de Groot, P. Leempoels, J. Witters, and F. Herlach, Solid State Commun. **37**, 681 (1981).
[20] B. Z. Malkin, V. F. Tarasov, and G. S. Shakurov, JETP Lett. **62**, 811 (1995).
[21] V. F. Tarasov, G. S. Shakurov, B. Z. Malkin, and C. A. Hutchison, Jr., J. Alloys Compd. **250**, 364 (1997).
[22] S. A. Al'tshuler and B. M. Kozyrev, *Electron Paramagnetic Resonance of Compounds of Elements of the Intermediate Groups; Nauka, Moscow (1972).*
[23] A. Abragam and B. Bleaney, *Electron Paramagnetic Resonance of Transition Ions* [Clarendon Press, Oxford (1970); Russ. Vols. 1 and 2, Mir, Moscow (1972, 1973)].
[24] R. G. Barnes, R. L. Mossbauer, E. Kankeleit, and J. M. Poindexter, Phys. Rev. A **136**, 175 (1964).
[25] A. Abragam, *The Principles of Nuclear Magnetism* [Clarendon Press, Oxford (1961); Izd. Inostr. Lit., Moscow (1963)].
[26] A. Abragam and M. Goldman, *Nuclear Magnetism: Order and Disorder* [Clarendon Press, Oxford (1982); Mir, Moscow (1984)].
[27] B. Bleaney, Proc. R. Soc. London, Ser. A **370**, 313 (1980).
[28] R. Yu. Abdulsabirov, I. S. Konov, S. L. Korableva, S. N. Lukin, and M. S. Tagirov, M. A. Teplov, Zh. Éksp. Teor. Fiz. **76**, 1023 (1979) [Sov. Phys. JETP **49**, 517 (1979)].
[29] L. K. Aminov, M. S. Tagirov, and M. A. Teplov, Zh. Éksp. Teor. Fiz. **79**, 1322 (1980) [Sov. Phys. JETP **52**, 669 (1980)].
[30] I. S. Konov and M. A. Teplov, Fiz. Tverd. Tela (Leningrad) **18**, 1114 (1976) [Sov. Phys. Solid State **18**, 636 (1976)].

[31] H. P. Christensen, Phys. Rev. B **19**, 6573 (1979).
[32] F. L. Aukhadeev, R. Sh. Zhdanov, M. A. Teplov, and D. N. Terpilovskiĭ, Fiz. Tverd. Tela (Leningrad) **23**, 2225 (1981) [Sov. Phys. Solid State **23**, 1303 (1981)].
[33] A. K. Kupchikov, B. Z. Malkin, D. A. Rzaev, and A. I. Ryskin, Fiz. Tverd. Tela (Leningrad) **24**, 2373 (1982) [Sov. Phys. Solid State **24**, 1348 (1982)].
[34] W. F. Krupke and J. B. Gruber, Phys. Rev. A **139**, 2008 (1965).
[35] R. Yu. Abdulsabirov, A. V. Vinokurov, A. A. Kazantsev, S. L. Korableva, B. Z. Malkin, S. I. Nikitin, A. L. Stolov, M. S. Tagirov, and D. A. Tayurskiĭ, *32nd All-Russia Conference on Low-Temperature Physics* [in Russian], Kazan, October 3–6, 2000, *Abstracts of LT Section*, LTp6, 78, Kazan (2000).
[36] A. V. Vinokurov, B. Z. Malkin, A. I. Pominov, and A. L. Stolov, Fiz. Tverd. Tela (Leningrad) **30** 3426 (1988) [Sov. Phys. Solid State **30**, 1966 (1988)].
[37] A. V. Klochkov, V. V. Naletov, I. R. Mukhamedshin, Kh. Suzuki, M. S. Tagirov, and D. A. Tayurskiĭ, JETP Lett. **66**, 266 (1997).
[38] A. V. Klochkov, S. P. Kurzin, I. R. Mukhamedshin, D. R. Nabiullin, V. V. Naletov, H. Suzuki, I. Kh. Salikhov, M. S. Tagirov, D. A. Tayurskii, and R. Sh. Zhdanov, Appl. Magn. Reson. **14**, 525 (1998).
[39] B. G. Vekhter, A. Z. Kazeĭ, M. D. Kaplan, and Yu. F. Popov, JETP Lett. **54**, 578 (1991).
[40] K. Ahrens and G. Schaack, Phys. Rev. Lett. **42**, 1488 (1979).
[41] G. Schaack, Z. Phys. B **26**, 49 (1977).
[42] W. Dorfler, H. D. Hochheimer, and G. Schaack, Z. Phys. B **51**, 153 (1983).
[43] M. Dahl and G. Schaack, Z. Phys. B **56**, 279 (1984).
[44] M. Dahl, G. Schaack, and B. Schwark, Europhys. Lett. **4**, 929 (1987).
[45] M. Dahl, Z. Phys. B **72**, 87 (1988).
[46] I. M. Krygin and A. D. Prokhorov, Zh. Éksp. Teor. Fiz. **86**, 590 (1984) [Sov. Phys. Solid State **59**, 344 (1984)].
[47] D. A. Tayurskiĭ and M. S. Tagirov, JETP Lett. **67**, 1040 (1998).
[48] L. K. Aminov, A. A. Kudryashov, M. S. Tagirov, and M. A. Teplov, Zh. Éksp. Teor. Fiz. **86**, 1791 (1984) [Sov. Phys. JETP **59**, 1042 (1984)].
[49] B. I. Kochelaev, Dokl. Akad. Nauk SSSR **166**, 833 (1966) [Sov. Phys. Dokl. **11**, 130 (1966)].
[50] M. N. Aliev and B. I. Kochelaev, Izv. Vyssh. Uchebn. Zaved. Fiz. **2**, 7 (1968).
[51] H. P. Moll, J. Van Tol, M. S. Tagirov, and D. A. Tayurskii (unpublished).
[52] D. A. Tayurskii, M. S. Tagirov, and H. Suzuki, Physica B **284–288**, 1686 (2000).
[53] J. Kuriplach, J. Sebek, and R. M. Mueller, J. Low Temp. Phys. **120**, 401 (2000).
[54] J. Sebek, R. M. Mueller, R. Simons, and J. Kuiplach, J. Low Temp. Phys. **120**, 435 (2000).
[55] A. Abragam and M. Goldman, Rep. Prog. Phys. **41**, 395 (1978).
[56] V. A. Atsarkin, *Dynamic Polarization of Nuclei in Solid Insulators* [in Russian], Nauka, Moscow (1980).
[57] M. P. Vaĭsfel'd, Fiz. Tverd. Tela (Leningrad) **14**, 3562 (1972) [*sic*].

Translated by Steve Torstveit

## QUANTUM LIQUIDS AND QUANTUM CRYSTALS

# Watergel—a new form of water condensed in liquid $^4$He

A. M. Kokotin and L. P. Mezhov-Deglin [a)]

*Institute of Solid State Physics, Russian Academy of Sciences, 142432 Chernogolovka, Moscow District, Russia*

(Submitted July 2, 2001; revised November 12, 2001)
Fiz. Nizk. Temp. **28**, 235–244 (March 2002)

The semitransparent layer (cloud) of impurity condensate formed on the interface between superfluid He II and the vapor during condensation of gaseous $^4$He containing impurity water vapor in a cell filled with superfluid helium at a temperature $T \leqslant 1.5$ K is transformed over time into an oval iceberg with an average diameter of $\sim 9$ mm, suspended on the walls of the glass cell under the surface of the liquid. Within the liquid helium, icebergs can exist at temperatures above $T_\lambda$ as well. At a vapor pressure $P = 150$ torr over the surface of normal liquid He I the temperature $T_d$ at which intense decomposition of the icebergs occurs is 2.5 K. When the pressure is increased to 760 torr the temperature $T_d$ increases to 4 K. In an atmosphere of gaseous $^4$He the ''dry'' icebergs extracted from He II at $T \sim 1.4$ K decompose on heating above 1.8 K. The decomposition of the icebergs is accompanied by the formation of a fine powder (apparently amorphous ice) on the bottom of the cell; the volume of this powder is nearly two orders of magnitude less than the volume of the initial icebergs, i.e., the total water content in an iceberg is $\leqslant 10^{20}$ molecules/cm$^3$. This estimate agrees with an estimate of the difference of the density of an iceberg and the density of the surrounding liquid $\rho_L$ (the ratio $\Delta\rho/\rho_L < 0.1$) from the results of observations of oscillations of the sample when thermoacoustic vibrations arise in a cell filled with liquid He I. In considering the structure of the icebergs it can be assumed that in helium vapor over the surface of He II the $H_2O$ impurity molecules agglomerate into clusters, so that the core of the impurity–helium water condensate in He II (a gel dispersion system) is formed by water nanoclusters surrounded by one or two layers of solidified helium, and the superfluid He II filling the pores between particles serves as the dispersion medium of the watergel. 
[DOI: 10.1063/1.1468519]

### INTRODUCTION

This article was prepared for publication in the special issue of the journal *Low Temperature Physics* commemorating the 100th anniversary of the birth of L. V. Shubnikov, one of the founders of the Kharkov school of science and the author of a series of brilliant experimental studies in the field of low-temperature physics. Shubnikov's name is familiar to the majority of physicists today from back in their student years in connection with the study of kinetic phenomena in metals in magnetic fields (the Shubnikov-de Haas effect) and fundamental studies of the properties of superconductors in magnetic fields. He is also remembered for studies of the properties of liquid and solid helium and later of crystals of other rare gases (''cryocrystals'' in the modern terminology). For one of the authors of this article (M.-D.) acquaintance with these papers 20 years after their publication played an important role in the choice of technique for investigating transport phenomena in solid helium. The volume of work that Shubnikov and his colleagues were able to accomplish at Kharkov in the 1930s during the brief period (less than 7 years) allotted to him by fate is indeed impressive. Especially now, when one can in all seriousness compare the conditions under which that work was done with the conditions that exist today in basic science in the territory of the former Soviet Union. This example can serve as inspiration for optimism and emulation.

In this paper we present the results of a study of the properties of metastable impurity–helium samples that form when a flow of gaseous $^4$He containing impurity water vapor is condensed on the surface of superfluid He II. Brief reports of the observation of a new form of water—a porous impurity–helium condensate permeated with superfluid helium—and a description of the experimental setup used to prepare the water samples have been published previously.[1–4]

It should be recalled that features of the behavior of impurity–helium condensates were first observed by Savich and Shalnikov more than 55 years ago.[5] It was observed that the properties and character of the interaction between impurity particles formed in the vapor over liquid helium depend not only on the composition of the impurity but also substantially on the properties of the liquid. For example, when gaseous $^4$He containing an air impurity was admitted into a Dewar containing normal He I (helium temperature $T > T_\lambda$) a fog arose in the vapor over the He I, i.e., the impurity molecules of the gas were joined into small clusters. When the

 

liquid was cooled below $T_\lambda$ the fog disappeared, i.e., the transition from normal He I to superfluid He II was accompanied by substantial changes in the size and rate of precipitation of the clusters in the vapor over the liquid as well as in the shape of the ''flakes'' formed in the volume of the liquid through the agglomeration of clusters. Moreover, upon subsequent heating of the liquid and the transition from He II to He I the flakes, containing a hydrogen impurity, decomposed into fine particles, with a ''halo'' forming above the decomposing flakes. These observations[5] served as a basis for the development of modern methods of obtaining metallic nanoparticles by the evaporation of a metal in liquid helium vapor. Judging from the data of electron microscope measurements,[6] the characteristic dimensions of iron nanoclusters prepared in this way for use in experiments on the visualization of the distribution of Abrikosov vortices in type-II superconductors ranged from a few nanometers to hundreds of nanometers, the average diameter of the particles being 5–7 nm.

The next step in this direction was the development of a new technique for preparing metastable impurity systems containing molecules and atoms (free radicals) of molecular gases by blowing jets of gaseous $^4$He containing impurity molecules and/or atoms of a gas to be studied into superfluid He II.[7,8] A gaseous mixture containing 1–3% impurity was passed beforehand through a liquid-nitrogen-cooled gas-discharge tube (dissociator) and was admitted into a Dewar containing He II through a narrow aperture $\sim 0.5$ mm in diameter in the bottom of the tube. The distance from the exit nozzle to the surface of the superfluid helium was $\sim 2$ cm. The relative concentration of impurity atoms of the molecular gas, e.g., $N_2$ or $D_2$, in the conical gas jet, with a sharp rim set against the surface of the liquid, reached 90%. The concentration of nitrogen atoms in the nitrogen condensate in He II was comparable to the concentration of $N_2$ molecules. This was many times larger than the estimates made in the monograph[9] as to the maximum achievable concentration of free radicals in a molecular matrix, which were calculated from the results of studies of the properties of samples prepared by deposition of the substance on a cold substrate in vacuum, i.e., the change in the preparation technique qualitatively altered the properties of the samples obtained.

Up-to-date information on the structure and properties of impurity–helium condensates formed in He II by molecular and rare gases and an extensive bibliography on this topic are given in Ref. 10. According to the data of x-ray studies, in cold vapor over the surface of He II the majority of impurity molecules and atoms join together into clusters with an average diameter of several nanometers, in agreement with the measurements of Ref. 6. The average dimensions of the solid particles in impurity–helium condensates of rare gases and nitrogen in He II reach 2–6 nm. Judging from the ultrasonic absorption, the characteristic sizes of the pores in these condensates are distributed over a wide range, from $\sim 8$ to $\sim 800$ nm.

The technique of Refs. 7–10 for preparing impurity condensates, which has acquitted itself well in experiments with molecular and rare gases, turns out to be unsuitable for working with substances whose triple point is much higher than the triple point of nitrogen, since the impurity condenses on the bottom of the gas-discharge tube and rapidly clogs the exit nozzle through which the helium vapor is blown. Furthermore, during preparation of a sample under a dense gas jet on the surface of He II and in the volume of the liquid, strong convective flows arise, leading to intense mixing of the liquid and possibly having a substantial effect on the properties of the impurity–helium condensate formed. Therefore, when doing a study of the properties of condensates of highly (water) or slightly (alcohol) polar liquids[1–4] we replaced the dissociator with a wide glass tube of inner diameter 9 mm, the lower part of which was filled with superfluid helium and served as a working cell for preparation of the sample.

We were quite interested in making an attempt to observe the new form of condensed water at low temperatures—a He-II permeated porous water condensate—which seemed to us very important for the development of both the condensed matter physics and natural sciences as a whole, since water is one of the most important substances for life, and the detection of traces of water in one form or another in the universe serves as an indicator of the possibility of existence of life on distant planets. It followed from the calculations[11] that even at room temperatures $H_2O$ molecules in the saturated vapor over the liquid should join into clusters. The trapping of water clusters consisting of several molecules—linear isomeric chains of the type $(H_2O)_N$ for $N \leqslant 6$ or three-dimensional ''cages'' for $N > 6$—by drops of He II with a diameter of around 50 nm traveling through a vessel containing water vapor was successfully observed in the experiments of Ref. 12. Unfortunately, the behavior of the water clusters upon the coalescence of the drops of He II was not investigated there.[12] However, based on the results of Refs. 5–12, it is reasonable to assume that individual molecules and small clusters of $H_2O$ introduced into a working cell with a flow of gaseous $^4$He will agglomerate at the vapor–superfluid He II interface into nanoparticles with dimensions of the order of several nanometers. It is known that neutral impurity particles (except for impurities of alkali and alkaline-earth metals) in He II are surrounded by one or two layers of solidified helium. Therefore it is reasonable to suppose that the core of a porous impurity condensate accumulating below the surface of He II will consist of water nanoparticles (nanoclusters) surrounded by a layer of solidified helium. Since these solid particles and the superfluid liquid surrounding them interact strongly with each other and initially form a transparent gel-like layer of condensate, which is subsequently transformed into a denser iceberg, it is natural to call this condensate watergel.

As compared to highly porous aerogel, which is widely used for studying the behavior of superfluid liquid in a restricted geometry, watergel and impurity–gel condensates of molecular and rare gases in He II have this essential difference: the properties of the as-prepared impurity sample can vary noticeably in time or with increasing temperature of the He II; the size of the pores between solid particles varies over wide limits, from a few nanometers to several hundred nanometers, and the existence region of the sample is bounded on the low-temperature side.

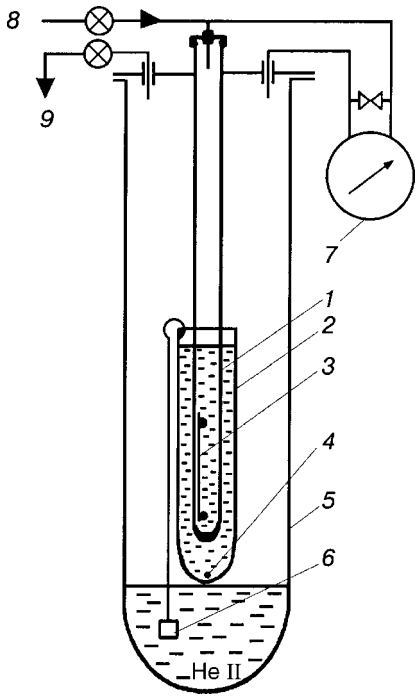


FIG. 1. Diagram of the low-temperature part of the device. *1*—Glass cell, *2*—outer test tube, *3*—metal needle holding thermometers, *4*—germanium thermometer, *5*—glass helium Dewar, *6*—thermomechanical pump, *7*—differential manometer, *8*—line for admission of the gaseous mixture, *9*—line for pumping out helium vapor from the Dewar.

## 1. SAMPLE PREPARATION TECHNIQUE

The construction of the low-temperature part of the apparatus is shown schematically in Fig. 1. A gaseous mixture containing around 3% $H_2O$ impurity molecules in $^4$He is admitted from an external filling system *8* into the working cell *1*, which is made from a glass tube with an inner diameter of 9 mm terminated with an aperture 1.5 mm in diameter. The lower part of the tube is located in a glass test tube *2*. The device is placed inside a glass helium Dewar *5*. Germanium thermometers *3* and *4* permit monitoring of the temperature distribution along the cell and at the bottom of the test tube. The test tube and cell can be periodically filled with superfluid liquid from an external helium bath by means of a thermal pump *6*. Gaseous $^4$He with a water vapor impurity is condensed on the He II surface in the cell *1*. Besides visual observations of the processes occurring in the cell as the impurity accumulates and as the condensate is heated, the progress of the experiment can be recorded by an externally mounted video camera connected to a monitor and computer.

Before the start of the experiment the temperature of the liquid $^4$He in the Dewar was lowered to $T \approx 1.4$ K by pumping out helium vapor through a valve *9*. For monitoring the rate of admission of the gas flow we used a differential manometer *7*, which could be used to measure the pressure difference between the gas in the tube *1* and in the Dewar *5* and as necessary to connect the cell with the external helium bath for equalization of the pressures. Observations showed that in the optimal regime of admission the pressure difference $\Delta P$ between the cell and external Dewar was $\approx 0.2$ torr, which corresponded to an average rate of admission of the gas $\sim 1$ cm$^3$/s under normal conditions. The temperature of the He II in the cell during the admission was elevated by no more than 0.03 K in comparison with the initial temperature. The heat released in the condensation of the gas flow on the He II surface ($\sim 5$ mW) was removed through evaporation of helium from the test tube *2*. For a mixture admission time $t \leqslant 15$ min the number of $H_2O$ molecules entering the working cell was $\leqslant 10^{22}$. Here a significant fraction of the impurity (more than 90% by our estimates) was condensed in the upper part of the tube in the form of several individual ice rings, separated by transparent bands. Apparently each of the ring corresponds to ice of a different structure: it is known[13] that at the triple point ice has a hexagonal structure, while when water is deposited in vacuum on a substrate cooled below nitrogen temperatures a layer of amorphous ice forms. The structure of the samples formed in the condensation of water clusters on a substrate cooled below 4 K, to say nothing of the surface of a superfluid liquid, had not been studied previously.

In the optimal regime of admission of the gas ($\Delta P \sim 0.2$ Torr, $T \sim 1.4$ K) a gel-like layer (cloud) of condensate, transparent to visible light, formed beneath the surface of the liquid helium and slowly ($\leqslant 0.5$ mm/min) drifted downward along the wall of the tube. Usually the admission was stopped when the average thickness of the layer reached 3–5 mm. At a constant temperature in the cell the cloud was suspended motionless at the walls at a depth of $\sim 1$ cm below the surface of the liquid. The form of the impurity sample was transformed over time ($\sim 10$ min) from a cloud with a shape that varied as it moved to a denser, judging from the decrease in its transmission of light, practically immobile ''iceberg'' of oval shape with an average diameter close to the diameter of the tube ($\sim 9$ mm), suspended on the walls of the cell. The change in shape of one of the icebergs in liquid helium as the temperature was raised can be assessed from the series of photographs shown in Fig. 2. By repeating the admission, one can prepare 3 or 4 icebergs stacked inside the cell, and the touching edges of the icebergs do not stick together as the temperature of the liquid is raised or when the icebergs are extracted from the He II.

## 2. EXPERIMENTAL RESULTS AND DISCUSSION

### 2.1. Evolution of the icebergs in superfluid He II and in an atmosphere of gaseous helium at temperatures below $T_\lambda$

At a constant temperature $T < 1.6$ K the shape of an immobile iceberg in He II remained practically unchanged over several hours. When the temperature of the He II was raised above 1.6 K, the average diameter of the icebergs decreased monotonically, and the icebergs became denser, judging from the decrease in the transmission of light. This was accompanied by rotations and displacements of the oval icebergs down into the volume of the cell as long as the lowest iceberg, if there were several, did not get hung up on the upper end of the needle *3* on which the thermometers were mounted in the cell or on one of the thermometers before reaching the bottom of the cell, i.e., the average diameter of the icebergs gradually decreased from $\sim 9$ to $\sim 6$ mm.

For comparison, we recall that in the case of impurity–helium samples of rare and molecular gases,[10] raising the temperature of the He II above 1.6 K was also accompanied by irreversible changes in the properties of the sample, in

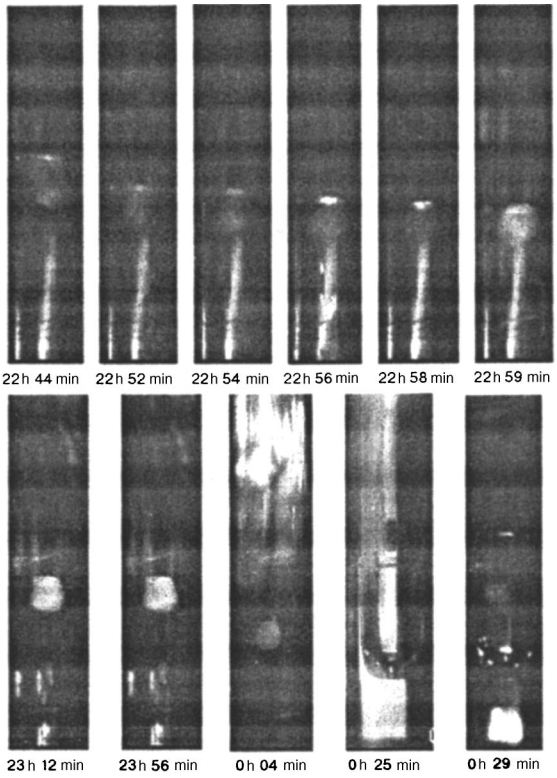


FIG. 2. Temporal evolution of the shape of the iceberg in liquid helium. The top row shows a monotonic lowering of the He II level in the cell at $T=1.4$ K. An iceberg moves downward into the volume of the liquid in jumps (see the first frame). In the bottom row, the three frames on the left were taken as the temperature in the He II was raised ($T\leqslant T_\lambda$), while the two frames on the right show the evolution of the shape of the iceberg in He I upon a slow increase in the temperature near $T\approx 2.3$ and at a pressure close to the saturated vapor pressure. The times at which the frames were taken are indicated below each frame.

particular, by growth of the ultrasonic absorption coefficient and by an increase in the average dimensions of the nanoparticles forming the solid core of the porous condensate, judging from x-ray measurements. The increase in the dimensions of the solid particles of the condensate was attributed in Ref. 10 to an increase in the diffusion coefficient of $^4$He atoms in the layer of solidified helium around each impurity particle and to surface diffusion of impurity molecules or atoms, promoting the coalescence of small clusters into larger aggregates.

As was mentioned in Refs. 1–3, upon a gradual ($\sim 0.1$ mm/min) decrease in the He II level in the cell at a constant temperature $T<1.6$ K over the course of a few minutes one can observe the top edge of an immobilely suspended iceberg sticking up above the surface of the He II. Then the iceberg abruptly subsides and again becomes suspended below the surface of the liquid. We were able to observe up to six successive slips of an iceberg as the level of the liquid was lowered. The abrupt slips of the iceberg were accompanied by small jumps in the pressure in the cell ($\Delta P\leqslant 1$ Torr), but the temperature of the He II remained practically unchanged, i.e., the jumps were caused by the flow of cold gas from the surface of the sample, which was warmed by the external light source. To decrease the amplitudes of these pressure jumps at the end of the admission of the gaseous impurity both inlets of the differential manometer *7* (Fig. 1) were connected to the external bath.

A still stronger flow of gaseous helium was observed as the temperature of icebergs freshly extracted from the He II at $T\sim 1.4$ K was slowly raised (the icebergs were stacked along the thermometer-holding needle *3* above the surface of the liquid layer remaining on the bottom of the cell). As long as the level of He II in the outer test tube *2* was higher than or touching the bottom of the cell *1*, bubbles of the gas emerging from the aperture at the bottom of the cell would periodically come up through the liquid layer. When the level of the liquid was lowered below the bottom of the cell by a small distance (0.5–2 mm) from the upper aperture, a clearly visible cone with a depth of $\sim 1$ mm could be seen on the flat surface of the He II, indicating the existence of a strong gas jet emerging from the cell. At this time the temperature of the icebergs, warmed by the external illuminator, increased monotonically from 1.4 to $\sim 1.6$ K, the indications of the upper and lower thermometers inside the cell being practically the same. If the cell was again filled with He II at a temperature of $\sim 1.4$ K, these observations were well reproducible upon a subsequent lowering of the level of liquid (although the icebergs did not float up behind the rising level of He II).

When the level of He II in the outer test tube was lowered further, the temperature of the icebergs and the gas surrounding them in the cell continued to increase monotonically to $T=1.8$ K. Above 1.8 K the readings of the thermometers began to diverge noticeably, the thermometer that was not in direct contact with one of the icebergs was heated faster. In the temperature interval 1.8–2.2 K the thermometer on which one of the icebergs rested registered sharp temperature jumps with an amplitude $\Delta T\sim 0.3$ K, accompanied by decomposition of the icebergs. Above 2.2 K the gas temperature inside the cell increased quite rapidly to $T\geqslant 4$ K, and here the readings of the two thermometers *3* again coincided. The decomposition of the icebergs was accompanied by the formation of a fine powder (apparently, amorphous ice[13]), which collected on the bottom of the cell. The total volume of the powder was nearly two orders of magnitude less than the volume of the initial icebergs. From this it is easy to estimate that more than 97% of the apparent volume of an iceberg is made up of solid and liquid helium, i.e., the total water content in the volume of an initial iceberg was $\leqslant 10^{20}$ $H_2O$ molecules/cm$^3$.

Continuing the comparison with impurity–helium condensates of rare and molecular gases,[10] we note that the samples of these condensates were not destroyed on heating in an atmosphere of gaseous $^4$He to $T\geqslant 7$ K, and the subsequent decomposition of the samples was accompanied by sublimation of the impurity, i.e., the structure and existence region of these samples differ substantially from the corresponding characteristics for watergel. In addition to the difference in the composition of the impurity particles, this may be due to the difference in the technique used to prepare the impurity–helium samples.

### 2.2. Icebergs in the normal liquid

Observations of the evolution of the form of icebergs immersed in liquid helium showed that the icebergs can exist

even at temperatures above $T_\lambda$ (see the last two frames in the lower row in Fig. 2). Therefore, the decomposition of the samples of water condensate on heating in a gaseous atmosphere at $T \geqslant 1.8$ K cannot be attributed solely to the transition of liquid helium in the pores from the superfluid He II to the normal liquid He I state and, accordingly, to the nonuniform heating of the surface of the porous samples under illumination by the external source as a consequence of the manyfold drop of the thermal conductivity of the liquid helium in the pores. Moreover, it turned out that the temperature $T_d$ at which the rapid decomposition of the icebergs in He I occurs depends strongly on the vapor pressure $P$ over the surface of the liquid. We recall that the density of liquid helium is maximum at a temperature approximately 0.003 K above $T_\lambda$, while the thermal conductivity of the normal liquid is so small that when warm gas from the external supply is admitted to the outer bath the temperature difference along the liquid He I column at the bottom of the cell and at the surface of the liquid can reach $\sim 2$ K. This allows us to study the existence region of the watergel in the normal liquid at different pressures. Observations showed that at a pressure $P \approx 150$ Torr the rapid decomposition of the icebergs begins at $T_d \approx 2.5$ K, and when the external pressure is increased to $P \approx 760$ Torr the temperature of decomposition of the icebergs reaches $T_d \approx 4$ K.

The results of a study of the existence region of the watergel are presented in Fig. 3. The continuous curve on the $P-T$ diagram is the boundary of the existence region of liquid $^4$He at the saturated vapor pressure. The black dots indicate the transition temperature $T_\lambda$ of the liquid from the normal to the superfluid state at the different pressures. The triangles correspond to the temperatures of decomposition of the gel in gaseous helium (1.8 K) and in the normal liquid. The crosses connecting the triangles are shown as an aid for visualizing the existence region of the watergel. At the end of the previous Section we pointed out that impurity–helium samples of molecular and rare gases are not destroyed on heating to $\sim 7$ K, i.e., the existence regions of the condensates formed by the molecular or rare gases and water vapor are markedly different.

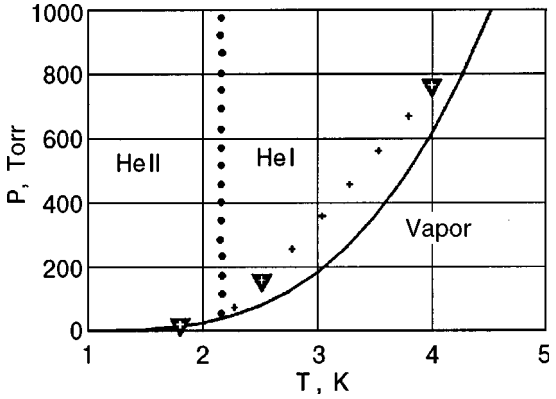


FIG. 3. $P-T$ phase diagram, showing the existence region of the icebergs. The solid curve describes the liquid–vapor transition at the equilibrium vapor pressure of $^4$He. The black dots indicate the transition region of the liquid from the normal to the superfluid state. The triangles indicate the temperatures at which the icebergs decompose upon heating in an atmosphere of gaseous $^4$He (1.8 K) and when immersed in He I at a pressure of 150 torr and at atmospheric pressure.

Increasing the temperature of the liquid in the surrounding test tube and in the cell above $T_\lambda$ was accompanied, as a rule, by the onset of low-frequency ($\sim 10$ Hz) acoustic vibrations in the working cell. Here the oscillations of the He I level in the cell were accompanied by vertical oscillations of the iceberg resting on the upper end of the needle on which the thermometers *3* were mounted (Fig. 1), i.e., the moving normal liquid entrained the iceberg with it. The amplitude of the oscillations of the liquid level in the cell reached $\sim 3$ mm, while the amplitude of the displacements of an iceberg with a diameter of around 6 mm was $\sim 1$ mm. If to a first approximation we neglect the friction of the iceberg and liquid against the walls of the cell (an oscillating viscous liquid is flowing around the solid sphere resting on the needle), then from the ratio of the amplitudes we can estimate that the density $\rho_I$ of the iceberg in He I at $T \sim 2.4$ K is slightly higher than the density of the surrounding liquid: $\Delta\rho/\rho_L = (\rho_I - \rho_L)/\rho_L \sim 0.01$. The density of an iceberg can also be estimated another way, assuming that at the instant it breaks away from the substrate the force of gravity is counterbalanced by the viscous forces; such an estimate leads to a ratio $\Delta\rho/\rho_L \leqslant 0.1$. Both of these estimates agree in order of magnitude with the estimate given above for the total water content ($\leqslant 10^{20}$ molecules/cm$^3$) in the iceberg. Better than order-of-magnitude agreement of the estimates cannot be expected, since the iceberg diameter decreases by almost a factor of 1.5, from $\sim 9$ to $\sim 6$ mm, as the temperature of the liquid increases from 1.4 to 2.4 K. Simultaneously with the change in the visual volume the size of the impurity particles can increase somewhat during thermocycling and, accordingly, the contribution to $\Delta\rho$ for the solid layer around the nanoparticles also changes, particularly since the solidification pressure of the liquid falls by almost a factor of two when the temperature decreases from 2.4 to 1.4 K, and the density of solid $^4$He on the melting curve is approximately 1.4 times higher than the density $\rho_L$ of superfluid helium at the saturated vapor pressure.

In any of the estimates the density of the iceberg floating in He II is approximately 1.3 times lower than the density of solid helium. It is unsurprising, therefore, that helium crystals that are formed in the solidification of pure He II which has been compressed above 25 atm break away from the walls and fall to the bottom of the experimental cell, while the icebergs are ''suspended'' beneath the surface of the liquid.

### 2.3. Phenomena at the interface

As a rule, the condensation of a gas flow was done at a constant or slowly lowering (at a rate of $< 10^{-1}$ mm/min) He II level in the working cell at a pressure difference $\Delta P \sim 0.2$ Torr. The time of admission of the gaseous mixture for preparation of a gel-like layer of condensate $\leqslant 5$ mm thick did not exceed 15 min. Then the admission was stopped, and after 10–15 min an iceberg formed under the surface of the He II. When the preparation of several icebergs was required, the process of gas admission was repeated. In this procedure a several-centimeter-long portion of the tube above the He II surface remained transparent, although a frosty-looking band of ice appeared in the upper part of the glass tube.

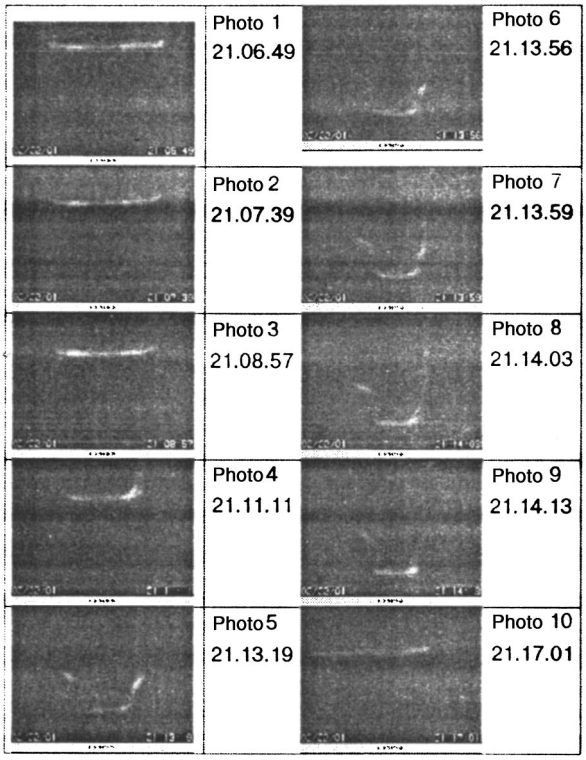


FIG. 4. Changes in the profile of the interface in the cell during the admission of gaseous $^4$He containing a water vapor impurity at a high rate of admission of the mixture; $\Delta P = 0.6$ Torr, $T = 1.4$ K. The numbers on the frames indicate the time at which they were taken (hours.minutes.seconds). The first and last frames correspond to the vapor–He II interface (the start of admission, and the end of admission; after the addition of liquid into the cell the He II level returned to its initial state).

At high pressures ($\Delta P \geqslant 0.6$ Torr) or for a prolonged admission of the gaseous mixture, the shape of the interface in the volume of the cell, observed on the monitor, varied noticeably with time. The initially flat interface (vapor–He II) began to curve noticeably, i.e., the layer of condensate grew not only below the surface of the He II but also along the vapor–liquid interface. An example of the evolution of the shape of the interface with time at $\Delta P \approx 0.6$ Torr and a constant temperature of the liquid 1.4 K is shown in Fig. 4. The change in shape of the boundary indicates that a transparent layer of impurity condensate, well wet by superfluid helium, is growing from the walls towards the center of the cell. If the pump *6* (see Fig. 1) is turned on and the He II level is increased abruptly to the initial position, then the interface, observed on the monitor, becomes flat again (vapor–He II boundary). If the liquid level is lowered gradually, the curved meniscus reappears. If the liquid level is dropped suddenly and a layer of ''dry'' condensate is exposed and illuminated by the external light source, after several minutes in the atmosphere of gaseous helium (the condensate absorbs visible light much more strongly than the helium or glass and it therefore is heated faster), instead of a transparent uniform layer, individual granules of ice appear on the glass walls. When the liquid level is restored to its initial state, the interface again appears flat, but granules of ice which are formed in the decomposition of the layer can be clearly discerned at the walls of the cell below the He II surface. Consequently, the metastable layer of impurity water condensate is wet by the He II much better than are the walls of the glass cell or the ice granules that form on the walls when the condensate, overheated by the light, decomposes. Unlike an iceberg, which floats beneath the surface of the liquid and interacts weakly with the walls of the cell, the layer of condensate that grows from the walls of the cell along the interface at a high rate of admission of the mixture does not move downward when the He II level is lowered, and the ice granules formed in the decomposition of the layer are held on the surface of the glass walls and do not fall to the bottom of the cell.

When the rate of admission of the mixture was increased further ($\Delta P > 1$ Torr) or when the interface was intensely illuminated by a lamp in an attempt to improve the conditions for observation of the growth of the layer of condensate, it was observed that during the condensation of the gas flow, gas bubbles form on the surface of the liquid in a manner reminiscent of boiling on the surface of a superfluid liquid. This can be explained by the formation and decomposition of a metastable layer of condensate, accompanied by the release of a rather larger amount of gaseous $^4$He. Simultaneously, ice granules appear on the walls of the cell, the shape and disposition of which remain practically unchanged when the temperature is raised to 4.2 K and then lowered again.

In a number of cases at high rates of admission of the impurity we observed the uncontrolled decomposition of the condensate layer at the interface, accompanied by strong pressure jumps in the cell ($\Delta P$ increased to 20 Torr), which led to expulsion of superfluid liquid together with the icebergs found in it from the working cell *1* into the test tube *2*. Judging from the readings of the thermometers *3* and *4*, the temperature of the liquid remained practically unchanged during this process. Extrusion of icebergs through an aperture 1.5 mm in diameter at the bottom of the cell led to decomposition, and a fine powder appeared on the bottom of the test tube *2* in the superfluid He II, the volume of the powder being much less than the volume of the initial condensate. After this the pressures in the cell and in the outer test tube were equalized, and He II from the test tube again returned to cell *1*.

As control observations showed, increasing the temperature of the liquid to 4.2 K and cooling to 1.4 K had practically no effect on the parameters of a powder created by extrusion, just as had been the case in the decomposition of the icebergs upon heating in $^4$He or in the decomposition of the layer of condensate at the liquid–vapor interface (ice granules on the walls of the cell), i.e., the decomposition of the icebergs is accompanied by a substantial change in the structure and properties of the water samples.

## CONCLUSION

The main results of our studies of the properties of the liquid-helium-permeated porous water condensate that forms when gaseous $^4$He containing a water vapor impurity is introduced into a cell filled with superfluid He II at $T \sim 1.4$ K are as follows:

1. At a low rate of admission of the mixture ($\Delta P \sim 0.2$ Torr) the as-prepared gel-like layer (cloud) of water condensate beneath the surface of the He II is transformed in a time

of $\sim 10$ min into a denser iceberg, having an oval shape with an average diameter close to the diameter of the cell ($d=9$ mm) and suspended on the walls of the cell in the He II volume. The shape of an iceberg remains unchanged at a constant temperature $T<1.6$ K.

This behavior is characteristic for gels formed in the interaction of a finely disperse suspension with a surrounding liquid matrix — a dispersion medium (sol–gel reaction).

2. As the temperature of the He II is increased above 1.6 K, the volume of the iceberg decreases monotonically, as is manifested in a gradual shift of the iceberg downward along the walls of the cell, i.e., the structure of the sample can change smoothly as the temperature of the liquid is raised.

One of the reasons for this may be the enlargement of the impurity nanoparticles and the decrease in the average size of the pores between the randomly packed particles, similar to what was observed in the experiments of Ref. 10.

3. The temperature interval in which icebergs exist depends strongly on the properties of the surrounding medium (Fig. 3). In an atmosphere of gaseous helium the icebergs decompose upon heating above 1.8 K, while in liquid He I at a pressure $P=1$ atm they can exist to 4 K.

In contrast to the water condensate, impurity condensates of rare and molecular gases begin to decompose intensely when the temperature of the surrounding medium is raised above 7 K.[10]

4. The total water content in the volume of the icebergs, according to an estimate based on the volumes of the initial sample and the powder formed upon the decomposition of the iceberg, was $\leqslant 10^{20}$ $H_2O$ molecules/cm$^3$. The density of the icebergs estimated from the observations of oscillations of the iceberg when acoustic vibrations arise in the cell containing He I, is not more than a few percent higher than the density of the surrounding liquid, i.e., approximately 1.3 times smaller than the density of solid $^4$He at the same temperatures.

The decomposition of the water condensate in a gaseous atmosphere is accompanied by the escape of a jet of cold helium. The properties of the ice powder forming in the decomposition do not change upon thermocycling in the interval 1.4–5 K. Consequently, the internal structure of the initial icebergs and the ice particles making up the powder is qualitatively different.

Using the results of studies of the properties of metallic clusters arising in the evaporation of a metal in dense helium vapor[6] and the properties of impurity–helium condensates of molecular and atomic gases,[7–10] it is natural to assume that the water condensate consists mainly of water nanoclusters with an average diameter of the order of 5 nm (i.e., one cluster can contain of the order of $10^3$ isomeric chains and/or three-dimensional "cages" of $H_2O$ molecules),[12] each of which is surrounded by a layer of solidified helium. The interaction of these neutral complexes with each other and with superfluid He II gives rise to a metastable porous condensate (watergel), the properties of which vary noticeably with changes in the properties of the surrounding medium. It follows from preliminary observations that the condensate formed upon condensation of a vapor of ethyl alcohol (a weakly polar liquid at room temperatures) is still less stable than the water condensate and can decompose even in He II.

The authors are grateful to Yu. A. Osip'yan for support of this research, to V. B. Efimov, V. B. Shikin, G. V. Kolmakov, A. A. Levchenko, E. V. Lebedeva, and M. Yu. Brazhnikov for helpful discussions and calculations, and to A. V. Lokhov and V. N. Khlopinskii for technical assistance. This study was supported in part by the Ministry of Industry, Science, and Technology of the Russian Federation as part of the Government Science and Technology Program "Topical Problems in Condensed Matter Physics" and also the Russian Foundation for Basic Research and the Moscow District Government, Grant 01-02-97037.1.

[a)]E-mail: mezhov@issp.ac.ru

[1] L. P. Mezhov-Deglin and A. M. Kokotin, JETP Lett. **70**, 756 (1999).
[2] L. P. Mezhov-Deglin and A. M. Kokotin, Physica B **284–288**, 103 (2000).
[3] L. P. Mezhov-Deglin and A. M. Kokotin, J. Low Temp. Phys. **119**, 385 (2000).
[4] L. P. Mezhov-Deglin and A. M. Kokotin, Prib. Tekh. Eksp. **2**, 159 (2001).
[5] P. Savich and A. Shalnikov, J. Phys. USSR **10**, 299 (1946).
[6] L. Ya. Vinnikov and A. O. Golubok, "High-resolution technique for direct observation of magnetic structure on the surface of type-II superconductors" [in Russian], Preprint of the Institute of Solid State Physics, Russian Academy of Sciences, Chernogolovka (1984), p. 9; L. Ya. Vinnikov, I. V. Grigor'eva, and L. A. Gurevich, "Vortex structure in single crystal HTSC superconductors," in *The Real Structure of HTSC Superconductors*, Vol. 23 of Springer Series in Material Science, edited by V. Sh. Shehtman, Springer (1993), p. 89.
[7] E. B. Gordon, L. P. Mezhov-Deglin, and O. F. Pugachev, JETP Lett. **19**, 63 (1974).
[8] E. B. Gordon, L. P. Mezhov-Deglin, O. F. Pugachev, and V. V. Khmelenko, Prib. Tekh. Éksp., No. 6, 247 (1975); Zh. Éksp. Teor. Fiz. **73**, 952 (1977) [Sov. Phys. JETP **46**, 502 (1997)].
[9] A. M. Bass and H. P. Broida (Eds.), *Formation and Trapping of Free Radicals*, Academic Press, New York (1960), Izd. Inostr. Lit., Moscow (1962).
[10] S. I. Kiselev, V. V. Khmelenko, D. M. Lee, V. Kiryukhin, R. E. Boltnev, E. B. Gordon, and B. Kreimer, Phys. Rev. (2002) (to be published).
[11] P. R. ten Wolde, D. W. Oxtoby, and D. Frenkel, Phys. Rev. Lett. **81**, 2695 (1998).
[12] K. Nauta and R. E. Miller, Science **287**, 293 (2000).
[13] V. F. Petrenko and R. W. Whitworth, *Physics of Ice*, Oxford University Press, New York (1999).

Translated by Steve Torstveit

## SUPERCONDUCTIVITY, INCLUDING HIGH-TEMPERATURE SUPERCONDUCTIVITY

# Magnetic-field and temperature dependence of the critical current in thin epitaxial films of the high-temperature superconductor $YBa_2Cu_3O_{7-\delta}$

Yu. V. Fedotov, S. M. Ryabchenko, É. A. Pashitskiĭ, A. V. Semenov,* and V. I. Vakaryuk

*Institute of Physics, National Academy of Sciences of Ukraine, pr. Nauki 46, 03028 Kiev, Ukraine*

V. M. Pan and V. S. Flis

*Institute of Metal Physics, National Academy of Sciences of Ukraine, pr. Vernadskogo 36, 03680 Kiev, Ukraine*

(Submitted October 15, 2001)
Fiz. Nizk. Temp. **28**, 245–261 (March 2002)

The magnetic-field dependence (in a field **H** applied along the normal to the film plane $z$) and temperature dependence of the critical current density $j_c$ are investigated in high-quality biaxially oriented epitaxial films of $YBa_2Cu_3O_{7-\delta}$, with maximum values of $j_c$ reaching $2\times10^6$ A/cm$^2$ in zero magnetic field at $T=77$ K. It is found that the value of $j_c(H_z,T)$, which is independent of $H_z$ in the low-field region $H_z<H_m$, is well approximated at $H_z>H_m$ by the function $j_c(H_z,T)/j_c(0,T)=\alpha\ln(H^*/H_z)$ over a rather wide region $0.95>j_c(H_z,T)/j_c(0,T)>0.3$. Here $H^*=H_m e^{1/\alpha}$ is proportional to $\tau=1-T/T_c$, at least in the temperature region where the measurements are made, and the parameter $\alpha$ is nearly independent of temperature. For the sample with the highest value of the critical current density for $H_z\to0$ an anomalously sharp transition from the low-field plateau to the logarithmic behavior is observed. Some published data on $j_c(H_z,T)$ in epitaxial thin films of HTSCs are analyzed, and it is shown that an approximation of the given form is also applicable to the results of other authors. Although the value of $j_c(H=0,\tau)$ itself, like the values of $H^*$, are substantially different for films investigated by different authors, the values of $\alpha$ obtained when their results are approximated by a logarithmic dependence are extremely close to one another and to the values found in our studies. A model is proposed which qualitatively explains the nature of the observed behavior of $j_c(H_z,T)$, and the basic properties of this model are discussed. It is shown that the approximately logarithmic dependence is due to a mechanism involving the depinning of the ensemble of Abrikosov vortices pinned at edge dislocations in the low-angle grain boundaries that exist in epitaxial thin films of HTSCs. A sharp transition from the plateau to the logarithmic segment is realized if at $H\approx H_m$ there is a change of the mechanism governing the critical current density, specifically, in the case when for $H<H_m$ the value of $j_c$ is limited more strongly by the transparency of the grain boundaries to the superconducting current than by the depinning of vortices in low fields. © *2002 American Institute of Physics.* [DOI: 10.1063/1.1468520]

### 1. INTRODUCTION

It has been shown in a large number of papers[1–7] that in epitaxial thin films of HTSCs the critical current density $j_c$ can reach values two or three orders of magnitude larger than in single crystals of the same substances, attaining values of $(2-3)\times10^6$ A/cm$^2$ and higher in zero magnetic field at $T=77$ K. This property of epitaxial thin films is important for practical applications and is usually attributed to a more effective vortex pinning in them (see reviews[8,9]).

In particular, a governing role in determining the value of the critical current in epitaxial films may be played by low-angle boundaries between single-crystal blocks (grains) misoriented in the $(a,b)$ plane; such grains are a characteristic element of the structure of epitaxial films obtained by various methods of deposition.[9] These grain boundaries (GBs) represent a quasiperiodic chain of edge dislocations (EDs). This, on the one hand, limits the admissible limiting value of the superconducting (SC) current in the sample as a result of local suppression of the SC order parameter near the GBs.[10,11] On the other hand, the high density of edge dislocations in the GBs can lead to an effective vortex pinning, promoting an increase in the critical current.

The magnetic-field dependence of the critical current density $j_c$ in HTSC epitaxial films has been investigated in many studies (see, e.g., Refs. 8 and 9 and references cited therein) in which the dependence of the current flowing in the plane of the film is measured as a function of the magnitude and direction of the applied magnetic field **H** at different temperatures. The angular dependence of $j_c$ generally exhibits features at angles $\theta_H=0$ and $\pi/2$ between the direc-

 

tion of **H** and the normal **z** to the film plane. The first of these features is attributed to vortex pinning on dislocations in the GBs parallel to the $c$ axis, and the second feature is usually attributed to the presence of a transition layer with misfit dislocations near the substrate. Depending on the features of the technology used to prepare the film, it may exhibit both of these features simultaneously or only one of them, e.g., at $\theta_H = 0$.[7–9,12]

In this paper we discuss only the experimental data obtained for the magnetic field **H** oriented along the normal **z** to the film surface, parallel to the $c$ axis ($\theta_H = 0$), and from now on the subscript $z$ on $H_z$ will in most cases be dropped.

Typical results described in the literature[13–16] for this case include the finding that the field dependence $j_c(H)$ can be divided into several segments corresponding to definite magnetic field intervals. In the first of these, for $H < 1-20$ mT (depending on the temperature $T$) the value of $j_c$ is independent of the applied field. At higher fields $j_c$ begins to decrease with increasing $H$. In the majority of papers (see, e.g., Refs. 9, 13, and 16) the authors identify an intermediate interval on this part of the $j_c$ curve, in which $j_c$ falls off by a nearly inverse square-root law, $H^{-1/2}$, after which $j_c$ begins to fall off with increasing field in proportional to the higher power $1/H$. The authors of the experimental studies call attention to the presence of a correlation between the observed $j_c(H)$ curves and the structural defects in the films. For example, in Ref. 13 it was pointed out that the value of the characteristic field at which the transition from the low-field plateau to the region of strong field dependence $j_c(H)$ occurs is related to the value of the dislocation density in the film (here dislocations not involved in the low-angle GBs are considered). The authors of Ref. 15 call attention to the presence of a correlation between the microstructure of the ''islands''—grains separated by GBs—and the character of the decline of $j_c(H,T)$ in epitaxial thin films of HTSCs.

The results of studies of $j_c(H,T)$ are usually discussed on the basis of various mechanisms of vortex (or vortex-lattice) depinning with allowance for the presence of pinning centers specific to epitaxial thin films: linear edge dislocations in the GBs. These boundaries, as a rule, form a two-dimensional mesh with the dimensions of the cells (grains) distributed randomly about some mean value, as is well seen with the aid of high-resolution electron microscopy (see, e.g., Refs. 17 and 18). Depending on the technology used to grow the films, the mean linear dimensions of the grains can range from a few tens of nanometers to hundreds of nanometers.

In particular, we have considered the mechanisms involving a transition from an ''irregular'' vortex lattice, each vortex of which is pinned at a dislocation distributed in a mesh of GBs to a more regular vortex lattice in which at least some of the vortices are forced to locate inside the grains, where there are no such effective pinning centers.[9] Here the dependence $j_c(H) \sim H^{-1/2}$ is usually attributed to an electromagnetic vortex–vortex interaction at an average distance between vortices $a_0 \sim B^{-1/2}$, where $B$ is the magnetic induction. For a thin slab, under the assumption of a uniform distribution of the magnetization, one has $B = H$ by virtue of the fact that the demagnetizing factor is close to unity for $\mathbf{H} \| \mathbf{z}$.

In this paper we investigate the magnetic-field and temperature dependence of the critical current density in high-quality epitaxial films of $YBa_2Cu_3O_{7-\delta}$ grown by the laser sputtering (ablation) method, with a critical temperature of the superconducting transition $T_c = 91$ K and a maximum value $j_c = 2 \times 10^6$ A/cm$^2$ in zero magnetic field at $T = 77$ K.

It was found that the value of $j_c(H_z,T)$, which in the low-field region $H_z < H_m$ is independent of $H$, is well approximated in the region $H_z > H_m$ by a relation $j_c(H_z,T)/j_c(0,T) = \alpha \ln(H^*/H_z)$, where the parameter $\alpha$ is nearly independent of temperature to within the measurement error, and the parameter $H^* = H_m e^{1/\alpha}$ is proportional to $\tau$, at least in the region of small $\tau$ where the measurements were made. For the sample with the largest value of $j_c(H = 0, T = 77$ K) the transition from the low-field plateau to the logarithmic dependence is extremely sharp.

Analysis of some published data on $j_c(H_z,T)$ in epitaxial thin films of HTSCs shows that an approximation of this form is applicable not only to our results but also to the results of other authors.[13–16] Although the values of $j_c(H = 0,\tau)$ and $H^*$ are substantially different for the films studied by different authors, the values of $\alpha$ turn out to be extremely close. Because of this, in the present paper we discuss a possible model that qualitatively explains the nature of the observed behavior of $j_c(H_z,T)$.

## 2. EXPERIMENT

### 2.1. Samples and measurement method

The samples used for the measurements in this study were obtained by deposition on a polished single-crystal substrate of (100) $LaAlO_3$ by laser evaporation of the materials to be deposited using a laser beam with a specially shaped profile (see Ref. 17 for a description of the technique). It follows from previous studies[18,19] that this method yields epitaxial $YBa_2Cu_3O_{7-\delta}$ films with $c$ axis oriented along the normal to their surface. A ''mesh'' of low-angle grain boundaries arises in the film plane. Typical angles between the $a$ and/or $b$ axes in adjacent grains are not more than a few degrees. The typical average dimensions of the grains range from 10 to 100 nm, depending on the deposition conditions.

It should be noted that previous high-resolution electron-microscope studies of transverse cuts of grown films[18] have shown that, depending on the deposition conditions, the GBs can be ''thin,'' 12–15 nm, or diffuse, smeared over 30–35 nm. It must be assumed that these cases correspond to a different structure of the dislocation walls and a different accumulation of defects near them.

In this study we investigated two films, R48 and R532, with the same thicknesses, each 300 nm, and the same dimensions in the plane, $\approx 0.5 \times 0.5$ cm, but obtained in different deposition regimes. Film R48 was deposited by evaporating $YBa_2Cu_3O_{7-\delta}$ by means of a two-beam solid-state Nd:YAG laser from two rotating stoichiometric targets at a substrate temperature of around 740–750 °C and an oxygen pressure in the chamber of around 0.2 mbar. The average

transverse size of the single-crystal grains obtained in this deposition regime, as monitored with an electron microscope, is 20–50 nm. The films grown in this regime usually have an extremely narrow (with respect to temperature) transition to the superconducting state and a high critical current density. Film R532 was grown in a regime that ordinarily produces films with a wider (in temperature) transition to the superconducting state and lower $j_c$.

Measurements of the critical parameters $j_c$ and $T_c$ of the HTSC films were made by a contactless low-frequency magnetic susceptibility method at a frequency of 937 Hz in the temperature interval 77–100 K and in a magnetic field between zero and 0.06 T. The contactless measurement technique used to measure the critical current density was justified in Refs. 20 and 21 with the use of a model of the critical state of type-II superconductors (the Bean model[22]). It is based on analysis of the dependence of the imaginary part of the complex magnetic susceptibility $\chi''$ of the samples on the amplitude of the alternating magnetic field $h_\sim$. The measured value of $\chi''(h_\sim)$ reaches a maximum at a certain value $h_\sim = h_m$. In the general case the value of $h_m$ depends on the critical current density and the shape and dimensions of the sample in a rather complicated way. It was shown in Ref. 20 that for a disk-shaped thin film in an alternating magnetic field perpendicular to the film, the relation between $j_c$ and $h_m$ should be described by the relation $j_c = 1.030 h_m / d_z$, where $d_z$ is the film thickness (here $j_c$ is in A/m,$^2$ $h_m$ is in A/m, and $d_z$ is in meters). It was shown in Ref. 21 that this same expression describes quite well the results of experiments on films of other isometric shapes, including squares.

It should be noted that in Refs. 20 and 21 the justification for the induction method of measuring $j_c$ from the amplitude of the exciting field $h_m$ at which $\chi''(h_\sim)$ reaches a maximum was based on the assumption that $j_c$ is independent of the magnetic field in the interval $-h_m < H < h_m$. In addition, the relation between $j_c$ and $h_m$ was obtained for the case when there is no external static magnetic field. Therefore, the use of this method for determining $j_c$ in a magnetic field and, moreover, in the field region where $j_c$ depends on $H$, requires further theoretical justification.

In Refs. 14 and 15 this method was used for measuring $j_c(H)$ in YBCO films in a rather wide field interval $0 \leqslant H \leqslant 5$ T. The authors of Ref. 14 pointed out that the application of a static field $H_z$ does not in and of itself modify the relations obtained in Refs. 20 and 21, provided that $j_c$ varies slowly with field. It can be expected that the method remains correct for measurements in a magnetic field if the relative variations in $j_c(H_z, T)$ in the interval $H_z \pm h_m$ are small.

The results of resistive measurements of $j_c(H)$ (by direct determination of the resistance of samples upon passage of a transport current)[9,16] are in good qualitative agreement with the results of contactless induction measurements. This provides additional justification for the applicability of the induction method for studying the field dependence of $j_c$.

We made a special check of the reproducibility of the values obtained for $h_m$ (and, hence, $j_c$) in measurements as the field was increased from zero to the maximum value and on the reverse path, as the applied field was decreased from the maximum value to zero. No differences were observed in the $j_c(H)$ curves within the measurement error for the two directions of change in the field.

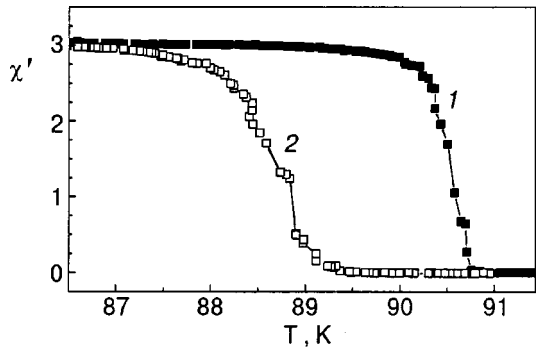


FIG. 1. Temperature dependence of $\chi'$ (in arbitrary units) for the films R48 (*1*) and R532 (*2*).

The value of $T_c$ was determined from the start of the sharp rise in $\chi''(T)$. The measurement error and the reproducibility of the values of $T_c$ were $\pm 0.1$ K.

### 2.2. Temperature dependence of the critical current at $H=0$

The temperature dependence of the critical current $j_c(0, T)$ was measured in the absence of a static external field (actually, in the magnetic field of the Earth, which at all measurement temperatures did not affect the value of the critical current). Initially, in a small inducing alternating field with amplitude $h_\sim \ll h_m$ we measured the temperature dependence of the real and imaginary parts of the magnetic susceptibility of the film samples. The results of the measurements of $\chi'(T)$ are presented in Fig. 1. From these results we can conclude that the film R48 has not only a higher critical temperature ($T_c = 90.9 \pm 0.1$ K) in comparison with film R532 ($T_c = 89.6 \pm 0.1$ K) but also a narrower (with respect to temperature) transition to the superconducting state (the rise of $\chi'(T)$ occurs in a narrower region), i.e., it is of higher quality and uniformity.

The temperature dependence of the critical current density $j_c(0, \tau)$ for these samples, calculated from the values of $h_m$ found from measurements of $\chi''(h_\sim)$ at each temperature, is plotted in Fig. 2 on a log–log scale. It is seen that the plots can be approximated by the power law

$$j_c(T) = J_n (1 - T/T_c)^s. \tag{1}$$

For the sample R48 the plot has two parts described by functions with different parameters: $J_n = (16.7 \pm 5.3) \times 10^7$ A/cm$^2$, $s = 1.93 \pm 0.10$ for $\tau = (1 - T/T_c) \leqslant 0.048$ and $J_n = (2.0 \pm 0.23) \times 10^7$ A/cm$^2$, $s = 1.20 \pm 0.05$ in the interval $0.048 \leqslant \tau \leqslant 0.154$. For sample R532 in the entire investigated interval $0.008 \leqslant \tau \leqslant 0.136$ these parameters have only one set of values $J_n = (5.1 \pm 0.35) \times 10^7$ A/cm$^2$ and $s = 1.99 \pm 0.03$, i.e., sample R532 has smaller absolute values of the critical current, and the change of the exponent in the power law (1) is not observed for it.

### 2.3. Magnetic-field dependence of the critical current density

Measurements of the magnetic-field dependence of the critical current $j_c(H_z, \tau)$ for the films R48 and R532 were made for a number of different temperatures in the interval

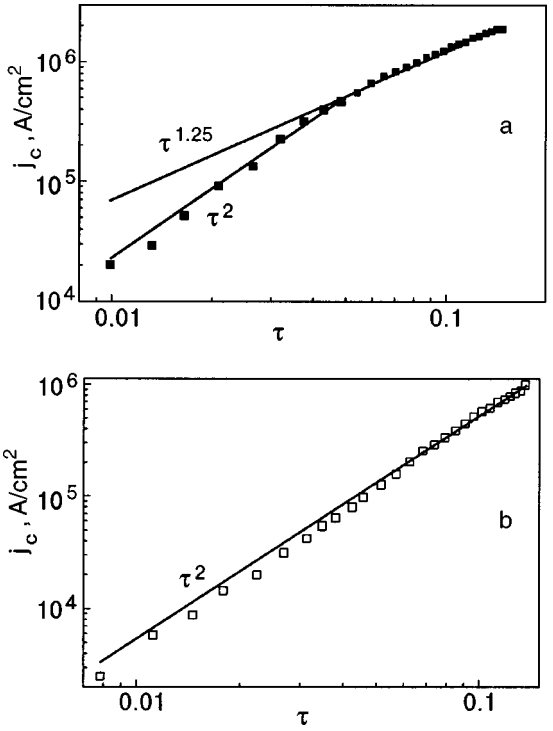


FIG. 2. Temperature dependence of the critical current density (plotted versus $\tau = 1 - T/T_c$) for films R48 (a) and R532 (b). The points are experimental, and the solid curves are the approximating functions $\tau^{1.25}$ and $\tau^2$.

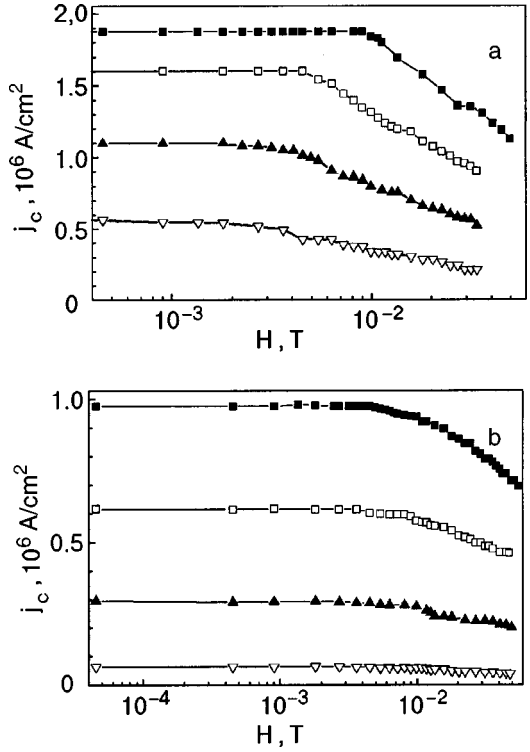


FIG. 3. Magnetic-field dependence of the critical current density in the films R48 (a) and R532 (b) for temperatures $T$ [K]: 77 (■); 80 (□); 83 (▲); 86 (▽). The curves are drawn through the points as a visual aid.

$T_c > T > 77$ K by the above-mentioned method of measuring $\chi''(h_\sim)$ at each value of the applied magnetic field. A static magnetic field $H$ up to 60 mT was applied along the normal to the surface of the film.

The $j_c(H_z)$ curves obtained for different values of the temperature are presented in Fig. 3 in a semilog plot, and the normalized function $j_c(H_z,\tau)/j_c(0,\tau)$ at same temperatures is plotted in Fig. 4.

As we see from these figures, the observed $j_c(H_z,\tau)$ curves for low fields $H < H_m$ contain a plateau on which $j_c$ is independent of field. The value of $H_m$, which determines the width of the plateau, increases with decreasing temperature. Then, after a rather sharp kink at the point $H = H_m$ (sharper for film R48 and somewhat less sharp for R532), a region in which $j_c$ falls off rather rapidly with increasing field appears.

It follows from the semilog plots that this dependence for the film R48 can be described by the relation

$$j_c(H_z,T)/j_c(0,T) = \alpha \ln(H^*/H_z). \tag{2}$$

The coefficient $\alpha$ found when the experimental data are approximated by Eq. (2) turns out to be practically independent of temperature (see Fig. 5), while the parameter $H^* = H_m e^{1/\alpha}$ that determines the field of the transition from the plateau $j_c(H_z,T) = j_c(0,T)$ to the logarithmic dependence (2) is temperature dependent. As we see from Fig. 6, which shows a plot of the values $H^*(\tau)$ found from the best fit for the film R48, this dependence can be approximated within the experimental error by the function

$$H^*(\tau) = H_{\text{eff}}\tau, \tag{3}$$

where for sample R48 $H_{\text{eff}} = 4.1 \pm 0.2$ T.

To convince ourselves that it is no accident that the experimental curves conform to a logarithmic dependence of $j_c(H_z,T)$ on the magnetic field, we also show a log–log plot of the same dependence $j_c(H_z,T)/j_c(0,\ T)$ for sample R48 (see Fig. 4b) with a plot of the relation $j_c(H_z) \sim H_z^{-1/2}$ which is often used for approximating experimental data of this kind. Also shown are the best-fit curves corresponding, for different temperatures, to relation (2) with the parameters $\alpha$ shown in Fig. 5 and with $H^*(\tau)$ corresponding to Eq. (3) for the indicated value of $H_{\text{eff}}$. We see from Fig. 4a and 4b that the logarithmic dependence (2) describes the results much better than does the power law.

For film R532 one can apparently also speak of the existence of a dependence of type (2) for $j_c(H)$, starting at certain values of the field, although the transition region from the plateau $j_c(H_z,T) = j_c(0,T)$ to this dependence is smeared out. To analyze the parameters of the field dependence of $j_c$ for this sample from the data obtained is rather complicated in view of the rather narrow interval of magnetic fields for which measurements were made.

The values found for $j_c(H_z)$ in the low-field plateau region ($0 < H_z < H_m$) for sample R48 corresponded to $h_m$ values of 10 mT at $T = 77$ K and 3 mT at $T = 86$ K, the closest temperature to $T_c$ for which the field dependence was measured. For sample R532 the corresponding value of $h_m$ at 77 K was approximately half as large, and at 86 K one-fifth as large, as for R48, in connection with the lower values of $j_c$. These values of $h_m$ are comparable to the widths of the low-field plateau on the $j_c(H_z,T)$ curves in our samples at the corresponding temperatures. With increasing applied field the values of $h_m$ decrease in proportion to the decrease in $j_c(H_z)$. From a comparison of these values of $h_m$ with the data of Figs. 3 and 4 it follows that for sample R48 it is only in a narrow transition region from the plateau to the logarith-

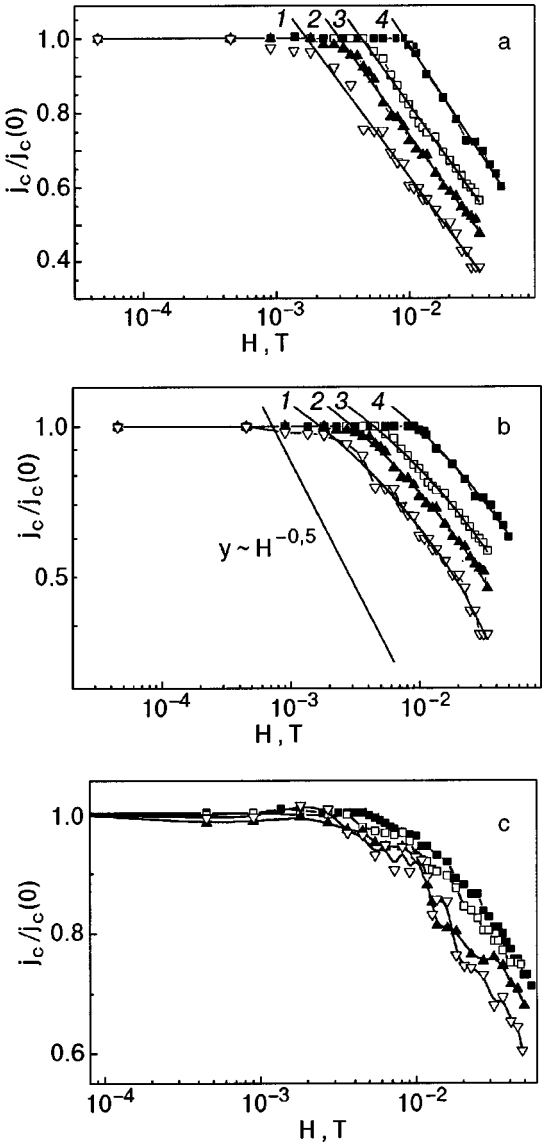


FIG. 4. Normalized magnetic-field dependence of the critical current density $j_c(H)/j_c(0)$ in the films R48 (a,b) and R532 (c) for various temperatures $T$ [K]: 77 (■); 80 (□); 83 (▲); 86 (▽). The curves *1*, *2*, *3*, and *4* are approximations according to relation (2) with $\alpha$ and $H^*$, respectively, equal to 0.208 and 0.206 T, 0.215 and 0.314 T, 0.215 and 0.458 T, and 0.234 and 0.643 T for curves *1–4*, respectively.

mic behavior that can one speak of an appreciable variation of $j_c(H_z)$ in the field interval $H_z \pm h_m$. One can therefore expect a certain apparent smoothing of the sharpness of this transition, although it looks anomalously sharp even under these conditions.

## 3. DISCUSSION OF THE RESULTS

### 3.1. Temperature dependence of the critical current density in zero field

As we have said, for sample R48 the power-law dependence $j_c(0,\tau) \propto \tau^s$ is characterized by the presence of a crossover at $\tau = 0.048$ from the value $s = 1.93 \pm 0.10$ to $s = 1.20 \pm 0.05$. This result agrees with the theoretical dependences $j_c(0,\tau) \propto \tau^2$ and $j_c(0,\tau) \propto \tau^{5/4}$ obtained on the basis of the model developed in Refs. 10 and 11, which describes a limitation on the supercurrent density flowing through low-

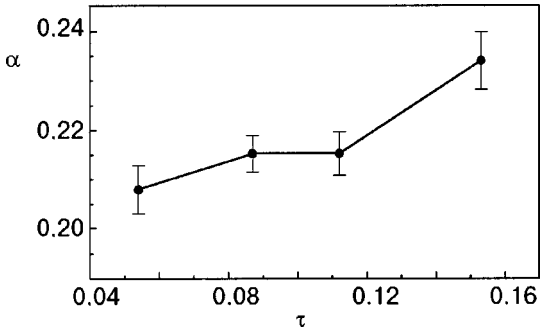


FIG. 5. Values of $\alpha$ found by fitting the magnetic-field dependence $j_c(H)$ in the film R48 by relation (2) for different temperatures ($\tau$). The line connecting the points is drawn as a visual aid.

angle boundaries between single-crystal grains in HTSC epitaxial films. This mechanism presupposes that the single-particle pinning force on vortices in low fields is so large that the critical current necessary for their depinning, $j_{c\,\mathrm{dep}}(H \to 0,\tau)$, exceeds the maximum superconducting current $j_{c\,\mathrm{tr}}(\tau)$ allowed by the transparency of the low-angle boundaries. As a result of this, the critical current density $j_c(0,\tau)$ in the film is equal to $j_{c\,\mathrm{tr}}(\tau)$.

The low-angle boundaries form a quasiperiodic chain of edge dislocations separated by a distance $d$ that depends on the mutual misorientation angle $\theta$ of the grains and is given by the Frank formula: $d(\theta) = b/2\sin(\theta/2) \approx b/\theta$, where $b$ is the modulus of the Burgers vector, which is equal in order of magnitude to the lattice constant. As was shown in Refs. 10 and 11, there exists a non-Josephson mechanism of suppression of the supercurrent flowing through such a boundary. In the framework of the given mechanism it is taken into account that the supercurrent flowing perpendicular to the boundary is spatially redistributed in the channels between the insulating cores of the edge dislocations. The maximum local value of this current density can reach that of the pair-breaking current, which is suppressed by the nonsuperconducting environment of these nuclei on account of the proximity effect. For the case of small angles $\theta$ it was found that the value of $j_{c\,\mathrm{tr}}(\tau)$ is described by a relation similar to (10). Here several regimes are possible, leading to different exponents $s$ in the power law (1) for $j_{c\,\mathrm{tr}}(\tau)$.

For small values of $\tau$, when the coherence length $\xi(T) = \xi_0/\sqrt{\tau}$ is rather large and exceeds $d(\theta)$, a function (1) with $s = 2$ should be realized, whereas in the region of larger

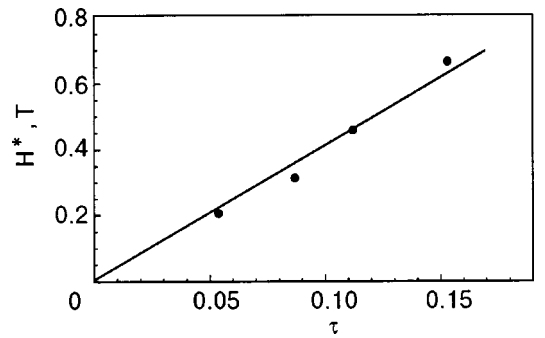


FIG. 6. Dependence on $\tau$ of the values obtained for $H^*$ by fitting the data on $j_c(H,\tau)/j_c(0,\tau)$ for the film R48 by relation (2) (●) and by approximating this dependence by the relation $H^* = \tau H_{\mathrm{eff}}$ with $H_{\mathrm{eff}} = 4.1$ T (—).

$\tau$, where $d(\theta) > \xi(\tau)$, there are two possible regimes, depending on the parameters $\Gamma_1$ and $\Gamma_2$ characterizing, respectively, the degree of local variation of the superconducting properties of the film near the boundaries (in particular, suppression of the superconducting order parameter $\Psi$ and of the pair-breaking current $j_0 \propto \Psi^3$) and the "geometric shadow" effect created by the insulating cores of the edge dislocations.

In the case of a rather small value of the parameter $\Gamma_2$, which corresponds to dislocation cores of small radius (i.e., a large transparency of the low-angle boundaries), when the condition $\Gamma_1\Gamma_2 \ll 2$ holds, with increasing $\tau$ a crossover from exponent $s=2$ to $s=3/2$ should be observed at a critical value $\tau_c$ determined from the condition $d(\theta)=2\xi(\tau_c)$. Such a crossover has been observed experimentally at $\tau_c = 0.048$ for a high-quality 50-nm thick $YBa_2Cu_3O_{7-\delta}$ epitaxial film investigated in Ref. 11.

At large values of the parameters $\Gamma_1$ and $\Gamma_2$, when $\Gamma_1\Gamma_2 \gg 2$, which corresponds to large (of the order of 10–20 Å) radii of the nonsuperconducting cores of the edge dislocations, according to Ref. 11 a crossover from $j_{c\,\mathrm{tr}}(\tau) \sim \tau^2$ to $j_{c\,\mathrm{tr}}(\tau) \sim \tau^{5/4}$ should be observed with increasing $\tau$. The results obtained for the film R48 (see Fig. 2a) clearly are in accord with this theoretical prediction. Starting from the value $\tau_c$ at which this crossover is observed and the experimental values of $j_c(\tau)$ on different sides of it, one can use formula (22) of Ref. 11 to estimate the values of the parameters $\Gamma_1$ and $\Gamma_2$ for the edge dislocations in the grain boundaries as $\Gamma_1 \approx 4$ and $\Gamma_2 \approx 3.6\sqrt{\tau}$.

In the case of large values of $\Gamma_2$ the region of the "geometric shadow" of the dislocation core becomes large. Then the width of the superconducting channel between dislocations can become smaller than $\xi(\tau)$ even at rather large values of $\tau$. In this case there will be a quadratic dependence $j_{c\,\mathrm{tr}}(\tau) \sim \tau^2$ in the entire interval of observations, which essentially corresponds to the formation of an S–N–S contact along the grain boundaries. It can be assumed that it is this case that is realized in the film R532.

The mechanism wherein the critical current density is limited by the transparency of the grain boundaries does not presuppose a magnetic-field dependence of $j_{c\,\mathrm{tr}}(\tau)$. Thus, if it is $j_{c\,\mathrm{tr}}(\tau)$ that limits the observed value of $j_c(0,\tau)$, then the magnetic-field dependence of $j_c(H,\tau)$ should have a plateau for all fields at which the condition $j_{c\,\mathrm{dep}}(H,\tau) \leqslant j_{c\,\mathrm{tr}}(\tau)$ holds.

Below, in an analysis of the magnetic-field dependence, we shall see that $j_{c\,\mathrm{dep}}(H,\tau)$ can also lead to a plateau at low fields. The possibility of distinguishing the situation $j_{c\,\mathrm{tr}}(\tau) \leqslant j_{c\,\mathrm{dep}}(H \to 0,\tau)$ and $j_{c\,\mathrm{tr}}(\tau) \geqslant j_{c\,\mathrm{dep}}(H \to 0,\tau)$ from the experimental data apparently reduces to an analysis of the possible temperature dependences of $j_{c\,\mathrm{tr}}(\tau)$ and $j_{c\,\mathrm{dep}}(H \to 0,\tau)$ and their comparison with experiment. In addition, it is expected that the sharpness of the transition from the plateau to the part with substantial magnetic-field dependence of $j_c$ will be different in these two cases.

We note that in Ref. 13, on the basis of estimates made there, the view was expressed that for the samples we investigated, the value of $j_c$ in low fields, corresponding to the plateau on the initial part of $j_c(H)$, is determined by the pair-breaking current. Here the pair-breaking current was equal, not even to the maximum local critical current density achieved in the flow of current through the dislocation wall, but to its average measured value.

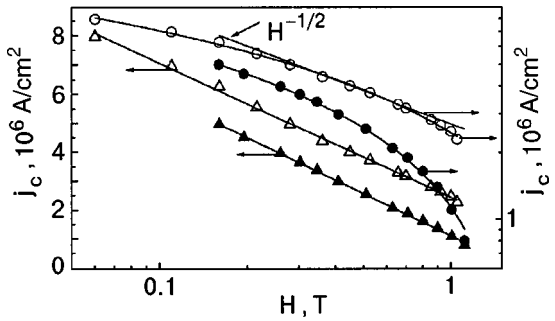


FIG. 7. Data on the magnetic-field dependence of $j_c(H)$ given in Fig. 36a of Ref. 9 for temperatures $T$ [K]: 54 (○,△); 81 (●,▲). The lines show the approximation of the data by relation (2) with the corresponding parameters. For comparison the approximation of the data for $T=54$ K by a function $j_c(H) \sim H^{-1/2}$ is also shown.

In the film R48, in which the dependence $j_c(H=0,\tau)$ exhibits the crossover expected on the basis of the model of Refs. 10 and 11, the value of $j_c(H=0,\tau)$ itself is large, in agreement with the estimates,[10,11] and one observes an extremely sharp transition from the plateau to the logarithmic part of $j_c(H,\tau)$. This suggests that the condition $j_{c\,\mathrm{tr}}(\tau) \leqslant j_{c\,\mathrm{dep}}(H \to 0,\tau)$ is met in it, and $j_c(H=0,\tau)$ is determined by $j_{c\,\mathrm{tr}}(\tau)$ in accordance with the model.[10,11]

In spite of the possibility of explaining the temperature dependence $j_c(H=0,\tau)$ in the R532 film on the basis of the model of Refs. 10 and 11, there are apparently insufficient data to support the conclusion that the relation $j_{c\,\mathrm{tr}}(\tau) \leqslant j_{c\,\mathrm{dep}}(H \to 0,\tau$ holds), which is necessary in order to invoke this model.

### 3.2. Magnetic-field dependence of the critical current density. Comparison with the data of other authors

The magnetic-field dependence of $j_c$ in the region $H > H_m$ is due to the growth of the density of vortices and enhancement of the interaction between them as the magnetic field is increased. We note that the presence of a low-field plateau on the $j_c(H)$ curve in epitaxial films has been reported repeatedly in the literature (see Refs. 9, 13–16 etc.). Nevertheless, we do not know of any published data for which $j_c(H)/j_c(0)$ on the descending part would be described by a relation of the form (2).

This raises the question of whether a dependence of the type (2) is characteristic for our samples only or if it applies to the results of measurements by other authors on analogous HTSC films. To check this we took the results of Ref. 9 (see Fig. 36a of that paper), obtained from a resistive (four-probe) measurement of $j_c(H_z)$ at temperatures of 54 and 81 K. An analysis of those data is presented in Fig. 7, which shows the best-fit curves corresponding to expression (2) with the optimally chosen parameters and also a dependence of the type $j_c(H_z) \sim H_z^{-1/2}$. We see that a dependence of the type (2) gives a better (over a wider field interval) description of the results presented in Fig. 36a of Ref. 9 than does an inverse square-root dependence.

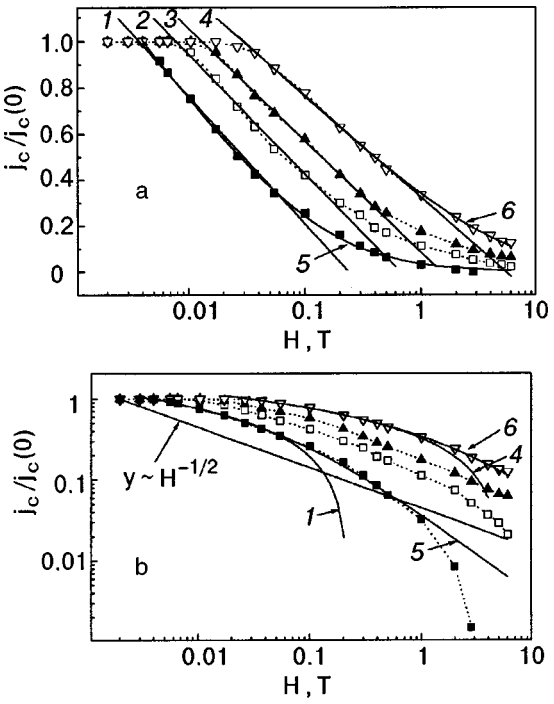


FIG. 8. Plots of $j_c(H,T)/j_c(0,T)$ constructed according to the data in Fig. 2 of Ref. 13 for temperatures $T$ [K]: 80 (■); 60 (□); 40 (▲); 4.2 (▽). The solid lines *1–4* correspond to relation (2) with parameters $\alpha$ and $H^*$ equal to 0.241 and 0.239 T, 0.225 and 0.667 T, 0.211 and 1.495 T, and 0.192 and 5.463 T. Curves *5* and *6* show an approximation of the data by relation (4) for 80 and 4.2 K, respectively. The dotted curves connect the points as a visual aid. For comparison the line corresponding to $y \sim H^{-1/2}$ is also shown.

We further analyzed the data presented in Ref. 13, where measurements of $j_c(H_z)$ were made by the torsional magnetometer method for a film with an annular cutout at temperatures of 80, 60, 40, and 4.2 K. The results of this analysis are shown in Fig. 8a in the form a log–log plot: the points are the data of Ref. 13, and the curves are the result of their approximation [on the initial part of $j_c(H_z)$] by Eq. (2) with the optimally chosen parameters. Here the parameter $\alpha$ was found to be 0.24, 0.22, 0.21, and 0.19 (for the four temperature values indicated above, respectively). The values of $H^*(\tau)$ found from the best fit are shown in Fig. 9. For temperatures 80–40 K the points conform to the straight line

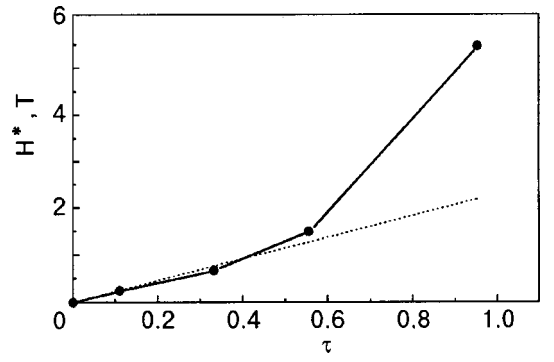


FIG. 9. Dependence of the values of $H^*$ found from an approximation of the data of Ref. 13 (see Fig. 8a of the present paper) by relation (2). The points are connected by a solid line for clarity. The dotted line corresponds to the relation $H^* = 2.3\tau$ T.

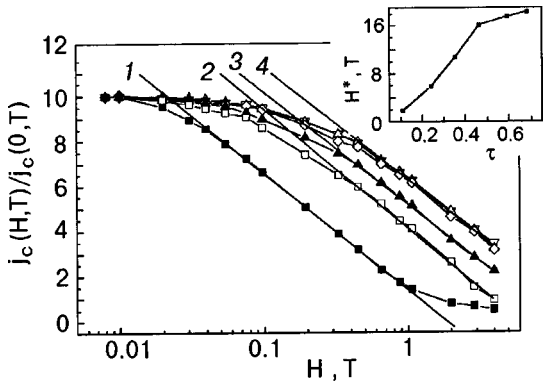


FIG. 10. Plots of $j_c(H,T)/j_c(0,T)$ constructed from the data shown in Fig. 8 of Ref. 14 for different $T/T_c$: 0.89 (■), 0.76 (□), 0.65 (▲), 0.53 (△), 0.41 (◇), and 0.32 (▽). The solid lines *1–4* correspond to equation (2) with the parameters $\alpha$ and $H^*$ equal to 0.225 and 1.846 T, 0.231 and 5.91 T, 0.218 and 10.7 T, and 0.217 and 18.26 T. The inset shows a plot of $H^*$ versus $\tau$.

$H^*(\tau) = 2.3\tau$ T. The value of $H^*$ for $T = 4.2$ K lies substantially above this line. We note that Fig. 9 corresponds to the plot of $B^*(T)$ given in Fig. 4 of Ref. 13 after a recalculation of the data to $\tau$ instead of $T$, since, in accordance with the method used to determine it in Ref. 13, $B^*$ corresponds to the quantity $H_m = H^* e^{-1/\alpha}$ introduced in Eq. (2) of the present paper. At the same time, $H_m(\tau) \propto H^*(\tau)$, since the value of $\alpha$ for the data of Ref. 13 and also for our results is nearly independent of temperature. Our fit to the data of Ref. 13 on the temperature dependence of $j_c(0,T)$ indicates a dependence linear in $\tau$: $j_c(0,T) = j_c(0,T \to 0)\tau$, for the sample investigated in that study.

It is seen in Fig. 8 that the data of Ref. 13 at all temperatures in low fields $H < H_m$ include a segment $j_c(H_z,T) = j_c(0,T)$, followed by somewhat wider (than in the case of film R48) regions of transition to a logarithmic dependence of the type (2). After that the dependence of the type (2) holds in the interval $0.95 \geqslant j_c(H_z,T)/j_c(0,T) \geqslant 0.25–0.3$, after which come segments of a slower dependence $j_c(\log H_z^{-1})$.

It should be noted that fitting the data[13] in Fig. 8 by a relation of the form

$$j_c(H_z,T)/j_c(0,T) = \alpha_1 \ln[(H_1^* + H_z)/H_z], \qquad (4)$$

which at low fields practically coincides with (2), allows one to describe the experimental data to good accuracy up to field values an order of magnitude larger than can be done using relation (2). The optimal values of $\alpha_1$ and $H_1^*$ are somewhat different from $\alpha$ and $H^*$. The curves for such a fit are also shown in Fig. 8.

Figure 10 shows the results of a fitting by relation (2) of the data for $j_c(H_z,T)/j_c(0,T)$ obtained from the data in Fig. 8 of Ref. 14. We see that these data are also well described by this relation, but the transition region from the plateau for $H_z < H_m$ to the logarithmic dependence here is considerably broadened in comparison with our results for sample R48 and/or the data of Ref. 13. The linear dependence $H^*(\tau) \sim \tau$ also holds for higher temperatures (small $\tau \leqslant 0.45$), and saturation appears at low temperatures (large $\tau \geqslant 0.6$).

It can be seen from Fig. 2 of Ref. 15 that the experimental data of that study can be approximated by relation (2) in an analogous way on the interval $0.2<j_c(H_z,T)/j_c(0,T)<0.87$.

We note that the results of approximating the data of Refs. 14 and 15 by relation (2) are close to our results for sample R532 from the standpoint of the width of the transition region from the plateau to the logarithmic dependence. The values of $j_c(0,T)$ for the samples studied in Refs. 14 and 15 are substantially lower than for R48 and the sample investigated in Ref. 13. In this sense the samples in Refs. 15 and 16 are also similar to R532.

At the same time, the sharp kink on $j_c(H_z,T)/j_c(0,T)$ at the transition from the plateau for $H_z<H_m$ to the logarithmic dependence for $H_z>H_m$ for our sample R48 does not have a complete analogy with the data of Refs. 13–15. Even in Ref. 13, where this transition is notably sharper than in Refs. 14 and 15, for example, it is less sharp than for sample R48.

### 3.3. Magnetic-field dependence of the critical current in epitaxial films. A model and its consequences

To simplify the problem, let us assume that the only operative pinning centers for vortices in epitaxial thin films are rectilinear edge dislocations located in the dislocation walls of the grain boundaries and oriented parallel to the crystallographic axis $c$. All of the pinning centers of this kind are identical. These approximations do not affect the qualitative essence of the model and its consequences. If the concentration of edge dislocations is much larger than the vortex concentration $n$, then in this approximation one may neglect the ''entangling'' of the flux lines, and if a certain fraction $n_p$ of the vortices are pinned at the centers under discussion (linear defects), then the total pinning force for a vortex ensemble attempting to form a vortex lattice will be equal to $n_p F_{p\ \mathrm{ind}}$. In addition, the Lorentz force acting on this ensemble will be equal to $nF_{L\ \mathrm{ind}}$. Here $F_{p\ \mathrm{ind}}$ and $F_{L\ \mathrm{ind}}=F_{L\ \mathrm{ind}}(j)$ are the pinning force and Lorentz force, respectively, for an individual vortex.

Then the condition for collective breakaway of the vortices from the pinning centers (a jumplike transition to the ''flux flow'' regime) takes the form

$$(n_p/n)F_{p\ \mathrm{ind}}-F_{L\ \mathrm{ind}}(j_c)=0, \tag{5}$$

where the expression for the Lorentz force acting on an individual vortex has the standard form:

$$F_{L\ \mathrm{ind}}(j)=\frac{\phi_0}{c}j. \tag{6}$$

The pinning force on an individual edge dislocation lying normal to the plane of the film and parallel to the magnetic field depends on the dimensions of the core of the edge dislocation, on the state of the material (normal metal, insulator) in the core and in the region adjacent to it, and on the profile of the pinning potential well $\varepsilon_p(u)$, where $u$ is the displacement of the vortex axis, which is parallel to $z$, relative to the center of the core of the edge dislocation in the $(x,y)$ plane. In particular, for a model of single-particle pinning of a vortex on an edge dislocation with an insulating core of radius $r_c<\xi=\xi_0\tau^{-1/2}$, the maximum pinning force can be written in the form[23]

$$F_{p\ \mathrm{ind}}=\left(\frac{d\varepsilon_p(u)}{du}\right)_{\max}=\frac{9}{32}\left(\frac{2}{3}\right)^{1/2}\frac{\varepsilon_0 r_c^2}{\xi^3}\cong 0.23\frac{\varepsilon_0 r_c^2}{\xi^3}, \tag{7}$$

where $\varepsilon_0=(\phi_0/4\pi\lambda)^2$, $\lambda=\lambda_0\tau^{-1/2}$ is the penetration depth of the magnetic field, $(d\varepsilon_p(u)/du)_{\max}$ is the maximum value of the derivative with respect to the displacement of a vortex in the pinning potential well in the direction perpendicular to the axis of the dislocation, for a vortex oriented parallel to this axis.

Substitution of (6) and (7) into (5) leads to the expression

$$j_{c\ \mathrm{dep}}(H,\tau)/j_{c\ \mathrm{dep}}(0,\tau)=n_p(H)/n(H), \tag{8}$$

where

$$j_{c\ \mathrm{dep}}(0,\tau)=0.23\frac{c\phi_0 r_c^2}{(4\pi\lambda_0)^2\xi_0^3}\tau^{5/2}.$$

We see that the ratio $n_p/n$ is the only factor in (8) that depends on the magnetic induction $B$ in the film (which is equal to the external field $H_z$, since the demagnetizing factor is close to unity).

We note that expression (7) is obtained for a model of pinning at a dislocation with a small insulating core. In the case when the dimensions of the core are large (or when the core is a normal metal instead of an insulator), Eq. (7) will be somewhat different and may even lead to a different $\tau$ dependence of $j_{c\ \mathrm{dep}}(H=0,\tau)$. However, the proportionality of $j_{c\ \mathrm{dep}}(H,\tau)$ to $n_p/n$ does not change, and expression (8) remains valid, although with a different dependence for $j_{c\ \mathrm{dep}}(0,\tau)$. However, we will not discuss these cases in detail here.

In the absence of pinning centers an ensemble of $n$ vortices in a thin film placed in a magnetic field **H** perpendicular to its surface would form a regular hexagonal lattice with a lattice parameter $a\approx\sqrt{\phi_0/H}$. The presence of pinning centers causes this lattice to be distorted in such a way that the maximum number of vortices are located at the pinning centers for which the deviations from the positions corresponding to the sites of the regular lattice are as small as possible. Here a certain fraction of the vortices are forced to lie outside the pinning centers, i.e., they remain unpinned. The number of such vortices is determined by the number of the pinning centers in the sample and the configuration of their displacements and also the field-dependent vortex lattice parameter $a$. As a result, the ratio $n_p/n$ becomes dependent on $H$.

In a two-dimensional vortex lattice parallel to the $z$ axis, a vortex displaced by a distance $\delta\rho=\rho-\rho_0$ (here $\boldsymbol{\rho}=\mathbf{x}+\mathbf{y}$, $\rho=\sqrt{x^2+y^2}$) from the ''regular'' position at the point $\rho_0$, acquires an additional energy[24,25]

$$\varepsilon_{\mathrm{dist}}(\delta\rho)=\frac{\varepsilon_0}{a^2}(\delta\rho)^2=\frac{\phi_0 H}{(8\pi\lambda)^2}(\delta\rho)^2. \tag{9}$$

At the same time, having the vortex located at the pinning centers leads to an energy benefit equal to the pinning energy for a linear insulating defect parallel to the field:[25]

$$\varepsilon_p = -\frac{\varepsilon_0 r_c^2}{2\xi^2}; \quad r_c \ll \xi. \tag{10}$$

Here the pinning of the vortex is energetically favorable if the condition $\varepsilon_{\text{dist}}(\delta\rho)+\varepsilon_p<0$ holds.

As a result, the value of $\delta$, equal to the critical value of the displacement $\delta\rho$ up to which the vortex will remained pinned to an edge dislocation displaced from a regular position in the lattice, is

$$\delta = \frac{r_c}{\xi_0}\left(\frac{2\phi_0\tau}{H}\right)^{1/2} = \left(\frac{A\tau}{H}\right)^{1/2}. \tag{11}$$

The notation $A=2r_c^2\phi_0/\xi_0^2$ has been introduced for convenience.

Further, in order to find $j_{c\ \text{dep}}(H,\tau)$ according to Eq. (8), it is necessary to calculate the ratio $n_p(H)/n(H)$; this is the key feature of the model under study.

We restrict discussion to the magnetic field region in which $\delta$ is much greater than the distance $d$ between dislocations in the low-angle boundaries between grains. In this case $\delta$ actually characterizes the distance from a site of the regular vortex lattice to the nearest boundary between grains. On the other hand, since $\delta \ll a$ and $d \ll \langle L\rangle$, where $\langle L\rangle$ is the average linear dimension of the grains, the condition $a \gg \langle L\rangle$ can hold in this same field region. For fields sufficiently low as to ensure satisfaction of this condition and for a random distribution of grain boundaries, the probability of trapping a vortex at one of the pinning centers (i.e., on a linear edge dislocation in a low-angle grain boundary) is equal to the product of the probability that a point at which the electromagnetic energy of a given vortex is minimum (a site of the ''regular'' vortex lattice) will fall within a grain of a certain shape and size and the probability that this point lies a distance less than $\delta$ from the boundary of the grain. Suppose that the grains are square. Then the probability density for a site of the ''regular'' vortex lattice to fall within a grain with linear dimensions $L$ will be $W(L)\propto L^2P(L)$, where $P(L)$ is the probability density function of the grains with respect to $L$. The probability that this site will lie less than a distance $\delta$ from the grain boundary will be equal to the ratio of the area of a strip of width $\delta$ near the boundaries of the grain to the area $L^2$ of the whole grain:

$$\tilde{P}(L,\delta) = \begin{cases} 1, & L \leqslant 2\delta; \\ \dfrac{L^2-(L-2\delta)^2}{L^2}, & L > 2\delta. \end{cases} \tag{12}$$

As a result, we obtain the following expression for the critical current in terms of the fraction of pinned vortices:

$$j_{c\ \text{dep}}(H,\tau)/j_{c\ \text{dep}}(0,\tau) = n_p(H)/n(H) = \int_0^{2\delta} W(L)\,dL + \int_{2\delta}^{\infty} W(L)[1-(L-2\delta)^2/L^2]\,dL. \tag{13}$$

The dependence on the value of the applied field $H$ enters Eq. (13) only through the function $\delta(H)$.

Analysis of expression (13) for different distributions $W(L)$ (or $P(L)$) shows that if these distributions are characterized by the parameter $k=\langle L\rangle/\sigma$, where $\sigma$ is a width parameter of the distribution function, then for $k \gg 1$ the function $j_{c\ \text{dep}}(H,\tau)/j_{c\ \text{dep}}(0,\tau)$ calculated according to formula (13) is practically independent of the particular form of $W(L)$. It has a characteristic shape with a plateau at low fields followed by a decline. The declining segment is well described by the approximating relation (2) in an interval $0.9 > j_{c\ \text{dep}}(H,\tau)/j_{c\ \text{dep}}(0,\tau) > 0.3$ or even a little bit wider than that. With increasing $k$ the parameter $\alpha$ in (2), which characterizes the slope of the field dependence $j_{c\ \text{dep}}(H,\tau)$ near the inflection point in a semilog plot, tends toward the same limiting value $\approx 0.25$ regardless of the form of $W(L)$. When a rectangular distribution function is chosen, this value of $\alpha$ remains practically unchanged, even when $k$ is decreased to $k=1.1$. For a smoother distribution function the value of $\alpha$ corresponding to the best fit of the field dependence increases smoothly, starting at $k<4-5$, reaching a value $\approx 0.18$ as $k\to 1$. A comparison with experiment will allow one to choose the optimal value of $k$.

We note that the values of $\alpha$ indicated above were determined by equating the derivatives with respect to $\ln h$ of the approximating function $y=\alpha\ln(H^*/H)$ and of the function obtained from (13) at the point of its maximum slope. A determination of the optimal value of $\alpha$ in a comparison of the function (13) with the approximating function by the least-squares method in the interval $0.35 < j_{c\ \text{dep}}(H,\tau)/j_{c\ \text{dep}}(0,\tau) < 0.85$ will lead to somewhat smaller values of this parameter in comparison with that determined from the derivative with respect to $\ln H$ at the point of maximum slope, whereas the values of $H^*$ come out somewhat higher.

The value of $H^*$ obtained from fitting the corresponding segment (13) by relation (2) increases with increasing $\langle L\rangle$. From this standpoint one can understand qualitatively the growth $B^*=H_m=H^*e^{-1/\alpha}$ mentioned in Ref. 13 for samples containing, in addition to grain boundaries, edge dislocations inside the grains, oriented normal to the film surface. The presence of such dislocations can be taken into account effectively in the framework of the model considered above as a decrease of $\langle L\rangle$, which will lead to growth of $B^*=H_m\propto H^*$ ($\alpha$ is possibly independent of $\tau$). For the same reason, apparently, the values of $H^*$ will be significantly larger when the data of Ref. 14 are approximated by a logarithmic dependence than in the case of our sample R48 or the data of Ref. 13. In addition, it should be assumed that in the case of Ref. 14 there were pinning centers with a weaker pinning, which will lead to substantially lower values of $j_{c\ \text{dep}}(0,\tau)$.

Our most thorough analysis of expression (13) was done for the case of a distribution function of the gamma type, which has been found[15] to agree with the experimentally measured size distribution of the grains. This distribution has the form

$$P(L) = \frac{\mu^\nu}{\Gamma(\nu)} L^{\nu-1} e^{-\mu L}, \tag{14}$$

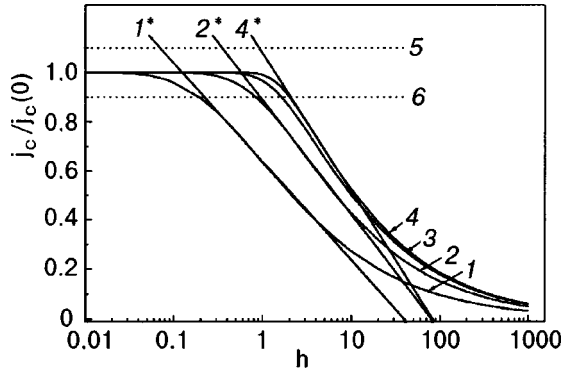


FIG. 11. Plots of $j_{c\,\mathrm{dep}}(h)/j_{c\,\mathrm{dep}}(h=0)$ constructed according to formula (16) for different $k$: 1.01 (*1*), 2 (*2*), 4 (*3*), 8 (*4*). Lines *1**, *2**, and *4** are the approximating functions $j_{c\,\mathrm{dep}}(h)$ of the type $\alpha \ln(h^*/h)$ for the descending part, corresponding to values of $\alpha$ and $h^*$ equal to 0.185 and 33.5, 0.203 and 80.04, and 0.244 and 83.11, respectively. The values of $\alpha$ and $h^*$ were taken from a least-squares fit to curves *1*, *2*, and *4*. Lines *5* and *6* illustrate schematically the cases $j_{c\,\mathrm{tr}}(0) > j_{c\,\mathrm{dep}}(H\to 0)$ and $j_{c\,\mathrm{tr}}(0) < j_{c\,\mathrm{dep}}(H\to 0)$.

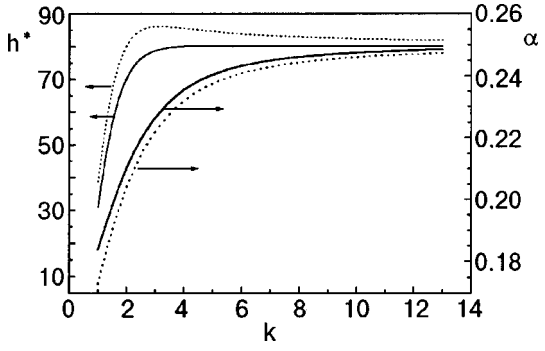


FIG. 12. Curves of $\alpha(k)$ and $h^*(k)$ obtained from an approximation of the descending part of $j_{c\,\mathrm{dep}}(h)$ by a function of the type $\alpha \ln(h^*/h)$. The solid curves show the result of a fit according to the values of the derivatives at the inflection points of the curves; the dotted curves are the result of a least-squares fit.

where $\nu=(\langle L\rangle/\sigma)^2=k^2$, $\mu=\langle L\rangle/\sigma^2=k^2/\langle L\rangle=k/\sigma$. The distribution function found experimentally in Ref. 15 is best fit by (14) for $\nu=2.57$ ($k=1.60$) and $\langle L\rangle=18$ nm.

In the case of square grains it corresponds to the following density for the distribution of areas occupied by the grains as a function of their linear dimensions:

$$W(L)=\frac{\mu^{\nu+2}}{\Gamma(\nu+2)}L^{\nu+1}\mathrm{e}^{-\mu L}. \tag{15}$$

Integration of expression (13) with this distribution density gives

$$j_{c\,\mathrm{dep}}(H,\tau)/j_{c\,\mathrm{dep}}(0,\tau) = 1-\frac{k^4\frac{1}{h}\Gamma\left[k^2,\frac{k^2}{\sqrt{h}}\right]-\frac{2k^2}{\sqrt{h}}\Gamma\left[1+k^2,\frac{k^2}{\sqrt{h}}\right]+\Gamma\left[2+k^2,\frac{k^2}{\sqrt{h}}\right]}{\Gamma[2+k^2]}, \tag{16}$$

where $\Gamma[x]$ and $\Gamma[x,x']$ are the complete and incomplete Euler gamma functions, respectively, and $h=H\langle L\rangle^2/(4A\tau)$.

In Fig. 11 the function (16) is plotted as a function of $h$ for different $k$. We see that the curves have a plateau at small $h$ and then, after an inflection, the sharpness of which increases with increasing $k$, a region of logarithmic dependence. After that the dependence on $\ln h$ becomes less steep. By approximating the logarithmic part by the expression $j_{c\,\mathrm{dep}}(H,\tau)/j_{c\,\mathrm{dep}}(0,\tau)=\alpha\ln(h^*/h)$, one can find the optimal values of $\alpha$ and $h^*=H^*\langle L\rangle^2/(4A\tau)$, which depend on the parameter $k$ of the distribution function (14). Here $\alpha$ takes on values from 0.248 for $k\gg 1$ to 0.186 for $k\to 1$ when it is determined from the derivative at the point of maximum slope. The functions $\alpha(k)$ and $h^*(k)$ determined both from a comparison of the derivatives and by the least-squares method are shown in Fig. 12.

It should be noted that the area of the film cannot be completely filled by square grains with a continuous random distribution with respect to sizes $L$. The simplest way of achieving dense filling is realized in the case of rectangular grains with an independent random distribution of the dimensions $L_x$ and $L_y$, which is described by the product of functions $P(L_x)$ and $P(L_y)$ given by relation (14), for example. In that case the fraction of pinned vortices is equal to

$$n_p/n=1-\frac{1}{\Gamma^2(v)}[\Gamma(\nu,2\mu\delta)-2\mu\delta\Gamma(\nu-1,2\mu\delta)]^2. \tag{17}$$

In spite of the difference of the analytical expressions (16) and (17), the field dependences corresponding to them are extremely close (differing in the slope near the inflection point by not more than 5%), which confirms the aforementioned weak influence of the detailed shape of the distribution function on $j_c(H_z,T)$.

Thus the results of our measurements and Refs. 14 and 15 can be described by distribution function (14) with the corresponding values of the parameter $k$. The values of $H^*$ can also be matched with the distribution (14) by a suitable choice of the values of $\langle L\rangle$.

In the case of the experimental data obtained for our film R48, with a sharp kink in the field dependence $j_c(H_z,T)$ at a point $H=H_m$, it must be assumed further that the condition $j_{c\,\mathrm{tr}}(\tau)\leqslant j_{c\,\mathrm{dep}}(H\to 0,\tau)$ holds for all the temperatures at which measurements were made (except, perhaps, the highest temperature $T=86$ K, which corresponds to $\tau=0.055$). Without this condition there is no distribution function that can account for the observed sharp transition of the $j_c(H_z,T)/j_c(0,T)$ from the plateau to the logarithmic part. We note that our estimates of $j_{c\,\mathrm{tr}}(\tau)$ based on the formulas in Ref. 11 and the value of $j_{c\,\mathrm{dep}}(0,\tau)$ show that these quantities are of the same order and that their ratio depends on the detailed structure of the pinning potential and the grain boundaries and also on $\tau$. In the case of thin films with the highest values of $j_c(H=0,\tau)$, such as sample R48, one can expect that $j_{c\,\mathrm{tr}}(\tau)\leqslant j_{c\,\mathrm{dep}}(H\to 0,\tau)$ for $\tau>\tau_{\mathrm{cr}}$, where $\tau_{\mathrm{cr}}$ is the threshold value for having $j_{c\,\mathrm{tr}}(\tau)/j_{c\,\mathrm{dep}}(H\to 0,\tau)\leqslant 1$ or $>1$.

According to the above analysis, when the sign of this inequality changes one should simultaneously observe both a decrease in the sharpness of the transition of $j_c(H)$ from the plateau to the logarithmic dependence and a change in the exponent $s$ of the power law (1) for $j_c(H=0,\tau)$. Thus for

films with $j_{c\,\mathrm{tr}}(0,\tau) \leqslant j_{c\,\mathrm{dep}}(H\to 0,\tau)$ this can be another reason for the crossover in $j_c(H=0,\tau)$, in addition to the cause argued in Refs. 10 and 11.

The transition of $j_c(H)$ from the plateau to the logarithmic part is also quite sharp for the data of Ref. 13, although it is somewhat more smeared that for the film R48. Some smoothing of the kink may be caused by scatter in the parameters of different grain boundaries in the same sample. There are apparently not yet enough data to justify any assertions about the sign of the inequality $j_{c\,\mathrm{tr}}(\tau)/j_{c\,\mathrm{dep}}(H\to 0,\tau) > 1$ or $<1$ in this case, although most likely the condition $j_{c\,\mathrm{tr}}(\tau)/j_{c\,\mathrm{dep}}(H\to 0,\tau) < 1$ will be realized here as well. This assumption is preferable, since such a sharp inflection from the plateau to the logarithmic part as in Ref. 13 is also difficult to obtain for reasonable parameters of the distribution function $W(L)$ such that the observed value of $\alpha$ is also obtained when the data of Ref. 13 are approximated by relation (2). At the same time, our sample R532 and the samples studied in Refs. 14 and 15 can with complete justification be classed with those for which $j_{c\,\mathrm{tr}}(\tau)/j_{c\,\mathrm{dep}}(H\to 0,\tau) > 1$.

Let us mention another feature of approximating the experimental data by the results of a calculation of (13) with the functions (12) and (14). The parts of $j_c(H_z,T)/j_c(0,T)$ directly following the logarithmic part, when one tries to describe them by means of formula (16) [or the experimental data of Ref. 13 by formula (4)] go lower than in the calculation using Eq. (11) for $\delta(H)$. However, excellent agreement is achieved when one uses in (12) and (13) the following expression for $\delta(H)$:

$$\delta(H) = \left( \frac{A\tau}{H(1+\gamma H)} \right)^{1/2} \tag{18}$$

with $\gamma \ll 1$. Here the results of a calculation of (13) with the distribution function (14) reduces to (16) but with $h$ replaced by $h(1+\gamma h)$. The optimal values of $\gamma$ found in the fitting do not agree with the values expected on the basis of the assumption that the pinning energy at an edge dislocation depends on the field in proportion to $(1-H/H_{c2})$.

Previously we have pointed out that the model that we have used in analyzing $j_{c\,\mathrm{dep}}(H,\tau)$—a statistically independent distribution of sites of the vortex lattice and the lines of the grain boundaries—has limitations at high fields. It may be that the feature noted when the experimental data are approximated by formula (16) or (17) stems from a limitation on the applicability of our proposed model for calculating $\tilde{P}(L,\delta)$, viz., formula (12), on the high-field side. This question will be addressed separately.

We also note that the proposed model gives a temperature dependence $H^* \sim \tau$. This temperature dependence is well satisfied in the region $0.05 < \tau < 0.3-0.5$ for all the experimental data for which a comparison was made. At larger values of $\tau$ a deviation from this dependence is observed for the data of Refs. 13 and 14, and, as we have said, these deviations are of different character.

The predicted dependence $H^* \sim \tau$ is found in the region in which the Ginzburg–Landau theory is valid, i.e., for small $\tau$. Therefore we will not comment on the deviations from this dependence in the region where $\tau$ becomes large.

## 4. CONCLUSION

In summary, we have established here that the magnetic-field dependence of the critical current density in epitaxial thin films of $YBa_2Cu_3O_{7-\delta}$ containing low-angle boundaries between grains, for a magnetic field applied perpendicular to the film plane, a plateau region where $j_c$ is practically independent of $H$ is followed by a segment with a logarithmic magnetic-field dependence of the form $j_c(H_z,T)/j_c(0,T) = \alpha \ln(H^*/H)$. Then the dependence of $j_c$ on the logarithm of the field becomes less steep and is satisfactorily approximated by a dependence $j_c(H_z,T) \sim H_z^{-1/2}$. A similar behavior is characteristic for the $j_c(H_z,T)$ data obtained by different authors.

In the present study, for the sample with the highest critical current [$j_c(H_z=0,\ T=77\ \mathrm{K}) > 10^6\ \mathrm{A/cm^2}$] we have observed experimentally an anomalously sharp transition (a kink!) in $j_c(H_z,T)$ from the plateau at low fields to the logarithmic region. In addition, we have first called attention to the possibility of making the logarithmic approximation (2) and to the fact that the values of $\alpha$ obtained by fitting this approximation to the data of different authors turn out to be practically the same and nearly independent of temperature (within the measurement error).

The observed dependence $j_c(H_z,T)$ is explained on the basis of a model with pinning of an ensemble of Abrikosov vortices on edge dislocations in the grain boundaries, which are ''dislocation walls.'' The vortex lattice turns out to be mismatched with the spatial distribution of grain boundaries, which contain chains of closely spaced dislocations. Here, up to a certain value of the field this mismatch is small, and all the vortices remain pinned. After the applied field is increased above a certain limit, the mismatch grows, and for some of the vortices it is energetically favorable to be located not at the pinning centers—dislocations and grain boundaries—but inside the grains. As a result, a smaller current is needed to produce a Lorentz force on the ensemble of vortices (comprising the distorted vortex lattice) sufficient to break the vortices away from the pinning centers, i.e., a smaller current become sufficient for the onset of the ''flux flow'' regime.

On the assumption of a statistically independent distribution of grain boundaries and vortex lattice sites, we have obtained a general expression for $j_{c\,\mathrm{dep}}(H_z,T)/j_{c\,\mathrm{dep}}(0,T)$. We have shown that for any distribution function of the number of grains with respect to their characteristic linear dimension $L$, the resulting magnetic-field dependence of the critical current density can be approximated over a rather wide interval $0.3 < j_c(H_z,T)/j_{c\,\mathrm{dep}}(0,T) < 0.9$ by a logarithmic function. We have shown that the value of the parameter $\alpha$ in such an approximation is rather insensitive to the size distribution function of the grains, and also to the other parameters that take into account the properties of the sample. The parameter $\alpha$ varies within narrow limits as a function of the ratio of the average grain size $\langle L \rangle$ to the width $\sigma$ of the distribution function in the region of small $k = \langle L \rangle/\sigma \lesssim 1$.

At the same time, the value of the characteristic field of the transition from the plateau to the logarithmic dependence, $H_m = H^* \mathrm{e}^{-1/\alpha}$, depends on the value of the average grain size $\langle L \rangle$ itself for any $k$ and also depends on $k$ for $k \sim 1$. The sharpness of the transition from the plateau to the

logarithmic part increases with increasing $k$ in the region of small values of $k$ and ceases to depend on $k$ for $k \gg 1$.

As we have already pointed out, it is experimentally established that for films with a high value of $j_c(H_z \to 0, T = 77\ \mathrm{K}) > 10^6\ \mathrm{A/cm^2}$ an extremely sharp kink is observed on $j_c(H_z)$ in the transition region from the plateau to the logarithmic dependence. The sharpness of the transition cannot be reconciled with a model in which the critical current density in the absence of field is limited by the value $j_{c\ \mathrm{dep}}(0,T)$, i.e., by depinning of individual vortices under the influence of the Lorentz force.

We have shown that in this case the observed dependences of $j_c(H_z,T)/j_c(0,T)$ can be explained on the assumption that in the absence of field the critical current density is limited by the transparency of the low-angle grain boundaries to the supercurrent, $j_{c\ \mathrm{tr}}(T)$. The value of $j_{c\ \mathrm{tr}}(T)$ is practically independent of the applied field, i.e., in this case the situation $j_{c\ \mathrm{tr}}(T) < j_{c\ \mathrm{dep}}(0,T)$ is realized, and the sharp kink in $j_c(H_z,T)/j_c(0,T)$ occurs at the field $H_m$ for which $j_{c\ \mathrm{dep}}(H_m,T) = j_{c\ \mathrm{tr}}(T)$. According to an estimate made, the value of $j_{c\ \mathrm{dep}}(0,T)$ even in these cases should not be many times greater than $j_{c\ \mathrm{tr}}(T)$. Therefore the magnetic-field dependence of $j_{c\ \mathrm{dep}}(H,T)$, which governs $j_c(H_z,T)$ in fields $H > H_m$, corresponds immediately to the logarithmic region above $H_m$.

For one of the samples (R48) we observed the temperature dependence $j_{c\ \mathrm{tr}}(T) \sim \tau^{5/4}$ that had earlier been predicted theoretically[11] for one variant of the relationships among the parameters governing $j_{c\ \mathrm{tr}}(T)$. Unlike the dependences of the type $\tau^{3/2}$ and $\tau^2$ (Ref. 11) or $\tau$ (Ref. 13), this type of dependence had not been reported previously.

*E-mail: semenov@iop.kiev.ua

[1] P. Chaudhari, R. H. Koch, R. B. Laibowitz, T. R. McGuire, and R. J. Gambino, Phys. Rev. Lett. **58**, 2684 (1987).
[2] G. W. Crabtree, J. Z. Liu, A. Umezawa, W. K. Kwok, C. H. Sowers, S. K. Malik, B. W. Veal, D. J. Lam, M. B. Brodsky, and J. W. Downey, Phys. Rev. B **36**, 4021 (1987).
[3] V. M. Pan, S. V. Gaponov, G. G. Kaminsky, D. V. Kuzin, V. I. Matsui, V. G. Prokhorov, M. D. Strikovsky, and C. G. Tretiatchenko, Crystallogr. Rep. **29**, 392 (1989).
[4] L. Civale, A. D. Marwick, M. W. McElfresh, T. K. Worthington, A. P. Malozemoff, F. H. Holtzberg, J. R. Thompson, and M. A. Kirk, Phys. Rev. Lett. **65**, 1164 (1990).
[5] V. M. Pan, A. L. Kasatkin, V. L. Svetchnikov, and H. W. Zandbergen, Crystallogr. Rep. **33**, 21 (1993).
[6] V. F. Solovjov, V. M. Pan, and H. C. Freyhardt, Phys. Rev. B **50**, 13724 (1994).
[7] D. H. Lowndes, D. K. Christen, C. E. Klabunde, Z. L. Wang, D. M. Kroeger, J. D. Budai, Shen Zhu, and D. P. Norton, Phys. Rev. Lett. **74**, 2355 (1995).
[8] V. M. Pan, *Physics and Material Science of Vortex States, Flux Pinning and Dynamics*, Vol. 26 of NATO ASI Series, edited by R. Kossowsky *et al.*, Kluwer, Dordrecht (1999), p. 1.
[9] V. M. Pan, Usp. Fiz. Met. **1**, 49 (2000).
[10] A. Gurevich and E. A. Pashitskii, Phys. Rev. B **57**, 13878 (1998).
[11] É. A. Pashitskii, V. I. Vakaryuk, S. M. Ryabchenko, and Yu. V. Fedotov, Fiz. Nizk. Temp. **27**, 131 (2001)[Low Temp. Phys. **27**, 96 (2001)].
[12] B. Roas, L. Schultz, and G. Saemann-Ischenko, Phys. Rev. Lett. **64**, 479 (1990).
[13] B. Dam, J. M. Huljbregtse, F. C. Klaassen, R. C. F. van der Geest, G. Doornbos, J. H. Rector, A. M. Testa, S. Freisem, J. C. Martínez, B. Stauble-Pumpin, and R. Griessen, Nature (London) **399**, 439 (1999).
[14] E. Mezzetti, R. Gerbaldo, G. Ghigo, L. Gozzelino, B. Minetti, C. Camerlingo, A. Monaco, G. Cuttone, and A. Roveelli, Phys. Rev. B **60**, 7623 (1999).
[15] G. Ghigo, D. Botta, A. Chiodoni, R. Generbaldo, L. Gozzelino, B. Minetti, C. Camerlingo, and C. Giannini, in *Proceedings of the 10th International Workshop on Critical Currents IWCC 2001*, June 4–7, 2001, edited by C. Jooss, Göttingen, Germany 2001, p. 100.
[16] V. A. Komashko, A. G. Popov, V. L. Svetchnikov, A. V. Pronin, V. S. Melnikov, A. Yu. Galkin, V. M. Pan, C. L. Snead, and M. Suenaga, Semicond. Sci. Technol. **13**, 209 (2000).
[17] I. Peshko, V. Flis, and V. Matsui, J. Phys. D **34**, 732 (2001).
[18] V. M. Pan, V. S. Flis, O. P. Karasevska, V. I. Matsui, I. I. Peshko, V. L. Svetchnikov, M. Lorenz, A. N. Ivanyuta, G. A. Melkov, E. A. Pashitskii, and H. W. Zandbergen, J. Supercond. Novel Incorporating Magnetism **14**, 105 (2001).
[19] V. Svetchnikov, V. Pan, Ch. Traeholt, and H. Zandbergen, IEEE Trans. Appl. Supercond. **AS–7**, 1396 (1997).
[20] R. Clem and A. Sánchez, Phys. Rev. B **50**, 9355 (1994).
[21] M. Wurlitzer, M. Lorenz, K. Zimmer, and P. Esquinazi, Phys. Rev. B **55**, 11816 (1995).
[22] C. P. Bean, Rev. Mod. Phys. **36**, 31 (1964).
[23] É. A. Pashitskii and V. Vakaryuk, Fiz. Nizk. Temp. **28**, 16 (2002)[Low Temp. Phys. **28**, 11 (2002)].
[24] D. R. Nelson and V. M. Vinokur, Phys. Rev. B **48**, 13060 (1993).
[25] G. Blatter, M. V. Feigelman, V. G. Geshkenbein, A. I. Larkin, and V. M. Vinokur, Rev. Mod. Phys. **66**, 1125 (1994).

Translated by Steve Torstveit

# Josephson effect in point contacts between "*f*-wave" superconductors

R. Mahmoodi

*Institute for Advanced Studies in Basic Sciences, 45195-159, Gava Zang, Zanjan, Iran*

S. N. Shevchenko

*B. Verkin Institute for Low Temperature Physics and Engineering of the National Academy of Sciences of Ukraine, 47 Lenin Ave., 61103 Kharkov, Ukraine*

Yu. A. Kolesnichenko*

*Institute for Advanced Studies in Basic Sciences, 45195-159, Gava Zang, Zanjan, Iran and B. Verkin Institute for Low Temperature Physics and Engineering of the National Academy of Sciences of Ukraine, 47 Lenin Ave., 61103 Kharkov, Ukraine*

(Submitted October 25, 2001)
Fiz. Nizk. Temp. **28**, 262–269 (March 2002)

A stationary Josephson effect in point contacts between triplet superconductors is analyzed theoretically for the most-probable models of the order parameter in $UPt_3$ and $Sr_2RuO_4$. The consequence of misorientation of the crystals in the superconducting banks on this effect is considered. We show that different models for the order parameter lead to quite different current-phase relations. For certain angles of misorientation a boundary between superconductors can generate a spontaneous current parallel to the surface. In a number of cases the state with a zero Josephson current and minimum of the free energy corresponds to a spontaneous phase difference. This phase difference depends on the misorientation angle and may possess any value. We conclude that experimental investigations of the current-phase relations of small junctions can be used for determination of the order parameter symmetry in the superconductors mentioned above. © *2002 American Institute of Physics.* [DOI: 10.1063/1.1468521]

## 1. INTRODUCTION

Triplet superconductivity, which is an analog of superfluidity in $^3$He, was first discovered in the heavy-fermion compound $UPt_3$ more than ten years ago.[1,2] Recently, a novel triplet superconductor $Sr_2RuO_4$ was found.[3,4] In these compounds, the triplet pairing can be reliably determined, for example, by Knight shift experiments,[5,6] but the identification of the symmetry of the order parameter is a much more difficult task. A large number of experimental and theoretical investigations done on $UPt_3$ and $Sr_2RuO_4$ are concerned with different thermodynamic and transport properties, but the precise order-parameter symmetry still remains to be worked out (see, for example, Refs. 7, 10–12, and original references therein).

Calculations of the order parameter $\hat{\Delta}(\hat{\mathbf{k}})$ in $UPt_3$ and $Sr_2RuO_4$ as a function of the momentum direction $\hat{\mathbf{k}}$ on the Fermi surface is a very complex problem. Some general information about $\hat{\Delta}(\hat{\mathbf{k}})$ can be obtained from the symmetry of the normal state: $G_{\text{spin-orbit}}\times\tau\times U(1)$, where $G_{\text{spin-orbit}}$ represents the point group with inversion, $\tau$ is the time-inversion operator, and $U(1)$ is a gauge transformation group. A superconducting state breaks one or more symmetries. In particular, a transition to the superconducting state implies the appearance of a phase coherence corresponding to breaking of the gauge symmetry. According to the Landau theory[13] of second-order phase transitions, the order parameter transforms only according to irreducible representations of the symmetry group of the normal state. Conventional superconducting states have the total point symmetry of the crystal and belong to the even unitary representation $A_{1g}$. In unconventional superconductors this symmetry is broken. The parity of a superconductor with inversion symmetry can be specified using the Pauli principle. Because for triplet pairing the spin part of $\hat{\Delta}$ is a symmetric second-rank spinor, the orbital part has to belong to an odd representation. In the general case the triplet pairing is described by an order parameter of the form $\hat{\mathbf{\Delta}}(\hat{\mathbf{k}})=i\mathbf{d}(\hat{\mathbf{k}})\hat{\boldsymbol{\sigma}}\hat{\sigma}_2$, where the vector $\hat{\boldsymbol{\sigma}}=(\hat{\sigma}_1,\hat{\sigma}_2,\hat{\sigma}_3)$, and $\hat{\sigma}_i$ are Pauli matrices in the spin space. A vector $\mathbf{d}(\hat{\mathbf{k}})=-\mathbf{d}(-\hat{\mathbf{k}})$ in spin space is frequently referred to as an order parameter or a gap vector of the triplet superconductor. This vector defines the axis along which the Cooper pairs have zero spin projection. If $\mathbf{d}$ is complex, the spin components of the order parameter spontaneously break time-reversal symmetry.

Symmetry considerations reserve for the order parameter considerable freedom in the selection of irreducible representation and its basis functions. Therefore in many papers (see, for example, Refs. 7, 10–12, 14–16) authors consider different models (so-called scenarios) of superconductivity in $UPt_3$ and $Sr_2RuO_4$, which are based on possible representations of crystallographic point groups. The subsequent comparison of theoretical results with experimental data makes it possible to draw conclusions about the symmetry of the order parameter.

In real crystalline superconductors there is no classification of Cooper pairing by angular momentum (*s*-wave, *p*-wave, *d*-wave, *f*-wave pairing, etc.). However, these terms are often used for unconventional superconductors in the

 

meaning that the point symmetry of the order parameter is the same as that for the corresponding representation of the $SO_3$ symmetry group of an isotropic conductor. In this terminology conventional superconductors can be referred to as *s*-wave. For example, "*p*-wave" pairing corresponds to the odd two-dimensional representation $E_{1u}$ of the point group $D_{6h}$ or the $E_u$ representation of the point group $D_{4h}$. The order parameter for these representations has the same symmetry as for the superconducting state with angular momentum $l=1$ of Cooper pairs in an isotropic conductor. If the symmetry of $\hat{\Delta}$ cannot be formally related to any irreducible representation of the $SO_3$ group, these states are usually referred to as hybrid states.

Apparently, in crystalline triplet superconductors the order parameter has a more complex dependence on $\hat{\mathbf{k}}$ in comparison with the well-known *p*-wave order parameter for superfluid phases of $^3$He. The heavy-fermion superconductor $UPt_3$ belongs to the hexagonal crystallographic point group ($D_{6h}$), and it is most likely that the pairing state belongs to the $E_{2u}$ ("*f*-wave" state) representation. The layered perovskite material $Sr_2RuO_4$ belongs to the tetragonal crystallographic point group ($D_{4h}$). Initially the simplest "*p*-wave" model based on the $E_u$ representation was proposed for the superconducting state in this compound.[8,9] However, this model was inconsistent with available experimental data, and later[10,11] other "*f*-wave" models of the pairing state were proposed.

Theoretical studies of the specific heat, thermal conductivity, and ultrasound absorption for different models of triplet superconductivity show considerable quantitative differences between calculated dependences.[7,10,11,16] The Josephson effect is much more sensitive to dependence of $\hat{\Delta}$ on the momentum direction on the Fermi surface. One of the possibilities for forming a Josephson junction is to create a point contact between two massive superconductors. A microscopic theory of the stationary Josephson effect in ballistic point contacts between conventional superconductors was developed in Ref. 17. Later this theory was generalized for a pinhole model in $^3$He (Refs. 18 and 19) and for point contacts between "*d*-wave" high-$T_c$ superconductors.[20,21] It was shown that current-phase relations for the Josephson current in such systems are quite different from those of conventional superconductors, and states with a spontaneous phase difference become possible. Theoretical and experimental investigations of this effect in novel triplet superconductors seem to be interesting and enable one to distinguish among different candidates for the superconducting state.

In Ref. 22 the authors study the interfacial Andreev bound states and their influence on the Josephson current between clean "*f*-wave" super-conductors both self-consistently (numerically) and non-self-consistently (analytically). The temperature dependence of the critical current is presented. However, in that paper there is no detailed analysis of the current-phase relations for different orientations of the crystals in the superconducting banks.

In this paper we theoretically investigate the stationary Josephson effect in a small ballistic junction between two bulk triplet superconductors with different orientations of the crystallographic axes with respect to the junction normal. In Sec. 2 we describe our model of the junction and present the full set of equations. In Sec. 3 the current density in the junction plane is calculated analytically for a non-self-consistent model of the order parameter. In Sec. 4 the current-phase relations for the most-likely models of "*f*-wave" superconductivity in $UPt_3$ and $Sr_2RuO_4$ are analyzed for different mutual orientations of the banks. We end in Sec. 5 with some conclusions.

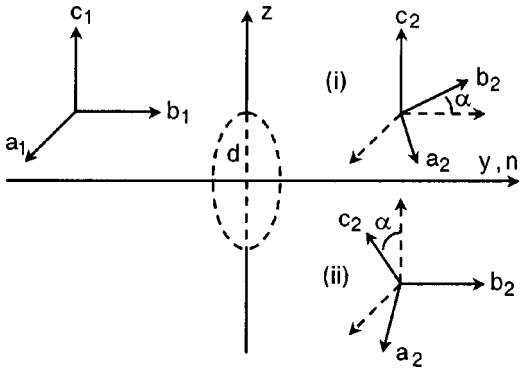


FIG. 1. Scheme of a contact in the form of an orifice between two superconducting banks, which are misorientated by an angle $\alpha$.

## 2. MODEL OF THE CONTACT AND FORMULATION OF THE PROBLEM

We consider a model of a ballistic point contact as an orifice of diameter $d$ in a partition impenetrable to electrons, between two superconducting half spaces (Fig. 1). We assume that the contact diameter $d$ is much larger than the Fermi wavelength and use the quasiclassical approach. In order to calculate the stationary Josephson current in point contact we use "transport-like" equations for $\xi$-integrated Green functions $\check{g}(\hat{\mathbf{k}},\mathbf{r},\varepsilon_m)$ (Ref. 23)

$$[i\varepsilon_m\check{\tau}_3-\check{\Delta},\check{g}]+iv_F\hat{\mathbf{k}}\nabla\check{g}=0, \tag{1}$$

and the normalization condition

$$\check{g}\check{g}=-1. \tag{2}$$

Here $\varepsilon_m=\pi T(2m+1)$ are discrete Matsubara energies, $v_F$ is the Fermi velocity, $\hat{\mathbf{k}}$ is a unit vector along the electron velocity, and $\check{\tau}_3=\hat{\tau}_3\otimes\hat{I}$; $\hat{\tau}_i$ $(i=1, 2, 3)$ are Pauli matrices in a particle-hole space.

The Matsubara propagator $\check{g}$ can be written in the form:[24]

$$\check{g}=\begin{pmatrix} g_1+\mathbf{g}_1\hat{\sigma} & (g_2+\mathbf{g}_2\hat{\sigma}_2)i\hat{\sigma}_2 \\ i\hat{\sigma}_2(g_3+\mathbf{g}_3\hat{\sigma}) & g_4-\hat{\sigma}_2\mathbf{g}_4\hat{\sigma}\hat{\sigma}_2 \end{pmatrix}; \tag{3}$$

as can be done for an arbitrary Nambu matrix. Matrix structure of the off-diagonal self-energy $\check{\Delta}$ in Nambu space is

$$\check{\Delta}=\begin{pmatrix} 0 & i\mathbf{d}\hat{\sigma}\hat{\sigma}_2 \\ i\hat{\sigma}_2\mathbf{d}^*\hat{\sigma} & 0 \end{pmatrix}. \tag{4}$$

Below we consider so-called unitary states, for which $\mathbf{d}\times\mathbf{d}^*=0$.

The gap vector $\mathbf{d}$ has to be determined from the self-consistency equation:

$$\mathbf{d}(\hat{\mathbf{k}},\mathbf{r}) = \pi T N(0) \sum_m \langle V(\hat{\mathbf{k}},\hat{\mathbf{k}}')\mathbf{g}_2(\hat{\mathbf{k}}',\mathbf{r},\varepsilon_m)\rangle, \tag{5}$$

where $V(\hat{\mathbf{k}},\hat{\mathbf{k}}')$ is a pairing interaction potential; $\langle ... \rangle$ stands for averaging over directions of an electron momentum on the Fermi surface; $N(0)$ is the electron density of states.

Solutions of Eqs. (1), (5) must satisfy the conditions for the Green functions and vector **d** in the banks of superconductors far from the orifice:

$$\check{g}(\mp\infty) = \frac{i\varepsilon_m \check{\tau}_3 - \check{\Delta}_{1,2}}{\sqrt{\varepsilon_m^2 + |\mathbf{d}_{1,2}|^2}}; \tag{6}$$

$$\mathbf{d}(\mp\infty) = \mathbf{d}_{1,2}(\hat{\mathbf{k}}) \exp\left(\mp \frac{i\phi}{2}\right), \tag{7}$$

where $\phi$ is the external phase difference. Equations (1) and (5) have to be supplemented by the boundary continuity conditions at the contact plane and conditions of reflection at the interface between superconductors. Below we assume that this interface is smooth and that electron scattering is negligible.

### 3. CALCULATION OF THE CURRENT DENSITY

The solution of Eqs. (1) and (5) allows us to calculate the current density:

$$\mathbf{j}(\mathbf{r}) = 2\pi e T v_F N(0) \sum_m \langle \hat{\mathbf{k}} g_1(\hat{\mathbf{k}},\mathbf{r},\varepsilon_m)\rangle. \tag{8}$$

We consider the simple model of a constant order parameter up to the surface. The pair breaking and the scattering on the partition and in the junction are ignored. This model can be rigorously found for calculations of the current density (8) in ballistic point contacts between conventional superconductors in the zero approximation in the small parameter $d/\xi_0$ ($\xi_0$ is the coherence length).[17] In anisotropically paired superconductors the order parameter changes at distances of the order of $\xi_0$ even near a specular surface.[25,26] Thus for calculations of the current (8) in the leading approximation in the parameter $d/\xi_0$ it is necessary to solve Eq. (5) near the surface of a semi-infinite superconductor. It can be done only numerically and will be the subject of our future investigations. Below we assume that the order parameter does not depend on coordinates and in each half space is equal to its value (7) far from the point contact. For this non-self-consistent model the current-phase relation of a Josephson junction can be calculated analytically. This makes it possible to analyze the main features of the current-phase relations for different scenarios of "*f*-wave" superconductivity. We believe that under this strong assumption our results describe the real situation qualitatively, as has been justified for point contacts between "*d*-wave" superconductors[20] and pinholes in $^3$He.[27] It was also shown in Ref. 22 that for a contact between "*f*-wave" superconductors there is also good qualitative agreement between the self-consistent and non-self-consistent solutions (although, of course, quantitative distinctions are present).

In a ballistic case the system of 16 equations for functions $g_i$ and $\mathbf{g}_i$ can be decomposed into independent blocks of equations. The set of equations which enables us to find the Green function $g_1$ is

$$iv_F\hat{\mathbf{k}}\nabla g_1 + (\mathbf{g}_3\mathbf{d} - \mathbf{g}_2\mathbf{d}^*) = 0; \tag{9}$$

$$iv_F\hat{\mathbf{k}}\nabla \mathbf{g}_- + 2i(\mathbf{d}\times\mathbf{g}_3 + \mathbf{d}^*\times\mathbf{g}_2) = 0; \tag{10}$$

$$iv_F\hat{\mathbf{k}}\nabla \mathbf{g}_3 - 2i\varepsilon_m\mathbf{g}_3 - 2g_1\mathbf{d}^* - i\mathbf{d}^*\times\mathbf{g}_- = 0; \tag{11}$$

$$iv_F\hat{\mathbf{k}}\nabla \mathbf{g}_2 + 2i\varepsilon_m\mathbf{g}_2 + 2g_1\mathbf{d} - i\mathbf{d}\times\mathbf{g}_- = 0; \tag{12}$$

where $\mathbf{g}_- = \mathbf{g}_1 - \mathbf{g}_4$. Equations (9)–(12) can be solved by integrating over ballistic trajectories of electrons in the right and left half spaces. The general solution satisfying the boundary conditions (6) at infinity is

$$g_1^{(n)} = \frac{i\varepsilon_m}{\Omega_n} + iC_n \exp(-2s\Omega_n t); \tag{13}$$

$$\mathbf{g}_-^{(n)} = \mathbf{C}_n \exp(-2s\Omega_n t); \tag{14}$$

$$\mathbf{g}_2^{(n)} = -\frac{2C_n\mathbf{d}_n - \mathbf{d}_n\times\mathbf{C}_n}{-2s\eta\Omega_n + 2\varepsilon_m}\exp(-2s\Omega_n t) - \frac{\mathbf{d}_n}{\Omega_n}; \tag{15}$$

$$\mathbf{g}_3^{(n)} = -\frac{2C_n\mathbf{d}_n^* + \mathbf{d}_n^*\times\mathbf{C}_n}{2s\eta\Omega_n + 2\varepsilon_m}\exp(-2s\Omega_n t) - \frac{\mathbf{d}_n^*}{\Omega_n}; \tag{16}$$

where $t$ is the time of flight along the trajectory, $\mathrm{sgn}(t) = \mathrm{sgn}(z) = s$; $\eta = \mathrm{sgn}(v_z)$; $\Omega_n = \sqrt{\varepsilon_m^2 + |\mathbf{d}_n|^2}$. By matching the solutions (13)–(16) at the orifice plane ($t=0$), we find the constants $C_n$ and $\mathbf{C}_n$. Index $n$ numbers the left ($n=1$) and right ($n=2$) half spaces. The function $g_1(0) = g_1^{(1)}(-0) = g_1^{(2)}(+0)$, which determines the current density in the contact, is

$$g_1(0) = \frac{i\varepsilon_m(\Omega_1+\Omega_2)\cos\zeta + \eta(\varepsilon_m^2 + \Omega_1\Omega_2)\sin\zeta}{\vec{\Delta}_1\vec{\Delta}_2 + (\varepsilon_m^2 + \Omega_1\Omega_2)\cos\zeta - i\varepsilon_m\eta(\Omega_1+\Omega_2)\sin\zeta}. \tag{17}$$

In formula (17) we have taken into account that for unitary states the vectors $\mathbf{d}_{1,2}$ can be written as

$$\mathbf{d}_n = \vec{\Delta}_n \exp i\psi_n, \tag{18}$$

where $\vec{\Delta}_{1,2}$ are real vectors.

Knowing the function $g_1(0)$, one can calculate the current density at the orifice plane $\mathbf{j}(0)$:

$$\mathbf{j}(0) = 4\pi e N(0) v_F T \sum_{m=0}^{\infty} \int d\hat{\mathbf{k}}\hat{\mathbf{k}}\,\mathrm{Re}\, g_1(0), \tag{19}$$

where

$$\mathrm{Re}\, g_1(0) = \frac{[\Delta_1^2\Delta_2^2\cos\zeta + (\varepsilon_m^2 + \Omega_1\Omega_2)\vec{\Delta}_1\vec{\Delta}_2]\sin\zeta}{[\vec{\Delta}_1\vec{\Delta}_2 + (\varepsilon_m^2 + \Omega_1\Omega_2)\cos\zeta]^2 + \varepsilon_m^2(\Omega_1+\Omega_2)^2\sin^2\zeta} \tag{20}$$

or, alternatively,

$$\mathrm{Re}\, g_1(0) = \frac{\Delta_1\Delta_2}{2}\sum_{\pm}\frac{\sin(\zeta\pm\theta)}{\varepsilon_m^2+\Omega_1\Omega_2+\Delta_1\Delta_2\cos(\zeta\pm\theta)}, \tag{21}$$

where $\theta$ is defined by $\vec{\Delta}_1(\hat{\mathbf{k}})\vec{\Delta}_2(\hat{\mathbf{k}}) = \Delta_1(\hat{\mathbf{k}})\Delta_2(\hat{\mathbf{k}})\cos\theta$, and $\zeta(\hat{\mathbf{k}}) = \psi_2(\hat{\mathbf{k}}) - \psi_1(\hat{\mathbf{k}}) + \phi$.

Misorientation of the crystals would generally result in the appearance of current along the interface,[20,22] as can be calculated by projecting the vector **j** on the corresponding direction.

We consider a rotation $R$ only in the right-hand superconductor (see Fig. 1), (i.e., $\mathbf{d}_2(\hat{\mathbf{k}}) = R\mathbf{d}_1(R^{-1}\hat{\mathbf{k}})$). The $c$ axis in the left half space is chosen along the partition between superconductors (along the $z$ axis in Fig. 1). To illustrate results obtained by computing Eq. (19), we plot the current-phase relation for different below-mentioned scenarios of "*f*-wave" superconductivity for two different geometries corresponding to different orientations of the crystals to the right and to the left at the interface (see Fig. 1):

(i) The basal *ab* plane to the right is rotated about the $c$ axis by an angle $\alpha$; $\hat{\mathbf{c}}_1 \| \hat{\mathbf{c}}_2$.

(ii) The $c$ axis to the right is rotated about the contact axis ($y$ axis in Fig. 1) by an angle $\alpha$; $\hat{\mathbf{b}}_1 \| \hat{\mathbf{b}}_2$.

Further calculations require a certain model of the vector order parameter **d**.

## 4. CURRENT-PHASE RELATION FOR DIFFERENT SCENARIOS OF "*F*-WAVE" SUPERCONDUCTIVITY

The model which has been successful to explain properties of the superconducting phases in $UPt_3$ is based on the odd-parity $E_{2u}$ representation of the hexagonal point group $D_{6h}$ for strong spin-orbital coupling with vector **d** locked along the **c** axis of the lattice:[10] $\mathbf{d} = \Delta_0\hat{z}[\eta_1 Y_1 + \eta_2 Y_2]$, where $Y_1 = k_z(k_x^2 - k_y^2)$ and $Y_2 = 2k_xk_yk_z$ are the basis function of the representation.[1)] The coordinate axes $x$, $y$, $z$ here and below are chosen along the crystallographic axes $\hat{\mathbf{a}}$, $\hat{\mathbf{b}}$, $\hat{\mathbf{c}}$ as at the left in Fig. 1. This model describes the hexagonal analog of spin-triplet "*f*-wave" pairing. For the high-temperature *A*-phase ($\eta_2 = 0$) the order parameter has an equatorial line node and two longitudinal line nodes. In the low-temperature *B* phase ($\eta_2 = i$) or the axial state

$$\mathbf{d} = \Delta_0\hat{z}k_z(k_x + ik_y)^2 \tag{22}$$

the longitudinal line nodes are closed and there is a pair of point nodes. The *B* phase (22) breaks the time-reversal symmetry. The function $\Delta_0 = \Delta_0(T)$ in Eq. (22) and below describes the dependence of the order parameter **d** on temperature $T$ (in carrying out numerical calculations we assume $T = 0$).

Other candidates for describing the orbital states, which imply that the effective spin-orbital coupling in $UPt_3$ is weak, are the unitary planar state

$$\mathbf{d} = \Delta_0 k_z[\hat{x}(k_x^2 - k_y^2) + \hat{y}2k_xk_y] \tag{23}$$

[or $\mathbf{d} = \Delta_0(Y_1, Y_2, 0)$] and the non-unitary bipolar state $\mathbf{d} = \Delta_0(Y_1, iY_2, 0)$.[7] In Fig. 2 we plot the Josephson current-phase relation $j_J(\phi) = j_y(y=0)$ calculated from Eq. (19) for both the axial [with the order parameter given by Eq. (22)] and the planar [Eq. (23)] states for a particular value of $\alpha$ under the rotation of the basal *ab* plane to the right [the geometry (i)]. For simplicity we use a spherical model of the Fermi surface. For the axial state the current-phase relation is just a slanted sinusoid and for the planar state it shows a "$\pi$ state." The appearance of the $\pi$ state at low temperatures is due to the fact that different quasiparticle trajectories contribute to the current with different effective phase differences $\zeta(\hat{\mathbf{k}})$ [see Eqs. (19) and (21)].[19] Such a different behavior can be a criterion for distinguishing between the axial and the planar states, taking advantage of the phase-sensitive Josephson effect. Note that for the axial model the Josephson current formally does not equal zero at $\phi = 0$. This state is unstable (does not correspond to a minimum of the Josephson energy), and a state with a spontaneous phase difference (value $\phi_0$ in Fig. 2), which depends on the misorientation angle $\alpha$, is realized.

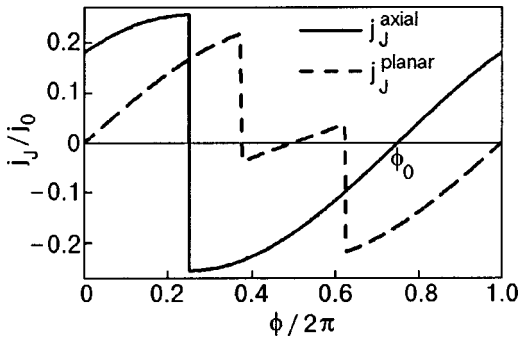


FIG. 2. Josephson current densities versus phase $\phi$ for axial (22) and planar (23) states in the geometry (i); misorientation angle $\alpha = \pi/4$; the current is given in units of $j_0 = (\pi/2)eN(0)v_F\Delta_0(0)$.

The remarkable influence of the misorientation angle $\alpha$ on the current-phase relation is shown in Fig. 3 for the axial state in the geometry (ii). For some values of $\alpha$ (in Fig. 3 it is $\alpha = \pi/3$) there are more than one state, which correspond to minima of the Josephson energy ($j_J = 0$ and $dj_J/d\phi > 0$).

The calculated $x$ and $z$ components (which are parallel to the surface) of the current $\mathbf{j}_s(\phi)$ are shown in Fig. 4 for the same axial state in the geometry (ii). Note that the current tangential to the surface as a function of $\phi$ is not zero when the Josephson current (Fig. 3) is zero. This spontaneous tangential current (see also Ref. 22) is due to a specific "proximity effect" similar to the spontaneous current in contacts between "*d*-wave" superconductors.[20,28] The total current is

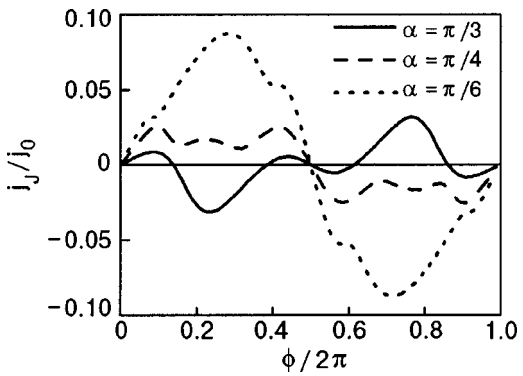


FIG. 3. Josephson current versus phase $\phi$ for the axial (22) state in the geometry (ii) for different $\alpha$.

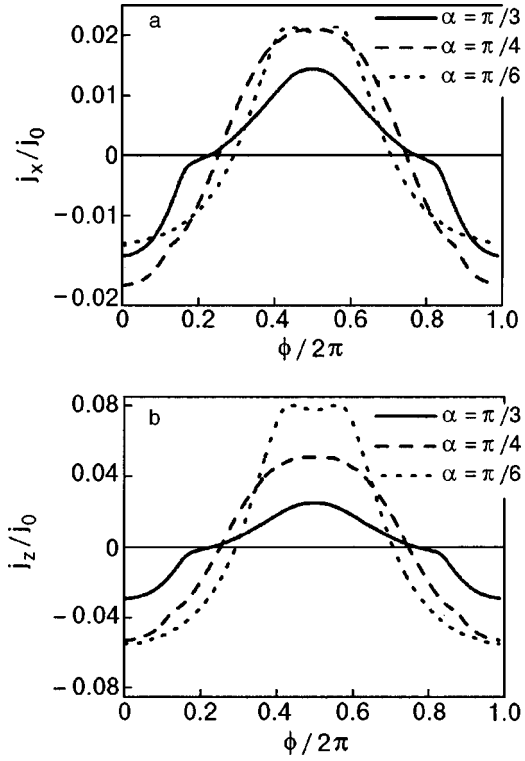


FIG. 4. The $x$ (a) and $z$ (b) components of the tangential current versus phase $\phi$ for the axial state (22) in the geometry (ii) for different $\alpha$.

determined by the Green function, which depends on the order parameters in both superconductors. As a result of this, for nonzero misorientation angles a current parallel to the surface can be generated. In the geometry (i) the tangential current for both the axial and planar states at $T=0$ is absent.

The first candidate for the superconducting state in $Sr_2RuO_4$ was the "$p$-wave" model[8]

$$\mathbf{d}=\Delta_0\hat{z}(\hat{k}_x+i\hat{k}_y). \tag{24}$$

Recently[11,12] it was shown that the pairing state in $Sr_2RuO_4$ most likely has lines of nodes. It was suggested that this can occur if the spin-triplet state belongs to a nontrivial realization of the $E_u$ representation of the group $D_{4h}$, with either $B_{2g}\otimes E_u$ (Ref. 12) or $B_{1g}\otimes E_u$ (Ref. 11) symmetry:

$$\mathbf{d}=\Delta_0\hat{z}\hat{k}_x\hat{k}_y(\hat{k}_x+i\hat{k}_y), \quad \text{for } B_{2g}\otimes E_u \text{ symmetry;} \tag{25}$$

$$\mathbf{d}=\Delta_0\hat{z}(\hat{k}_x^2-\hat{k}_y^2)(\hat{k}_x+i\hat{k}_y), \quad \text{for } B_{1g}\otimes E_u \text{ symmetry.} \tag{26}$$

Note that models (24)–(26) of the order parameter spontaneously break time-reversal symmetry.

Taking into account a quasi-two-dimensional electron energy spectrum in $Sr_2RuO_4$, we calculate the current (19) numerically using the model of a cylindrical Fermi surface. The Josephson current for the hybrid "$f$-wave" model of the order parameter Eq. (26) is compared to the "$p$-wave" model (Eq. (24)) in Fig. 5 (for $\alpha=\pi/4$). Note that the critical current for the "$f$-wave" model is several times smaller (for the same value of $\Delta_0$) than for the "$p$-wave" model. This different character of the current-phase relations enables us to distinguish between the two states.

In Figs. 6 and 7 we present the Josephson current and the tangential current for the hybrid "$f$-wave" model for different misorientation angles $\alpha$ (for the "$p$-wave" model it equals zero). Just as in Fig. 2 for the "$f$-wave" order parameter (22), in Fig. 6 for the hybrid "$f$-wave" model (25) the steady state of the junction with zero Josephson current corresponds to a nonzero spontaneous phase difference if the misorientation angle $\alpha\neq 0$.

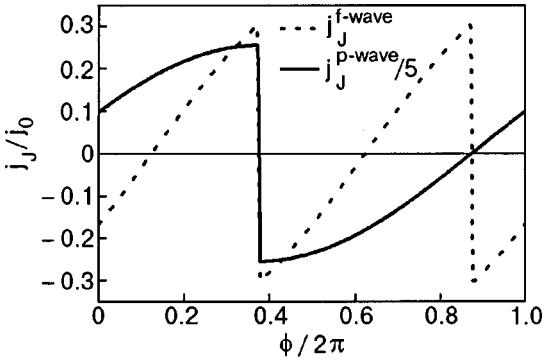


FIG. 5. Josephson current versus phase $\phi$ for hybrid "$f$-wave" and "$p$-wave" states in the geometry (i); $\alpha=\pi/4$.

## CONCLUSION

We have considered the stationary Josephson effect in point contacts between triplet superconductors. Our analysis is based on models with "$f$-wave" symmetry of the order parameter belonging to the two-dimensional representations of the crystallographic symmetry groups. It is shown that the current-phase relations are quite different for different models of the order parameter. Because the order parameter phase depends on the momentum direction on the Fermi surface, misorientation of the superconductors leads to a spontaneous phase difference that corresponds to zero Josephson current and to the minimum of the weak-link energy. This phase difference depends on the misorientation angle and can possess any values. We have found that in contrast to the "$p$-wave" model, in the "$f$-wave" models the spontaneous current may be generated in a direction which is tangential to the orifice plane. Generally speaking this current is not equal to zero in the absence of the Josephson current. We demonstrate that the study of the current-phase relation of a small Josephson junction for different crystallographic orientations of the banks enables one to assess the applicability of different models to the triplet superconductors $UPt_3$ and $Sr_2RuO_4$.

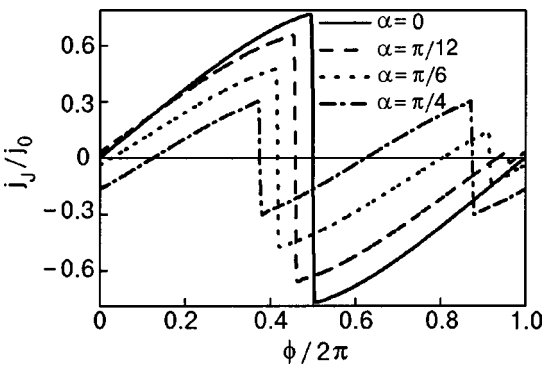


FIG. 6. Josephson current versus phase $\phi$ for the hybrid "$f$-wave" state in the geometry (i) for different $\alpha$.

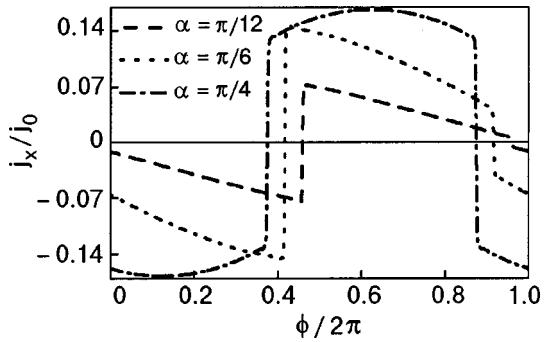


FIG. 7. Tangential current density versus phase $\phi$ for the hybrid "*f*-wave" state in the geometry (i) for different $\alpha$.

It is clear that such experiments require very clean superconductors and perfect structures of the junction because of pair-breaking effects of nonmagnetic impurities and defects in triplet superconductors. The influence of single impurities and interfacial roughness in the plane of the contact, which may essentially decrease the critical current of the junction, will be analyzed in our next paper.

We would like to thank A. N. Omelynanchouk for many helpful discussions. One of the authors (Yu. K.) acknowledges the Institute for Advanced Studies in Basic Sciences, and personally Y. Sobouti and M. R. H. Khajehpour for hospitality.

*E-mail: kolesnichenko@ilt.kharkov.ua

[1)]Strictly speaking, in crystals with a strong spin-orbit coupling the spin is a "bad" quantum number, but the electronic states are twofold degenerate and can be characterized by pseudospins.

[1] V. Müller, Ch. Roth, D. Maurer, E. W. Scheidt, K. Lüders, E. Bucher, and H. E. Bömmel, Phys. Rev. Lett. **58**, 1224 (1987).
[2] Y. J. Qian, M. F. Hu, A. Schedenstrom, H. P. Baum, J. B. Ketterson, D. Hinks, M. Levy, and B. K. Sarma, Solid State Commun. **63**, 599 (1987).
[3] Y. Maeno, H. Hashimoto, K. Yoshida, S. Nashizaki, T. Fujita, J. G. Bednorz, and F. Lichenberg, Nature (London) **372**, 532 (1994).
[4] Y. Maeno, Physica C **282–287**, 206 (1997).
[5] H. Tou, Y. Kitaoka, K. Ishida, K. Asayama, N. Kimura, Y. Ōnuki, E. Yamamoto, and K. Maezawa, Phys. Rev. Lett. **77**, 1374 (1996).
[6] K. Ishida, H. Mikuda, Y. Kitaoka, K. Asayama, Z. Q. Mao, Y. Mori, and Y. Maeno, Nature (London) **396**, 658 (1998).
[7] K. Machida, T. Nishira, and T. Ohmi, J. Phys. Soc. Jpn. **68**, 3364 (1999).
[8] T. M. Rice and M. Sigrist, J. Phys.: Condens. Matter **7**, L643 (1995).
[9] D. F. Agterberg, T. M. Rice, and M. Sigrist, Phys. Rev. Lett. **78**, 3374 (1997).
[10] M. J. Graf, S.-K. Yip, and J. A. Sauls, Phys. Rev. B **62**, 14393 (2000).
[11] T. Dahm, H. Won, and K. Maki, Preprint, cond-mat/0006301 (2000).
[12] M. J. Graf and A. V. Balatsky, Phys. Rev. B **62**, 9697 (2000).
[13] L. D. Landau and E. M. Lifshits, *Statistical Physics, Part 1*, Pergamon, New York (1979).
[14] M. J. Graf, S.-K. Yip, and J. A. Sauls, J. Low Temp. Phys. **114**, 257 (1999).
[15] M. Sigrist, D. Agterberg, A. Furusaki, C. Honerkamp, K. K. Ng, T. M. Rice, and M. E. Zhitomirsky, Physica C **317–318**, 134 (1999).
[16] H. Won and K. Maki, Europhys. Lett. **52**, 427 (2000).
[17] I. O. Kulik and A. N. Omelyanchouk, Fiz. Nizk. Temp. **4**, 296 (1978) [Sov. J. Low Temp. Phys. **4**, 142 (1978)].
[18] J. Kurkijärvi, Phys. Rev. B **38**, 11184 (1988).
[19] S.-K. Yip, Phys. Rev. Lett. **83**, 3864 (1999).
[20] M. H. S. Amin, A. N. Omelyanchouk, and A. M. Zagoskin, Phys. Rev. B **63**, 212502 (2001).
[21] M. Fogelström, S. Yip, and J. Kurkijärvi, Physica C **294**, 289 (1998); S. Yip, Phys. Rev. B **52**, 3087 (1995).
[22] Yu. S. Barash, A. M. Bobkov, and M. Fogelström, Preprint, cond-mat/0107059 (2001).
[23] G. Eilenberger, Z. Phys. **214**, 195 (1968).
[24] J. W. Serene and D. Rainer, Phys. Rep. **101**, 221 (1983).
[25] L. J. Buchholts, M. D. Rainer, and J. A. Sauls, J. Low Temp. Phys. **101**, (1995).
[26] M. Matsumoto and M. Sigrist, Preprint, cond-mat/9902265 V. (1999).
[27] J. Viljas, Preprint, cond-mat/0004246 V (2000).
[28] M. Fogelström and S.-K. Yip, Phys. Rev. B **57**, R14060 (1998); T. Löfwander, V. S. Shumeiko, and G. Wendin, Phys. Rev. B **62**, R14653 (2000).

This article was published in English in the original Russian journal. Reproduced here with stylistic changes by AIP.

# $MgB_2$: Synthesis, sound velocity, and dynamics of the vortex phase

T. V. Ignatova, G. A. Zvyagina, I. G. Kolobov, E. A. Masalitin, and V. D. Fil'[a)]

*B. Verkin Institute for Low Temperature Physics and Engineering, National Academy of Sciences of Ukraine, pr. Lenina 47, 61103 Kharkov, Ukraine*

Yu. V. Paderno, A. N. Bykov, V. N. Paderno, and V. I. Lyashenko

*I. N. Frantsevich Institute of Problems in Materials science, National Academy of Sciences of Ukraine, ul. Krzhizhanovskogo 3, 03142 Kiev, Ukraine*

(Submitted November 27, 2001)
Fiz. Nizk. Temp. **28**, 270–274 (March 2002)

The sound velocity is measured in polycrystalline $MgB_2$ synthesized from the constituent elements, and the bulk modulus in compression and the Debye temperature are calculated. The conversion of an elastic wave into electromagnetic radiation is investigated in the mixed state. The dynamic parameters of the vortex lattice are estimated. © *2002 American Institute of Physics.* [DOI: 10.1063/1.1468522]

## SYNTHESIS AND REAL STRUCTURE

Magnesium diboride powder was obtained by synthesis from the elements Mg (98% pure) and B (99.5% pure) in an argon medium. The powder was sintered in a high-pressure chamber of the anvil-cell type with a lenticular cell. The necessary compression was provided by a hydraulic press with a 6300 kN force. The powder was heated to the required temperature, not by the conventional indirect heating,[1] but by passing a current through the cylindrical samples to be sintered, which gave a more uniform temperature distribution over the volume of the sample. The preliminary compaction of the powder was done by a cold two-sided pressing at pressures of up to 1.3 GPa. The pressed sample was placed in a capsule of graphitic boron nitride, which was mounted in the working channel of the high-pressure chamber. After completion of the sintering cycle the material was cooled under pressure, and then the pressure was reduced to atmospheric. The rate of buildup and relief of the pressure was 0.5 GPa/s. During the heating and cooling stages the temperature was changed at a rate of 100 deg/s. The chosen construction of the cell of the high-pressure chamber provided for hydrostatic compression of the material to be sintered to pressures of up to 4.5 GPa and heating to temperatures of up to 2000 K with holds of up to 300 s.

According to the data of an x-ray analysis the samples contained magnesium diboride $MgB_2$ and an insignificant amount of manganese oxide MgO.

Microstructural and fractographic studies of the samples were carried out on a Camebax CX-50 setup. The x-ray microspectral analysis established the presence of the characteristic lines of magnesium, boron, and oxygen.

A study of the real structure of the samples was done by the thin-foil and diffraction microanalysis methods with the use of a PÉM-U transmission electron microscope.

The results of the study showed that the samples are characterized by appreciable scatter in the grain sizes: in addition to very fine particles ($d \approx 0.1$ $\mu$m) there are also rather large ones (up to 30 $\mu$m), in agreement with the results of Ref. 2.

Some of the large grains are highly fragmented, apparently as a result of the deformation during the preparation of the sample. It was noticed that those grains had a high density of defects, contained fine microcracks and pores, and had large dislocation pileups (Fig. 1). The data of electron microanalysis also attest to strong fragmentation: most of the reflections were smeared into arcs.

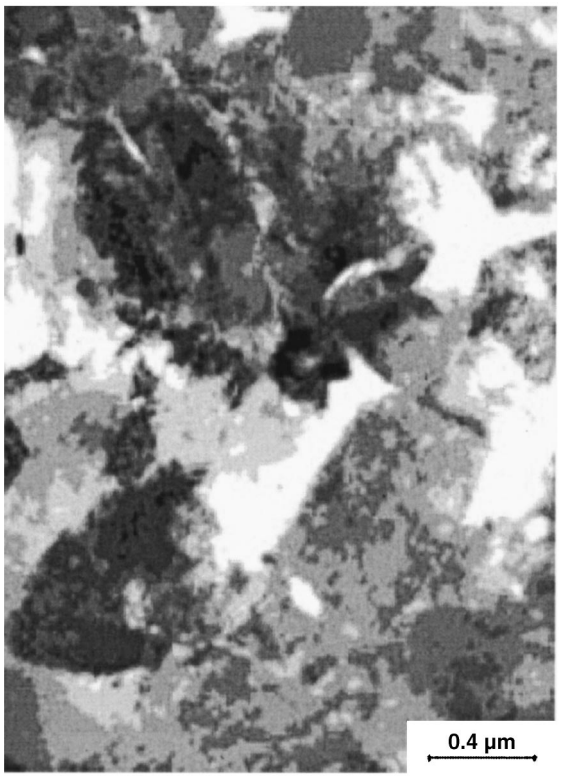


FIG. 1. Typical picture of the real structure of the $MgB_2$ sample, demonstrating the substantial inhomogeneity of the structure and the presence of appreciable scatter in the size of the grains.

 

In addition to the fragmented grains, there were also rather large ($d>5$ $\mu$m) low-defect grains having a cubic configuration, which is characteristic of the compound MgO, which crystallizes in a cubic structure.

In certain parts of the structure, in particular, near pores and along the boundaries of individual, clearly faceted grains, the presence of interlayers of an amorphous phase, similar to that observed in Ref. 3, was noted.

## SOUND VELOCITY

As far as we know, no experimental results from measurements of the sound velocity in $MgB_2$ have been published yet. In imperfect samples the most reliable data on the sound velocity can be obtained only by analysis of the first signal, which has passed through the sample along the shortest path. Interconversion of different modes at inhomogeneities (including at grain boundaries) makes the more distant reflections less suitable for measurements, as does to use of some version of a resonance method.

The method used in this paper was modified somewhat from that described in Ref. 4. In essence it consists in the measurement, in a fixed frequency interval, of the phase–frequency characteristics of two acoustic lines, consisting of delay lines with a sample between them and delay lines without a sample. The difference of the phase–frequency curves in the absence of interference distortions in the sample is a straight line with a slope determined by the sound velocity that is sought. For millimeter sample lengths the error of measurement of the absolute value of the frequency at frequencies of $\sim$55 MHz lies in the range 0.2–0.3% at a signal-to-noise ratio of $\sim$3.

The velocity values measured at $T=77$ K (acoustic path length $\sim$4 mm), viz., $V_t=4.83\times10^5$ cm/s and $V_l=8.2\times10^5$ cm/s are only effective values, since defects (pores, microcracks) decrease the sound propagation velocity.[5] The $MgB_2$ sample under study had a well-defined geometric shape, making it possible to estimate its porosity ($\sim$0.13) rather accurately by a simple weighing. Using the approach proposed in Ref. 5, we obtained the corrected values of the velocities: $V_t=5.12\times10^5$ cm/s and $V_l=8.76\times10^5$ cm/s. Finally, the limitations imposed in the porous-medium model make this procedure much more uncertain than the error of measurement of the effective values of the velocity. The values obtained are considerably lower than the calculated values,[6] although it may be that the correction introduced is not complete, since it does not make allowance for the presence of microcracks. Starting from the corrected values of the velocities and the x-ray density, we calculated the bulk modulus ($B_0=110$ GPa) and Debye temperature ($\Theta_D=787$ K). The latter value is close to that corresponding to the quantities obtained from heat-capacity measurements ($\Theta_D=746$–$800$ K; see the literature cited in Ref. 6).

## DYNAMICS OF THE VORTEX PHASE

The critical temperature ($T_c=37$ K) and transition width ($\delta T_c\approx2$ K) are determined from the measurements of the high-frequency magnetic susceptibility.

To estimate the dynamical parameters of the vortex lattice we have for the first time used the method proposed in Ref. 7, wherein they are extracted from data on the conversion of transverse sound into an electromagnetic field. The sound wave vector **q** was oriented parallel to the external magnetic field **H** and orthogonal to the $MgB_2$–free-space interface. The electromagnetic radiation was registered by a coil oriented with the plane of its windings also parallel to **H**. The amplitude and phase of the Hall component of the electromagnetic field were measured (the electric field vector $\mathbf{E}_H$ was orthogonal to the displacement vector **u** in the sound wave). Such experiments had been done before (but only the amplitude $\mathbf{E}_H$ had been recorded) on either low-temperature[8] or high-temperature[9] superconductors, and a simplified theoretical approach to their description is proposed forth in Ref. 10. However, the relations obtained in Ref. 10 do not admit a correct passage to the limit of the normal state, as will be necessary in order to obtain quantitative information (see below).

A more detailed analysis in the framework of the continuum approximation and the two-fluid model[7] leads to the relation

$$E_H=\frac{1}{c}B\dot{u}\left(\frac{k_L^2+k_{ns}^2}{q^2+k_L^2+k_{ns}^2}\right)\times\left(\frac{\alpha^*}{\alpha^*+q^2(B^2/4\pi)(k_L^2/q^2+k_L^2+k_{ns}^2}\right). \quad (1)$$

Here $B$ is the induction in the sample, which is practically equal to the external field $H$ except in a narrow field region around $H_{c1}$. The wave numbers appearing in (1) have the following model dependences on temperature and field:

$$k_L^2=\lambda^{-2}(1-t^4)(1-b),$$

$$k_{ns}^2=2i\delta^{-2}[1-(1-t^4)(1-b)],$$

where $\lambda$ is the low-temperature penetration depth in the Meissner phase, $\delta$ is the skin penetration depth ($\delta^{-2}=2\pi\omega\sigma_n/c^2$; $\sigma_n$ is the conductivity of the normal metal), $t=T/T_c$, and $b=B/B_{c2}$ ($T_c$ and $B_{c2}$ are the critical values of the temperature and magnetic field).

The complex quantity $\alpha^*=i\omega\eta+\alpha_L$ ($\eta$ is the coefficient of friction and $\alpha_L$ is the Labusch "spring" parameter) describes the dynamics of the vortex lattice, which vibrates during the propagation of an elastic wave. Bardeen and Stephen[11] gave a simple estimate for $\eta$: $\eta=BB_{c2}\sigma_n/c^2$. It may be noted that $\alpha_L\to0$ for $b\to1$.

For $b=1$ we have $k_L=0$ and $k_{ns}^2=2i\delta^{-2}$, and Eq. (1) reduces to the known expression for a normal metal in the local limit.[12] In the normal state the phase of $E_H$ leads $\dot{u}$ by $\varphi_0=\arctan(q^2\delta^2/2)$, and $|E_Hc/\dot{u}|$ varies linearly with $H$, with a slope $(1+\tan^2\varphi_0)^{-0.5}$. According to published data,[13] for $MgB_2$ the penetration depth $\lambda$ lies in the range 800–2000 Å. At the frequencies used here $q\sim\delta^{-1}\sim10^3$, and therefore for $(1-b)>10^{-2}$ and at practically any temperature we have $k_L\gg q,|k_{ns}|$, and relation (1) reduces to the simpler form

$$E_H=\frac{1}{c}B\dot{u}\left(\frac{\alpha^*}{\alpha^*+q^2(B^2/4\pi)}\right), \quad (2)$$

which is suitable all the way down to the Meissner state. We emphasize that the factor multiplying $q^2$ in Eq. (2), unlike the situation in Eq. (1), is not identical to the bending modulus $C_{44}$ of the vortex lattice, since the latter should soften as $H_{c2}$ is approached.[14] For $(1-b)\ll 1$ ($\omega\eta \approx 2B_{c2}^2/4\pi\delta^2$, $\alpha_L \approx 0$, $k_{ns}^2 \approx 2i\delta^{-2}$) both Eqs. (2) and (1) reduce to the corresponding relation for the normal metal at any value of $k_L^2$. This means that even in an ideally homogeneous sample the electric field $E_H$ changes continuously (without a jump) at the transition of $H$ through $H_{c2}$. As $H$ is decreased further, the evolution of $E_H$ depends on the relationship between $\omega\eta$, $\alpha_L$, and the elastic modulus $C_{44}=B^2/4\pi$ of the vortex lattice. Obviously, sooner or later the situation $|\alpha^*| \gg C_{44}$ will arise, and in that case the phase of $E_H$ will coincide with the phase of $\dot{u}$, and $|E_H c/\dot{u}|$ will also vary linearly with the field, but now with a unit slope. Thus in the case $\lambda^{-2} \gg q^2, \delta^{-2}$ relation (2) describes the behavior of $E_H$ in the entire field interval from $H_{c2}$ to $H_{c1}$.

The measured $E_H$ curves are presented in Fig. 2. In view of the limited range of magnetic fields accessible in our measurements, informative experiments could be done only at rather high temperatures. We see that the phase of the signal at the transition of $H$ through $H_{c2}$ changes by approximately $\varphi_0 \approx 50°$ [Fig. 2a]. The ratio of the slopes ($\sim 1.6$) in the regions of linear variation of $|E_H|$ is in good agreement with

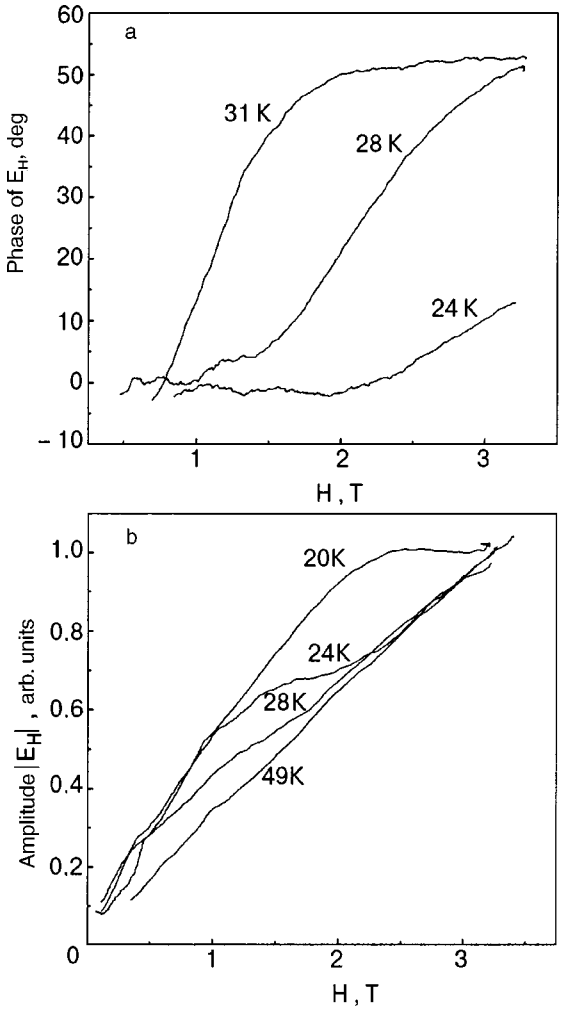


FIG. 2. Field dependence of the phase (a) and amplitude (b) of the Hall component of the radiated electromagnetic field at different temperatures.

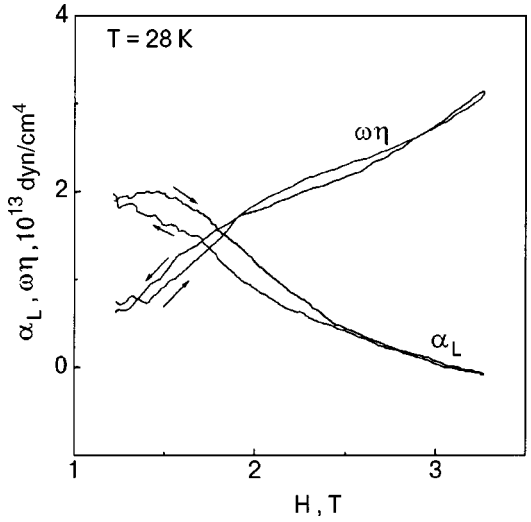


FIG. 3. Reconstruction of the coefficient of friction $\omega\eta$ and Labusch parameter $\alpha_L$.

the value that follows from our analysis: $\sqrt{1+\tan^2\varphi_0}$ [Fig. 2b]. Knowing $\varphi_0$, we can estimate the depth of the skin layer in the normal phase at the frequencies used here ($\delta \approx 2.3\times 10^{-3}$ cm) and the resistivity at $T \geqslant T_c$ ($\rho_n = 12.5\ \mu\Omega\cdot$cm).

Relation (2) can easily be inverted to extract the real and imaginary parts of $\alpha^*$ from experimental data without any additional assumptions. Of course, this can be done in the case when one is able to track the variation of both the modulus and phase of $E_H$ in the accessible magnetic field region. It is also obvious that this procedure is doable only in that field region where the amplitude and phase of $E_H$ deviate noticeably from their limiting values. The result of such a construction is shown in Fig. 3.

As expected, $\eta$ varies practically linearly with applied field. For a known $\sigma_n$, the slope of this relation is determined, in accordance with Ref. 11, by the value of $H_{c2}$. Extrapolation of the data in Fig. 3 by a straight line passing through the origin gave $H_{c2} \approx 3.2$ T, practically equal to the field that determines the beginning of the change in the phase of $E_H$ at $T=28$ K [Fig. 2a]. This means that in the $MgB_2$ sample under study, $H_{c2}$ is limited by the condition of overlap of the cores of the vortices and not by the Clogston paramagnetic limit.[12]

It is seen from the results presented in Fig. 2 that the main change in the phase of $E_H$ is practically finished by the start of the deviation of $|E_H|$ from the linear dependence characterizing the normal phase. This means that in this stage the inequality $\omega\eta < \alpha_L \leqslant q^2 C_{44}$ holds, and $\alpha_L$ can be estimated either by inverting relation (2) with $\alpha^* \approx \alpha_L$ or simply from the relation $\alpha_L \approx q^2 H_m^2/4\pi$, where $H_m$ is the characteristic field at which the transition of $|E_H|$ from one linear trend to another occurs. In particular, for $T=20$ K an estimate of the Labusch parameter gives $\alpha_L \sim 4\times 10^{13}$dyn/cm$^4$. Using the order-of-magnitude relation $\alpha_L \approx BI_c/cr$, where $I_c$ is the critical current and $r$ is the characteristic spatial scale of the pinning potential, which for $H \gg H_{c1}$ is close to the period of the vortex structure, we obtain $I_c \approx 3\times 10^4$ A/cm$^2$ ($T=20$ K, $H \approx 3$ T).

This study was supported by the Government Founda-

tion for Basic Research of the Ministry of Education and Science of Ukraine.

[a)]E-mail: fil@ilt.kharkov.ua

[1] J. Nagamatsu, N. Nakagawa, T. Muranaka, Y. Zenitani, and J. Akimitsu, Nature (London) **410**, 63 (2001).
[2] J. Q. Li, L. Li, Y. Q. Zhou, Z. A. Ren, G. C. Che, and Z. X. Zhao, Preprint, cond-mat/0104350 (2001).
[3] D. C. Larbalestier, M. O. Rikel, L. D. Cooley, A. A. Polyanskii, J. Y. Jiang, S. Patnaik, X. Y. Cai, D. M. Feldmann, A. Gurevich, A. A. Squitier, M. T. Naus, C. B. Eom, E. E. Hellstrom, R. J. Cava, K. A. Regan, N. Rogado, M. A. Hayward, T. He, J. S. Slusky, P. Khalifah, K. Inumaru, and M. Haas, Nature (London) **410**, 186 (2001).
[4] E. V. Bezuglyĭ, N. G. Burma, I. G. Kolobov, V. D. Fil', M. Vitebskiĭ, A. N. Knigavko, N. M. Lavrinenko, S. N. Barilo, D. I. Zhigunov, and L. E. Soshnikov, Fiz. Nizk. Temp. **21**, 86 (1995) [Low Temp. Phys. **21**, 452 (1995)].
[5] H. Ledbetter and S. Datta, J. Acoust. Soc. Am. **79**, 239 (1986).
[6] P. Ravindran, P. Vajeeston, R. Vidya, A. Kjekshus, and H. Fjellvag, Preprint, cond-mat/0102522.
[7] V. D. Fil', Nizk. Temp. **27**, 1347 (2001) [Low Temp. Phys. **27**, 993 (2001)].
[8] L. A. Vienneau and B. W. Maxfield, Phys. Rev. B **11**, 4339 (1975).
[9] H. Haneda and T. Ishiguro, Physica C **235–240**, 2076 (1994).
[10] D. Dominguez, L. Bulaevskii, B. Ivlev, M. Maley, and A. R. Bishop, Phys. Rev. B **51**, 15649 (1995).
[11] J. Bardeen and M. J. Stephen, Phys. Rev. **140**, A1197 (1965).
[12] A. N. Vasil'ev and Yu. P. Gaĭdukov, Usp. Fiz. Nauk **141**, 431 (1983) [Sov. Phys. Usp. **26**, 952 (1983)].
[13] C. Buzea and T. Yamashita, Preprint, cond-mat/0108265.
[14] E. H. Brandt, J. Low Temp. Phys. **26**, 709 (1977).
[15] A. M. Clogston, Phys. Rev. Lett. **9**, 266 (1962).

Translated by Steve Torstveit

## LOW-TEMPERATURE MAGNETISM

# Features of the magnetic behavior of $Mn_{2-x}Cr_xSb$ alloys in the low-temperature state

V. I. Val'kov, V. I. Kamenev,* S. A. Buzhinsky, and N. A. Romanova

*A. A. Galkin Donetsk Physicotechnical Institute, National Academy of Sciences of Ukraine, ul. R. Lyuksemburg 72, 83114 Donetsk, Ukraine*

(Submitted October 8, 2001; revised November 12, 2001)
Fiz. Nizk. Temp. **28**, 275–281 (March 2002)

The spontaneous and magnetic-field-induced first-order magnetic phase transitions in single-crystal samples of the alloy system $Mn_{2-x}Cr_xSb$ (symmetry space group $P4/nmm$) are investigated in samples with $x=0.06$ and $x=0.12$. It is found that the spontaneous first-order transitions from the high-temperature to the low-temperature phase are not accompanied by complete vanishing of the magnetization. At the induced transitions the magnetization before and after the transition is an increasing linear function of field. It is concluded on the basis of the results that the ground state in these alloys cannot be one of collinear antiferromagnetism, as had been thought previously. Other possibilities for interpreting the ground state and the mechanisms of order–disorder transitions inherent to magnets with itinerant carriers of magnetism are examined. It is conjectured that the local magnetic moment has a ferromagnetic and a periodic component which are formed by itinerant $d$ electrons and coexist in low- and high-temperature phases. © *2002 American Institute of Physics.* [DOI: 10.1063/1.1468523]

### INTRODUCTION

Intermetallic alloys of the system $Mn_{2-x}Cr_xSb$ with the tetragonal crystal lattice $C38$ (symmetry space group $P4/nmm$) are known for their unique magnetic behavior. Ferrimagnetic (FiM) in the high-temperature state, they lose a large fraction of their magnetization on cooling. As the chromium concentration is increased (to $x=0.035$) the magnetization initially decreases as a result of two successive first-order phase transitions (through an intermediate phase) followed by yet another first-order transition.[1–8] In spite of the large number of experimental and theoretical papers devoted to the study of this phenomenon, no consensus has been reached as to its nature. The most important disagreement, in our view, is in the interpretation of the magnetic structure of the low-temperature (LT) state of the alloys. In particular, according to Ref. 1, at the transition to the LT state of the alloy with $x=0.03$ its magnetization decreases from 40 to 4 $G\cdot cm^3/g$. At the same time, neutron-diffraction studies[2] reveal the presence of collinear antiferromagnetic (AF) ordering of the magnetic moments in the LT state, which presupposes zero magnetization. It is clear that resolving this contradiction is an important problem not only for establishing the true magnetic structure of alloys of the particular system $Mn_{2-x}Cr_xSb$ but may also lead to fundamentally new approaches to the interpretation of neutron-diffraction results and to the establishment of new mechanisms of formation of the macroscopic magnetic properties of matter.

This paper is devoted to refining the magnetic structure of the LT state of the system $Mn_{2-x}Cr_xSb$ by an experimental study of the response of this system to a magnetic field. We analyze the possible reasons for the aforementioned contradiction and propose a way of resolving it based on taking into account the peculiarities of the formation of the magnetically ordered state in a substance in the presence of itinerant carriers of magnetism.

### SAMPLES AND METHODS OF STUDY

These studies were done on the same single-crystal samples of $Mn_{2-x}Cr_xSb$ with $x=0.06$ and $x=0.12$ as in Ref. 9. The magnetic properties were studied in static (up to 12 kOe, inclusive) and pulsed (up to 200 kOe) magnetic fields. In static fields the balance and vibrational methods were used to determine the temperature dependence and fields dependence of the magnetization. In pulsed magnetic field the isothermal curves of the magnetization versus field were studied by an induction method of measurement. The changes of the parameters of the crystal lattice and phase state of the samples at the phase transition were determined by the x-ray diffraction method on a DRON-3.0 diffractometer in Ni$K_\alpha$ radiation from the shift and change in intensity of the reflections from the (400) and (007) planes (diffraction angles $2\theta\sim 108°$ and 124°). For this the single-crystal samples of the respective alloys were preliminarily adjusted and mounted in the reflecting position in a low-temperature attachment to the diffractometer, where they were cooled by a flow of gaseous nitrogen. The temperature of the samples during the recording of the reflections was stabilized to within 0.2 K. The error in the determination of the lattice parameters was not more than $10^{-3}$ Å. The error in the determination of the phase composition of the samples was 3%.

### RESULTS OF THE EXPERIMENTAL STUDIES

Figure 1 shows the temperature dependence of the magnetization $\sigma$ of $Mn_{2-x}Cr_xSb$ samples with $x=0.06$ and 0.12

 

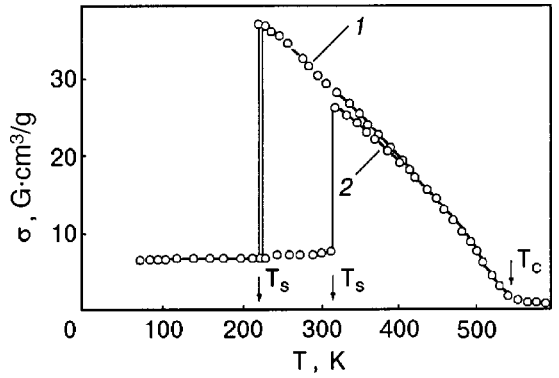


FIG. 1. Temperature dependence of the magnetization $\sigma$ of alloys of the system $Mn_{2-x}Cr_xSb$ in a magnetic field of 12 kOe parallel to the $c$ axis of the crystals for samples with different chromium concentrations $x$: 0.06 (*1*), 0.12 (*2*).

in a static magnetic field $H=11$ kOe directed along the tetragonal axis $c$ of the crystals. As we see from Fig. 1, the temperature behavior of the samples of both compositions is qualitatively similar and is in good agreement with the results of Ref. 1. As the temperature is lowered, a high-temperature (HT) magnetically ordered (according to Ref. 2, ferrimagnetic) state arises, starting at $T_c \sim 530$ K. When a certain critical temperature $T_s$ is reached, equal to 305 K for $x=0.12$ and to 220 K for $x=0.06$, the magnetization decreases in a jump, attesting to the transition of the samples to the LT state (antiferromagnetic in the opinion of the authors of Ref. 1). This transition exhibits temperature hysteresis: 3 K for $x=0.12$ and 12 K for $x=0.06$, indicating that this can be characterized as a pronounced first-order phase transition. The temperature interval in which the transition from the HT to the LT state occurs is around 8 K. It should be noted that the values of the specific magnetization of the samples in the LT state are lower than in the HT state but are still nonzero, and at low temperatures these values are the same for the samples of both compositions.

The response of the samples of both compositions to an external magnetic field is also qualitatively similar. The features of this response in the different magnetically ordered states can be seen from the results obtained for the sample with $x=0.12$, for example. These results are presented in Fig. 2, which shows the magnetization curves $\sigma(H)$ of the crystal in static (Fig. 2a) and pulsed (Fig. 2b and 2c) magnetic fields oriented parallel and perpendicular to the tetragonal axis for different temperatures corresponding to different magnetically ordered states of the sample. It follows from an analysis and comparison of the curves in Fig. 2 that:

In the HT state the $c$ axis is the easy axis, as is clearly illustrated by curves *1* and *2* in Fig. 2a.

2. In the LT state there is practically no axial anisotropy of the magnetization (the $\sigma(H)$ curves for $H\|c$ and $H\perp c$ coincide; see curve *3* in Fig. 2a).

3. In the HT state for sufficiently high fields the magnetization increases linearly with increasing field strength. The rate of growth of the magnetization, $d\sigma/dH$ for $H\|c$ and $H\perp c$ are the same, amounting to $4.5\times10^{-2}$ G·cm$^3$/(g·kOe) and are practically independent of temperature (see curves *3* in Fig. 2b and 2c).

4. The magnetization in the LT state occurs in two stages

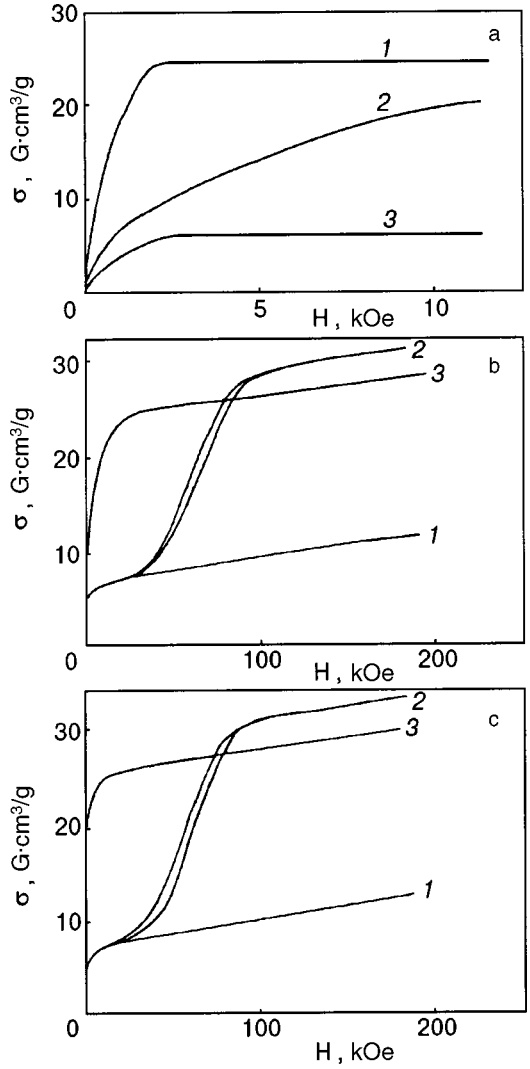


FIG. 2. Magnetization curves of the alloy $Mn_{1.88}Cr_{0.12}Sb$ in various fields for different orientations of the field $H$ relative to the tetragonal axis $c$ of the crystal and different temperatures: a—static field, $T=346$ K, $H\|c$ (*1*), $H\perp c$ (*2*); $H\|c$, $H\perp c$, $T=292$ K (*3*); b—pulsed field, $H\perp c$, $T=77$ K (*1*), $T=312$ K (*2*), $T=334$ K (*3*); c—pulsed field, $H\|c$, $T=77$ K (*1*), $T=312$ K (*2*), $T=334$ K (*3*).

(curves *2* in Fig. 2b and 2c). In low magnetic fields the $\sigma(H)$ curve has the typical form for a ferro- or ferrimagnet (see also curve *3* in Fig. 2a). The change in magnetization in high magnetic fields has a threshold character. The $\sigma(H)$ curves have a region of anomalously sharp growth to a value exceeding the magnetization in the HT state. The reverse, decreasing path of the magnetization occurs with field hysteresis. Outside of this region the field dependence of the magnetization is linear and close to that in the HT state.

The position of the region of sharp change in $\sigma(H)$ can be characterized by the field values $H_{c1}$ and $H_{c2}$ in Fig. 2b, in which the change reaches one-half of its value during the increase and decrease of the field, respectively. Figure 3 shows plots of $H_{c1}$ and $H_{c2}$ versus temperature for the samples with $x=0.06$ and 0.12.

The behavior of the crystal structure near the temperature of the phase transition between the HT and LT states is illustrated by the x-ray diffraction results shown in Fig. 4 for the case of the crystal with $x=0.06$, in which the magnetostriction effect is more strongly expressed on account of the

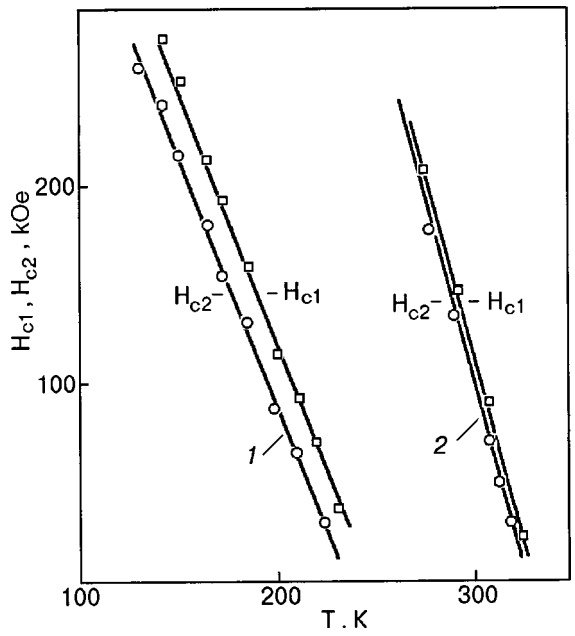


FIG. 3. Temperature dependence of the critical inducing fields $H_c$ for alloys of the $Mn_{2-x}Cr_xSb$ system: $x=0.06$ (*1*), $x=0.12$ (*2*).

larger magnetization jump at the phase transition than for the sample with $x=0.12$. As we see from the temperature dependence of the parameters of the tetragonal crystal lattice $a$ and $c$ shown in Figs. 4a and b, the transition to the LT state is accompanied by jumplike changes in the lattice parameters: an increase in $a$ by 0.11% and a decrease in $c$ by 0.42%. The inset in Fig. 4b shows the temperature dependence of the concentration $I_{LT}$ of the LT phase in the crystal at the forward and reverse phase transitions, constructed on the basis of the relative changes with temperature of the intensities of the x-ray peaks from the (007) planes in the LT and HT

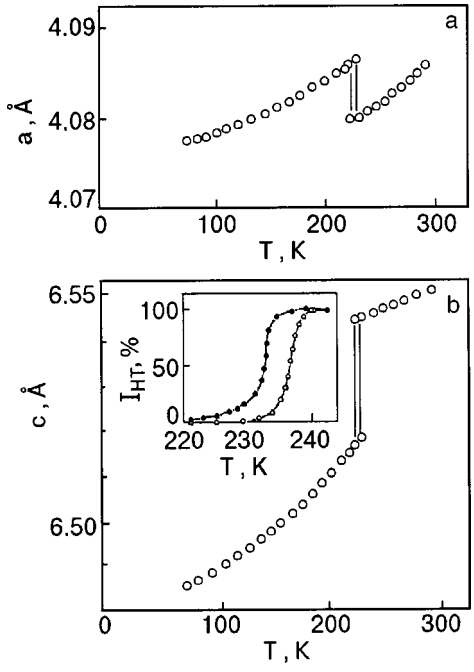


FIG. 4. Temperature dependence of the crystal lattice parameters $a$ and $c$ for a sample with $x=0.12$ (the inset shows the variation of the concentration of the LT phase $I_{LT}(T)$ near the phase transition temperature).

states. It follows from $I_{LT}(T)$ that the width of the heterophase region at the transition is not more than 10 K. It should be noted that the shape and intensity of the peaks from the (007) and (400) planes and also the area under these peaks remain unchanged at the transition. This once again attests to the high quality of the samples and provides a basis for asserting that the HT and LT states are crystallographically homogeneous outside of the heterophase region.

## DISCUSSION OF THE EXPERIMENTAL RESULTS

Taking into account the results obtained above, let us return to the analysis of the possible causes of the existence of nonzero magnetization in $Mn_{2-x}Cr_xSb$ alloys at low temperatures under the condition that their LT state is antiferromagnetically ordered.

1. It seems natural to assume that the HT phase does not disappear completely at the phase transition, and at low temperatures both antiferromagnetically and ferrimagnetically ordered macroscopic regions coexist in the sample. Such a state might arise on account of a nonuniform distribution of ingredients in the sample or could be the result of of so-called ''smeared'' transitions. Such transitions have been observed in several ferroelectrics.[10] Their characteristic signature is the energetically favorable coexistence of alternating phases in a wide region of temperatures and pressures.

However, in the present case this cause seems unlikely in view of the following circumstances. First, no traces of the HT phase are observed in the x-ray patterns at low temperatures (see Fig. 4b), even though the ratio of the magnetizations of the sample in the HT and LT states near $T_s$ (Fig. 1) indicates that the fraction of that phase should amount to $\sim 20\%$. Second, the phase transition occurs in a narrow ($\sim 8$ K) temperature interval. Given the strong dependence of $T_s$ on $x$ (see Fig. 1), these facts attest to the high quality and uniformity of the samples. Third, the LT state lacks the anisotropy of the magnetization process that is characteristic for the HT state (see Fig. 2b and 2c). Finally, the nonzero magnetization cannot be a consequence of the coherent precipitation of the FiM phase $Mn_{1.070}Cr_{0.11}Sb$, with a Curie temperature of $\sim 360$ K, which was observed in Ref. 9. If it were, the temperature dependence of the magnetization of the samples in the LT state in Fig. 1 would have the characteristic shape of the curves for a precipitated phase, like those shown in Ref. 9. All of this evidence points to the fact that the spontaneous magnetism in the LT phase is not a simple manifestation of the presence of macroscopic regions of the FiM phase, and other ideas are needed in order to understand it. One such idea might be the coexistence of ferromagnetism and antiferromagnetism as canted antiferromagnetism.

A particular case of such coexistence is realized in the intermediate phase $I_F$ observed in $Mn_{2-x}Cr_xSb$ alloys with $x<0.035$.[2] Those alloys exhibit two first-order magnetic transformations as the temperature is lowered: FiM–$I_F$ and $I_F$–AF, accompanied by a decrease in volume of the crystal-chemical cell and magnetization. Here, as in alloys with a larger chromium concentration, the LT phase, provisionally designated as AF, also has a finite value of the spontaneous magnetization. In Ref. 5 the stability of the magnetic structure of the intermediate phase was analyzed on the basis of

the Heisenberg model, which required imposing specific restrictions that are not obviously satisfiable. This circumstance is due to the properties of the regular Heisenberg model, in which the canted structure turns out to be energetically unfavorable.[11]

A completely different situation exists in the case of itinerant carriers of magnetism, which, in our view, play an important role in the formation of the magnetic properties of the alloys in question. Indeed, according to the neutron diffraction data,[2] the values of the local magnetic moments in the octahedral and tetrahedral interstices of the lattice in alloys of the system $Mn_2Sb$–$Cr_2Sb$ are not proportional to an integer value of the spin, and the order–disorder transitions are always accompanied by a change in their moduli. This may be a consequence of the collectivization of the *d* electrons. Therefore, in interpreting the magnetic properties of the alloys under study it is reasonable to employ certain ideas of the spin-fluctuation theory of itinerant magnetism[12,13] and to indicate its most characteristic features. One of these is the possibility of describing certain electronic states in transition metal alloys which are created by mobile *d* electrons but which admit the existence of magnetic moments localized at lattice centers. The spatial variation of the magnetic moment in a lattice with centers enumerated by the index $j$ and with radius vector $\mathbf{R}_j$ arises as a consequence of the band motion of the electrons and can be described with the use of a wave vector $\mathbf{Q}$: $\mathbf{M}_j = \mathbf{M}_O + \mathbf{M}_Q \cos(\mathbf{Q}\cdot\mathbf{R}_j)$. The quantity $\mathbf{Q}$ is determined by the topology of the Fermi surface. Here, in contrast to the Heisenberg model with localized *d* electrons, the uniform $\mathbf{M}_O$ and periodic $\mathbf{M}_Q \cos(\mathbf{Q}\cdot\mathbf{R}_j)$ components are not mutually exclusive.[12] The relative orientation of the Fourier components $\mathbf{M}_O$ and $\mathbf{M}_Q$ determines the type of phase coexistence. A parallel orientation describes ferrimagnetism in an alloy with crystallographically equivalent centers of the same chemical type (such a case is impossible in the Heisenberg model). A mutually perpendicular arrangement of these components corresponds to the canted structure.[12–14] This means that regardless of the symmetry of the lattice and the presence of anisotropy in the crystal, states in which ferromagnetic, antiferromagnetic, and ferrimagnetic properties coexist are possible. The thermodynamics of such states is described by interrelated order parameters, in the capacity of which we use the uniform and periodic Fourier components of the magnetic moment.[12,15] Such a thermodynamic approach was used previously for a model description of the magnetic properties of the alloys $Fe_{a-x}Mn_xAs$ ($a \approx 1.6$).[16] Since the alloys $Fe_{a-x}Mn_xAs$ and the alloys investigated in the present study are isostructural (symmetry space group $P4/nmm$, with magnetic atoms located in octahedral and tetrahedral positions of the C38 crystal lattice), the thermodynamic potential constructed in Ref. 16 may be used to describe the magnetic properties of the system $Mn_{2-x}Cr_xSb$ as well. The standard analysis of such a potential shows that under certain conditions the temperature dependence and field dependence of the magnetization of the system have the form shown in Figs. 5 and 6. Figure 5 also shows the possible configurations of the ferromagnetic vector $\tilde{\mathbf{M}}$ (heavy arrows) and antiferromagnetic vector $\mathbf{M}$ (light arrows) in relation to the crystal cell. The cell is denoted schematically by circlets.

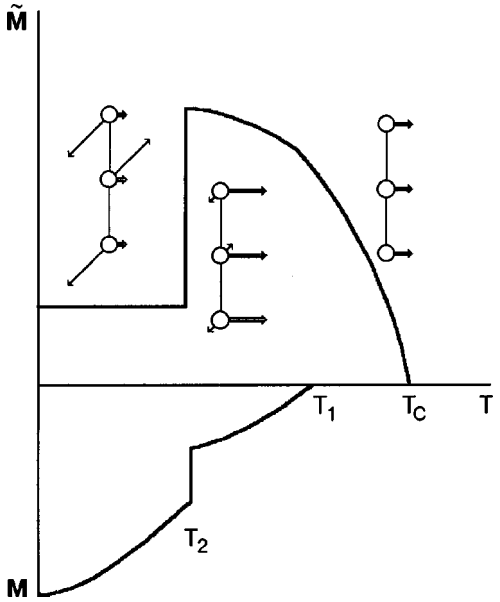


FIG. 5. Possible temperature dependence of the ferromagnetic vector $\tilde{\mathbf{M}}$ and antiferromagnetic vector $\mathbf{M}$ allowed by the model of coexisting order parameters.

They are separated from each other by a distance equal to the lattice constant $c$ along the tetragonal axis. The vectors $\tilde{\mathbf{M}}$ and $\mathbf{M}$ are, respectively, the algebraic sums of the uniform and periodic Fourier components of the magnetic moments in the octahedral and tetrahedral positions of the lattice. A more detailed explanation of Figs. 5 and 6 can be found in Ref. 16. Here we note only that the magnetization of the system is determined by the magnitude of the vector $\tilde{\mathbf{M}}$. The temperature dependence $\tilde{\mathbf{M}}(T)$ agrees qualitatively with the temperature dependence of the magnetization $\sigma$ obtained experimentally.

In the phase of coexistence of the order parameters the saturation magnetization can have an especially strong dependence on the external magnetic field, since it can rather

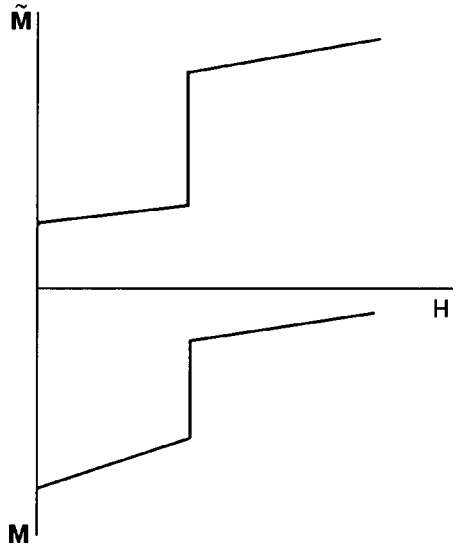


FIG. 6. Dependence of the ferromagnetic and antiferomagnetic vectors on the external field $\mathbf{H} \| \tilde{\mathbf{M}}$ according to the model of coexisting order parameters.

easily increase the uniform and decrease the periodic Fourier components of the magnetic moment while conserving its square modulus. In the presence of only a ferromagnetic order parameter a change of the saturation magnetization can occur only through a change in the modulus of the magnetic moment and would require a large expenditure of energy (of the order of the energy of the intra-ion exchange interaction of the *d* electrons). The monotonic increase of the magnetization under the influence of the magnetic field, which we observed experimentally at the lowest temperatures, where the paraprocess is practically absent, can be regarded as yet another piece of evidence for the two-component nature of the magnetic moment in the alloys under study.

Temperature dependence of the order parameter can lead to magnetic phase transitions of the order–disorder type,[12–16] for which the magnetically ordered state is determined by the local characteristics of the lattice sites and is not due to separation of the material into macroscopic phases. The LT–HT transitions investigated here, which lead to a decrease of the magnetization, are possibly due to a redistribution of the spin density between these components in favor of the periodic component (Fig. 5). The anisotropic properties can also change in this case if the total magnetic moment deviates from the tetragonal axis as a result of the transition. The field dependence of the magnetization, represented by curve *3* in Fig. 2a and curves *1* in Fig. 2b and 2c, are consistent with these conclusions.

The investigated mechanism for the order–disorder transitions is due, first, to the interaction and competition of magnetic modes having wave vectors of different symmetry. Then the exchange striction, which was given considerable attention in Refs. 4 and 5 as being the main mechanism for the order–disorder transitions in $Mn_{2-x}Cr_xSb$ alloys, may be a consequence and not a cause of the observed transitions.

## CONCLUSION

As a result of magnetic and x-ray studies of single-crystal samples of the alloy system $Mn_{2-x}Cr_xSb$ we have obtained the following results:

a) We have established the existence of a spontaneous magnetization in the LT phase, where the neutron diffraction data suggests an AF ordering of the magnetic moments.

b) We have observed first-order phase transitions induced by high magnetic fields from the LT to the HT state and a strong linear dependence of the saturation magnetization on the field in those phases.

c) We have shown that the features of the magnetic behavior of these compounds is not a consequence of inhomogeneity of the samples or the presence of remnants of the HT phase in the LT phase.

On the basis of an analysis of the results obtained, we have proposed a new point of view as to the classification of the magnetically ordered phases in $Mn_{2-x}Cr_xSb$ alloys and the mechanisms of the phase transitions between these phases. We have conjectured that ferromagnetic and antiferromagnetic components of the magnetic moment can coexist in the LT and HT states. A direct check of this conjecture might be made by a neutron diffraction study of these materials, the analysis of which should be done with allowance for the peculiarities due to the itinerant character of the carriers of magnetism.

The authors thank Prof. K. Berner of the University of Göttingen, Germany for furnishing the single-crystal samples of the system $Mn_{2-x}Cr_xSb$.

*E-mail: kamenev@host.dipt.donetsk.ua

[1] F. J. Darnell, W. H. Cloud, and H. S. Jarrett, Phys. Rev. **130**, 647 (1963).
[2] A. E. Austin, E. Adelson, and W. H. Cloud, Phys. Rev. **131**, 1511 (1963).
[3] W. H. Cloud, Phys. Rev. **168**, 637 (1965).
[4] C. Kittel, Phys. Rev. **120**, 335 (1960).
[5] H. S. Jarrett, Phys. Rev. A **130**, 942 (1964).
[6] T. Kanomata, Y. Hasebe, T. Ito, H. Yoshida, and T. Kaneko, J. Appl. Phys. **69**, 4642 (1991).
[7] T. Kanomata, T. Kawashima, T. Kaneko, H. Takahshi, and N. Mori, Jpn. J. Appl. Phys. **30**, 541 (1991).
[8] M. Ohashi, Y. Yamaguchi, and T. Kanomata, J. Magn. Magn. Mater. **104–107**, 925 (1992).
[9] Ch. Kleeberg, E. Kraus, K. Barner, T. Gron, and U. Sondermann, Radiation Eff. and Defects Solids **143**, 1 (1997).
[10] V. M. Ishcuk, Ferroelectrics **209**, 569 (1998).
[11] É. L. Nagaev, *Magnets with Complex Exchange Interactions* [in Russian], Nauka, Moscow (1988).
[12] T. Moriya, *Spin Fluctuations in Magnets with Itinerant Electrons* [in Russian], Mir, Moscow (1988).
[13] M. Isoda, J. Magn. Magn. Mater. **27**, 235 (1982).
[14] D. R. Penn, Phys. Rev. **142**, 350 (1965).
[15] M. Shimizu, J. Magn. Magn. Mater. **45**, 144 (1984).
[16] V. I. Val'kov and E. A. Khapalyuk, Fiz. Tverd. Tela (St. Petersburg) **39**, 889 (1997) [Phys. Solid State **39**, 791 (1997)].

Translated by Steve Torstveit

# Mechanism for the changes with temperature of the EPR spectrum of the $Fe^{3+}$ ion in polycrystalline materials containing complexes with a multiwell potential

V. N. Vasyukov*

*A. A. Galkin Physicotechnical Institute, National Academy of Sciences of Ukraine, ul. R. Lyuksemburg 72, 83114 Donetsk, Ukraine*

(Submitted October 12, 2001; revised November 15, 2001)
Fiz. Nizk. Temp. **28**, 282–287 (March 2002)

The temperature dependence of the EPR spectrum of the $Fe^{3+}$ ion in polycrystalline materials is investigated on the basis of a numerical modeling of the spectrum. A comparison is made of the changes in the spectrum with temperature for two different mechanisms. The first mechanism involves the temperature dependence of the parameters of the spin Hamiltonian, and the second the existence of a system with a multiwell potential. A comparison of the outcomes for these two mechanisms with the experimental data shows that the second mechanism is the governing one. In that mechanism a change in the occupation of the excited vibronic states leads to a change in the shape of the EPR spectrum. The possibility of obtaining additional information about the parameters characterizing the distribution of the vibronic states over energy is demonstrated. © *2002 American Institute of Physics.*
[DOI: 10.1063/1.1468524]

Unusual temperature dependence of the EPR spectrum of the $Fe^{3+}$ ion in a number of organic materials was observed in Refs. 1–4. The objects of study were nitrozo-$\beta$-naphthol $Na[FeO_6(C_{10}H_8N)_3]$ in Ref. 1, an $Fe^{3+}$-ion magnetic center in polyaniline in Ref. 2, bromcresol green $C_{21}H_{14}Br_4O_5S$ in Ref. 3, and caolinite in Ref. 4. The resulting absorption line of the EPR spectrum in those papers[1–4] was represented in the form a superposition of two resonance lines and a nonresonant background. The first line is described by an effective $g$ factor of $\approx 4.3$, the second by $g \approx 2$. Changing the temperature leads to a change of the relative integral intensities of the resonance lines. Line *1* ($g \approx 4.3$) has a maximum intensity at a temperature of 4.2 K. Increasing the temperature leads to a decrease of the intensity of line *1*. At $T = 300$ K line *1* is not observed for any of the materials investigated in Refs. 1–4. The relative intensity of line *2* ($g \approx 2$) has its maximum value for $T = 300$ K. Resonance lines *1* and *2* were referred to in Refs. 1–4 as the low-temperature and high-temperature EPR spectra. The change in intensities has the appearance of a redistribution of the intensity between the low- and high-temperature spectra. In Refs. 1–4 it was assumed that the observed temperature dependence of the EPR spectrum is a manifestation of the properties of a system with a multiwell potential. A manifestation of the Jahn–Teller effect (in the usual understanding of it) for the $Fe^{3+}$ ion is unlikely, since it is an *s* ion. Therefore, it was assumed in Refs. 1–4 that the $Fe^{3+}$ ion is a magnetic probe, the spectrum of which reflects the dynamics of the molecules of the nearest-neighbor environment.

The conjecture made in Refs. 1–4 as to the nature of the mechanism responsible for the change of the EPR spectrum with temperature is insufficiently well justified and is based on the analogous behavior of the EPR resonance line of the well-studied magnetic center formed by the Jahn–Teller ion $Cu^{2+}$ in an octahedral environment. An alternative mechanism for the observed changes in the spectrum is also possible. This would involve the temperature dependence of the zero splitting parameter $D$ of the spin Hamiltonian describing the EPR spectrum. The goal of this study is to investigate the influence of the temperature dependence of the parameter of the spin Hamiltonian on the EPR spectrum and to determine to most effective mechanism for temperature-induced changes in the spectrum of the $Fe^{3+}$ ion in a polycrystalline substance.

The most complete compendium of previously published results of calculations of the EPR spectrum of the $Fe^{3+}$ ion in polycrystalline materials is presented in Ref. 5. The EPR spectra have been studied in more detail for the limiting values of the initial splitting parameter $D \gg h\nu$ and $D \ll h\nu$, for which calculations have been done in analytical form. In the region of the intermediate values $D \approx h\nu$ the EPR spectrum can be modeled only by numerical methods. According to the results presented in Ref. 5, for $D \gg h\nu$ and $E = D/3$ the EPR spectrum of the $Fe^{3+}$ ion in a polycrystalline material is represented by a single resonance line with an effective $g$ factor of $\approx 4.3$. For $D \ll h\nu$ the most intense line of the EPR spectrum has $g \approx 2.0$

Resonance lines with such a $g$ factor were observed in Refs. 1–4 at various temperatures. The maximum intensity of line *1* ($g \approx 4.3$) occurs at low (helium) temperatures, while that of line *2* ($g \approx 2.0$) occurs at high (room) temperatures.

If it is assumed that the change of the spectrum with temperature in Refs. 1–4 is due to the temperature dependence of the parameter $D$, then, according to the experimental data[1–4] and the results presented in Ref. 5, for satisfaction of the conditions $D > 10h\nu$ and $D < h\nu/10$ the parameter $D$ should vary in a range of values from 0.03 to 3 $cm^{-1}$.

To study the influence of the temperature dependence of $D$ on the EPR spectrum, we have done a numerical calculation and modeling of the EPR spectrum of the $Fe^{3+}$ ion for values of the zero splitting parameter $D = 0.001 - 3$ $cm^{-1}$. For modeling the absorption line shape the frequency of the microwave field plays a key role. In this study the calculations were done for the most often used X band of frequencies. For definiteness we chose the frequency $\nu = 9.24$ GHz, which was used in Refs. 1–4.

 

The procedure used to calculate the absorption line shape for each value of the parameter $D$ is as follows. The direction of the magnetic field relative to the direction of the symmetry axis of the magnetic center was specified. The direction of the magnetic field is described by the two angles $\theta$ and $\varphi$ of a spherical coordinate system. For the specified field direction the energies of the spin states were calculated as functions of the magnitude of the magnetic field. These functions and the value of the quantum $h\nu$ were used to determine the resonance fields. The transition probabilities were calculated for each value of the resonance field. It was assumed that the resonance line of each transition has a Lorentzian shape. It was assumed that the linewidth $\Delta H_0$ is independent of temperature and, for definiteness, equal to 0.04 kOe. The resulting absorption line was obtained by averaging over all orientations of the magnetic field.

The spin Hamiltonian of the ion $Fe^{3+}$ was chosen in the form

$$H=g\beta(\mathbf{H}\cdot\mathbf{S})+D[S_z^2-S(S+1)/3]+E(S_x^2-S_y^2), \qquad (1)$$

where $\beta$ is the Bohr magneton, $H$ is the external magnetic field, $S_x$, $S_y$, and $S_z$ are the spin operators, and $D$ and $E$ are the second-order zero splitting parameters. The parameter $D$ describes the anisotropy of the magnetic center along the principal symmetry axis, while the parameter $E$ is determined by the rhombic distortions of the nearest-neighbor environment; $g$ is the $g$ factor of the spin multiplet. For the $Fe^{3+}$ ion this usually has the value $g=2.0$.

For comparison with the experimental results the calculations were done under the condition of maximal rhombic distortion of the environment of the magnetic ion, $E=D/3$, which apparently holds quite well for the magnetic centers studied in Refs. 1–4. This is indicated by the absence of splitting of line *1* (Ref. 5).

The fourth-order initial splitting was not taken into account in view of the smallness of those parameters in comparison with the second-order terms and also for the reason that the determinative experimental results were obtained for polycrystalline materials.

The results of these calculations are presented in Fig. 1, which shows the absorption line shape of the $Fe^{3+}$ ion in a polycrystalline sample for the following values of the zero splitting parameter: $D=0.001$, 0.02, 0.05, 0.08, 0.09, 0.15, 0.2, 0.3 $cm^{-1}$. We see that there are three regions of $D$ values. The first can be taken as $D<0.08$ $cm^{-1}$. In this region one observes a central, most intense resonance line with $g=2.0$ and peaks symmetrically located on both sides, and the resonance line *1* is absent in this region of $D$ values. The second region is for $D>0.1$ $cm^{-1}$ ($D>h\nu/3$). In that region the resonance line *1* is observed in the EPR spectrum. It should be noted that for $D>0.3$ $cm^{-1}$ the EPR spectrum has the same shape as the spectrum for $D=0.3$ $cm^{-1}$, which is shown in Fig. 1. In the third region, $0.08\leqslant D\leqslant 0.1$ $cm^{-1}$, the EPR spectrum is a set of rather intense resonance lines, some of which cannot even approximately be assigned to either line *1* or line *2*. According to the data of Fig. 1, line *1* is observed for $D>h\nu\approx 0.3$ $cm^{-1}$ and may also be observed for $h\nu/3<D<h\nu$.

To understand the reasons for the appearance of two resonance lines (*1* and *2*) in the EPR spectrum of polycrystalline materials it is necessary to analyze the dependence of the resonance fields on the orientation of the magnetic field and the transition probabilities. The dependence of the resonance fields on the orientation of the of the external magnetic field for values of the parameter $D$ from the three different regions is shown in Fig. 2. The transition probabilities depend on the values of the parameters of the spin Hamiltonian, the frequency of the microwave field, and the orientation of the external magnetic field relative to the axis of symmetry of the magnetic center, and therefore the calculation was done for all the ''allowed'' and ''forbidden'' resonance transitions.

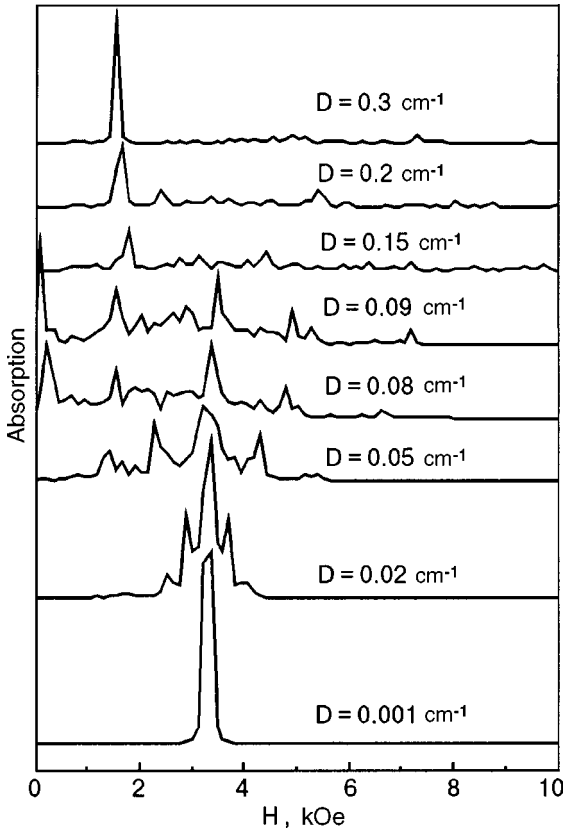


FIG. 1. Dependence of the absorption line shape in the EPR spectrum of the $Fe^{3+}$ ion in a polycrystalline material on the value of the initial splitting parameter.

In Fig. 2a an arrow indicates the resonance field whose absorption line is the basis for the formation of line *1* in the polycrystalline material. The resonance field forming line *2* is indicated by an arrow in Fig. 2c. A characteristic feature of these resonance fields is that they depend weakly on the orientation of the magnetic field.

It should be noted that the plot in Fig. 2b does not contain resonance fields forming the resonance lines *1* and *2*.

If the shape of the EPR spectrum in Fig. 1 is compared with the absorption line shape obtained experimentally in Refs. 1–4, it can be concluded that the mechanism responsible for the temperature dependence of the EPR spectrum of the $Fe^{3+}$ ion in polycrystalline materials[1–4] cannot be due to the temperature dependence of the zero splitting parameter. In Refs. 1–4 the resonance lines *1* and *2* are observed simultaneously over practically the entire temperature interval from liquid-helium temperature to room temperature. The

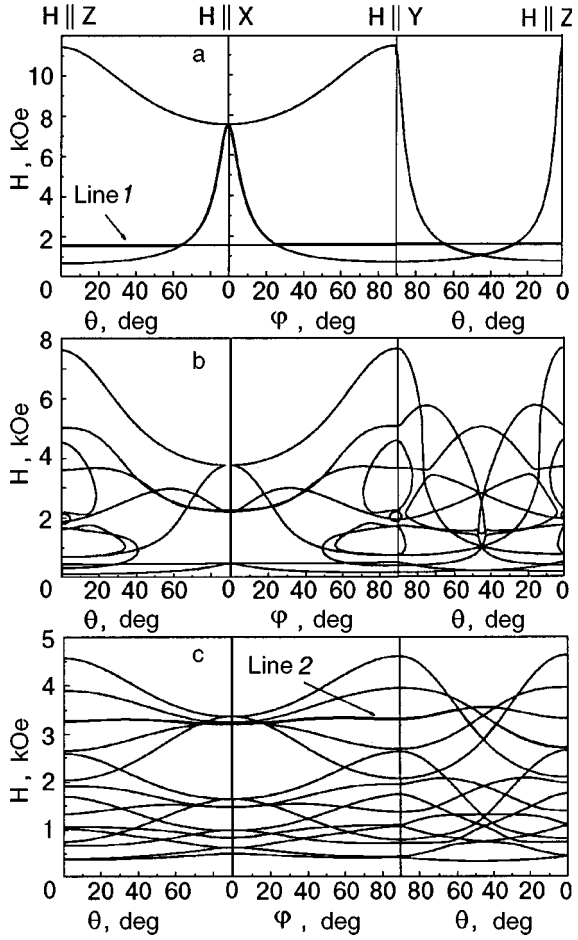


FIG. 2. Dependence of the resonance fields on the direction of the external magnetic field for $D=1.0$ (a), 0.1 (b), and 0.03 $cm^{-1}$ (c).

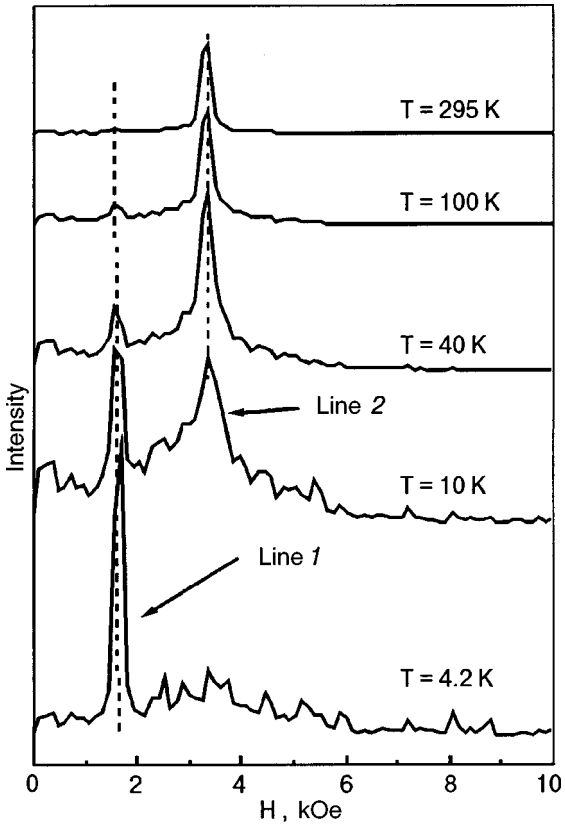


FIG. 3. Changes with temperature of the EPR spectrum of the $Fe^{3+}$ ion in a polycrystalline material for $D_0=0.2$ $cm^{-1}$, $\varepsilon_0=10$ $cm^{-1}$.

results presented in Fig. 1 show that lines *1* and *2* cannot be observed simultaneously if the temperature dependence of the EPR spectrum is governed by the mechanism based on the temperature dependence of the zero splitting parameter. Furthermore, we see in Fig. 1 that for $D<0.08$ $cm^{-1}$ the EPR spectrum is not a single line *2* but a set of partially or completely allowed resonance lines.

To model the absorption line shape that should be observed in the case of a mechanism based on the appearance of a multiwell system it is necessary to determine the dependence of the $D$ values for the various vibronic states on the energies of these states. An exact solution of this problem presents significant difficulties, especially since the causes giving rise to the multiwell system have not been studied in full measure. For a qualitative analysis it can be supposed that this dependence has the form

$$D=D_0\exp[-(\varepsilon/\varepsilon_0)^2\ln 2], \tag{2}$$

where $D$ is the zero splitting corresponding to the vibronic state with energy $\varepsilon$ for the multiwell system, and $D_0$ is the maximum value of the zero splitting, which corresponds to the ground vibronic state. The parameter $\varepsilon_0$ determines the height of the barrier separating the potential wells of the multiwell system. According to Refs. 3 and 4, $\varepsilon_0 \sim 15$ $cm^{-1}$. For observation of line *1* at low temperatures it is necessary that the parameter $D_0 \geqslant 0.15$ $cm^{-1}$ (see Fig. 1). If it is assumed that $D_0=0.2$ $cm^{-1}$, then the absorption line of the $Fe^{3+}$ ion in polycrystalline materials at temperatures $T=4.2$, 10, 40, 100, and 295 K will have the shape shown in Fig. 3. These absorption lines can be obtained as a result of a summation of the contributions from the set of vibronic states, which are characterized by different values of the energy $\varepsilon$ and of the parameter $D$ corresponding to this energy. The occupation $N$ of the vibronic state with energy $\varepsilon$ can be written as

$$N=N_0\exp(-\varepsilon/kT)/\sum_{n=1}^{\infty}\exp(-\varepsilon_n/kT), \tag{3}$$

where $N_0$ is the number of magnetic centers in the crystal.

The temperature dependence of the EPR spectrum (see Fig. 3) agrees well with the experimental temperature dependence of the spectrum in Refs. 1–4. It should be noted first that lines *1* and *2* are observed simultaneously over practically the entire temperature interval. Furthermore, it is seen in Fig. 3 that decreasing the temperature leads not only to a decrease in the intensity of line *2* but also to an increase in its width. This suggests that the mechanism responsible for the temperature dependence of the EPR spectrum of the $Fe^{3+}$ ion in the polycrystalline materials investigated in Refs. 1–4 is determined by the properties of the physical system having the multiwell potential.

The temperature dependence of the spectrum is determined by the temperature dependence of the occupation of the vibronic states of the system. At helium temperature the excited states are weakly occupied. The main contribution comes from the ground state and the states located near it. For these states $D$ is close to its maximum value, and there-

fore line *1* has the highest intensity. Increasing the temperature leads to occupation of the above-barrier states ($\varepsilon > \varepsilon_0$) and, hence, to an increase in the intensity of line *2*. The transition of the magnetic centers to over-barrier states leads to a decrease in the number of magnetic centers found in under-barrier states. As a result of this, the intensity of line *1* decreases with increasing temperature. It should be noted that in order to have a significant decrease in the intensity of line *1* it is necessary that at high temperatures the number of magnetic centers found in the over-barrier states be significantly larger than the number of magnetic centers in under-barrier states.

The absorption line shapes shown in Fig. 3 were calculated using an infinite number of discrete vibronic states of the system. The line shape for the lower states, corresponding to values of the parameter $D=0.001$ cm$^{-1}$ and 20 values in the interval $D=0.01-0.2$ cm$^{-1}$ were calculated by the method described previously for Fig. 1. The line shapes for some of these states are shown in Fig. 1. In calculating the data presented in Fig. 3, the barrier height $\varepsilon_0$ was taken equal to 10 cm$^{-1}$. Therefore, states with $D>0.1$ cm$^{-1}$ are under-barrier, and those with $D\leqslant 0.1$ cm$^{-1}$ are over-barrier. The line shapes of the highly excited states ($D<0.001$ cm$^{-1}$) were assumed to be the same as for the state with $D=0.001$ cm$^{-1}$. In the calculation of the occupation numbers the sum in relation (3) is broken into two parts. In the first part the energy of the vibronic states is determined from the specified values of the parameter $D$ according to expression (2). In calculating the second part of the sum, corresponding to highly excited vibronic states ($D<0.001$ cm$^{-1}$), it was assumed that in this region of energies the vibronic states are equidistant, which made it possible to calculate the second part of the sum analytically.

The integral intensity of any EPR resonance line decreases with increasing temperature. The mechanism for this temperature dependence involves a change in the occupation of the resonance states of the spin multiplet. In order to demonstrate the manifestations of the properties of the multiwell system in purest form, this mechanism was not taken into account in the calculation of the resonance lines in Fig. 3. However, the intensity of line *2* at $T=295$ K is noticeably lower than the intensity of line *1* at $T=4.2$ K. The reason for this is that the average value of the energy of the occupied vibronic states increases with increasing temperature.

There is another noteworthy feature of the data presented in Fig. 3. With decreasing temperature the absorption line becomes less ''smooth.'' The lower the temperature, the greater the intensity of the additional peaks distributed over the entire interval of magnetic fields. This is outwardly similar to a noise signal. The cause of this behavior is apparently due to the discreteness of the $D$ values chosen for the description of the vibronic states. At high temperatures the states are occupied more uniformly, and this leads to better averaging. At low temperatures the main contribution comes from a few states located near the ground state. At the chosen discreteness this is 3–4 states. Since this feature is absent in the experimental curves,[1–4] it should be assumed that the splitting of the vibronic states is considerably smaller than that which was assumed in the calculation of the data in Fig. 3 ($\Delta D=0.01$ cm$^{-1}$).

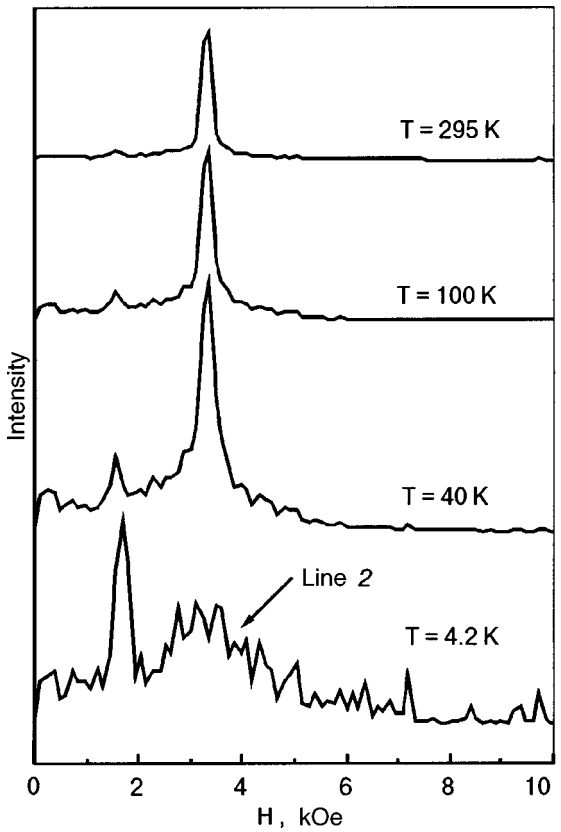


FIG. 4. Changes with temperature in the EPR spectrum of the $Fe^{3+}$ ion in a polycrystalline material for $D_0=0.15$ cm$^{-1}$, $\varepsilon_0=10$ cm$^{-1}$.

The absorption line shape (see Fig. 3) depends to a significant degree on the distribution (2). Figure 4 shows the changes in the EPR spectrum with temperature for $D_0=0.15$ cm$^{-1}$. As we see from a comparison of the data in Figs. 3 and 4, line *2* can be observed experimentally at liquid-helium temperature. Decreasing the parameter $D_0$ leads to a decrease in the intensity of line *2* observed at $T=4.2$ K. If the parameter $D_0\leqslant 0.1$ cm$^{-1}$ ($D_0\leqslant h\nu/3$), then the resonance line *1* may not be observed experimentally. Here the features of the multiwell system are manifested in the features of the temperature dependence of the width of line *2*.

*E-mail: vvasyukov@mail.ru

[1] V. P. D'yakonov, V. N. Vasyukov, V. A. Shapovalov, E. I. Aksiment'eva, H. Szymczak, and S. Piechota, Fiz. Tekh. Vysokikh Davlenii **8**, 60 (1998).
[2] V. N. Vasyukov, V. P. D'yakonov, V. Shapovalov, E. I. Aksiment'eva, and H. Szymczak, S. Piechota, Fiz. Nizk. Temp. **26**, 363 (2000) [Low Temp. Phys. **26**, 265 (2000)].
[3] V. V. Chabanenko, V. N. Vasyukov, R. O. Kochkanjan, M. M. Nechitailo, H. Szymczak, S. Piechota, and A. Nabjalek, Fiz. Nizk. Temp. **28**, 66 (2002) [Low Temp. Phys. **28**, 49 (2002)].
[4] V. N. Vasyukov, V. V. Shapovalov, S. A. Schwarz, M. H. Rafailovich, J. C. Sololov, V. A. Shapovalov, and V. A. Beloshenko, J. Magn. Reson. **154**, 15 (2001).
[5] Ya. G. Klyava, *EPR Spectroscopy of Disordered Solids* [in Russian], Znanie, Riga (1988).

Translated by Steve Torstveit

# Raman scattering in a $LiNiPO_4$ single crystal

V. I. Fomin, V. P. Gnezdilov,* V. S. Kurnosov, A. V. Peschanskii, and A. V. Yeremenko

*B. Verkin Institute for Low Temperature Physics and Engineering of the National Academy of Sciences of Ukraine, 47 Lenin Ave., 61103, Kharkov, Ukraine*

H. Schmid, J.-P. Rivera, and S. Gentil**

*Department of Inorganic, Analytical and Applied Chemistry, University of Geneva, CH-1211 Geneva 4, Switzerland*

(Submitted November 1, 2001)
Fiz. Nizk. Temp. **28**, 288–296 (March 2002)

The complete Raman spectra of a single crystal of $LiNiPO_4$ for a wide temperature range are reported. Of the 36 Raman-active modes predicted by group theory, 33 have been detected. The spectra are successfully analyzed in terms of internal modes of the $(PO_4)^{3-}$ group and external modes. Multiphonon Raman scattering is also discussed. Low-frequency lines, observed in the antiferromagnetic phase, are assigned to magnon scattering and are discussed briefly. © *2002 American Institute of Physics.* [DOI: 10.1063/1.1468525]

## INTRODUCTION

The lithium orthophosphate of nickel belongs to a family of antiferromagnets with the general formula $LiMPO_4$ (where $M=Fe^{2+}$, $Mn^{2+}$, $Co^{2+}$, $Ni^{2+}$) and which are known to be magnetoelectrics.[1,2] In the paramagnetic phase these compounds have the same orthorhombic space group *Pnma*, but the magnetic groups in their antiferromagnetic phase are partly different. All of them allow the occurrence of the linear magnetoelectric (ME) effect. The mechanisms responsible for the ME effect in $LiMPO_4$ remain an open question.

The majority of experimental investigations of the linear ME effect in $LiMPO_4$ compounds realized so far have been restricted to the study of the quasistatic properties, i.e., to measurement of the quasistatic magnetic (electric) moment induced by an external quasistatic electric (magnetic) field. Much less attention has been paid to the spectrum of elementary excitations and to the influence of ME interaction on excited states. The nature of the large value of the ME coefficient in $LiCoPO_4$ is not yet clear. It may lie in the specific arrangement of the low-energy electronic energy levels of the magnetic ion and their interaction with a vibrational spectrum.

The motivation for the present study is manifold. One of the objectives is to determine the frequency and symmetry of the long-wavelength, or $\mathbf{k}=0$, Raman-active phonons and to compare them with the results of group theory analysis, based on both the factor-group and site-symmetry methods.

At low temperature $LiNiPO_4$ undergoes a transition to an antiferromagnetic (AF) phase, and thus additional lines due to light scattering by spin waves, both first and second order, may be observed in the Raman spectra.

Owing to the ME effect the Raman spectrum may be more complicated in the AF phase due to an additional mechanism of light scattering predicted by Pradhan.[3] The origin of the mechanism resides in the possible (via ME) interaction of the electric (magnetic) vector of the incident light with the magnetic (electric) vector of the scattered light. The effect should be proportional at least to the value of the ME coefficients at the frequency of visible light, which are unknown. The ''Pradhan'' lines in the spectrum may in principle be separated via their difference given by the polarization selection rules.

Motivated by the above considerations, a Raman scattering study of $LiNiPO_4$ has been undertaken. In this paper we are reporting spectra of the observed elementary excitations in the frequency region from 4 to 1200 $cm^{-1}$ and at temperatures between 5 and 300 K.

## SYNTHESIS OF $LiNiPO_4$ SINGLE CRYSTALS AND EXPERIMENTAL PROCEDURE

Single crystals of the orthophosphates $LiMPO_4$ ($M=Mn,Fe,Co,Ni$) can be obtained by conventional solution growth (see, e.g., Refs. 4 and 5) in LiCl flux. This high-temperature halide solvent is advantageous as it consists partially of an element present in the final compound and has rather low viscosity in the molten phase, favoring stable growth. Different experimental variants according to the following reactions are possible for obtaining the starting orthophosphate:

$$M(OH)_2+NH_4H_2PO_4+Li_3PO_4\rightarrow LiMPO_4+NH_3+H_2O, \quad (1)$$

$$M_3(PO_4)_2+Li_3PO_4\rightarrow 3LiMPO_4, \quad (2)$$

$$MCl_2+Li_3PO_4\rightarrow LiMPO_4+2LiCl. \quad (3)$$

For each of these reactions, a stoichiometric molar ratio of reacting materials is required. Reaction (2) was first used for the synthesis of $LiMnPO_4$ crystals by dissolving the starting reactants in LiCl, followed by cooling.[6] The method was later modified slightly for the growth of $LiFePO_4$ crystals[7] and adapted for the growth of single crystals of the entire series $LiMPO_4$, with M = Mn, Fe, Co and Ni.[8]

In the present study, for growing $LiNiPO_4$ single crystals, reaction (3) was used and performed in a LiCl flux, allowing us to obtain single crystals large enough for physi-

 

cal experiments ($\sim$ 1–5 $mm^3$). The molar ratio between $LiNiPO_4$ and LiCl in the starting mixture was optimized at 1:3. Platinum crucibles of 30 ml volume were filled with a maximum of 45 g of a stoichiometric mixture of the powders, followed by a pre-melting at 800 °C. Due to the high volatility of the solvent, the crucibles were sealed by argon arc welding and a hole of $\sim$50 $\mu$m diameter was drilled through the lid in order to equilibrate the pressure.

The growth temperature profile was as follows: 1) heating in 5 h to 890 °C, 2) soaking at 890 °C for 4 h, 3) slow cooling at 0.755 °C/h to 715 °C, 4) slow cooling at 1.4 °C/h to 680 °C and 5) crystal recovery at 680 °C. The crystal recovery from the molten flux was the last critical problem to be solved for obtaining weakly stressed crystals. For this purpose the crucible was rapidly removed from the furnace, two holes were pierced in the lid, and the remaining liquid was quickly poured on a porous ceramic.

The Raman spectra were measured on a $LiNiPO_4$ single crystal of high optical quality. The sample was cut as a rectangular parallelepiped with edges of 4.2, 3.0, and 2.4 mm, parallel to the crystallographic axes *a*, *b*, *c* of the orthorhombic cell, respectively. Since the *a*, *b*, and *c* axes correspond to the principal axes of the dielectric tensor, this sample shape minimized errors due to birefringence in polarized Raman measurements. The system of coordinates was chosen to be $X \| a$, $Y \| b$, and $Z \| c$.

The Raman spectra were recorded with a Jobin-Yvon U-1000 double monochromator equipped with a cooled photomultiplier and photon counting electronics. The right-angle scattering geometry was used. In order to reduce the beam-induced heating of the sample and to enhance the scattered light intensity, the 632.8 nm line of a He-Ne laser operating at powers up to 30 mW was used in the experiments. For the yellow-orange crystals of $LiNiPO_4$, the transmission window is centered in the region of $\sim$573 nm.[9,10] The temperature interval 4.2–300 K was covered by using a special optical cryostat. The sample was kept in an exchange gas atmosphere.

## STRUCTURAL AND MAGNETIC FEATURES OF $LiNiPO_4$

The lithium orthophosphates $LiMPO_4$ ($M = Co^{2+}$ or $Ni^{2+}$) are isostructural with the minerals lithiophilite (M = Mn) and triphilite (M = Fe), which belong to the olivine family.[1,11,12] The orthorhombic unit cell contains four formula units and is described by space group *Pnma* ($D_{2h}^{16}$) (Ref. 12). The crystal structure can be understood as a nearly hexagonal close packing of oxygen atoms. Each phosphorus atom in the crystal is surrounded by four oxygen atoms, creating a distorted tetrahedral $(PO_4)^{3-}$ group with $C_s(m \perp b)$ point symmetry. The $Ni^{2+}$ and $Li^{2+}$ ions occupy positions with site symmetry $C_s$ and $C_i$, respectively. They are surrounded by distorted octahedra of oxygen atoms. The nickel ions lie in puckered planes perpendicular to the *a* axis. Adjacent planes are separated by $PO_4$ tetrahedra sharing corners and edges with the $LiO_6$ octahedra.

Above $T_N = 19.1$ K the crystal manifests paramagnetic behavior.[13] Below $T_N$ a relatively strong AF coupling between nearest-neighbor nickel ions occurs within the puckered plane via –Ni–O–Ni-superexchange pathways.[11,13,14] However, there is no direct or first-order superexchange (via one common ion) coupling between the moments in different planes, and only higher-order interactions are possible, involving the phosphate groups as an ''exchange bridge.'' Each $Ni^{2+}$ has a net of at least four antiferromagnetic Ni–O–P–ONi links to $Ni^{2+}$ ions in adjacent planes. According to neutron scattering data,[13,14] the antiferromagnetic ordering takes place with preservation of the unit cell. The spins of the nickel ions lie along the crystal axis *c* and alternate up and down. Until recently the magnetic space and point groups were considered to be $Pnm'a$ and $mm'm$, respectively.[11] Recent neutron diffraction work has shown that a space-modulated spin structure occurs in a narrow temperature range close to $T_N$ with a magnetic incommensurate short–range order persisting up to about 40 K.[15,16]

The magnetic field dependence of the polarization induced via the ME effect in $LiNiPO_4$ shows a so-called ''butterfly loop'' feature both when the magnetic field *H* is applied along the *a* axis, i.e., perpendicular to the spin direction (*c* axis),[17] as well as for *H* applied along the spin direction.[18] Usually such behavior appears due to the presence of a spontaneous magnetic moment in a compound (see, e.g., Refs. 19 and 20). Since such a small spontaneous magnetization was recently found[21] for the related $LiCoPO_4$, also showing ''butterfly loops,''[2] the occurrence of a spontaneous magnetization in $LiNiPO_4$ can be expected, too. Thus a symmetry lower than $mm'm$ will be required.

In spite of the fact that the $mm'm$ symmetry forbids a spontaneous magnetic moment, it was recently shown theoretically that a ''butterfly loop'' can also be realized in 4-sublattice fully compensated antiferromagnets with an ''indirect cross'' magnetic structure.[22] In such a structure the above-mentioned symmetry $mm'm$ allows spin canting in pairs of adjacent sublattices, but the resulting magnetic moment of a pair is ''hidden,'' because another spin pair fully compensates it in the unit cell. However, this mechanism does not seem to apply to $LiNiPO_4$ because, as stated above, it is very likely that the ''butterfly loops'' are due to a spontaneous magnetization.

## GROUP THEORY ANALYSIS OF FUNDAMENTAL VIBRATIONS

A group theory analysis of the $LiMPO_4$ family of compounds was done in Ref. 23. Let us summarize the essential results. In all of them the unit cell contains 4 formula units. The vibrational representation $\Gamma_{\text{vibr}}$ of the 84 normal modes at the center of the Brillouin zone ($\mathbf{k} = 0$) is distributed on the irreducible representations of the $D_{2h}$ point group as follows: $\Gamma_{\text{vibr}} = 11A_g + 7B_{1g} + 11B_{2g} + 7B_{3g} + 10A_u + 14B_{1u} + 10B_{2u} + 14B_{3u}$. Among them there are 3 acoustic modes, 45 antisymmetrical modes, active in IR absorption for the $B_{1u}$, $B_{2u}$, and $B_{3u}$ representations, and 36 symmetrical Raman-active optical modes. The latter modes correspond to the polarization of the excited and scattered light in the chosen coordinate system as: $A_g$-$(XX)$, $(YY)$, $(ZZ)$, $B_{1g}$-$(XY)$, $(YX)$, $B_{2g}$-$(XZ)$, $(ZX)$, and $B_{3g}$-$(YZ)$, $(ZY)$.

In a first-order approximation, the vibrations can be separated into internal vibrations ($\Gamma_{\text{int}}$) of the $(PO_4)^{3-}$ tetrahedra and external vibrations in which they move and rotate as solid units. The external vibrations are separated into the translational motions of the center-of-mass of $(PO_4)^{3-}$,

$Li^+$ and $Co^{2+}$ ions ($\Gamma_{trans}$) and hindered rotations (liberations) of the $(PO_4)^{3-}$ ions ($\Gamma_{libr}$). Such separation is rather arbitrary and may be used in the group-theory analysis for clarity only. In fact, they are not completely independent. The analysis gives the following representation for the above-listed types of vibration:

$$\Gamma_{int}=6A_g+3B_{1g}+6B_{2g}+3B_{3g}+3A_u+6B_{1u}+3B_{2u}+6B_{3u},$$

$$\Gamma_{trans}=4A_g+2B_{1g}+4B_{2g}+2B_{3g}+5A_u+6B_{1u}+4B_{2u}+6B_{3u},$$

and

$$\Gamma_{libr}=A_g+2B_{1g}+B_{2g}+2B_{3g}+2A_u+B_{1u}+2B_{2u}+B_{3u}.$$

Theoretically, a static splitting due to the $C_s$ crystal-field symmetry and a dynamic splitting due to the presence of 4 formula units in the unit cell could take place for the frequencies of the internal vibrations of $(PO_4)^{3-}$ tetrahedra. Experimentally, this may or may not be observed, depending on the crystal field effects.

## EXPERIMENTAL RESULTS AND DISCUSSION

Polarized Raman spectra of a $LiNiPO_4$ single crystal, taken at 5 K for different orientations of the sample sufficient to classify the symmetry types of all the Raman-active modes, are shown in Fig. 1. The intense lines which persist when the temperature rises from $T<T_N$ to room temperature are identified here as first-order phonon excitations. The symmetry assignments were made by means of polarization measurements and are listed in Table I. Some ''leak through'' of forbidden lines in certain polarization configurations is evident in these spectra, arising from slight misorientation of the crystal and/or the wide-angle-aperture optics which is used in the experiments to collect scattered light. The Raman spectra of $LiNiPO_4$ are very similar to those of $LiCoPO_4$ (Ref. 23).

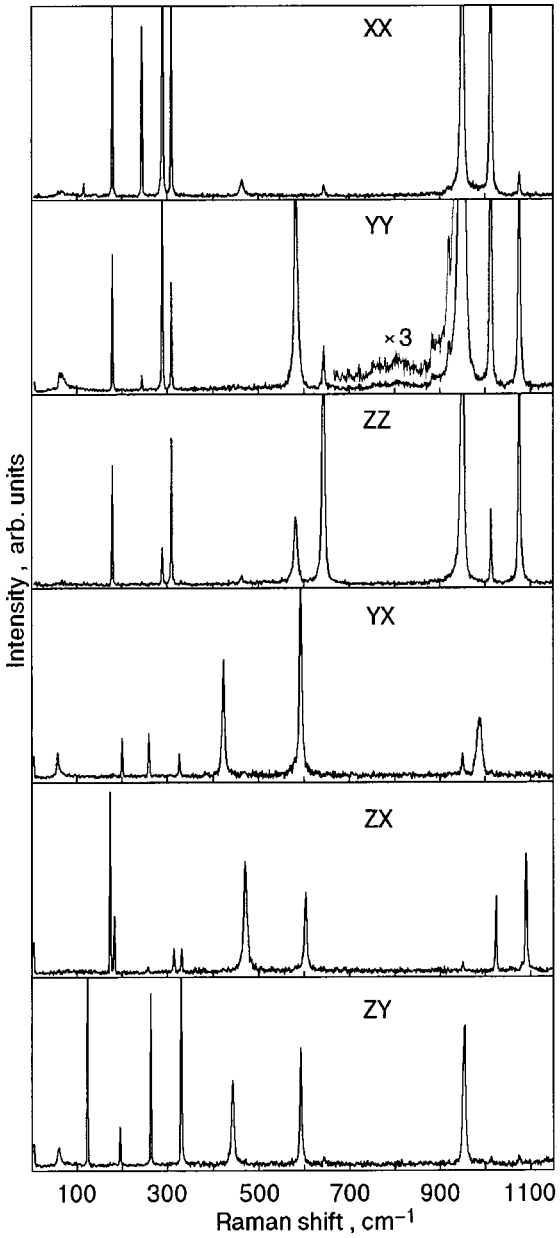


FIG. 1. Low-temperature (5 K) polarized Raman spectra of a $LiNiPO_4$ single crystal. The spectral resolution is 2.0 $cm^{-1}$.

### Study of internal modes

Characteristic phonon lines with frequencies higher than 400 $cm^{-1}$ are observed. The lines were identified in accordance with their closeness to the frequencies of the fundamental vibrational modes of a free $PO_4$ tetrahedron, which are 980 ($\upsilon_1$), 365 ($\upsilon_2$), 1082 ($\upsilon_3$), and 515 ($\upsilon_4$) $cm^{-1}$ (Ref. 24). The reducible vibrational representation of a free $PO_4$ tetrahedron decomposes to $A_1+E+F_1+3F_2$ irreducible representations of its $T_d$ symmetry group. The internal modes are labeled using Herzberg's notation[24] as: $\upsilon_1$ ($A_1$, symmetric P–O stretching), the doubly degenerate $\upsilon_2$ ($E$, symmetric O–P–O bond bending), the triply degenerate $\upsilon_3$ ($F_2$, antisymmetric P–O stretching), and the triply degenerate $\upsilon_4$ ($F_2$, antisymmetric O–P–O bond bending). The remaining modes $F_1$ and $F_2$ are external and correspond to rotation and translation of $PO_4$ as a whole unit, respectively.

In $LiNiPO_4$ the point symmetry of $(PO_4)^{3-}$ ions is $C_s$, which is lower than the $T_d$ symmetry of the free ion, and hence the degeneracy of the free ion frequencies must be lifted as: $A_1\rightarrow A'$, $E\rightarrow A'+A''$, $F_1\rightarrow A'+2A''$, $F_2\rightarrow 2A'+A''$. Since there are four $(PO_4)^{3-}$ ions within the primitive unit cell, there are four times as many modes of each species. They can be further related to the $D_{2h}$ factor-group symmetry of the crystal, giving the rules: $4A'\rightarrow A_g+B_{2g}+B_{1u}+B_{3u}$ and $4A''\rightarrow B_{1g}+B_{3g}+A_u+B_{2u}$. As a result, the internal phonons at $\mathbf{k}=0$ in the $LiNiPO_4$ crystal originate from the fundamental vibrational modes of a free $PO_4$ tetrahedron as shown in the following scheme: $\upsilon_1\rightarrow A_g+B_{2g}+B_{1u}+B_{3u}$, $\upsilon_2\rightarrow A_g+B_{1g}+B_{2g}+B_{3g}+A_u+B_{1u}+B_{2u}+B_{3u}$, $\upsilon_3$ and $\upsilon_4\rightarrow 2A_g+B_{1g}+2B_{2g}+B_{3g}+A_u+2B_{1u}+B_{2u}+2B_{3u}$. The frequencies of the phonons may be split due to a dynamical effect.

In the crystal, the value of frequency splitting of the $\upsilon_i$ ($i=1-4$) modes of the phosphate group is an indicator of the strength of the coupling to an environment. In the absence of interaction between them, the modes in quartets $A_g+B_{2g}+B_{1u}+B_{3u}$ and $B_{1g}+B_{3g}+A_u+B_{2u}$, which origi-

TABLE I. Experimentally observed frequencies ($cm^{-1}$) of vibrational excitations of the $LiNiPO_4$ single crystal at 5 K (300 K) and their classification.

| Type of vibrations | | Symmetry of vibrations | | | |
|---|---|---|---|---|---|
| | | $A_g$ | $B_{1g}$ | $B_{2g}$ | $B_{3g}$ |
| External | | 114.0 (111.5) | | | 122.0 (119.5) |
| | | | – | 172.0 (170.0) | |
| | | 175.5 (175.0) | | 182.0 (181.5) | |
| | | | | | 193.5 (189.0) |
| | | 242.5 (238.0) | 199.0 (195.0) | | |
| | | | | 255.5 (252.0) | |
| | | | 258.0 (256.0) | | |
| | | 287.5 (282.5) | | | 262.0 (258.5) |
| | | 308.0 (303.5) | | | |
| | | | | 313.0 (310.0) | |
| | | | 325.0 (320.5) | | |
| | | | | | 329.0 (324.5) |
| | | | | 329.5 (325.5) | |
| Internal $PO_4$ | $E(\nu_2)^*$ | 462.5 (459.0) | 422.5 (417.5) | | 442.5 (437.0) |
| | | | | 470.5 (467.5) | |
| | $F_2(\nu_4)^*$ | 581.5 (580.0) | 592.5 (591.5) | | 592.0 (591.0) |
| | | 642.0 (640.0) | | 603.0 (601.0) | |
| | | | | – | |
| | $A_1(\nu_1)^*$ | 948.5 (948.5) | | – | |
| | $F_2(\nu_3)^*$ | | 986.0 (987.5) | | 953.0 (952.0) |
| | | 1011.5 (1010.5) | | | |
| | | | | 1023.0 (1022.5) | |
| | | 1074.5 (1072.0) | | | |
| | | | | 1090.0 (1088.0) | |

*Irreducible representations and the internal mode indexes of a free $PO_4$ tetrahedron.[24]

nate from $A'$ and $A''$ types of vibrations, respectively, would each have the same frequency. Unfortunately, to the best of the authors' knowledge, no IR work has yet been done for this single crystal.[1)] Hence we have no experimental data about IR-active phonons with $B_{1u}$, $B_{3u}$, and $B_{2u}$ symmetry ($A_u$ phonons are neither IR nor Raman active), which belong to the above-mentioned quartets, and so we have no way of calculating the full range of frequency splitting of the $v_i$ modes in the crystal. Nevertheless the frequency separation of $A_g$ and $B_{2g}$, and of $B_{1g}$ and $B_{3g}$ modes indicate that dynamical effects are far from negligible (see Table I). It should be noted that the $B_{2g}$ component of the stretching mode $v_1$ is weak and difficult to observe.

The separation of fundamental vibrations into internal and external ones is valid in the case where the respective vibration frequencies differ considerably. Although the lowest Raman-active internal modes at ~420 $cm^{-1}$ are quite far from the highest external modes at ~330 $cm^{-1}$, the situation is not so clear for antisymmetrical modes. For example, the external antisymmetrical vibrations which involve translational motions of light $Li^+$ ions, are expected to be higher in frequency. Nevertheless, the internal-external modes approximation still retains the merit of providing a good basis for understanding the $\mathbf{k}=0$ modes in the $LiMPO_4$ compound.

### Study of external modes

Following the scheme given above, all sharp lines below 330 $cm^{-1}$ and above 100 $cm^{-1}$ are assigned to the external librational and translational modes. An essential difference between the *XX*, *YY*, and *ZZ* diagonal components of the scattering tensor, belonging to $A_g$ symmetry, reflects the considerable anisotropy of the $LiNiPO_4$ structure (Fig. 1). It is

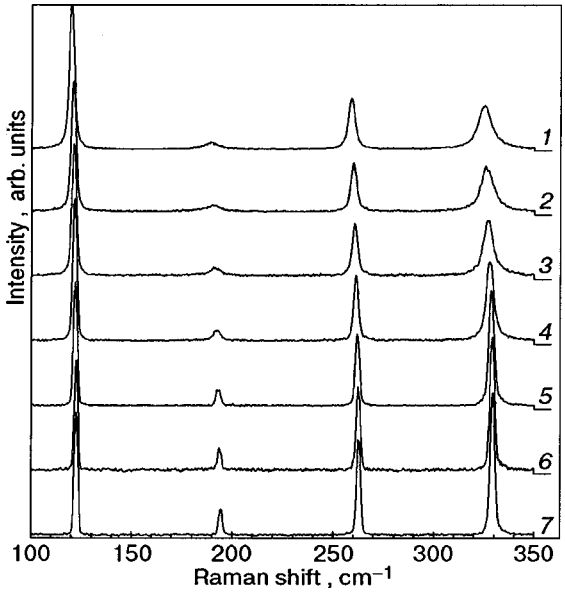


FIG. 2. Temperature behavior of the $B_{3g}$ external modes in $LiNiPO_4$. The numbers indicate the temperature in K: 300 (*1*), 250 (*2*), 200 (*3*), 150 (*4*), 90 (*5*), 25 (*6*), 5 (*7*). The spectral resolution is 2.0 cm$^{-1}$.

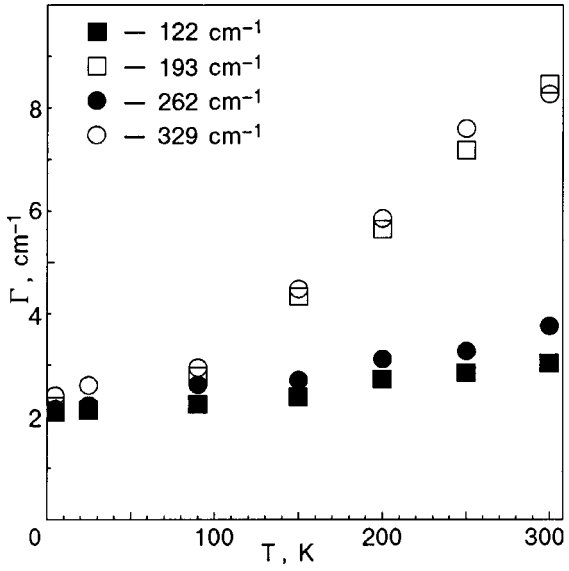


FIG. 3. Temperature dependence of the width Γ at half height of the phonon lines in the low-frequency $B_{3g}$ spectrum (see Fig. 2).

evident from Table I that the correct number of bands with $A_g$, $B_{2g}$, and $B_{3g}$ symmetry are present, while the number of $B_{1g}$ peaks is deficient. Only 3 peaks are clearly visible in the spectra of appropriate polarization. Since the crystal undergoes no structural phase transitions, the phonon lines show only a weak frequency shift and broadening with increasing temperature. The total shift of all phonon lines in the temperature range from 4.2 to 300 K does not exceed 5 cm$^{-1}$ (Table I).

An assignment of these lines to rotational and translational modes is conditional, because they have the same symmetry and, hence, may strongly interact with one another. We can only say something about the specific contribution of rotation and translation in each real mode in the crystal. It is known[26] that the temperature dependence of the phonon linewidth is determined mainly via two mechanisms: (i) anharmonicity of the corresponding vibrational mode and (ii) relaxation processes which may be related to many-particle decay or accidental reorientation, typical for atomic complexes. The first mechanism provides a linear temperature dependence of the spectral linewidth, while the second one is represented as Arrhenius-like contribution to the line broadening.

The reorientational motions in the $LiMPO_4$ crystals can be accomplished by the $(PO_4)^{3-}$ tetrahedra only during their hindered rotations. Hence the $B_{3g}$ modes at 174.5 and 323 cm$^{-1}$ in the $LiCoPO_4$ have been preferentially assigned to liberations,[23] due to the essential contribution of the mechanism (ii) to the temperature dependence of their widths. It is interesting that only the $B_{3g}$ spectrum shows an essential difference in the character of line broadening (Fig. 2). In the frequency range of external vibrations the $B_{3g}$ spectrum contains 2 translational and 2 librational modes. The first pair may be described as translational motions of the $Ni^{2+}$ ions relative to the $(PO_4)^{3-}$ ions parallel to the crystal axis *b*. The second one is represented by linear combinations of in-phase, around axis *a*, and out-of-phase, around axis *c*, rotations of four $(PO_4)^{3-}$ tetrahedra in the unit cell. The experimental results for the temperature dependence of the damping of the corresponding $B_{3g}$ modes at 193 and 329 cm$^{-1}$ in $LiNiPO_4$ are found to be similar to $LiCoPO_4$ (Fig. 3). This supports our assignment of these modes to ones of predominantly rotational character. In the other polarizations the temperature behavior of linewidths does not show enough difference to give preference to one of the two mechanisms of broadening. Thus the classification of the external modes remains, of course, qualitative.

#### Second-order vibrational spectra

In addition to one-phonon peaks, there are weak features around 750, 811, 887, and 919 cm$^{-1}$ in the polarizations corresponding to the diagonal components of the scattering tensor, which we assign to two-phonon scattering (see Fig. 1). A more prominent structure is evident in *YY* polarization. In the off-diagonal Raman polarizations the second-order spectrum is weak.

The bands at 887 and 919 cm$^{-1}$ can be assigned to the two-phonon excitation and overtone of 442.5 and 462.5 cm$^{-1}$ bending modes, respectively. Of course they can also be formed by combinations of other modes with approximately correct frequencies, such as: (581.5+308), (592.5 +325), and (582+329) cm$^{-1}$.

The broad bands at 750 and 811 cm$^{-1}$ are very likely the combination of O–P–O bond bending vibrations $v_2$ and $v_4$ and some external modes, for example: (462+287.5), (581.5+242.5), (422.5+325), (470.5+329.5), (442.5 +329) cm$^{-1}$. In contrast to overtones, the combined bands arise from two-particle processes, which involve pairs of phonons with the only restriction that the sum wave vector must be zero. If phonons in the pair have some frequency dispersion, they produce broad bands in a second-order Raman spectrum.

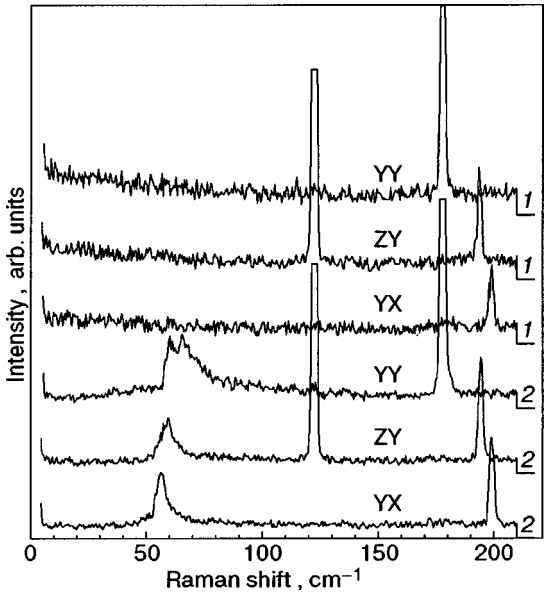


FIG. 4. Low-frequency spectra of $LiNiPO_4$ at 25 (*1*) and 5 (*2*) K. The sharp lines at 122, 177.5, 193.5, and 199 $cm^{-1}$ are the vibrational modes. The spectral resolution is 2.0 $cm^{-1}$.

### Low-frequency excitations in AF phase

In the low-frequency Raman spectra of $LiNiPO_4$ a set of lines appears at $T<T_N$. Representative spectra in three experimental geometries, recorded at temperatures above and below $T_N$ and covering the frequency range 0–210 $cm^{-1}$, are shown in Fig. 4. Well below $T_N$ the *YY* spectrum comprises a peak at 60 $cm^{-1}$, accompanied by a broad asymmetric band which shows a maximum intensity at 66.5 $cm^{-1}$, and the cutoff frequency is about 130 $cm^{-1}$. There is a peak at 58.5 $cm^{-1}$ in the *ZY* spectrum and a peak at 56.5 $cm^{-1}$ with a shoulder on the low-frequency side of the *YX* spectrum. No visible features were observed in the *XZ* spectrum, and so it is not reproduced here. The observed peaks are attributed to magnon scattering, because they vanish above $T_N=19.1$ K. However, a definite assignment of the lines to distinct excitations modes is not possible at the present stage of investigation. There are no data on the magnon dispersion curves nor results of antiferromagnetic resonance experiments from which the energy of a zone-center ($\mathbf{k}=0$) magnon at $T=0$ K may be estimated. For the time being we can only note that the number of observed lines in the Raman spectra of $LiNiPO_4$ at $T\ll T_N$ exceeds the number that may be predicted by the square two-dimensional model of the antiferomagnet used in Ref. 13.

## CONCLUSION

Finally, we summarize the present results and the remaining problems. The Raman spectrum of $LiNiPO_4$ displays reasonable agreement with group theory predictions. The internal-external modes approximation is satisfactory for the lattice dynamics of $LiMPO_4$ compounds. The vibrations of the $(PO_4)^{3-}$ ions may be treated by the site-group method. The observed splitting of the $\upsilon_2$, $\upsilon_3$, and $\upsilon_4$ modes of the ''free'' tetrahedral complex indicate that in $LiNiPO_4$ the host-lattice phosphate interaction and the dynamic coupling between $(PO_4)^{3-}$ complexes is not weak.

Due to the anharmonicity of the vibrational modes, overtones, and two-phonon excitations, which are combinations of the external and the bending vibrations of the $(PO_4)^{3-}$ complexes, are observed in the Raman spectra.

We have revealed no violations of the polarization selection rules below the Néel temperature of $LiNiPO_4$ which may be connected with the Pradhan mechanism of light scattering in ME crystals.[3] Thus the effect is considered to be weak[1] and hence will be difficult to observe in this compound. The static values of the ME susceptibility in $LiNiPO_4$ are considerably smaller than in $LiCoPO_4$, as experiments[2] have shown. Assuming that the magnetoelectric coefficients are not much changed at optical frequencies from their static values, there is a chance to observe them in $LiCoPO_4$. In addition, detailed investigations of phonons by infrared absorption are necessary. To the best of the authors' knowledge, no IR work has yet been done on these single crystals, and such experiments would be very helpful in the discussion of this new effect in Raman scattering.

The evidence of long-range antiferromagnetic order is observed in the form of the appearance of additional lines at 56.5, 58.5, 60 $cm^{-1}$ and of a broad asymmetric band at 66.5 $cm^{-1}$ at temperatures below $T_N$. Their frequencies and behavior with changing temperature allow them to be identified as the Raman scattering on spin-wave excitations. A definite assignment of the lines to distinct excitations is not possible at the present stage of investigation. Detailed experimental data on the temperature and magnetic-field dependence of the low-frequency Raman spectrum of $LiNiPO_4$ remain a topic for future study.

The authors thank Prof. N. F. Kharchenko for helpful discussions and steady interest in the work.

*E-mail: gnezdilov@ilt.kharkov.ua
**New address: Swiss Federal Institute of Technology Lausanne, Materials Department, Laboratory of Ceramics, CH-1015 Lausanne, Switzerland.

[1)] The only published data[25] concern IR spectra of polycrystalline samples of $Li_{1-3x}Fe_xNiPO_4$ ($0<x<0.15$).

[1] M. Mercier, J. Gareyte, and E. F. Bertaut, Acad. Sci., Paris, C. R. B **264**, 979 (1967).
[2] J.-P. Rivera, Ferroelectrics **161**, 147 (1994).
[3] T. Pradhan, Phys. Scr. **45**, 86 (1992).
[4] H. J. Scheel and D. Elwell, *Crystal Growth from High-Temperature Solutions*, Academic Press, London (1975).
[5] W. Tolksdorf, in *Handbook of Crystal Growth. Vol. 2: Bulk Crystal Growth*, D. T. J. Hurle (Ed.), North-Holland Elsevier Science Publishers, Amsterdam (1994), Part 2a, Chap 10, p. 563.
[6] F. Zambonini and L. Malossi, Z. Kristallogr. **80**, 442 (1931).
[7] R. E. Newnham, R. P. Santoro, and M. J. Redman, J. Phys. Chem. Solids **26**, 445 (1965).
[8] M. Mercier, *These de doctorat d'Etat*, Faculte des Sciences, Universite de Grenoble, France (1969).
[9] G. E. Rossman, R. D. Shannon, and R. K. Waring, J. Solid State Chem. **39**, 277 (1981).
[10] A. Belletti, R. Borromei, R. Cammi, and E. Cavalli, Phys. Status Solidi B **163**, 281 (1991).
[11] R. P. Santoro, D. J. Segal, and R. E. Newnham, J. Phys. Chem. Solids **27**, 1192 (1966).
[12] I. Abrahams and K. S. Easson, Acta Crystallogr., Sect. C: Cryst. Struct. Commun. **49**, 925 (1993).
[13] D. Vaknin, J. L. Zarestky, J. E. Ostenson, B. C. Chakoumakos, A. Goni, P. J. Pagliuso, T. Rojo, and G. E. Barberis, Phys. Rev. B **60**, 1100 (1999).
[14] R. P. Santoro, R. E. Newnham, and S. Nomura, J. Phys. Chem. Solids **27**, 655 (1966).

[15] D. Vaknin and J. L. Zarestky, *Abstract [24.006]*, in *The 2000 March Meeting of the American Physical Society*, Minneapolis, March 23, 2000.
[16] D. Vaknin *et al.* (to be published).
[17] I. Kornev, M. Bichurin, J.-P. Rivera, S. Gentil, H. Schmid, A. G. M. Jansen, and P. Wider, Phys. Rev. B **62**, 12247 (2000).
[18] I. Kornev *et al.* (to be published).
[19] E. Ascher, H. Rieder, H. Schmid, and H. Stossel, J. Appl. Phys. **37**, 1404 (1966).
[20] M. Senthil Kumar, J.-P. Rivera, Z. G. Ye, S. D. Gentil, and H. Schmid, Ferroelectrics **204**, 57 (1997).
[21] N. F. Kharchenko, Yu. N. Kharchenko, R. Szymchak, M. Baran, and H. Schmid, Fiz. Nizk. Temp. **27**, 1208 (2001) [Low Temp. Phys. **27**, 895 (2001)].
[22] I. E. Chupis, Fiz. Nizk. Temp. **26**, 574 (2000) [Low Temp. Phys. **26**, 422 (2000)].
[23] V. I. Fomin, V. P. Gnezdilov, V. S. Kurnosov, A. V. Peschanskii, V. V. Eremenko, S. Gentil, and J.-P. Rivera, Fiz. Nizk. Temp. **25**, 1107 (1999) [Low Temp. Phys. **25**, 829 (1999)].
[24] G. Herzberg, *Infrared and Raman Spectra of Polyatomic Molecules*, Van Nostrand, New York (1975).
[25] A. Goni, L. Lezama, M. I. Arriortua, G. E. Barberis, and T. Rojo, J. Mater. Chem. **10**, 423 (2000).
[26] M. M. Suschinsky, *Raman Scattering Spectra of Molecules and Crystals* [in Russian], Nauka, Moscow (1969).

This article was published in English in the original Russian journal. Reproduced here with stylistic changes by AIP.

## LOW-DIMENSIONAL AND DISORDERED SYSTEMS

# Infrared spectra of thin films of cryocondensates of an isotopic water mixture

A. Aldijarov, A. Drobyshev,* and S. Sarsembinov

*Kazakh State National University, Tole bi 96, 480012 Almaty, Kazakhstan*
(Submitted September 28, 2001; revised November 13, 2001)
Fiz. Nizk. Temp. **28**, 297–303 (March 2002)

The spectral characteristics of thin films of vacuum condensates of an isotopic water mixture consisting of 10% $H_2O$, 50% HDO, and 40% $D_2O$ are investigated. The cryocondensates are obtained on a metallic mirror at a temperature of 30 K and a pressure of the gas phase over the substrate during the cryodeposition of $6.7\times10^{-4}$ Pa. The IR spectra are investigated in the frequency range 4200–400 $cm^{-1}$ for films of different thicknesses ($d=0.1$–$2.5$ $\mu$m). It is found that the increasing thickness of the water film during the course of the condensation leads to substantial changes in the spectral reflectivity in the range of characteristic frequencies of the intramolecular vibrations—an increase in the absorption intensity and in the width of the spectral bands. It is found that for $d\geqslant2.5$ $\mu$m a film of water cryocondensate is optically transparent over a wide spectral interval. © *2002 American Institute of Physics.*
[DOI: 10.1063/1.1468526]

### INTRODUCTION

The optical properties of cryocondensates of water and heavy water have been investigated in quite a few papers. Some of these papers can truly be called classic.[1–3] While mainly aimed at ascertaining the interrelationship between the parameters of the intermolecular interaction and the structure of ices, they laid a reliable foundation for further study of such objects, including variously stimulated structural–morphological transformations. In the last two decades an active research on the properties of solid and heavy water at low temperatures has resumed: in addition to a number of new experiments of a purely scientific, basic-research interest, there is also the need to solve a wide range of applied problems. These are mainly in connection with prolonging the service life of artificial objects in space, nuclear power, the development of laser technology based on matrix-isolated impurity cryocondensates, etc. Here, thanks to the advent of a unique new method, it has become possible to attack experimental problems of a higher level. These can be arbitrarily divided into three research areas:

— The study of cluster formation processes in epitaxial layers.[4,5] Here the objects of study are monolayers of deposited water. Based on the IR spectra obtained, one can reach conclusions as to the structure of the clusters forming on cold substrates.

— The use of the cryomatrix isolation technique for obtaining information about the character of the changes in the characteristic intramolecular vibrations of isolated molecules and about their interaction with each other, including aggregate formation processes of various orders.[6,7]

— The classical study of thin films of cryovacuum condensates, the thickness of which is comparable to the wavelength of the characteristic intramolecular vibrations.[8–10] Such studies, as a rule, yield data on the growth rate and thermophysical and optical characteristics of cryovacuum condensates as functions of the thermodynamic parameters of the deposition. On the basis of the results obtained, one can draw preliminary conclusions as to the structure of the cryocondensate and its transformations.

This is the approach that was implemented in the present study and in some previous papers. For the past decade we have been studying the relationships governing the formation of vacuum cryocondensates with various kinds of intramolecular symmetry.[9–11] However, the circumstances set forth below have made it necessary to do additional research on the cryodeposition processes and the properties of cyrovacuum condensates, particularly water and heavy water.

1. The previous studies were done on film samples more than 3 $\mu$m thick. Thus possible size effects manifested in thinner samples would have escaped our notice.

2. The data obtained concerning the possible existence of structural modifications of heavy-water vacuum condensates in a wide temperature interval[9] have required additional, more detailed investigation, including the study of thin films.

3. A decisive role in the formation of various types of ices is played by the hydrogen bond. Its influence on the state of the interacting molecules is expressed in a change in the spectral characteristics of cryocondensates at frequencies in the ranges of the characteristic vibrations. This influence may be different, depending on the type of vibrations and the degree of connectedness of the molecules. In this sense the study of the condensation processes for an isotopic water mixture and the measurement of the IR spectra of the films obtained can promote an understanding of the physical processes occurring in the course of the cryocondensation of water vapor on a cooled substrate.

Thus the main problem of these studies was to investigate the influence of the thickness of heavy-water cryocondensate films on the spectral reflectivity of the substrate–film system at frequencies in the range of the characteristic vibra-

 

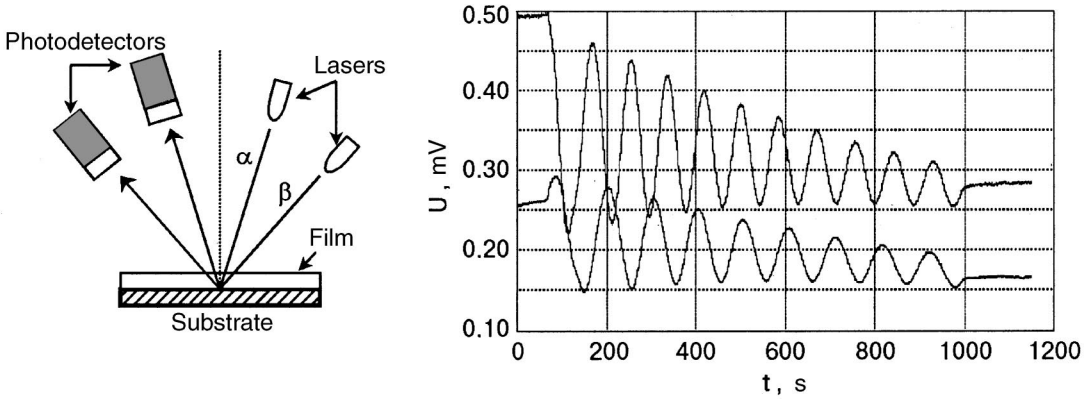


FIG. 1. Diagram of the experiment and typical interferograms of a heavy-water cryocondensate film for different angles of incidence of the laser beam.

tions of the molecules $H_2O$, HDO, and $D_2O$.

## EXPERIMENTAL APPARATUS AND MEASUREMENT TECHNIQUES

Measurements were made on the experimental apparatus described in detail in Ref. 10. It is a universal cryogenic vacuum spectrophotometer with which one can also measure the refractive indices, growth rate, and thickness of cryocondensate films. For these measurements the apparatus was equipped with a two-beam laser interferometer. The vacuum for the apparatus[10] was produced by a NORD-250 ion pump with a residual pressure of $6.7\times10^{-6}$ Pa. To study thin cryocondensate films it is necessary to ensure that residual gases are not condensed with the substance to be studied, and this requires improving the limiting vacuum in the chamber. For this purpose the apparatus was further equipped with an NVK-320-5 cryocondensation pump, which made it possible to pump the chamber down beforehand to a pressure of $6.7\times10^{-8}$ Pa.

We also modified the temperature stabilization system of the cryostat of the apparatus. The cryostat was mounted on the upper low-temperature flange of the microcryogenic machine of a Gifford–McMahon system. The temperature stabilization system used previously could not maintain the temperature to the level desired. By mounting additional heaters and monitoring the experiment with a computer, we were able to maintain the temperature of the condensation surface to within 0.05 K.

A diagram of the experiment and typical interferograms of the growth of a cryocondensate film are shown in Fig. 1.

As in Ref. 10, to obtain the reflection spectra of the samples we used an IKS-29 IR spectrometer. In the apparatus described in Ref. 10 the measurements were made in a single-beam mode, which complicated the processing of the spectra because of the high noise level. To improve the quality of the IR spectra we set up an optical bypass channel to permit making measurements in the two-beam mode. As a result, the quality of the spectra obtained was improved significantly. The accuracy of the spectral measurements was $0.75\ \mathrm{cm}^{-1}$ with a resolution $R=850$, according to the documentation for the spectrometer.

To monitor the isotopic composition of the water we made mass-spectrometric measurements with an IPDO-1 (which measures the partial pressures of the residual gases). On the basis of the mass spectra obtained (Fig. 2), the mass composition of the water was calculated as 10% $H_2O$, 50% HDO, and 40% $D_2O$. The measurement error was 3–5%.

## DISCUSSION OF THE RESULTS

The IR reflection spectra of water cryocondensate films of different thickness are presented in Figs. 3 and 4. All of the samples were condensed from the gas phase under identical conditions—the substrate temperature was 30 K, and the pressure of the gas phase during the cryodeposition was maintained at $6.7\times10^{-4}$ Pa. The data in Fig. 3 correspond to a the frequency range of the characteristic stretching vibrations of the $D_2O$ molecule. Figure 4 shows the IR spectra in the frequency region of the deformation angular vibrations.[6] These results we obtained in the single-beam mode of the interferometer.

For visual clarity, all of the spectra have been shifted relative to one another along the vertical while preserving the scale. The dotted lines mark the frequencies of the characteristic vibrations of the bonds indicated.

As an aid to analysis of the results, the values of the main characteristic frequencies of the intramolecular vibrations of heavy water in different states are listed in Table I.

It is seen from the figures that all of the main lines corresponding to the characteristic frequencies of intramolecular vibrations are present in the spectra. The character of the IR spectra changes as the thickness of the samples increases. Not only is there an increase in the amplitude of the absorp-

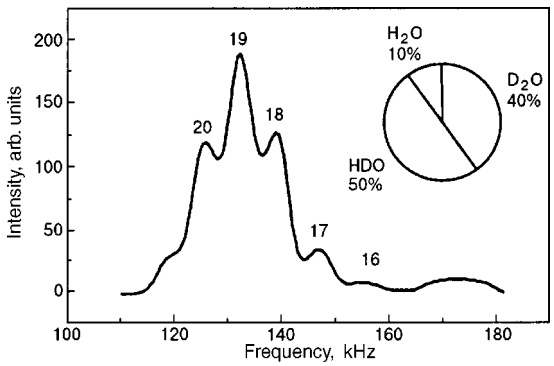


FIG. 2. Results of mass-spectrometric measurements of the composition of the isotopic water mixture.

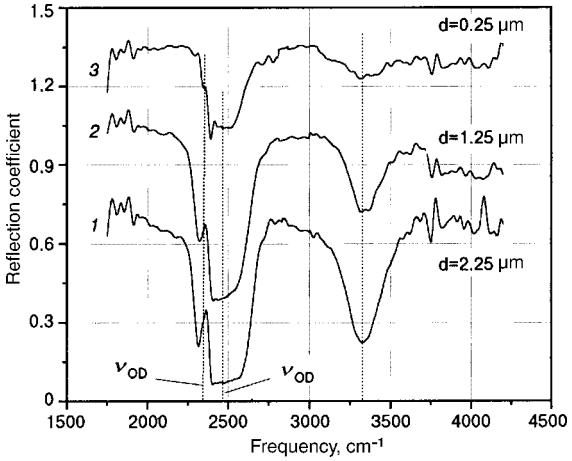


FIG. 3. IR reflection spectra of heavy-water cryocondensate films of different thickness in the frequency range of the stretching vibrations. The spectra are shifted along the vertical by 0 (*1*), +0.3 (*2*), +0.6 (*3*).

tion spectra in the region of the characteristic frequencies, but absorption bands which had been indistinct at small thicknesses appear.

A more detailed analysis of the results reveals the following features of the spectra shown.

1. In the frequency interval 3000–3500 $cm^{-1}$ (Fig. 5) there is a pronounced absorption peak whose intensity depends substantially on the thickness of the sample. It most likely corresponds to the characteristic O–H stretching vibration of the HDO molecule.[1,12] In this interval one also observes an absorption band of the stretching vibrations of $H_2O$. However, in the latter case the librational vibrations of $H_2O$ should appear at a frequency of 840 $cm^{-1}$, but these are not observed. In addition, the concentration of $H_2O$ in the isotopic water mixture is low and cannot lead to such a significant absorption peak. Thus this absorption band can be attributed with a high degree of reliability to the O–H bond in the HDO molecule.

We see in Fig. 5 that the maximum of the absorption in this band occurs in the frequency interval 3325–3350 $cm^{-1}$. At the same time, according to Refs. 1 and 12, the maximum of the absorption of the O–H stretching vibrations in the

TABLE I. Fundamental characteristic frequencies of the intramolecular vibrations of heavy water in different states.

| State of molecule | Symmetric stretching, $\nu_{OD}$ | Asymmetric stretching, $\nu_{OD}$ | deformation angular, $\nu_2$, $\nu_R$ | Ref. |
|---|---|---|---|---|
| | $cm^{-1}$ | | | |
| Gaseous state | 2666 | 2789 | 1179($\nu_2$) | 11 |
| Monomolecule in adlayer | 2655 | 2765 | 1178($\nu_2$) | 6 |
| *Ih* phase | 2332 | 2425 | 1210($\nu_2$), 640($\nu_R$) | 1 |

HDO molecule is found at a frequency of 3277 $cm^{-1}$. This discrepancy may be due to the difference of the intermolecular interactions via the hydrogen bonds, i.e., we are comparing structurally different ices. In Refs. 1 and 12 the ice *Ih*, formed at 173 K, was studied. In our case a cryocrystal with a nonhexagonal structure was formed on the substrate.

2. The frequency interval 2200–2700 $cm^{-1}$ is the region of stretching vibrations of the $D_2O$ molecule and the D–O bond in the HDO molecule. The strong absorption peak is apparently a superposition of these vibrations. In Figs. 3 and 6 we see that increasing the thickness of the cryocondensate film leads not only to an increase in the intensity but also to broadening of the absorption bands in the spectrum. At the same time, the fine structure observed on the absorption peak (Fig. 7) indicates that the samples are transparent in a wide spectral interval. This conclusion is also confirmed by analysis of the interferograms of the growth of heavy-water cryocondensate films (Fig. 1).

Figure 6 shows the spectra of different thicknesses of the cryocondensates of the isotopic water mixture in the frequency interval 2000–3000 $cm^{-1}$ in comparison with the clean substrate. These data were obtained in the two-beam mode of the IR spectrometer. As is clearly seen in Fig. 6, as the thickness of the film increases, a pronounced absorption line appears at a frequency $\nu = 2297$ $cm^{-1}$. The interpretation of this peak from the standpoint of intramolecular vibrations is not obvious. If it is a symmetric stretching vibration,

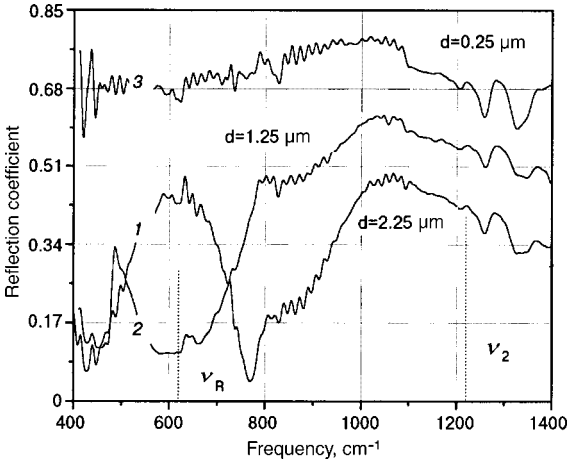


FIG. 4. IR reflection spectra of heavy-water cryocondensate films of different thickness in the frequency range of the deformation vibrations. The spectra are shifted by 0 (*1*), +0.06 (*2*), +0.2 (*3*).

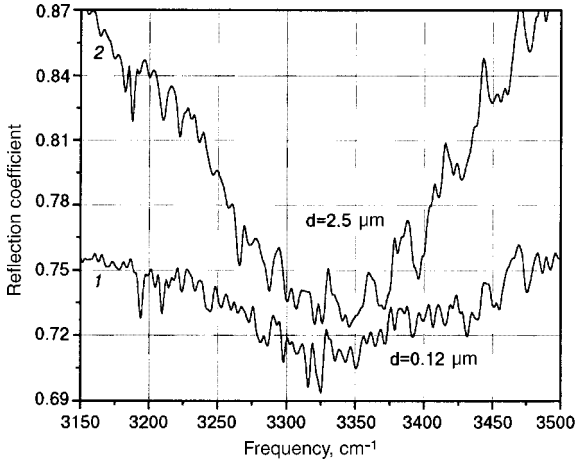


FIG. 5. Fragment of the IR reflection spectra of heavy-water cryocondensate films of different thickness in the frequency interval 3000–3500 $cm^{-1}$. The spectra are shifted by 0 (*1*), +0.14 (*2*).

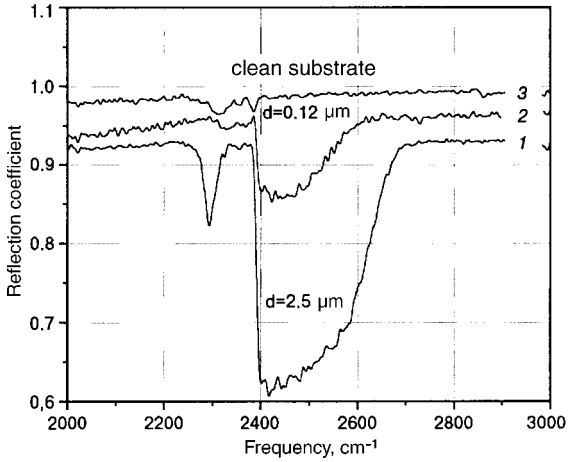


FIG. 6. IR reflection spectra of heavy-water cryocondensate films of different thickness, obtained during measurements in the two-beam mode. The spectra have been shifted by 0 (*1*), +0.06 (*2*), +0.045 (*3*).

then it is shifted to lower frequencies. For comparison, according to the data of Ref. 1, $\nu_1 = 2332\ \mathrm{cm}^{-1}$ for ice *Ih*.

A more obvious explanation for the appearance of the band at $\nu = 2297\ \mathrm{cm}^{-1}$ is that it belongs to the so-called associative vibrations of the $H_2O$ molecule. According to Ref. 14, it is an overtone or combination of lattice modes and can be interpreted as the trebled frequency of the librational vibrations of the water molecule or as an interaction of librational and deformation vibrations.[12] This conjecture also explains the low amplitude of the band, which accords with the low concentration of $H_2O$ in the isotopic water mixture.

A more detailed view of the region of stretching vibrations is shown in Fig. 7. In analyzing the data of Fig. 7 one notices another important feature. The spectra for samples of different thickness have several spectral regions with similar configurations: $a-a'$, $b-b'$, $c-c'$. Their appearance may be the result of two causes. One of these involves processes of cluster formation of water molecules. The data in Ref. 4 are interpreted as being the observation of polyaggregates with characteristic frequencies that are in fair agreement with the results in question. In particular, a dimer adsorbed on the substrate, according to the data of Ref. 4, has a characteristic bond frequency $\nu_{OD} = 2492\ \mathrm{cm}^{-1}$, which may be associated to our selected intervals $c-c'$.

Another mechanism for the appearance of fine structure may be perturbation of the stretching vibrations by the hydrogen bond. This should also give rise to the corresponding overtones. In addition, it is possible that the observed features of the fine structure are due to a separation of the vibrations of the O–D bond of the $D_2O$ and HDO molecules.

Another feature of the spectra shown in Fig. 7 is the obvious relative shift of the selected configurations for films of different thickness. As the film thickness increases, the corresponding frequencies are shifted upward. Since the samples were all grown under identical conditions, this is most likely not due to structural transformations but is rather a size effect. The specific mechanism for this effect is not yet clear.

3. The interval $400-1400\ \mathrm{cm}^{-1}$ corresponds to librational and deformation angular vibrations of the water molecules and to their modes excited by the hydrogen bonds of different configurations.[1] The absorption band in the frequency interval $1220-1270\ \mathrm{cm}^{-1}$ corresponds to a deformation vibration of the $D_2O$ molecule. The vibration of the HDO molecule most likely corresponds to the band in the frequency interval $1300-1450\ \mathrm{cm}^{-1}$.

As we see in Figs. 4 and 8, changing the thickness of the sample affects the fundamental angular deformation vibration $\nu_2$ of heavy water and HDO. This is particularly noticeable for the frequency range of the excited angular vibrations, specifically in the frequency interval $400-900\ \mathrm{cm}^{-1}$. Increasing the thickness of the sample from $d = 1.25$ to 2.5 $\mu$m leads to significant rearrangement of the spectrum in this frequency interval (curves *1* and *2* in Fig. 4). While curve *2* is in completely satisfactory agreement with the data of Ref. 1 (considering the difference in temperatures and methods of sample preparation), the appearance of the reflection peak at $600\ \mathrm{cm}^{-1}$ for a film thickness $d = 2.5$ $\mu$m does not have an obvious explanation. It is clearly not an interference effect—the film thickness is too small for the given wavelengths of the incident radiation. It can hardly be the result of a bulk ''turning'' of the hydrogen bonds, either, since the thickness

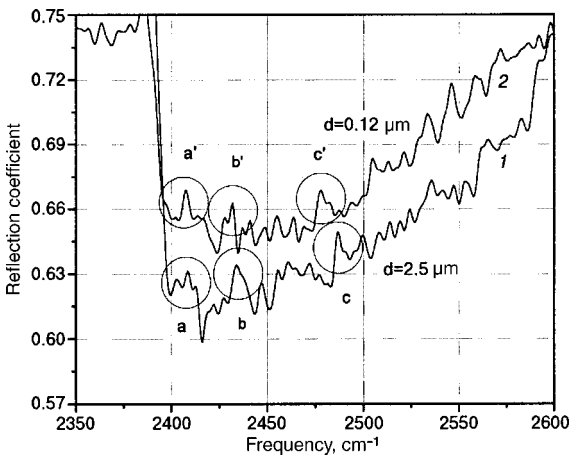


FIG. 7. Fragment of the IR reflection spectra of heavy-water cryocondensate films of different thickness in the frequency range of the stretching vibrations. The spectra have been shifted by 0 (*1*), −0.15 (*2*).

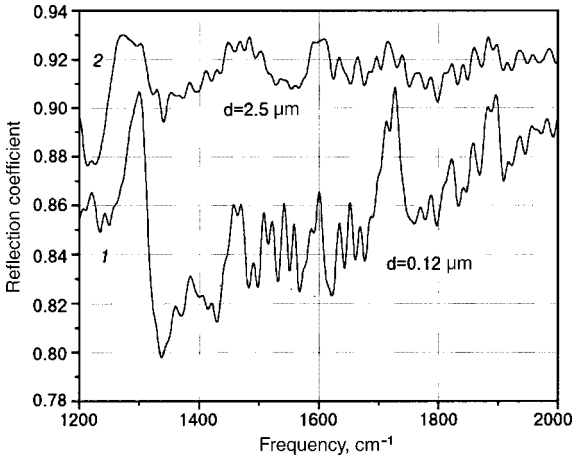


FIG. 8. Fragment of the IR reflection spectra of heavy-water cryocondensate films of different thickness in the frequency interval $1200-2000\ \mathrm{cm}^{-1}$. The spectra have been shifted by 0 (*1*), 0.02 (*2*).

TABLE II. Change in the frequency of the stretching vibrations and enthalpy of the hydrogen bond when the film thickness changes from 0.12 to 2.5 $\mu$m.

| Frequency interval, $cm^{-1}$ | Type of bond | $\nu_{2.5\,\mu m}$ | $\nu_{0.12\,\mu m}$ | $\Delta\nu$ | $\Delta H$, J/mole |
|---|---|---|---|---|---|
| | | | $cm^{-1}$ | | |
| 3000–3500 | O—H in HDO | 3327 | 3345 | −18 | 5.15 |
| 2200–2700 | O—D in $D_2O$ and HDO | 2497 | 2467 | 30 | −8.59 |

of the film is already too large for that. Nevertheless, it is clear that with increasing thickness of the film substantial changes occur in it which also affect the character of the spectra in other frequency intervals (Fig. 8).

In particular, we see in Fig. 8 that in the process of growth of the cryocondensate film the IR spectra become smoother with increasing thickness. One possible explanation of this could be that metastable states of the solid phase occur during the formation of the thin films of the cryocondensate. As the film grows, the previously formed layer simultaneously undergoes a transition to a stable state, and this is reflected in the spectrum.

4. Hydrogen bonds. It is known[13] that the formation of a hydrogen bond is accompanied by a lowering of the frequency of the stretching vibration and an increase in the intensity of the absorption at the corresponding frequencies. These changes, according to Badger and Bauer,[13] are related to the energy of the bonds that are being formed by the simple relation (for the heavy-water molecule)

$$\Delta\nu_{OD} = -\frac{\Delta H}{0.024},$$

where $\Delta H$ is the change in enthalpy of the O–D valence bond in the static field of the hydrogen bond. Using this relation, we have calculated the change in enthalpy of the hydrogen bond as the film thickness increases. The calculations were done for frequencies corresponding to the half-width of the absorption band (Table II). We see that an increase in the film thickness is accompanied by a change in enthalpy of the hydrogen bond, this change being of a different character for different types of molecules.

Analysis of the data presented in Table II suggests that an increase in the film thickness leads to a weakening of the O–D hydrogen bond for the $D_2O$ and HDO molecules and an enhancement of the O–H hydrogen bond for the HDO molecule.

## CONCLUSION

1. Heavy-water cryocondensate films formed at a temperature of 30 K are optically transparent for $d \leqslant 2.5$ $\mu$m over a wide spectral interval.

2. The increase in thickness of heavy-water films during condensation at a substrate temperature of 30 K leads to substantial changes in the spectral reflectivity in the region of characteristic frequencies of intramolecular vibrations. This is expressed in an increase in both the energy of the absorption and the width of the spectral bands.

3. As the thickness of the film increases, a sharp absorption peak arises at a frequency $\nu = 2297$ $cm^{-1}$. This is apparently an overtone or combination of lattice modes and can be interpreted as the trebled frequency of the librational vibrations of the water molecule or as an interaction of librational and deformation vibrations.

4. On the spectra of samples of different thickness there are regions of complex configuration that can be explained as being due the formation of clusters of water molecules. As the thickness of the film increases, the frequencies corresponding to these identified regions increase.

5. Calculations using the Badger–Bauer relation have shown that an increase in the film thickness is accompanied by a change in the enthalpy of the hydrogen bond, and that this change is of a different character for different types of molecules.

The authors thank A. Tulegenov for taking part in the experiments and in a discussion of the results.

*E-mail: drobyshev@nursat.kz

[1] J. E. Bertie and E. Whalley, J. Chem. Phys. **40**, 1637 (1964).
[2] J. E. Bertie and E. Whalley, J. Chem. Phys. **40**, 1646 (1964).
[3] J. E. Bertie, E. Whalley, and L. D. Calvert, J. Chem. Phys. **38**, 840 (1963).
[4] H. Ogasawara, J. Yoshinobu, and M. Kawai, J. Chem. Phys. **111**, 70038 (1999).
[5] J. N. Harvey, J. O. Jung, and R. B. Gerber, J. Chem. Phys. **110**, 8747 (1998).
[6] R. M. Bentwood, A. J. Barnes, and W. J. Orville-Thomath, J. Mol. Spectrosc. **34**, 391 (1980).
[7] J. B. Paul, J. Chem. Phys. **109**, 10201 (1998).
[8] M. S. Westley, G. A. Baratta, and R. A. Baragiolla, J. Chem. Phys. **108**, 3313 (1998).
[9] A. S. Drobyshev and D. N. Garipogly, Fiz. Nizk. Temp. **22**, 812 (1996) [Low Temp. Phys. **22**, 625 (1996)].
[10] A. S. Drobyshev and T. A. Prokhodtseva, J. Low Temp. Phys. **119**, 431 (2000).
[11] E. F. Barker and W. W. Sleator, J. Chem. Phys. **3**, 660 (1935).
[12] J. E. Bertie, E. Whalley, and H. J. Labbe, J. Chem. Phys. **50**, 4501 (1969).
[13] G. N. Zatsepina, *Physical Properties and Structure of Water* [in Russian], Izd. MGU, Moscow (1987).
[14] R. Zimmerman and G. Pimentel, *Advances in Molecular Spectroscopy*, New York (1962).

Translated by Steve Torstveit

# Electromagnetic surface waves in layered conductors

V. M. Gokhfeld*

*A. A. Galkin Donetsk Physicotechnical Institute, National Academy of Sciences of Ukraine, ul. Rosy Lyuksemburg 72, 83114 Donetsk, Ukraine*

(Submitted October 26, 2001)
Fiz. Nizk. Temp. **28**, 304–310 (March 2002)

An integral dispersion relation is derived and used to investigate the spectral and relaxation properties of surface plasma oscillations in layered conductors with a quasi-two-dimensional character of the charge-carrier motion. The results demonstrate significant differences from the case of an isotropic metal. © *2002 American Institute of Physics.* [DOI: 10.1063/1.1468527]

## 1. INTRODUCTION

Surface plasma oscillations (i.e., high-frequency electromagnetic waves of the Rayleigh type)[1,2] containing a longitudinal component of the electric field and localized near a metal–vacuum interface (or, in general, a conductor–insulator interface) were observed and given a qualitatively clear theoretical interpretation[3] several decades ago. Review articles[4,5] and special chapters in the monograph[6] (see also the literature cited in these sources) give a rather detailed exposition of the problem. However, the hydrodynamic theory developed in them is actually based on the isotropic Drude–Lorentz model of the metal and is applicable to real conducting crystals only in its broad outlines. At the present time there is considerable research attention devoted to synthetic metal-like compounds, including some of organic origin, having a pronounced layered or chainlike crystal structure and a sharp—reaching several orders of magnitude—anisotropy of both the static and high-frequency electrical conductivity. As a rule, such objects are characterized by an effectively reduced dimensionality of the electron energy spectrum, i.e., by open Fermi surfaces of the ''corrugated cylinder'' or ''corrugated plane'' type.[7]

The influence of anisotropy of the electron dispersion relation on the properties of surface plasmons can be taken into account in a consistent way only within the framework of a microscopic description based on the kinetic equation and the correct solution of the boundary-value problem for a metallic half space.[1)] Such an approach leads to an integral dispersion relation, the solution of which (in each geometrically different particular case) makes it possible to describe in a unified way both the dispersion and damping of surface plasma waves.

Under certain simplifying assumptions we will do this in the present paper for a layered conductor with a quasi-two-dimensional energy spectrum of the charge carriers.

## 2. DERIVATION OF THE DISPERSION RELATION

Let the wave vector $\mathbf{k}$ and inner normal $\mathbf{n}$ to the plane surface of the sample be directed along principal (assumed to be mutually perpendicular) crystallographic axes. We consider a so-called TM wave, in which the electric field vector lies in the $(\mathbf{k},\mathbf{n})$ plane. We proceed from the Maxwell equation

$$\nabla\cdot\left(\frac{\partial\mathbf{E}}{\partial t}+4\pi\mathbf{j}\right)=0 \tag{1}$$

and (for now) neglect retardation due to the finite speed of light, leaving only a scalar potential in the definition of the field: $\mathbf{E}=-\nabla\varphi$. Then in the vacant half space $x_n<0$ a monochromatic wave has the form

$$\mathbf{E}\equiv\begin{pmatrix}E_k\\E_n\end{pmatrix}=E_n(-0)\begin{pmatrix}i\\1\end{pmatrix}\exp(i\mathbf{k}\cdot\mathbf{x}+k\mathbf{n}\cdot\mathbf{x}-i\omega t) \tag{2}$$

(in the formulas below, the common temporal factor $\exp(-i\omega t)$ will be dropped). Inside the metal ($x_n\geqslant 0$) the current density

$$\mathbf{j}\equiv-e\langle\mathbf{v}\psi\rangle\equiv-\frac{2e}{(2\pi\hbar)^3}\int\frac{dS_F}{v}\mathbf{v}\psi \tag{3}$$

should be calculated using the kinetic equation

$$v_n\frac{\partial\psi}{\partial x_n}+i\left(\mathbf{k}\cdot\mathbf{v}-\omega-\frac{i}{\tau}\right)\psi=-e\mathbf{v}\cdot\mathbf{E} \tag{4}$$

for the nonequilibrium part $\psi$ of the electron distribution function. Here $\mathbf{v}$ is the electron velocity, and the averaging in (3) is done over the Fermi surface $S_F$. Thus we are adopting a sharp boundary of the metal with no conduction current outside it. For other conducting objects such as rarefied plasmas, a model in which the boundary is macroscopically diffuse, such as was used in Ref. 8, may be more realistic. Incidentally, it was the authors of Ref. 8 who pointed out the desirability of a microscopic (i.e., using the kinetic equation) description of the surface plasma oscillations.

Since we are interested in high frequencies, comparable to the plasma frequency and substantially larger than the inverse relaxation time of the carriers at low temperatures, we neglect both the bulk and surface scattering of the carriers. The first of these means taking the limit $\omega+i/\tau\to\omega+i0$ in the kinetic equation,[2)] while the second means adopting a ''specular'' boundary condition for it:[3)]

$$\psi(+0,v_n)=\psi(+0,-v_n). \tag{5}$$

Condition (5) substantially simplifies the application of the Fourier method for solving the system of equations (1)–(4): if the function $E_k(x_n)$ is now continued to the negative $x_n$ semiaxis in an even manner and the function $E_n(x_n)$ in an odd manner, then the function $\psi(x_n)$ continued in accor-

 

dance with (4) will not have a jump (unknown and requiring special calculation) at $x_n=0$, and the current through the boundary will automatically be zero. As a result, after Fourier transformation with respect to the coordinate $x_n$ (with index $q$) the current density is expressed in terms of the nonlocal conductivity tensor $\sigma_{\alpha\beta}$ in the same way as in an unbounded metal:

$$\tilde{j}_\alpha(k,q)=\sigma_{\alpha\beta}\tilde{E}_\beta(k,q);$$

$$\sigma_{\alpha\beta}=ie^2\left\langle\frac{v_\alpha v_\beta}{\omega-\mathbf{Q}\cdot\mathbf{v}}\right\rangle;\quad \mathbf{Q}\equiv\mathbf{k}+\mathbf{n}q(\alpha,\beta=k,n). \tag{6}$$

In the Fourier transform (denoted by a tilde) the solution of the system of equations (1)–(4) with a given value of the normal component of the field at the boundary ($E_n(+0)$) has the form

$$\tilde{\mathbf{E}}=2E_n(+0)\frac{\mathbf{Q}}{iQ^2\epsilon(\mathbf{Q},\omega)}; \tag{7}$$

$$\epsilon(\mathbf{Q},\omega)\equiv1+\frac{4\pi i}{\omega}\sigma(\mathbf{Q},\omega)=1+\frac{4\pi e^2}{\omega Q^2}\left\langle\frac{(\mathbf{Q}\cdot v)^2}{\mathbf{Q}\cdot\mathbf{v}-\omega}\right\rangle. \tag{8}$$

Here $\epsilon(\mathbf{Q},\omega)$ is just the dielectric function of the infinite metal with respect to longitudinal electromagnetic oscillations with wave vector $\mathbf{Q}\equiv\mathbf{k}+\mathbf{n}q$.

In a microscopic treatment both field components must be continuous at the metal–vacuum interface. From this condition, calculating $E_k(+0)$ by inverse Fourier transformation of expression (7) and equating it to $E_k(-0)$ in Eq. (2), we obtain a dispersion relation in the form of an integral equation:

$$1+\frac{k}{\pi}\int_{-\infty}^{+\infty}\frac{dq}{Q^2\epsilon(\mathbf{Q},\omega)}=0. \tag{9}$$

Together with definition (8), Eq. (9) in principle solves the stated problem, enabling one to find the spectrum and collisionless damping of surface waves for any specified dispersion relation of the charge carriers.

### 3. ELECTRON DISPERSION RELATION

We use the simple but characteristic model of a quasi-two-dimensional energy spectrum of charge carriers in layered conductors which was proposed in Ref. 13:

$$\varepsilon(\mathbf{p})=\frac{p_x^2+p_y^2}{2m}-\frac{\hbar v_{z0}}{a}\cos\left(\frac{ap_z}{\hbar}\right). \tag{10}$$

Here $\mathbf{p}$ is the quasimomentum, $a$ is the period of the crystal lattice in the direction of weak conduction (the $0Z$ axis), and $v_{z0}$ is the maximum $z$ projection of the electron velocity. The latter is assumed small compared to $v_F\equiv\sqrt{2\varepsilon_F/m}$, so that the Fermi surface is a slightly corrugated open cylinder whose axis coincides with $p_z$, and the parameter that serves to characterize the anisotropy of the local values of the high-frequency conductivity is

$$\mu=\frac{\langle v_z^2\rangle}{\langle v_x^2\rangle}=\frac{v_{z0}^2}{v_F^2}. \tag{11}$$

The square of the plasma frequency for bulk waves propagating perpendicular to the layer (along $0Z$) is reduced in this same ratio:

$$\Omega_\perp^2=4\pi e^2\langle v_x^2\rangle=\frac{4\pi Ne^2}{m}\equiv\Omega^2;$$
$$\Omega_z^2=4\pi e^2\langle v_z^2\rangle=\mu\Omega^2 \tag{12}$$

($N$ is the concentration of free carriers).

In this model the longitudinal dielectric function for the principal directions of the wave vector $\mathbf{K}$, i.e., parallel and perpendicular to the $0Z$ axis, is easily calculated to be

$$\epsilon_z(K,\omega)=1+\frac{\kappa^2}{K^2}\left(1-\frac{\omega}{\sqrt{\omega^2-K^2v_{z0}^2}}\right); \tag{13}$$

$$\epsilon_\perp(K,\omega)=1+\frac{\kappa^2}{K^2}\left(1-\frac{\omega}{\sqrt{\omega^2-K^2v_F^2}}\right), \tag{14}$$

where

$$\kappa\equiv\sqrt{4\pi e^2\langle1\rangle}=\Omega\sqrt{2}/v_F=(2e/\hbar)\sqrt{m/a} \tag{15}$$

is the static screening decrement;[4] for $a\sim10^{-7}$ cm this gives $\kappa\sim10^8$ cm$^{-1}$. Formula (13) is exact (see Ref. 14), and Eq. (14) is accurate to higher orders in $\mu$.

Another manner of description is possible, wherein the layered conductor is represented as a periodic set of purely two-dimensional conducting layers separated by insulating layers with a specified dielectric constant (see, e.g., Refs. 15–17 and the references cited therein). However, such a model applies more to artificial superlattices with a mesoscopic period, in which the motion of the electrons in each layer can be considered as independent. If one is talking about a crystal with a layered structure and with a metallic type of conductivity both parallel and perpendicular to the layers, it is preferable to treat it in terms of a quasi-two-dimensional electron spectrum. Of course, a quantitative description of the electrodynamics of real layered metals such as tetrathiafulvalene salts $(BEDT–TTF)_2I_3$ can require a generalization of model (10), e.g., with the anisotropy of the Fermi surface in the basal plane taken into account.[18]

### 4. ACTIVATION FREQUENCIES OF SURFACE PLASMONS

Let us now return to the dispersion relation (9) (see also Eq. (8)) and transform it by calculating—as a zeroth approximation in $k$—the residue of the integral at small absolute values of $Q$ (at the point $q=ik\sqrt{\epsilon_{0k}/\epsilon_{0n}}$). The equation becomes

$$k\int_{(c)}\frac{dq}{\pi Q^2\epsilon(\mathbf{Q},\omega)}=-1-\epsilon_{0n}^{-1}\sqrt{\epsilon_{0n}/\epsilon_{0k}}\equiv G(\omega), \tag{16}$$

where the contour $(c)$ passes along the real $q$ axis but bypassing the indicated point from above. The right-hand side of (16) does not depend on $k$: it is determined by the local values of the partial dielectric functions for the crystallographic directions parallel to $\mathbf{k}$ or $\mathbf{n}$,

$$\epsilon_{0\alpha}=1-\frac{4\pi e^2\langle v_\alpha^2\rangle}{\omega^2}\equiv1-\frac{\Omega_\alpha^2}{\omega^2}\ (\alpha=k,n), \tag{17}$$

where $\Omega_\alpha$ are the corresponding activation frequencies of the bulk plasma oscillations [see Eq. (12)]. In those cases when one of the vectors **k** or **n** is orthogonal to the layers (we call these cases A and B, respectively) we have

$$G(\omega)=\frac{\omega^2}{\sqrt{(\Omega^2-\omega^2)(\mu\Omega^2-\omega^2)}}-1; \tag{18}$$

while if both vectors lie in the plane of the layers (case C) then we must set $\mu=1$ in (18). This function takes on positive values starting at the frequencies

$$\omega_\mu=\Omega\sqrt{\mu/(1+\mu)} \ \text{(in cases A, B)}$$
$$\text{and} \ \ \omega_1=\Omega/\sqrt{2} \ \text{(in case C)}, \tag{19}$$

which thus give the start of the surface plasmon spectrum in neglect of retardation ($c\to\infty$). We see that geometry C is actually equivalent to the case of an isotropic metal and can be used for comparison with it.

## 5. APPROXIMATE SOLUTION OF THE DISPERSION RELATION

In solving Eq. (16), it should be taken into account that the only surface waves amenable to direct experimental observation[5)] are those with comparatively long wavelengths, i.e., with wave numbers $k$ small in comparison to the corresponding parameters of the electronic subsystem of the metal, such as $\kappa$ or $k_F$ (in ''good'' metals these quantities are of the same order of magnitude). Therefore it is reasonable to limit consideration to the lowest approximation in $k$, in which the dispersion relation can be rewritten as

$$k(\omega)\int_{-\infty+i0}^{+\infty+i0}\frac{dq}{\pi q^2\epsilon(\mathbf{n}q,\omega)}=G(\omega)\equiv G(f,\mu) \tag{20}$$

(in some of the formulas below it will be convenient to use the reduced frequency $f\equiv\omega/\Omega$). The denominator of the integrand is then given by formula (13) or (14) and the integral is evaluated in an elementary manner: in cases A and C it is equal to the sum of the residue at the point

$$q_0(f)=i\kappa\sqrt{1-g(f)}, \ \ g(f)\equiv f\frac{f+\sqrt{f^2+8}}{4}, \tag{21}$$

and the contribution from the branch point

$$q_1(f)=\frac{\kappa f}{\sqrt{2}}=\frac{\omega+i0}{v_F}. \tag{22}$$

This latter contribution, i.e., the integral along the corresponding cut in the complex $q$ plane, is purely imaginary and describes Landau collisionless damping: it inevitably occurs in a system in which there are particles moving in phase with the wave.

In case B, on the other hand, as we see from a comparison of expressions (13) and (14), the result of the integration reduces to the previous result with the substitution $f\to f/\mu$. *Summarizing what we have said, we can present the results in the form*

$$\text{A)} \quad \mathbf{k}\|0Z: \ k[R(f)-i\Gamma(f)]=\kappa G(f,\mu); \tag{23}$$

$$\text{B)} \quad \mathbf{n}\|0Z: \ k[R(f/\sqrt{\mu})-i\Gamma(f/\sqrt{\mu})]=\kappa G(f,\mu); \tag{24}$$

$$\text{C)} \quad \mathbf{k}\times\mathbf{n}\|0Z: \ k[R(f)-i\Gamma(f)]=\kappa G(f,1), \tag{25}$$

where $R/\kappa$ and $\Gamma/\kappa$ are the real and imaginary parts of the integral in (20):

$$R(f)=\frac{1}{\sqrt{1-g(f)}}\frac{f^2}{f^2-g^3(f)}; \tag{26}$$

$$\Gamma(f)=\frac{f\sqrt{2}}{\pi}\int_0^\infty\frac{du}{\sqrt{1+u^2}}\frac{u^2}{1+(1+f^2(1+u^2)/2)^2u^2}. \tag{27}$$

Near the start of the spectrum

$$G(f,\mu)\approx(1+\mu)(f-f_\mu)f_\mu^{-3}; \ \ f_\mu=\sqrt{\mu/(1+\mu)} \tag{28}$$

[see Eqs. (18) and (19)], and in the remaining functions of the reduced frequency $f$ we can, as an approximation, substitute $f=f_\mu$. Thus the dispersion relation for surface waves has the form

$$\omega(k)\approx\Omega\sqrt{\mu/(1+\mu)}\left(1+\mu\frac{R-i\Gamma}{(1+\mu)^2}\frac{k}{\kappa}\right), \tag{29}$$

where, as is easy to compute using formulas (26) and (27), the quantities $R$ and $\Gamma$ in the particular cases under discussion take the following values:

$$\text{A)} \quad R(\sqrt{\mu/(1+\mu)})\approx 1;$$
$$\Gamma(\sqrt{\mu/(1+\mu)})\approx -0.449\sqrt{i}\ln\sqrt{i},$$
$$\text{B)} \quad R(1/\sqrt{(1+\mu)})\approx\sqrt{3/2}\mu^{-3/2};$$
$$\Gamma(1/\sqrt{(1+\mu)})\approx\Gamma(1)\approx 0.096;$$
$$\text{C)} \quad R(\sqrt{(1/2)})\approx 3.512; \Gamma(\sqrt{1/2})\approx 0.114. \tag{30}$$

The group velocity of the oscillations $V=\mathrm{Re}(\partial\omega/\partial k)$ is determined by the quantity $R$ and, consequently, in the leading approximation in $\mu\ll 1$ has the values

$$\text{A)} \ V\approx v_{z0}\frac{\mu}{\sqrt{2}}; \quad \text{B)} \ V\approx v_F\frac{\sqrt{3}}{2}; \quad \text{C)} \ V\approx 0.439v_F. \tag{31}$$

The velocity is anomalously low ($V\propto\mu^{3/2}$) for a wave propagating along a crystal boundary which is perpendicular to the layers; such waves may find use in so-called as delay lines. We also note the specific (stemming from the smallness of the anisotropy parameter) smallness of the relative damping $\Gamma/R$ in cases A and B; in case C, which is qualitatively equivalent to an isotropic metal, the collisionless damping only happens to be small numerically.

## 6. CONCERNING THE EXACT SOLUTION

It should be pointed out that the use of the lowest approximation in $k$ [i.e., going to Eq. (20)], although it is justified physically, is not at all necessary from a calculational standpoint: at least a numerical calculation of the dispersion curves can be carried out directly from formula (9). In the symmetric case C, on the other hand, for which $\epsilon(\mathbf{Q},\omega)=\epsilon_\perp(Q,\omega)$ [see Eq. (14)], an exact dispersion relation is easily obtained in analytical form as well. Calculating the residue of the integral in (16) at the point $\mathrm{Q}\equiv(k^2+q^2)^{1/2}=q_0(f)$, we obtain

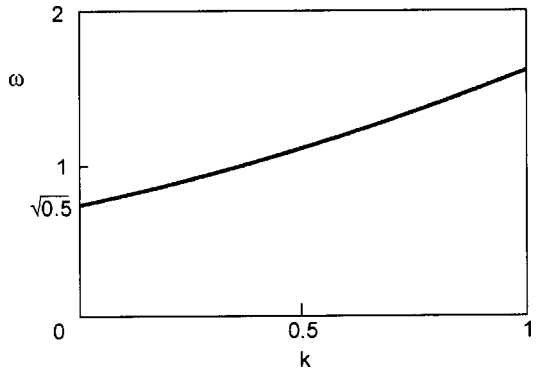


FIG. 1. Dispersion of a surface mode in the symmetric case C (in neglect of retardation). The frequency is in units of $\Omega$, the wave number in units of $\kappa$ [see formulas (12) and (15)].

$$R(f,k)=\frac{1}{\sqrt{1+k^2/\kappa^2-g(f)}}\,\frac{f^2}{f^2-g^3(f)}, \tag{32}$$

where the function $g(f)$ is defined in Eq. (21). Substituting (32) for $R(f)$ in relation (25) and neglecting the small damping, we obtain

$$k(f)=\kappa H(f)\left(\frac{1-g(f)}{1-H^2(f)}\right)^{1/2},$$

$$H(f)\equiv\frac{2f^2-1}{1-f^2}\left(1-\frac{g^3(f)}{f^2}\right). \tag{33}$$

This dependence is not too different from linear (see Fig. 1), thus confirming that the approximation used above is of sufficient accuracy.

## 7. ON THE POSSIBILITY OF AN INVERTED SPECTRUM

The results obtained permit a qualitative analysis of a possibility discussed repeatedly in the literature: an inverted surface-plasmon spectrum—according to Ref. 6, a fall-off of $\omega(k)$ at small $k$ has been observed experimentally. Since the function $R(\omega)$ is positive [Eq. (26)] while $G(\omega)$ is sign-varying [Eqs. (18) and (28)], our equations (20) and (23)–(25) in principle admit negative values of $k$ as well, but that would mean unbounded growth of the field in the vacant half space [for $x_n\to-\infty$; see Eq. (2)]. However, if the vacant (or insulating) region is a layer of finite thickness, e.g., in a waveguide between two metallic surfaces, then growing solutions in it are admissible, and they can lead to a fall-off of $\omega(k)$ in the initial part of the spectrum.

## 8. RETARDATION EFFECTS

Let us now take into account the finiteness of the speed of light $c$ and consider the dispersion of TM modes in the long-wavelength limit, i.e., for wave numbers $k$ comparable to $\omega/c$. This means that instead of (1) we must solve the Maxwell equation

$$c^2\nabla\times(\nabla\times\mathbf{E})=\omega^2\mathbf{E}+4\pi i\omega\mathbf{j}. \tag{34}$$

Applying the Fourier method under the same assumptions as in Sec. 2 and matching the solutions obtained for the metal and vacuum, we easily obtain the general dispersion relation

$$\int_{-\infty}^{+\infty}dq\,\frac{\epsilon_n p^2-k^2}{\pi D}=\sqrt{k^2-p^2}, \tag{35}$$

where

$$D(q,k,\omega)\equiv Q^2\epsilon(\mathbf{Q},\omega)-p^2(\epsilon_k\epsilon_n-S^2);$$

$$\epsilon_\alpha\equiv 1+\frac{4\pi i\sigma_{\alpha\alpha}}{\omega};\quad S\equiv\frac{4\pi i\sigma_{kn}}{\omega};\quad k>p\equiv\frac{\omega}{c} \tag{36}$$

[see Eqs. (6) and (8); the latter inequality ensures that the field falls off with distance from the metal]. This equation is more complicated than (9) [Eq. (26), of course, goes over to (9) for $p\to 0$], but since the characteristic velocities in the electron subsystem are much less than $c$, the second term in $D$ must be considered small. Therefore, when calculating the integral in (35) for sufficiently small $k$, we are justified in limiting consideration to only the residue at small $Q$, i.e., to substitute into $D$ the local values of the dielectric functions $\epsilon_{0\alpha}$ from (17); in the local case, cross conductivity is absent, $S_0=0$. As a result, the dispersion relation for long wavelengths has the form

$$k^2=\frac{\omega^2}{c^2}\,\epsilon_{0n}\frac{1-\epsilon_{0k}}{1-\epsilon_{0k}\epsilon_{0n}}. \tag{37}$$

The specifics of a layered conductor are manifested here only in the difference of the values of the local conductivity parallel to and perpendicular to the layers. Using definition (12), we obtain for the three geometries considered:

$$\text{A)}\quad \mathbf{k}\|0Z:\ k(\omega)=\frac{\omega}{c}\left[\mu\,\frac{\Omega^2-\omega^2}{\mu\Omega^2-\omega^2(1+\mu)}\right]^{1/2};$$

$$\text{B)}\quad \mathbf{n}\|0Z:\ k(\omega)=\frac{\omega}{c}\left[\frac{\mu\Omega^2-\omega^2}{\mu\Omega^2-\omega^2(1+\mu)}\right]^{1/2};$$

$$\text{C)}\quad \mathbf{k}\times\mathbf{n}\|0Z:\ k(\omega)=\frac{\omega}{c}\left[\frac{\Omega^2-\omega^2}{\Omega^2-2\omega^2}\right]^{1/2}. \tag{38}$$

Thus in the long-wavelength limit we have a nearly free electromagnetic wave ($\omega\approx kc$); then, in accordance with (19), the frequency goes to the limiting value $\Omega\sqrt{\mu/(1+\mu)}$, but in a different manner in cases A and B; in case C, as in an isotropic metal, this value is $\Omega/\sqrt{2}$. The corresponding plot for $\mu=0.1$ is shown in Fig. 2.

Of course, the ''local'' result (37), (38) can be obtained by simply solving the problem macroscopically, i.e., by expressing the current in (34) in terms of the local values of the conductivity tensor and then matching the tangential components of the field $E_k$ and the normal components of the electric displacement $\epsilon_{0n}E_n$ (in vacuum $\epsilon_{0n}\equiv 1$). However, we deemed it useful to give the general form of the integral-equation dispersion relation (35) and (36).

## 9. CONCLUSION

In summary, we have observed a number of features in the spectrum and damping of plasma waves of the TM type propagating along the surface of a layered conducting crystal in comparison with an isotropic metal having the same carrier concentration (or with the symmetric case C, when the Fermi surface is isotropic in the $(\mathbf{k},\mathbf{n})$ plane:

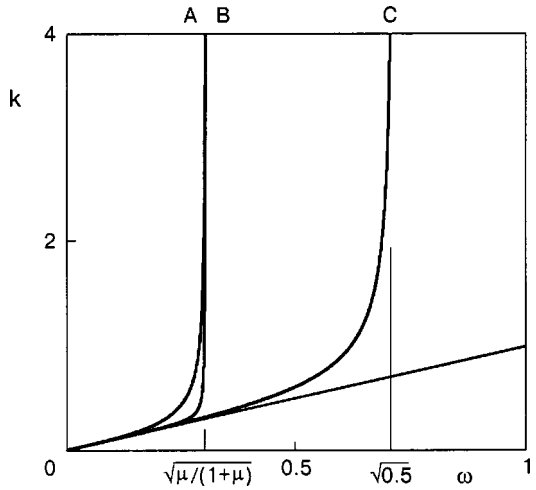


FIG. 2. Dispersion curves (with retardation taken into account) in the long-wavelength region in geometries A, B, and C; $\mu=0.1$. The frequency is in units of $\Omega$, the wave number in units of $\Omega/c$ [see Eq. (12)].

—The activation frequency is lowered substantially in the asymmetric cases, when either the wave vector or the normal to the surface is orthogonal to the layers [A and B in Eq. (19)].

—The surface mode propagating perpendicular to the layers is strongly slowed: its group velocity turns out to be much smaller than even the small Fermi velocity in this direction [case A in Eq. (31)].

—The relative damping (we are talking about collisionless damping in the regime $\omega\tau\gg 1$), i.e., the ratio $\Gamma/R$, turns out to be small in all three geometries (30). However, while in case C this smallness is only numerical, in the asymmetric cases A and B, which are characteristic for a layered conductor, it stems from the smallness of the anisotropy parameter $\mu$.

These properties of layered conducting crystals may be of significant interest from the standpoint of their practical use in microwave devices.

*E-mail: gokhfeld@host.dipt.donetsk.ua

[1)]Plasma waves in thin films and quantum effects are not considered in this paper.

[2)]A small imaginary admixture to the frequency—with positive sign—should be understood below wherever necessary for convergence or for choosing the necessary branches of the corresponding expressions.

[3)]Strictly speaking, the ''specular'' condition is justified only for an ideal boundary of the sample, parallel to a crystallographic reflection plane and repeating its symmetry, or in cases when small angles of incidence of the particles are important (see Ref. 9), as in case B considered below, for which the surface is parallel to the layers. However, in the well-known problems of the electrodynamics of metals, taking surface scattering into account ordinarily leads only to a numerical factor in the results (see, e.g., Refs. 10–12). It is important only when there is a significant group of carriers that collide quite frequently with the surface, e.g., in thin films and/or in a magnetic field.

[4)]In model (10) the density of states $\langle 1\rangle$, and with it the screening decrement $\kappa$, are independent of the energy $\varepsilon$. This is a more general property of a quasi-two-dimensional electron spectrum than is model (10); see Ref. 14.

[5)]In such experiments the wavelength is fixed by means of a diffraction grating positioned near the sample and, of course, having a period greater than the microscopic length $1/\kappa$ or $1/k_F$ (Ref. 17).

[1] J. Rayleigh, Proc. London Math. Soc. **17**, 4 (1885).
[2] R. Stoneley, Proc. R. Soc. London, Ser. A **106**, 416 (1924).
[3] R. H. Ritchie, Prog. Theor. Phys. **29**, 607 (1963).
[4] R. C. Browm and N. H. March, Phys. Rep. C **24**, 77 (1976).
[5] G. Barton, Rep. Prog. Phys. **42**, 963 (1979).
[6] N. H. March and M. Parrinello, *Collective Effects in Solids and Liquids*, Adam Hilger [Bristol (1982); Mir, Moscow (1986)].
[7] J. Vosnitza, *Fermi Surfaces of Low-Dimensional Organic Metals and Superconductors*, Vol. 134 of Springer Tracts in Modern Physics, Springer (1996).
[8] A. Ya. Blank and V. L. Berezinskiĭ, Zh. Éksp. Teor. Fiz. **75**, 2317 (1978) [Sov. Phys. JETP **48**, 1170 (1978)].
[9] A. F. Andreev, Usp. Fiz. Nauk **105**, No. 1, 447 (1971) [Sov. Phys. Usp. **14**, 1113 (1972)].
[10] G. E. Reuter and E. N. Sondheimer, Proc. R. Soc. London, Ser. A **195**, 336 (1948).
[11] L. E. Hartmann and J. M. Luttinger, Phys. Rev. **151**, 430 (1966).
[12] V. M. Gokhfel'd, M. I. Kaganov, and G. Ya. Lyubarskiĭ, Zh. Éksp. Teor. Fiz. **92**, 523 (1987) [Sov. Phys. JETP **65**, 295 (1987)].
[13] V. M. Gokhfel'd, M. I. Kaganov, and V. G. Peschanskiĭ, Fiz. Nizk. Temp. **12**, 1173 (1986) [Sov. J. Low Temp. Phys. **12**, 661 (1986)].
[14] V. M. Gokhfeld and V. G. Peschansky, *Nonlocal Acoustoelectronic Effects in Metals and Layered Conductors*, Sov. Sci. Rev. A **17**, Phys. Harwood Academic Publisher (1993).
[15] L. N. Bulaevskiĭ, Usp. Fiz. Nauk **116**, 449 (1975) [Sov. Phys. Usp. **18**, 514 (1975)].
[16] V. M. Gvozdikov, Fiz. Nizk. Temp. **26**, 776 (2000) [Low Temp. Phys. **26**, 569 (2000)].
[17] T. Ando, A. Fowler, and F. Stern, ''Electronic properties of two-dimensional systems,'' Rev. Mod. Phys. **54**, No. 2, 437–672 (1982) [Russian translation], Mir, Moscow (1985).
[18] V. M. Gokhfel'd, V. G. Peschanskiĭ, and D. A. Toryanik, Fiz. Nizk. Temp. **24**, 371 (1998) [Sov. J. Low Temp. Phys. **24**, 281 (1998)].

Translated by Steve Torstveit

## PHYSICAL PROPERTIES OF CRYOCRYSTALS

# Spectral function and character of the motion of a conduction electron in an orientationally disordered molecular cryocrystal

V. M. Loktev*

*N. N. Bogolyubov Institute of Theoretical Physics, National Academy of Sciences of Ukraine, ul. Metrologicheskaya 14-b, 03143 Kiev, Ukraine; KPI National Technical University, pr. Pobedy 37, 03056, Kiev, Ukraine*

S. G. Sharapov

*N. N. Bogolyubov Institute of Theoretical Physics, National Academy of Sciences of Ukraine, ul. Metrologicheskaya 14-b, 03143 Kiev, Ukraine; Institut de Physique, Universite de Neuchatel, CH-2000 Neuchatel, Switzerland*

H. Beck

*Institut de Physique, Universite de Neuchatel, CH-2000 Neuchatel, Switzerland*
(Submitted September 19, 2001; revised October 30, 2001)
Fiz. Nizk. Temp. **28**, 311–320 (March 2002)

The spectral function of an excess particle (electron or hole) moving in a molecular cryocrystal having no long-range orientational order is calculated. It is shown that the spectral function, on the assumption of exponential decay (in time and space) of the correlations between the angles specifying the direction of the axes of the molecules, changes sharply when disorder appears. The motion of the particle is transformed from coherent to incoherent (diffusive), in qualitative agreement with the results of recent $\mu$SR studies of the motion of electrons in $\beta$-$N_2$. © *2002 American Institute of Physics.* [DOI: 10.1063/1.1468528]

### 1. INTRODUCTION

The muon spin relaxation ($\mu$SR) method has become a very popular tool in recent years for research on solids. In this method the spectral and relaxation characteristics are measured for muons $\mu^+$ and the bound states which they form with electrons (muonium atoms Mu$\equiv\mu^+e^-$; see, e.g., the review[1]). The time of formation of Mu is largely determined by the electron mobility, which can vary by several orders of magnitude in insulators. The corresponding delay time of the spin-resonance signal from Mu in comparison with the signal from $\mu^+$, or the delay in the formation of muonium, is registered in a magnetic field, where the spin of the Mu atom has its own precession frequency and relaxation rate which are substantially different from those of the $\mu^+$ spin. If the electron mobility is high, then the time delay of the signal from the precessing Mu spin is short, usually $10^{-10}$ s or less; otherwise (e.g., in the case of low polaron mobility or localization of the electron) it is much longer and can reach $10^{-6}$ s. Thus this method affords a reliable and comparatively direct way of determining the kinetic parameters of the motion (coherent–incoherent) of quasiparticles, including electrons,[1)] in lattices, on the one hand, and of obtaining data by which to assess the degree and character of disorder in a crystal, on the other.

This method is particularly effective in insulating media, where the density of intrinsic electrons in the conduction band is vanishingly small, and the density of electrons injected into the crystal is not so large that the single-particle transport is complicated by appreciable contributions from electron–electron interaction effects which would have to be taken into account. Under these conditions the factors impeding the free—coherent—motion of an isolated fermion through the crystal are the intrinsic excitations of the crystal (phonons, librons in molecular systems), defects, and, finally, various types of disorder (static or dynamic). In particular, an example of the onset of disorder in a pure crystal (i.e., one without specially introduced defects or impurities) is provided by the nitrogen $N_2$ cryocrystal, in which at normal pressure and a temperature $T_{\alpha\beta}\approx 35.6$ K a first-order phase transition occurs from the low-temperature, completely ordered $\alpha$ phase (structure $Pa3$) to the high-temperature plastic $\beta$ phase, where the molecules, while preserving their translational order on going to a hexagonal lattice $P6_3/mmc$, become orientationally disordered.[2,3] Therefore, while in $\alpha$-$N_2$ one can speak of librons and their frequencies and dispersion,[4–6] the character and causes of the dynamic disorder in $\beta$-$N_2$, in which the $N_2$ molecules execute an angular rotational motion intermediate between the completely standard librations with respect to a fixed direction with an azimuthal angle $\theta_\beta\approx 55°$ (Ref. 2) and a nearly free precession with respect to the angle of elevation $\varphi$ in the basal plane, have not been conclusively established. There are only indications that there is a large entropy contribution to the free energy of the disordered state.[8] On the whole, the study of $\beta$-$N_2$ on the basis of model pair potentials in the mean-field approximation[5–10] has permitted determination of the main parameters of the intermolecular interaction, which

 

lead to the correct value of $T_{\alpha\beta}$ and also show that taking the corrections between pairs of rotating molecules (rotators) into account leads to a slight lowering of the free energy of the system.[3)]

Such a conclusion is extremely important, since it allows one to talk on a phenomenological level not about orientational disorder, which is in general hard to justify completely in a system of interacting molecules, but about the absence of long-range orientational order, which, as we shall see, admits description with the use of orientational correlation functions containing two physically obvious parameters—the orientational correlation length $\xi_{\rm or}$ and correlation time $\tau_{\rm or}$.

Apparently the first to measure the transport of excess electrons in a molecular crystal were Storchak *et al.*,[12] who investigated the solid solution $Ar_x(N_2)_{1-x}$ over a wide range of concentrations $x$. At rather high Ar concentrations (up to 20–25%), when this solution, as is confirmed by independent thermal[13] and structural[14] data, is found in an orientational glass state, its $\mu$SR response changes sharply. Based on this, the authors of Ref. 12 reached the quite natural conclusion that a localization of the moving light particle (electron) occurs in the disordered medium $Ar_x(N_2)_{1-x}$, in analogy to the localization of diffusing impuritons in quantum crystals (see Ref. 1). It should be noted, however, that in the quantum systems mentioned the defect potential can be comparable to or even considerably larger than (by several order of magnitude, as in the case of quantum diffusion) the bandwidth, which is considerably wider in classical molecular crystals of the $N_2$ type.[3] It is also important that systems such as $Ar_x(N_2)_{1-x}$, in which the disorder is not spontaneous but is due to the presence of an impurity subsystem, lose not only the orientational symmetry but, strictly speaking, the translational symmetry as well. And it is difficult to say *a priori* which of these has the more substantial effect on the transport of a quantum particle. Moreover, it is known[15,16] that the absence of long-range structural (or, equivalently, translational) order in itself will soon affect the dynamic structure function of low-dimensional dynamic lattices.

It is clear from what we have said that the cryocrystal $\beta$-$N_2$, as a plastic cryosystem, can in a certain sense be regarded as directly opposite example: first, in it the orientational disorder is spontaneous, for it is due to intrinsic (thermodynamic) causes; second, it is homogeneous, since it remains pure and preserves its full translational invariance; third, and last, its unquestionably 3D lattice can be considered weakly anisotropic to a good approximation.

We thus arrive at a rather concrete question concerning the motion of a conduction electron in an orientationally disordered molecular crystal. An attempt to answer it by proceeding from the form of the spectral function characterizing this motion for the particular case of the $\beta$-$N_2$ cryocrystal is the subject of this paper.

## 2. HAMILTONIAN OF THE CRYSTAL AND THE CORRELATION FUNCTION OF THE ORIENTATIONS

Before starting our calculation of the spectral function of the crystal, let us recall that the $N_2$ molecule is formed from N atoms, which have an outer electron configuration $2s^2p^3$. Here the $p_x$, $p_y$, and $p_z$ states of the $p$ shell form bonding and antibonding molecular orbitals such that the lowest state of the $N_2$ molecule is $^1\Sigma_g^+$, in which all 6 outer electrons completely fill the first of these molecular states. Then an extra electron entering the crystal and making one of the molecules charged can occupy any of the antibonding $p$ orbitals (the states $^3\Sigma_u^-$, $^5\Sigma_g^+$, and $^7\Sigma_u^-$) but most likely the one that forms the band with the greatest width or lowest energy. Thus the energy gap between the corresponding band of conducting states and the ground state of the insulating crystal will most likely be substantially less than the value 10 eV indicated in Ref. 12, where it was recently conjectured that the conduction band of the $N_2$ crystal is formed from the high-lying $3s$ states of the N atom, i.e., is found in the energy region where the crystal exhibits dipole absorption. However, values $\approx 2-3$ eV are completely sufficient in order to be able to neglect the presence of thermal electrons in a conduction band formed from antibonding states of the $N_2$ molecule.

The Hamiltonian of an electron moving through the crystal can be written in the simplest approximation as

$$H_{\rm el}=\frac{1}{2}\sum_{\mathbf{n},\boldsymbol{\rho}}\sum_{\sigma} t_{\mathbf{n},\mathbf{n}+\boldsymbol{\rho}}(\theta_{\mathbf{n}},\varphi_{\mathbf{n}};\theta_{\mathbf{n}+\boldsymbol{\rho}},\varphi_{\mathbf{n}+\boldsymbol{\rho}})a^{+}_{\mathbf{n}\sigma}a_{\mathbf{n}+\boldsymbol{\rho}\sigma}, \tag{1}$$

which is completely adequate for describing molecular crystals in the tight binding approximation.[3] In Eq. (1) the operators $a^{+}_{\mathbf{n}\sigma}$ and $a_{\mathbf{n}+\boldsymbol{\rho}\sigma}$ are the creation and annihilation operators for an electron with spin $\sigma$ on the nearest-neighbor molecules $\mathbf{n}$ and $\mathbf{n}+\boldsymbol{\rho}$, the orientations of which are specified by the angles $\theta_{\mathbf{n}}$, $\varphi_{\mathbf{n}}$, and $\theta_{\mathbf{n}+\boldsymbol{\rho}}$, $\varphi_{\mathbf{n}+\boldsymbol{\rho}}$, respectively; $t_{\mathbf{n},\mathbf{n}+\boldsymbol{\rho}}(\theta_{\mathbf{n}},\varphi_{\mathbf{n}};\theta_{\mathbf{n}+\boldsymbol{\rho}},\varphi_{\mathbf{n}+\boldsymbol{\rho}})$ is the matrix element for the hopping of an electron between these molecules. Although the dependence of $t_{\mathbf{n},\mathbf{n}+\boldsymbol{\rho}}(\theta_{\mathbf{n}},\varphi_{\mathbf{n}};\theta_{\mathbf{n}+\boldsymbol{\rho}},\varphi_{\mathbf{n}+\boldsymbol{\rho}})$ on the rotation angles can in principle be arbitrary, $\beta$-$N_2$ has one substantial simplification, noted above: the disorientation of the $N_2$ molecules in the crystal is specified solely by the angles of elevation $\varphi_{\mathbf{n}}$, since all of the azimuthal angles are the same: $\theta_{\mathbf{n}}=\theta_{\beta}$. Taking this fact into account substantially simplifies the calculation, since it makes the function $t_{\mathbf{n},\mathbf{n}+\boldsymbol{\rho}}(\theta_{\beta};\theta_{\mathbf{n}+\boldsymbol{\rho}};\varphi_{\mathbf{n}+\boldsymbol{\rho}})$ essentially a two-parameter one. Then the transition from the operators $a^{+}_{\mathbf{n}\sigma}$ and $a_{\mathbf{n}\sigma}$ specified in Eq. (1) in the proper quantization axes to the laboratory frame is equivalent, as is easily verified, to multiplying them by the phase factor $\exp(\pm i\varphi_{\mathbf{n}})$, which is entirely due to the $p$ character of the molecular states. Assuming here that the angles $\varphi_{\mathbf{n}}$ and $\varphi_{\mathbf{n}+\boldsymbol{\rho}}$ of the nearest-neighbor molecules are sufficiently correlated, as was stated in Ref. 8, we neglect the corresponding gradients in the Hamiltonian $H_{\rm el}$, reducing it to the standard form:

$$H_{\rm el}=\sum_{\mathbf{k},\sigma}\varepsilon(\mathbf{k})a^{+}_{\mathbf{k}\sigma}a_{\mathbf{k}\sigma}, \tag{2}$$

where in the effective mass approximation and in neglect of the weak anisotropy of the hexagonal lattice of $\beta$-$N_2$ we have $\varepsilon(\mathbf{k})\equiv t(\mathbf{k},\theta_{\beta})\approx \mathbf{k}^2/2m^*$, where $\mathbf{k}$ and $m^*$ are the wave vector and effective mass of the charged particle moving in the crystal.

The dispersion $\varepsilon(\mathbf{k})$ is nothing more than the kinetic energy, reckoned from the bottom of the conduction band, of an electron in a crystal lattice (in particular, that of $\alpha$-$N_2$) with long-range translational and orientational order. If for

some reason one of these is absent (in the case of $\beta$-$N_2$ that would be the orientational order), it becomes practically impossible to calculate the function $\varepsilon(\mathbf{k})$ in explicit form. One can, however, find the spectral function, which corresponds to the density of states of an electron in the conduction band of this medium. For this it is necessary to calculate the Matsubara Green's function

$$G(\mathbf{n},\tau) = -G(\mathbf{n},\tau+\beta) = -\langle a_{\mathbf{n}\sigma}(\tau) e^{i\varphi_{\mathbf{n}}(\tau)} a^{+}_{\mathbf{0}\sigma} e^{-i\varphi_{\mathbf{0}}(0)}\rangle \approx G^{(0)}(\mathbf{n},\tau) D_{\mathrm{or}}(\mathbf{n},\tau), \quad (3)$$

in which

$$G^{(0)}(\mathbf{n},\tau) = -\langle a_{\mathbf{n}\sigma}(\tau) a^{+}_{\mathbf{n}\sigma}\rangle \quad (4)$$

is the Green's function of an electron in the ideal crystal, $\tau$ is the imaginary time, $\beta \equiv 1/T$, and

$$D_{\mathrm{or}}(\mathbf{n},\tau) = \langle e^{i\varphi_{\mathbf{n}}(\tau)} e^{-i\varphi_{\mathbf{0}}(0)}\rangle \quad (5)$$

is the correlation function of the orientations, or angles, the form of which must be chosen on physical considerations. The notation in (3) reflects the fact the the creation or annihilation of an electron on some molecule with an arbitrary orientation with respect to the angle $\varphi$ corresponds to states specified in the proper reference frame (i.e., the frame tied to the molecule and its axis), and, just as in the case of the Hamiltonian, the necessary transition to the laboratory frame reduces for the $p$ functions to a phase factor. However, unlike the Hamiltonian operator (2), in which the direct hop of an electron is due solely to the nearest-neighbor molecules, the orientations of which are close, the distance $|\mathbf{n}|$ between the corresponding angles in (5) is arbitrary, since the difference $\varphi_{\mathbf{n}} - \varphi_{\mathbf{0}}$ can have any value from 0 to $2\pi$. We also note that the factorization used in (3) corresponds to the long-wavelength approximation, which was adopted in deriving (2), or to neglecting terms describing the indirect scattering of an electron on fluctuations of the orientations, and also presupposes that the function $G(\mathbf{n},\tau)$, like $\varepsilon(\mathbf{k})$, is independent of the variable $\sigma$ in view of the absence of any spin interactions. Importantly, the smallness of the gradients characterizes only the smoothness of the spatial variation of the angles $\varphi_{\mathbf{n}}$ and also, generally speaking, of $\theta_{\mathbf{n}}$; here the energy and momentum of the electron can be arbitrary (of course, within the limits of the conduction band and Brillouin zone). The use of the extremely simple dispersion relation is not fundamental and is done mainly to permit carrying out the calculation in analytical form.

Now writing the frequency–momentum representation for (3), we easily obtain an expression in the form a convolution:

$$G(\mathbf{k}, i\omega_n) = T \sum_{m=-\infty}^{\infty} \int \frac{d^3\rho}{(2\pi)^3} G^{(0)}(\mathbf{p}, i\omega_m) \times D_{\mathrm{or}}(\mathbf{k}-\mathbf{p}, i\omega_n - i\omega_m), \quad (6)$$

where

$$G^{(0)}(\mathbf{k}, i\omega_n) = \frac{1}{i\omega_n - \varepsilon(\mathbf{k})} \quad (7)$$

is the Fourier transform of the correlation function (4) with the Matsubara Fermi frequencies $\omega_{\mathbf{n}} = \pi T(2n+1)$, and

$$D_{\mathrm{or}}(\mathbf{q}, i\Omega_n) = \int_0^{\beta} d\tau \sum_{\mathbf{n}\neq 0} e^{i\Omega_n \tau - i\mathbf{q}\mathbf{n}} D_{\mathrm{or}}(\mathbf{n},\tau) \quad (8)$$

is the Fourier transform of the correlation function (5), in which $\Omega_{\mathbf{n}} = 2\pi T n$ is the Matsubara Bose frequency.

While the form of the function $G^{(0)}(\mathbf{n},\tau)$ can be recovered directly from the Fourier representation known for it [see, e.g., Eq. (7)], the function $D_{\mathrm{or}}(\mathbf{n},\tau)$ must be specified, as we have said. Its behavior in space and time are determined by the form of the intermolecular interaction, which, even for such a comparatively simple molecule as $N_2$ in the ground state, contains contributions from several different components.[3–10] Clearly the calculation of this function for the rotator subsystem at finite temperature is a separate problem and is generally a laborious task. Therefore, being interested only in the behavior of the spectral characteristics of the electron, we choose it in a rather general and simple form which conforms to the principle of decay of correlations and the asymptotic behavior at large distances in 3D systems:[17]

$$D_{\mathrm{or}}(\mathbf{n}) = \frac{\tau_0}{|\mathbf{n}|} e^{-|\mathbf{n}|/\xi_{\mathrm{or}}}. \quad (9)$$

The function (9), which contains the parameter $r_0$ having dimensions of length and being equal in order of magnitude to the intermolecular distance, is given for the static case, when the decay, which corresponds to the orientational correlation length $\xi_{\mathrm{or}}$, occurs in space. No doubt $\xi_{\mathrm{or}}$ is a function of $T$, with a form that depends on a number of factors (interactions, spatial dimensionality). These, as a rule, make $\xi_{\mathrm{or}}$ a decreasing function of $T$. Its concrete form has been established only for certain physical situations, in particular, for the high-temperature phase in the Berezinskii–Kosterlitz–Thouless transition.[18] In the present case of the $\alpha$–$\beta$ transition in solid nitrogen there is a first-order phase transition, in connection with which the behavior of $\xi_{\mathrm{or}}$, which necessarily satisfies the condition $d\xi_{\mathrm{or}}(T)/dT < 0$, can hardly manifest critical behavior on approach to $T_{\alpha\beta}$, and the $\beta$ phase arising after the transition is apparently immediately characterized by a quantity $\xi_{\mathrm{or}}(T)$ which is finite and decays smoothly with increasing $T$; this is essentially the only physical parameter characterizing the disordered orientational subsystem of $\beta$-$N_2$ in the case of static disorder.

The Fourier transform (8) for the correlation function (9) (and, in essence, a screened Coulomb potential) has the standard form:

$$D_{\mathrm{or}}(\mathbf{q}, i\Omega_n) = \frac{\delta_{n0}}{T} \frac{4\pi r_0}{\mathbf{q}^2 + \xi_{\mathrm{or}}^{-2}}. \quad (10)$$

Following Refs. 19 and 20, we can generalize expression (10) after obtaining the space–time form for the correlation function $D_{\mathrm{or}}(\mathbf{r},t)$, basing the specified frequency–momentum representation on it. Indeed, suppose it has the form

$$D_{\mathrm{or}}(\mathbf{q}, i\Omega_n) = \frac{4\pi c^2}{T[c^2\mathbf{q}^2 + c^2\xi_{\mathrm{or}}^{-2} + \Omega_n^2 + 2\tau_{\mathrm{or}}^{-1}|\Omega_n|]}, \quad (11)$$

in which $c$ is a constant with dimensions of velocity, and $\tau_{\mathrm{or}}$ is a characteristic time which, as we shall see, describes the rate of decay of the orientational correlations. Then, doing the inverse Fourier transformation of (11) with respect to

frequencies, we obtain an expression for the retarded Green's function, the temporal part of which can be written as follows:

$$D_{\rm or}^R(\mathbf{q},t\gg\tau_{\rm or})\sim\begin{cases}\exp(-t/\tau_{\rm or}), & c^2q^2>\tau_{\rm or}^{-2}-c^2\xi_{\rm or}^{-2};\\ \exp(-t/\tilde{\tau}_{\rm or}), & c^2q^2<\tau_{\rm or}^{-2}-c^2\xi_{\rm or}^{-2},\end{cases} \tag{12}$$

where $\tilde{\tau}_{\rm or}^{-1}\equiv\tau_{\rm or}^{-1}-\sqrt{\tau_{\rm or}^{-2}-c^2(\mathbf{q}^2+\xi_{\rm or}^{-2})}$ $(>0)$. We note that in both cases the expression obtained for $D_{\rm or}^R(\mathbf{q},t)$ agrees with the correction function proposed previously,

$$D_{\rm or}^R(\mathbf{r},t)=\left(\frac{r_0}{r}\right)^{T/2\pi j}\exp\left(-\frac{t}{\tau_{\rm or}(T)}-\frac{r}{\xi_{\rm or}(T)}\right), \tag{13}$$

which describes the space–time behavior of the correlations of the angles in the spin 2D $XY$ model[21] ($J$ is the exchange interaction constant). At the same time, it should be noted that formulas (12) and (13) are actually not identical, since, as follows from (12), the correlation decay rate determined by them depends on the wave vector. In particular, it is minimum for $\mathbf{q}=0$ and reaches a maximum value $\tau_{\rm or}^{-1}$ when $c^2q^2>\tau_{\rm or}^{-1}-c^2\xi_{\rm or}^{-2}$. This behavior possibly attests to the fact that at large $|\mathbf{n}|$ the orientations are so independent that their corrections no longer ''feel'' any kind of excitations of the medium which have an energy that depends on $\mathbf{q}$. In this sense the proposed phenomenological form (11) is the most most general, regardless of the concrete form of the spectrum of excitations of the disordered orientational subsystem of the molecular medium. In addition, the phenomenological parameters $\xi_{\rm or}$ and $\tau_{\rm or}$, having a simple physical meaning, cannot, strictly speaking, be completely arbitrary, and, for example, in the theory of critical phenomena there is a relation between them: when $T\to T_c+0$, then $\xi_{\rm or}\to\infty$ and $\tau_{\rm or}\to\infty$ (Ref. 21). However, in considering the case of a first-order transition, we will assume these parameters to be independent. We note, finally, that the largest contribution to the convolution (6) is from the term with $n=m$, which is the contribution from the static correlation function. In other words, it is the spatial decay of the static angular correlations that primarily affects the motion of an electron in a crystal lacking long-range orientational order.

The latter is extremely important, since we are talking about a medium in which the orientational order parameter is equal to zero and whose properties can be specified only by a correlation function (so-called correlational ordering). The specifics of $\beta$-$N_2$ which were noted above and which greatly simplify the calculation consist in the partial preservation of order or the constancy of the projection of the $N_2$ molecules onto the $C_3$ axis of the crystal. This, however, is not reflected in the character of its ground state, where the transverse (with respect to the $C_3$ axis) projections of the intramolecular axes are completely disordered (correlations aside), and the corresponding azimuthal angle and, principally, the correlation length and correlation time, are independent of temperature.

It can be assumed that after defining the correlation function in the form (13) the specifics of the system under consideration are to a certain degree lost, and the subsequent calculation in some way or other pertains to a rather broad class of media in which the motion of a particle (or quasiparticle) occurs against a background that is disordered with respect to some parameter. A necessary condition for this is that the Green's function of the particle in such a medium can be represented in the factorized form (3), which is not always obvious and requires checking in each individual case. Another important consideration is the possibility of using the free-particle Hamiltonian; otherwise, the long-wavelength approximation is inapplicable, and the scattering processes omitted in (2) will need to be taken into account directly.

### 3. DIFFERENT CASES OF ORIENTATIONAL CORRELATIONS

The spectral function of an electron is defined by the relation

$$A(\mathbf{k},\omega)=-\frac{1}{\pi}\,\mathrm{Im}\,G(\mathbf{k},\omega+i0), \tag{14}$$

where the Green's function is given by Eq. (3); here

$$G(\mathbf{k},i\omega_n)=\int_{-\infty}^{\infty}d\omega\,\frac{A(\mathbf{k},\omega)}{i\omega_n-\omega} \tag{15}$$

and, consequently,

$$G^{(0)}(\mathbf{p},i\omega_n)=\int_{-\infty}^{\infty}d\omega\,\frac{A^{(0)}(\mathbf{p},\omega)}{i\omega_n-\omega}. \tag{16}$$

The spectral function $A_{\rm or}(\mathbf{q},\Omega)$ is defined in the same way,

$$A_{\rm or}(\mathbf{q},\Omega)=-\frac{1}{\pi}\,\mathrm{Im}\,D_{\rm or}(\mathbf{q},\Omega+i0), \tag{17}$$

and

$$D_{\rm or}(\mathbf{q},i\Omega_n)=\int_{-\infty}^{\infty}d\Omega\,\frac{A_{\rm or}(\mathbf{q},\Omega)}{i\Omega_n-\Omega}. \tag{18}$$

Obviously, in an orientationally ordered phase the spectral function of an electron is

$$A(\mathbf{k},\omega)=A^{(0)}(\mathbf{k},\omega)=\delta(\omega-\varepsilon(\mathbf{k})), \tag{19}$$

which differs from the usual spectral function (see Ref. 22) by the absence of the chemical potential in the argument of the $\delta$ function. The latter circumstance is due to the fact that we are considering only excess electrons in an insulator, at a low enough density of which a Fermi surface is not formed.

The spectral density corresponding to (11) has the form

$$A_{\rm or}(\mathbf{q},\Omega)=-\frac{8r_0c^2}{T}\,\frac{\Omega\tau_{\rm or}^{-1}}{(\Omega^2-c^2\mathbf{q}^2-c^2\xi_{\rm or}^{-2})^2+4\Omega^2\tau_{\rm or}^{-2}}. \tag{20}$$

Now, substituting (16) and (18) into (6) and summing over the Matsubara frequencies, we arrive at the final expression for (14), which is represented by the integral

$$A(\mathbf{k},\omega)=\int_{-\infty}^{\infty}d\nu\left[\frac{1}{1+e^{\nu/T}}-\frac{1}{1-e^{(\nu-\omega)/T}}\right]\times\int_{\rm BZ}\frac{d^3p}{(2\pi)^3}A^{(0)}(\mathbf{p},\nu)A_{\rm or}(\mathbf{k}-\mathbf{p},\omega-\nu), \tag{21}$$

where the integration over $\mathbf{p}$ is limited to the Brillouin zone BZ. In the given form, expression (21) includes both the static case, for the description of which it is sufficient to limit

consideration to the correlation function $D_{or}(\mathbf{q}, i\Omega_n)$ in the form (10), and the dynamic case, described by formula (11). For convenience we shall consider these cases separately in view of the circumstance that, for example, the first of them—the static case—admits an analytical treatment.

### 3.1. Static orientational correlations

The formal calculations in the static case are analogous to those done in Refs. 11 and 19 for a 2D system, and so here we will only give the final result:

$$A(\mathbf{k},\omega)=\frac{A_0}{2\sqrt{W\varepsilon(\mathbf{k})}}\ln\frac{(\sqrt{\varepsilon(\mathbf{k})}+\sqrt{\omega})^2+\Omega_{or}}{(\sqrt{\varepsilon(\mathbf{k})}-\sqrt{\omega})^2+\Omega_{or}}\theta(\omega)\theta(W-\omega), \tag{22}$$

where $\Omega_{or}\equiv 1/(2m^*\xi_{or}^2)$ is the characteristic energy, which plays the role of a gap arising in the spectrum of long-wavelength correlations of the orientations as a result of their exponential decay, $W\equiv 1/(2m^*r_0^2)$ is the width of the conduction band, and $\theta(x)$ is the step function. The constant $A_0$, which is a function of $\mathbf{k}$ and $\Omega_{or}$ in (22), is chosen so as to satisfy the relation[22]

$$\int_{-\infty}^{\infty} d\omega A(\mathbf{k},\omega)=1. \tag{23}$$

Note the logarithmic character of the spectral function (22) and the circumstance that even for $\xi_{or}\to\infty$ it does not go over to $A^{(0)}(\mathbf{k},\omega)$ because of the presence of the "algebraic" factor $1/|\mathbf{n}|$ in the correlation function (9). The expression for $A(\mathbf{k},\omega)$ attests to the fact that the maximum of the spectral function is formed at energy $\omega\approx\varepsilon(\mathbf{k})$, and its intensity $\sim\ln\xi_{or}$, i.e., it grows very slowly. We also see from (22) that the spectral function for the case of static correlations is equal to zero in the regions both below the bottom and above the top of the conduction band, as is ensured the $\theta$ functions. Examples of the explicit form of the function $A(\mathbf{k},\omega)$ for different values of the correlation lengths are shown in Fig. 1, from which we see how fast the spectral function becomes practically independent of the energy $\omega$ with decreasing $\xi_{or}$.

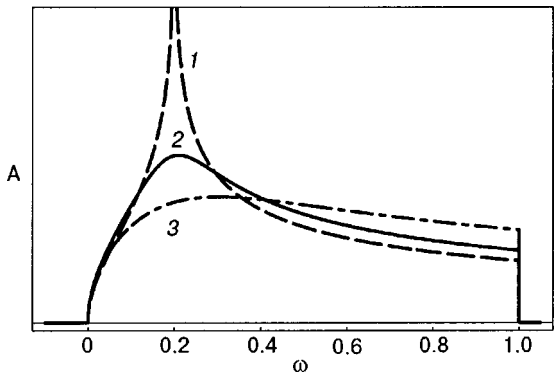


FIG. 1. Transformation of the spectral function $A(\mathbf{k},\omega)$ for an electron in a molecular crystal when only the static orientational disorder is taken into account, for different values of $\Omega_{or}$ or $\xi_{or}(\equiv 1/\sqrt{2m^*\Omega_{or}})$: *1*—$\Omega_{or}=0$, or $\xi_{or}=\infty$; *2*—$\Omega_{or}=10^{-3}$, or $\xi_{or}=31.6a$; *3*—$\Omega_{or}=10^{-2}$, or $\xi_{or}=10a$ ($a\sim r_0$ is the lattice constant, and the frequency $\omega$ is given in units of the conduction bandwidth, which in the numerical calculation was set equal to $W=1/(2m^*a^2)$ and was reckoned from the bottom of the band). The value of the energy $\mathbf{k}^2/2m^*=0.2W$.

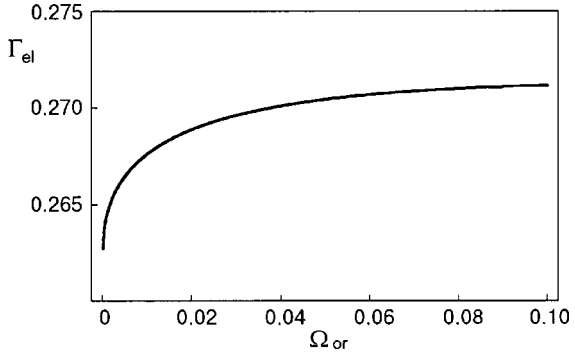


FIG. 2. Dependence of $\Gamma_{el}$ on $\Omega_{or}\equiv 1/(2m^*\xi_{or}^2)$. The normalization and the value of $\mathbf{k}^2/2m^*$ are the same as in Fig. 1.

In Fig. 2 we give the width $\Gamma_{el}$ of the distribution of the spectral density as a function of $\xi_{or}$; here $\Gamma_{el}$ was estimated from the relation $\Gamma_{el}=\sqrt{\langle\omega^2\rangle-\langle\omega\rangle^2}$, where $\langle\omega\rangle$ and $\langle\omega^2\rangle$ are the first and second moments of the function $A(\mathbf{k},\omega)$. The quantity $\Gamma_{el}^{-1}$ directly specifies the electron lifetime $\tau_{el}$ in a state with a given energy, and the smaller $\varepsilon_{el}$, the faster the free motion of the electron is transformed into incoherent motion.

### 3.2. Dynamic orientational correlations

The case of dynamic correlations requires integration of expression (21) with the spectral density (20) for the correlation function $D_{or}$. Doing the integral over momenta,[4)] we arrive at the final result

$$A(\mathbf{k},\omega)=\int_{-\infty}^{\infty} d\nu\left[\frac{1}{1+e^{(\nu+\omega)/T}}-\frac{1}{1-e^{\nu/T}}\right]f(\mathbf{k},\omega;\nu)\,\theta(\omega+\nu), \tag{24}$$

where we have used the following notion:

$$f(\mathbf{k},\omega;\nu)=\frac{A_0}{4\pi T}\frac{1}{\sqrt{W\varepsilon(\mathbf{k})}}\left(\arctan\frac{x_+-a}{b}-\arctan\frac{x_--a}{b}\right);$$

$$a=\frac{\omega^2}{2mc^2}-\Omega_{or};\quad b=\frac{\omega}{mc^2\tau_{or}};\quad x_\pm=(\sqrt{\varepsilon(\mathbf{k})}\pm\sqrt{\omega+\nu})^2. \tag{25}$$

Formula (24) was integrated numerically, and the corresponding curves are given in Fig. 3. The main difference from Fig. 1 is that the spectral function has acquired a long-wavelength part (the region $\omega<0$) and a short-wavelength part ($\omega>W$). Its qualitative behavior corresponds to the static case over a wide range of values of the correlation time $\tau_{or}$. This weak dependence of the spectral function on the corresponding relaxation time is typical for all such calculations.[11,20]

## 4. DISCUSSION AND CONCLUDING REMARKS

Our calculations of the spectral function of a conduction electron in an orientationally disordered but correlated medium have demonstrated the high sensitivity of this function to the appearance of disorder. Having a $\delta$-function-like character in a crystal with long-range order, this function becomes practically structureless even in the case of a correla-

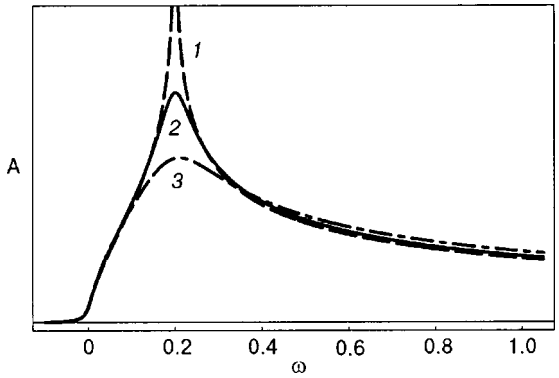


FIG. 3. Transformation of the spectral function $A(\mathbf{k},\omega)$ for an electron in a molecular crystal with allowance for the dynamic orientational disorder, for different values of $\Omega_{or}$ or $\xi_{or}(\equiv 1/\sqrt{2m^*\Omega_{or}})$: *1*—$\Omega_{or}=0$, or $\xi_{or}=\infty$; *2*—$\Omega_{or}=10^{-3}$, or $\xi_{or}=31.6a$; *3*—$\Omega_{or}=10^{-2}$, or $\xi_{or}=10a$. The inverse correlation time $\tau_{or}^{-1}=0.05W$. The normalization with respect to $\omega$ and the value of $\mathbf{k}^2/2m^*$ are the same as in Fig. 1.

tion length $\xi_{or}$ much greater than the lattice constant. In such a situation it is inappropriate to speak of coherent motion of the particle—it is transformed into diffusive motion and is in essence isotropic (provided, of course, that no electric field initial applied to the crystal). Random walks of the particle, which, as we know,[23] correspond to its diffusion in the medium, prevent or significantly decrease the probability that such a particle will encounter another object, an effect that occurs in the case of an electron and muon in solid $\beta$ nitrogen. If such a change in the motion does occur, then the signal from the bound state (Mu atom) will be delayed or absent altogether. In this case can one unambiguously pose the question of Anderson localization of the electron? It is undoubtedly present in impure (especially quantum) cyrocrystals, where it is promoted by the potential relief of the medium itself, which can have barriers (see Ref. 1) that cannot be overcome or are strongly suppressed for tunneling of a particle with a certain energy. However, in the case when impurities are absent and the medium on average is translationally ordered, the transition from coherent (free) motion characterized by a definite value of the momentum to incoherent (diffuses) motion is not due to the localization effect *per se* but is a consequence of scattering on excitations (in the example considered above, orientational) of the crystal. It can also be noted that Anderson localization is inherent to systems with a spread of single-particle levels (diagonal disorder[24]); in $\beta$-$N_2$ the physical situation is different, and the randomness (or spread of values) has to do with the kinetic term. It would seem that whatever its dispersion, it should always ''smear out'' the particle, although the extended states arising in this way will not be characterized by a definite momentum.

Thus the experiments of Ref. 12 actually provide grounds for concluding that the absence of long-range order in cryocrystals has a substantial influence on the transport characteristics (in particular, the mobility) of excess particles. However, it apparently does not yet follow from the data obtained that the slow formation of muonium is unambiguous evidence of localization of electrons in the solid insulating cryocrystal $Ar_x(N_2)_{1-x}$. We recall that the molecular parameters of the Ar atom and $N_2$ molecule are close;[3] on the other hand, for an electron injected into the system (unlike the case of doped semiconductors or doped HTSC systems) the neutral impurity atom Ar does not create a Coulomb well that could trap (localize) it. Therefore, the process of diffusion of the electron will continue until the probability of finding it at an arbitrary point of the crystal becomes independent of the coordinate, but the electron will not be localized in this case. If we estimate the width $\Gamma_{el}$ of the spectral distribution, we see (Fig. 2) that it is practically equal to $(0.25-0.27)W$, and the electron relaxation time $\tau_{el} \cong \Gamma_{el}^{-1}$. With the value $W\sim 10^2-10^3$ cm$^{-1}$, as is usually the case in cryocrystals,[3] this means that the electron will lose coherence over a time $\tau_{el}\sim 10^{-11}-10^{-12}$ s. Its mobility $\mu\sim\tau_{el}$ also becomes extremely small in this case.

Nevertheless, there is no doubt that $\mu$SR studies of the electron mobility in cryocrystals and its dependence on such characteristics as the orientational order/disorder, impurity content, temperature, etc. will open up new possibilities for studying both individual, mutually noninteracting quantum particles and the properties of the matrices in which they move.

This study was supported by the Swiss National Science Foundation (SCOPES Project 7UKPJ062150.00/1 and Grant 2000-061901.00/1). V.M.L. thanks A. P. Brodyanskiĭ for consultation on a question concerning the structure of the disordered phase of the nitrogen cryocrystal.

*E-mail: vloktev@bitp.kiev.ua

[1)]Everywhere below we use the term electron with the understanding that it could also be a hole or even a small-radius exciton.

[2)]In principle, the experimental data (x-ray diffraction, neutron scattering, etc.) admit interpretation in terms of a different picture—static disorder in which there are 12 equivalent positions of the $N_2$ molecules in space group $P6_3/mmc$ with the same angle $\theta_\beta$ between the axis of the molecule and the $C_6$ axis of the crystal.[7] However, dynamic disorder with uncorrelated rotations of the molecules about this axis is more widely accepted today.

[3)]Here it is appropriate to mention that taking into account the correlations between nearest-neighbor molecules in the hexagonal planes as in Ref. 8 showed that the angle between the latter should be 180°. It would seem, however, that ''ternary'' correlations, i.e., correlations with a 120° angle between nearest neighbors, would be a better match from a symmetry standpoint with a plane having a 6-fold axis. Then such a structure would be analogous to the 120° triangular spin structure of $\beta$-$O_2$, which also lacks long-range order.[11] However, exploring this question is beyond the scope of this paper.

[4)]Since it is done first, the cutoff at the upper limit is unnecessary, and it is sufficient to introduce a cutoff in the final integration over the frequency $\nu$ instead.

[1] V. G. Storchak and V. N. Prokof'ev, Rev. Mod. Phys. **70**, 929 (1998).
[2] T. A. Scott, Phys. Rep. **27**, 89 (1976).
[3] B. I. Verkin, and A. F. Prikhot'ko (Eds.), *Cryocrystals* [in Russian], Naukova Dumka, Kiev (1983).
[4] A. P. J. Jansen, W. J. Briels, and A. P. van der Avoird, J. Chem. Phys. **81**, 3648 (1984).
[5] A. P. van der Avoird, W. J. Briels, and A. P. J. Jansen, J. Chem. Phys. **81**, 3658 (1984).
[6] W. J. Briels, A. P. J. Jansen, and A. P. van der Avoird, J. Chem. Phys. **81**, 4118 (1984).
[7] J. C. Raich, N. C. Gillis, and T. R. Koehler, J. Chem. Phys. **61**, 1411 (1974).
[8] A. P. J. Jansen, J. Chem. Phys. **88**, 1914 (1988).
[9] V. V. Goldman and M. L. Klein, J. Chem. Phys. **64**, 1521 (1975).
[10] P. V. Dunmore, J. Low Temp. Phys. **24**, 397 (1976).
[11] V. M. Loktev and S. G. Sharapov, Fiz. Nizk. Temp. **26**, 1214 (2000) [Low Temp. Phys. **26**, 899 (2000)].

[12] V. G. Storchak, D. G. Eshchenko, J. H. Brewer, G. D. Morris, S. P. Cotrell, and S. F. J. Cox, Phys. Rev. Lett. **85**, 166 (2000).
[13] L. C. Ward, A. M. Saleh, and D. G. Haase, Phys. Rev. B **27**, 1832 (1983).
[14] H. Klee and K. Knorr, Phys. Rev. B **43**, 8658 (1991).
[15] H. J. Mikeska, Solid State Commun. **13**, 73 (1973).
[16] F. Weling, A. Griffin, and M. Carrington, Phys. Rev. B **28**, 5296 (1983).
[17] H. E. Stanley, *Introduction to Phase Transitions and Critical Phenomena*, Oxford University Press, Oxford (1987).
[18] J. M. Kosterlitz, J. Phys. C **7**, 1046 (1974).
[19] V. P. Gusynin, V. M. Loktev, and S. G. Sharapov, Zh. Éksp. Teor. Fiz. **117**, 1143 (2000) [JETP **90**, 993 (2000)].
[20] V. P. Gusynin, V. M. Loktev, R. M. Quick, and S. G. Sharapov, Preprint cond-mat/000727; Physica C (in press).
[21] D. L. Huber, Phys. Lett. **68**, 125 (1978).
[22] A. A. Abrikosov, L. P. Gorkov, and I. E. Dzyaloshinski, *Methods of Quantum Field Theory in Statistical Physics*, Dover, New York (1975).
[23] Yu. B. Gaĭdideĭ and A. A. Serikov, Theor. Math. Phys. **27**, 242 (1976).
[24] J. M. Ziman, *Models of Disorder*, Cambridge University Press, London (1979).

Translated by Steve Torstveit